Synthesis and Characterization of Rare Earth Doped Ternary Spinel Matrices using Non-Ceramic Routes for Luminescent and Biomedical Applications

Thesis submitted to

UNIVERSITY OF CALICUT

in partial fulfilment of the requirements
for the award of the degree of

DOCTOR OF PHILOSOPHY IN PHYSICS
under the Faculty of Science

By

Vinitha N

Under the guidance of

Dr Mini Krishna K
Associate Professor

Post Graduate and Research Department of Physics
Vimala College (Autonomous), Thrissur - 680009, Kerala, India
September 2025

Dr Mini Krishna K
Associate Professor
PG and Research Department of Physics
Vimala College (Autonomous), Thrissur-9

22/09/2025

CERTIFICATE

Certified that the work presented in this thesis entitled “Synthesis and Characterization of Rare Earth Doped Ternary Spinel Matrices using Non-Ceramic Routes for Luminescent and Biomedical Applications” is based on the authentic record of research carried out by Ms Vinitha N under my guidance in the Post Graduate and Research Department of Physics, Vimala College (Autonomous), Thrissur – 680 009 and has not been included in any other thesis submitted for the award of any degree and has been found to have no plagiarism using the software approved by UGC / University.

Dr Mini Krishna K
(Supervising Guide)

Dr. MINI KRISHNA K
Head, Department of Physics
Vimala College (Autonomous)
Thrissur-9

Email: minikrishna@vimalacollege.edu.in

DECLARATION

I hereby declare that the work presented in the thesis entitled "Synthesis and Characterization of Rare Earth Doped Ternary Spinel Matrices using Non-Ceramic Routes for Luminescent and Biomedical Applications" is based on the original work done by me under the guidance of Dr Mini Krishna K and has not been included in any other thesis submitted previously for the award of any degree. The contents of the thesis are undergone plagiarism check using 'iThenticate' software at C.H.M.K. Library, University of Calicut, and the similarity index found within the permissible limit. I also declare that the thesis is free from AI generated contents.

Vinitha

Thrissur
22/09/2025

Vinitha N
(Research Scholar)

Dr. MINI KRISHNA K
Head, Department of Physics
Vimala College (Autonomous)
Thrissur-9

Dr Mini Krishna K
(Supervising Guide)

Dedicated to all my teachers, friends & family

Acknowledgements

I express my heartfelt gratitude to my guide, Dr Mini Krishna K, for her unwavering support and invaluable guidance throughout the course of this work. Despite her demanding schedule, she always found time to mentor me, offering insights that consistently elevated the quality of my research. Her immense patience, constant encouragement, and motherly support were a source of strength and inspiration, enabling me to complete this work successfully. I will always remain deeply grateful for her genuine care and the confidence she instilled in me at every stage of this journey.

I am truly grateful to all my teachers for their inspiring guidance, continuous support, and for shaping both my academic and personal growth. I am especially thankful to Dr V P Joseph for introducing me to Dr Mini Krishna and for his initial guidance, which laid the foundation for my work.

I would like to extend my sincere thanks to all the teachers Dr Sr Ritty J Nedumbara, Dr Malini K A, Dr Veena Gopalan E, Dr Dhanya Johnson, Dr Jovia Jose, Ms Laveena Varghese, Mr Santhosh P Jose, Dr Aneesh George, Dr Regina Jose, Ms Anjaly Jose & Dr Litty Mathew Irimpan of the Department of Physics, Vimala College (Autonomous), Thrissur for their constant support, encouragement, and guidance throughout my research journey. I am also thankful to the laboratory staff Mrs Merina, Mrs Kochuthressia and Mr Soyson for their unconditional support. I am truly grateful for the positive academic environment they have created and their willingness to help at every step, which greatly contributed to the successful completion of my work.

Loving thanks to my dear colleagues Ms Sharon V S, Ms Smitha Bhaskaran, Ms Resmi T and Ms Haripriya V K, for their constant support, encouragement, and companionship extended towards me throughout. Their presence made every challenge easier and every success more meaningful. A very special thanks to my dear friends, Ms Rachana R and Ms Aswathy M, for always being by my side with their unwavering support and heartfelt friendship that meant the world to me throughout this journey.

I extend my sincere thanks to our respected Principal Dr Sr Beena Jose for providing a supportive academic environment, and to the library and office staff for their kind assistance and cooperation throughout the course of my work. I also fondly remember and thank all the staff members and research scholars of other departments for their friendly support, helpful discussions, and the collaborative spirit that enriched my research experience.

I gratefully acknowledge the financial support provided by KSCSTE through KSCSTE Research Fellowship programme, which played a crucial role in facilitating my research work.

I gratefully acknowledge the support provided by various research facilities and instrumentation centers that contributed to the successful completion of my work. I extend my sincere thanks to DST-FIST, DST-CURIE, and DBT-STAR programs of Vimala College for the research infrastructure. I extend my thanks to the Department of Physics, St. Thomas College (Autonomous), Thrissur, Department of Biotechnology, St. Mary's College (Autonomous), Thrissur for their instrumental support. I also thank Dr. Manoj A L, Department of Chemistry, St. Joseph's College (Autonomous), Irinjalakuda for his valuable help, as well as Amala Cancer Research Centre, Thrissur, STIC-CUSAT, USIC-Alagappa University for access to advanced analytical instruments and technical assistance.

I am forever grateful to my parents especially my Amma for her unconditional love, relentless hard work, and all the sacrifices she made for me. Her strength, selflessness, and unwavering support have been the foundation of everything I have achieved.

I am deeply thankful to my husband Akhil for his unconditional love, immense patience, and constant care, and for all the silent sacrifices he made while standing beside me through every struggle of this journey. I sincerely thank my precious daughters Aadvika and Anvaya for their patience and sacrifice that played a vital role in the success of this journey.

I sincerely thank my mother-in-law, father-in-law, and all my dear relatives for their unwavering support, blessings, and encouragement throughout this journey.

I wholeheartedly thank all the loving souls who stood by me with their prayers, kindness, and encouragement, making this journey a meaningful and fulfilling one.

I thank Almighty for His countless blessings, for guiding me throughout in adverse circumstances, and for the grace He bestowed upon me throughout this journey.

To the silent strength behind my perseverance,

Vinitha

Vinitha N

Abstract

Synthesis and Characterization of Rare Earth Doped Ternary Spinel Matrices using Non-Ceramic Routes for Luminescent and Biomedical Applications

Synthesis techniques do significantly influence the optical, magnetic, electronic and catalytic properties of materials, particularly in the nanometric dimension. The prime motive of the present work was to check the feasibility of three non-refractory routes - co-precipitation, hydrothermal and auto-combustion – to facilitate nanophosphor synthesis at temperatures well below 1000 °C. Structural, morphological, and optical properties were investigated using X-ray diffraction (XRD), fourier transform infrared (FTIR) spectroscopy, transmission electron microscopy (TEM), scanning electron microscopy (SEM), diffuse reflectance spectroscopy (DRS), photoluminescence (PL), and colorimetric analysis.

Optimization of synthesis parameters such as temperature and duration of synthesis, pH, post-calcination temperature, etc. were done for all the three synthesis routes in pure $ZnAl_2O_4$*. Further, the influence of* Eu^{3+} *and* Tb^{3+} *doping on luminescent behaviour of the ternary spinel were explored. The study also probed into the possibility of generating a white emission, through co-doping in* $ZnAl_2O_4$ *matrix, thereby enhancing the material potential for use in lighting and display technologies. The viability of the green auto-combustion procedure, using Moringa oleifera leaf extract as the natural fuel, was extended towards synthesis of other* AB_2O_4 *spinel systems (A – Zn, Mg; B – Al, Cr).*

Beyond luminescence, the synthesized pristine $ZnAl_2O_4$*, prepared via the three routes, were evaluated for photocatalytic degradation of methylene blue dye, where catalyst dosage and pH played critical roles. Biomedical potential was examined through in-vitro cytotoxicity analysis against Dalton's lymphoma ascites (DLA) and normal spleen cells. The photocatalytic, cytotoxic, and anti-bacterial response against E. coli. of selected green systems were also done.*

Overall, the study demonstrates the versatility of rare earth-doped spinel matrices synthesized via non-ceramic and green routes, underscoring their applicability in luminescent devices, photocatalysis, and biomedical systems. Future recommendations include exploring alternative dopants and microwave assisted synthesis, extending the eco-friendly approach to other spinel systems, and broadening applications across advanced functional materials.

Keywords: *Co-precipitation, Hydrothermal method, Green auto-combustion method, white light emission, ternary spinels.*

സംക്ഷേപം

പ്രകാശോത്സർജകവും ജൈവചികിത്സാ പ്രയോഗങ്ങൾക്കുമായി നോൺ-സെറാമിക് മാർഗങ്ങളിലൂടെ റെയർ-എർത്ത് മെറ്റൽസ് ഡോപ്പുചെയ്ത ത്രിതല സ്പിനൽ മാട്രിക്സുകളുടെ സംയോജനവും സ്വഭാവവിശകലനവും

സിന്തസിസ് സാങ്കേതികവിദ്യകൾ, പ്രത്യേകിച്ച് നാനോമീറ്റർ അളവിലുള്ള വസ്തുക്കളുടെ ഓപ്റ്റിക്കൽ, മാഗ്നറ്റിക്, ഇലക്ട്രോണിക്, കാറ്റലിറ്റിക് ഗുണങ്ങളെ ഗണ്യമായി സ്വാധീനിക്കുന്നു. ഈ ഗവേഷണത്തിന്റെ പ്രധാന ലക്ഷ്യം 1000 °C-ൽ താഴെയുള്ള താപനിലയിൽ നാനോഫോസ്ഫർ സിന്തസിസിന് സഹായിക്കുന്നതിനായി മൂന്ന് നോൺ-റിഫ്രാക്ടറി മാർഗങ്ങൾ — കോ-പ്രെസിപിറ്റേഷൻ (co-precipitation), ഹൈഡ്രോതെർമൽ (hydrothermal), ഓട്ടോ-കമ്പഷൻ (auto-combustion) — പരിശോധിക്കുകയായിരുന്നു.

സാമ്പിളുകളുടെ ഘടനാ (structural), ആകൃതിശാസ്ത്ര (morphological), ഓപ്റ്റിക്കൽ ഗുണങ്ങൾ എക്സ്-റേ ഡിഫ്റാക്ഷൻ (XRD), ഫൊറിയർ ട്രാൻസ്ഫോം ഇൻഫ്രാറെഡ് (FTIR) സ്പെക്ട്രോസ്കോപ്പി, ട്രാൻസ്മിഷൻ ഇലക്ട്രോൺ മൈക്രോസ്കോപ്പി (TEM), സ്കാനിംഗ് ഇലക്ട്രോൺ മൈക്രോസ്കോപ്പി (SEM), ഡിഫ്യൂസ് റിഫ്ലക്ടൻസ് സ്പെക്ട്രോസ്കോപ്പി (DRS), ഫോട്ടോലുമിനിസെൻസ് (PL), കളറിമെട്രിക് അനാലിസിസ് എന്നിവ ഉപയോഗിച്ച് പഠനവിധേയമാക്കി.

ശുദ്ധ $ZnAl_2O_4$-ൽ എല്ലാ സിന്തസിസ് മാർഗങ്ങളിലും താപനില, സമയം, pH, പോസ്റ്റ് കാൽസിനേഷൻ ടെമ്പറേച്ചർ തുടങ്ങിയ സിന്തസിസ് പാരാമീറ്ററുകളുടെ ഒപ്റ്റിമൈസേഷൻ നടത്തി. തുടർന്ന്, Eu^{3+}, Tb^{3+} ഡോപ്പിംഗ് ടെർണറി സ്പിനലിനുള്ള ലൂമിനസെന്റ് സ്വഭാവത്തെ എങ്ങനെ സ്വാധീനിക്കുന്നു എന്നതും പരിശോധിച്ചു. $ZnAl_2O_4$ മാട്രിക്സിൽ കോ-ഡോപ്പിങ് വഴി വെള്ള നിറത്തിലുള്ള (white emission) പ്രകാശം സൃഷ്ടിക്കാനുള്ള സാധ്യതയും പഠിച്ചു, ഇതിലൂടെ ലൈറ്റിംഗ്, ഡിസ്പ്ലേ സാങ്കേതികവിദ്യകളിൽ വസ്തുവിന്റെ പ്രായോഗികത വർദ്ധിപ്പിക്കാനാകുമെന്നു തെളിഞ്ഞു. Moringa oleifera ഇലയുടെ സാരാംശം പ്രകൃതിദത്ത ഇന്ധനമായി ഉപയോഗിക്കുന്ന ഗ്രീൻ ഓട്ടോ-കമ്പഷൻ മാർഗ്ഗം Zn, Mg (A), Al, Cr (B) അടങ്ങിയ മറ്റ് AB_2O_4 സ്പിനൽ സിസ്റ്റങ്ങളിലേക്കും വ്യാപിപ്പിച്ചു.

പ്രകാശോദ്വേശനത്തിനുപുറമെ, മൂന്നു സിന്തസിസ് മാർഗങ്ങളിലൂടെ തയ്യാറാക്കിയ $ZnAl_2O_4$ മെതിലിൻ ബ്ലൂ ഡൈയുടെ ഫോട്ടോകാറ്റലിറ്റിക് ഡീഗ്രേഡേഷനായി പരിശോധിച്ചു, ഇവിടെ കാറ്റലിസ്റ്റിന്റെ അളവും pH-ഉം നിർണായകമായിരുന്നു. കൂടാതെ Dalton’s lymphoma ascites (DLA), normal spleen cells എന്നിവയ്ക്കെതിരെ ഇൻവിട്രോ-സൈറ്റോടോക്സിസിറ്റി അനാലിസിസ് നടത്തി, ഇ-കോളിക്കെതിരെ ആന്റി ബാക്റ്റീരിയൽ സ്വഭാവവും ഗ്രീൻ സിസ്റ്റംസിൽ തെരഞ്ഞെടുത്ത ചില സാമ്പിളുകളിൽ വിലയിരുത്തി.

ആകെ, നോൺ-സെറാമിക്, ഗ്രീൻ മാർഗങ്ങളിലൂടെ സിന്തസിസ് ചെയ്ത റെയർ-എർത്ത് മെറ്റൽസ് ഡോപ്പിംഗ് ചെയ്ത സ്പിനൽ മാട്രിക്സുകൾ, ലൂമിനസെന്റ് ഡിവൈസസ്, ഫോട്ടോ കറ്റാലിസിസ്, ബയോമെഡിക്കൽ സിസ്റ്റംസ് എന്നിവയിൽ വ്യാപകമായി പ്രയോഗിക്കാവുന്നതാണെന്ന് പഠനം തെളിയിക്കുന്നു. ഭാവി സാധ്യതകളിൽ, മൈക്രോവേവ് അസ്സിസ്റ്റഡ് സിന്തസിസ്, മറ്റ് സ്പിനൽ സിസ്റ്റംസിലേക്കുള്ള പരിസ്ഥിതി സൗഹൃദ മാർഗങ്ങളുടെ വ്യാപനം, ആൾട്ടർനേറ്റിവ് ഡോപന്റ്സുകളുടെ ഉപയോഗം, കൂടാതെ ഫങ്ക്ഷണൽ മെറ്റീരിയൽസ് മേഖലയിൽ വിപുലമായ പ്രയോഗങ്ങൾ എന്നിവ ഉൾപ്പെടുന്നു.

കീവേഡുകൾ: കോ-പ്രെസിപ്പിറ്റേഷൻ, ഹൈഡ്രോതെർമൽ രീതി, ഗ്രീൻ ഓട്ടോ-കമ്പഷൻ രീതി, വെളുത്ത പ്രകാശ വിസർജനം, ടെർണറി സ്പിനൽ.

Preface

Synthesis of oxide phosphor systems generally demands high temperature combustion procedures, well above 1000 °C, and result in crystalline materials with large particle sizes and limited surface area. Additionally, prolonged high-temperature treatments can lead to undesirable phase transitions or compositional variations, further limiting the material's functionality. Low temperature synthesis procedures are, hence, to be explored to enable surface modification and functionalisation of nanophosphors that can modify their electronic, optical, magnetic, mechanical, and thermal characteristics, for sensors and displays along with catalytic and biomedical applications.

The thesis focusses on the synthesis of AB_2O_4 ternary spinel oxides via three non-ceramic synthesis routes - co-precipitation, hydrothermal and moringa leaf extract assisted green auto-combustion. These methods offer better control over morphology, crystallinity, and phase purity, meanwhile, reducing the energy consumption and production costs, making them more sustainable and commercially viable.

Chapter 1 introduces the title encompassing topics such as nanomaterials, nanophosphors and the phenomenon of luminescence. The chapter unravels the mechanism of photoluminescence, the fundamental energy transfer mechanisms in phosphor materials, the oxide phosphor system in comparison to conventional sulphur-based systems, and the spinel AB_2O_4 structure. A literature survey on $ZnAl_2O_4$ matrix is presented towards the end and the objective of the current work is outlined.

Chapter 2 explains the experimental and characterization techniques employed throughout the entire research. The three nanoparticle synthesis routes used in the present study and the synthesis strategies adopted are briefed in detail. Structural characterization tools - X-Ray Diffraction (XRD) spectroscopy, Transmission Electron Microscopy (TEM) and Fourier Transform Infrared (FTIR) spectroscopy, morphological and compositional techniques - Scanning Electron Microscopy (SEM) and Energy Dispersive Spectroscopy (EDS) are detailed. Optical properties are examined via Diffuse Reflectance Spectral (DRS) analysis, Photoluminescence (PL) and colorimetric analysis. The chapter also briefs the photocatalytic, anti-bacterial and anti-cancerous procedures used in the present study.

Chapter 3 focusses on the co-precipitation synthesis of pure and RE doped $ZnAl_2O_4$. The method optimises the calcination temperature and synthesis pH using the analytical techniques XRD, FTIR, TEM-SAED, SEM-EDAX and DRS. Further, the extraction of primary color emissions via RE (RE = Eu, Tb) doping of the host matrix is demonstrated through PL and colorimetric investigations.

Chapter 4 delves into the hydrothermal synthesis of pure and rare-earth (RE = Eu, Tb) doped $ZnAl_2O_4$. The synthesis pH, temperature and duration of hydrothermal treatment, and post-calcination procedure was first optimized for pristine $ZnAl_2O_4$. The study also probed into the synthesis of RE (RE = Eu, Tb) doped $ZnAl_2O_4$, varying the dopant concentrations, and the luminescent properties were investigated through PL spectroscopy and chromaticity diagram analysis.

Chapter 5 discusses the co-precipitation and hydrothermal synthesis of co-doped (RE = Eu, Tb) zinc aluminate. The PL spectral analysis throws light on the possibility of white or near-white color emission on co-doping the host matrix. The emissions were also gauged via colorimetric coordinates.

Chapter 6 focusses on the green auto-combustion synthesis of pure, singly doped, and co-doped $ZnAl_2O_4$ using Moringa leaf extract. The phytochemical analysis of the aqueous extract of dried moringa leaves is presented. PL investigations explored the effect of dopant incorporation on emission intensity and investigates the potential for white light emission in both doped and co-doped samples. The feasibility of extending the green synthesis approach to other AB_2O_4 systems (A = Zn, Mg; B = Al, Cr) is also examined.

Chapter 7 probes the photocatalytic performance of $ZnAl_2O_4$ synthesized via the co-precipitation method, specifically examining the influence of catalyst dosage and pH on the degradation of methylene blue dye. Additionally, the photocatalytic efficiencies of $ZnAl_2O_4$ prepared through hydrothermal and Moringa leaf extract-assisted auto-combustion methods are compared under similar experimental conditions. The in-vitro cytotoxic effects of $ZnAl_2O_4$ are evaluated against normal spleen cells and Dalton's lymphoma ascites (DLA) cells obtained from the peritoneal cavity of tumor-bearing mice. Furthermore, the antibacterial activity against E. coli and the cytotoxic responses of AB_2O_4 (A = Zn, Mg; B = Al, Cr) matrices synthesized via auto-combustion are also comparatively assessed.

Chapter 8, the final chapter of the thesis, presents a comprehensive summary and conclusion of the entire research work. It also highlights potential directions for future studies.

List of Publications

INTERNATIONAL JOURNALS

1. **Vinitha N.**, Rachana R., Mini Krishna K. (2024). Low temperature co-precipitation synthesis of $ZnAl_2O_4$ nanophosphors probing its luminescent, antibacterial and anticancer potentials. Journal of Fluorescence, https://doi.org/10.1007/s10895-024-03814-6 - *IF = 3.1*
2. Rachana R., Aswathy M., **Vinitha N.**, Ancy Mariya., Mini Krishna K. (2024). An investigation on the photocatalytic and antibacterial response of green fluorescent carbon dots synthesized from corn flour. Zeitschrift für Physikalische Chemie, https://doi.org/10.1515/zpch-2024-0793 - *IF = 3.2*
3. R. Rachana, M. Aswathy, **N. Vinitha**, A.L. Manoj, K. Mini Krishna (2025). The role of synthesis methods on the structural, optical and photocatalytic response of $CaTiO_3$: A comparative study. Results in Surfaces and Interfaces, https://doi.org/10.1016/j.rsurfi.2025.100665 - *IF = 4.4*

CONFERENCE PROCEEDINGS

1. **N. Vinitha.**, K. Arathy., K. Mini Krishna. (2023). On the structural and optical characterization of zinc aluminate nanoparticles synthesized via green microwave route. Materials Today Proceedings, https://doi.org/10.1016/j.matpr.2023.11.133 -*Cite Score = 4.8*
2. **N. Vinitha.**, Jini K Jose., K. Mini Krishna. A study on the luminescent response of europium doped Barium Aluminate nanophosphor. AIP Conference Proceedings 2783, 020016 (2023), https://doi.org/10.1063/5.0158457 - *IF = 0.41*

3. **N. Vinitha**., Jisa Baby., K. Mini Krishna. Effect of annealing temperature on the structure of a ternary aluminate phosphor synthesized via co-precipitation. AIP conference proceedings 2082, 030034 (2019), https://doi.org/10.1063/1.5093852 *-IF = 0.41*

Paper Presentations

1. A paper on 'Exploring the white light emitting capability of ternary zinc aluminate by co-doping with Eu^{3+} and Tb^{3+} via co-precipitation route' at an international conference ICAMFC-2024 conducted by MES PONNANI college, Ponnani, Malappuram on 14-16 February 2024 – Won second best paper award
2. A paper on 'On the structural and optical characterization of zinc aluminate nanoparticles synthesized via green microwave route' at an international conference STAM-2023 conducted by MA college, Kothamangalam on 18-20 April 2023.
3. A poster on 'Effect of chromium doping on the structural and optical properties of microwave synthesized zinc aluminate nanophosphor' at an international conference ICFMAT-2023 conducted by Central university of Kerala, on 2-4 January 2023.
4. A poster on 'A Study on the Luminescent Response of Europium Doped Barium Aluminate Nanophosphor' at an international conference NANOICON-2022 held at CUSAT, Cochin on 11-15 January 2022.
5. A poster on 'Luminescent studies in Europium doped zinc aluminate nanophosphor' at a national seminar emMET-II held at Christ College, Irinjalakkuda on 24-25 January 2019.
6. A poster on 'The effect of annealing temperature on the structure of a ternary aluminate phosphor synthesized via co-precipitation' at an international conference ICONMAT 2019 held at CUSAT, Cochin on 2-5 January 2019.

Contents

Chapter No. Title Page No.

1 Introduction

2 Experimental techniques

3 Luminescent Studies in Pristine and RE (RE = Eu, Tb) Doped $ZnAl_2O_4$ Nanophosphor Synthesized using Co-Precipitation Technique

4 Luminescent Studies in Pristine and RE (RE = Eu, Tb) Doped $ZnAl_2O_4$ Nanophosphor Synthesized using Hydrothermal route

8 Summary and Future Recommendations

List of Figures

List of Tables

Chapter 1

INTRODUCTION

The chapter introduces nanomaterials, in particular nanophosphors and the phenomenon of luminescence. It discusses the mechanism of photoluminescence, the basic energy transfer mechanisms in phosphor materials, the oxide phosphor matrix in comparison to conventional sulphur-based systems, and the spinel AB_2O_4 *structure. A literature survey on* $ZnAl_2O_4$ *matrix is presented and the objective of the current work is outlined.*

1.1 Nanomaterials

Nanomaterials (NMs) have gained significant attention as a versatile category of resource with broad practical applications. A nanometre is roughly the length of five silicon atoms or ten hydrogen atoms arranged in a row. Materials are classified as nanomaterials if any of their dimensions fall within the range of 1 to 100 nm. However, the use of nanomaterials dates to ancient times, with humans unknowingly employing them for various applications long before their properties were scientifically understood. The term "nanometre" was first coined in 1914 by Richard Adolf Zsigmondy. Later, in 1959, American physicist and Nobel laureate Richard Feynman introduced the concept of nanotechnology in his famous speech at the annual meeting of the American Physical Society. In his talk, Feynman emphasized that the limitations of working at the atomic and molecular scales were not due to the laws of nature, but rather due to the lack of necessary tools and techniques. His vision laid the groundwork for the development of modern nanotechnology, earning him the title as the "father of nanotechnology" [1–5].

Nanomaterials, with at least one dimension ranging from sub-nanometre to 10 nm, exhibit unique behaviours compared to their bulk counterparts, such as a dramatic increase in reactivity. Their distinct physicochemical properties - size, shape, composition, and surface characteristics - play a crucial role in determining their activity and performance. Understanding the structure-property relationships of these materials requires comprehensive physicochemical characterization, which serves as the foundation for their application in various fields. Accurate determination of nanomaterial properties is a key area of focus in nanotechnology and demands the use of advanced, reliable techniques capable of probing the nanoscale with high sensitivity [6]. The development of various spectroscopic techniques has significantly accelerated research and innovation in nanotechnology. Today, nanotechnology is advancing rapidly, becoming an integral part of nearly every field related to material science. With the availability of powerful characterization and synthesis tools, researchers can now produce nanomaterials with more precise control over their dimensions. Nanotechnology stands as a prime example of an emerging technology, enabling the creation of engineered nanomaterials that enhance the performance of a wide range of products. Currently, nanomaterials are commercially utilized in diverse applications, including scratch-resistant paints, surface coatings, electronics, environmental remediation, sports equipment, sensors, and energy storage devices, highlighting their transformative potential across industries [7–10].

Nanomaterials have many applications in the fields of household, cosmetics, textiles, energy storage, sports, food and drinks, automotive industry, electronics, construction and engineering materials, medicine etc [11]. Nanomaterials are classified based on their dimensionality, morphology, state, and chemical composition. Bestowing to their dimensionality and shape, NMs can be grouped into four categories. Zero-dimensional (0D) nanomaterials, such as quantum dots (QDs), spherical NMs, and core-shell structures, have all their dimensions in the nanoscale. One-dimensional (1D) nanomaterials, like nanotubes, nanowires, and nanofibers, have one dimension outside the nanoscale, with the other two in the nanoscale. Two-dimensional (2D) nanomaterials, such as thin films and nanoplates, have only one dimension at the nanoscale, while the other two exceed it. Three-dimensional (3D) nanomaterials, including foams, honeycombs, and fullerenes, combine multiple nanocrystals and extend beyond the nanoscale in all dimensions. NMs can also be categorized based on their morphology, such as flatness, sphericity, and aspect ratio, and can be either isometric and uniform or inhomogeneous and agglomerated. The agglomeration, influenced by electromagnetic properties, surface charge, and functionalization, affects their hydrophobicity or hydrophilicity in liquids. Additionally, NMs are classified by their chemical composition into categories like carbonaceous NMs (e.g., fullerenes, CNTs, and graphene), metallic NMs (e.g., silver, copper, and zinc), and nanocomposites, which combine nanoparticles (NPs) with standard materials to enhance properties like mechanical strength or conductivity. QDs, a specific type of nanomaterial, are tiny semiconductor particles with unique optical and electronic properties due to quantum effects, absorbing and re-emitting light at specific wavelengths [8,12–15].

Among the most extensively studied types of nanomaterials are metal nanomaterials, metal oxide nanomaterials, bimetallic nanomaterials, composite nanomaterials, carbon-based nanomaterials, ceramic nanomaterials, and semiconductor nanomaterials. The properties of these nanomaterials are primarily determined by their size and the arrangement of atoms, which can vary significantly depending on factors such as the synthesis method, processing conditions, and material composition. These variations in atomic structure and size contribute to the unique and often enhanced properties of nanomaterials compared to their bulk counterparts, influencing their reactivity, strength, conductivity, and other performance characteristics [12,16].

Nanomaterials can be tailored by modifying their surface with various functional groups and chemical species, enabling the creation of specific active sites and the tuning of surface characteristics. This ability to functionalize nanomaterials gives them unique surface interactions, making them suitable for a wide range of applications across different fields. The properties of nanomaterials, such as electronic, optical, magnetic, mechanical, and thermal characteristics, can all be modified through these surface modifications. In this work, the focus is on exploring the electronic and optical properties of nanophosphors in detail, highlighting how their performance can enrich and enhance specific applications [8].

1.2 Nanophosphors

The optical properties of semiconductor nanoparticles are closely linked to their size, with a notable example being the blue shift in the band gap and the strong nonlinear response observed in CdS and CdSe nanoparticles in glass samples, first reported in the early 1980s. Subsequent studies on other semiconductor nanoparticles, such as ZnS, PbS, ZnSe, and CdSe, further confirmed the enhanced quantum properties exhibited by these materials. In recent years, substantial research efforts have been dedicated to understanding the physics of nanophosphors, particularly those in the category of doped nanocrystals (DNCs) and quantum dots. Advances in quantum confined 2D-electron gas structures have further propelled this research, driving innovations in device fabrication at the nanoscale. Although the challenge of developing such technologies is significant, the potential rewards are substantial [17].

Nanophosphors are nanostructured, inorganic, insulating materials that emit light efficiently when excited by particles or photons. A key area of research is the synthesis and characterization of rare earth (RE) doped nanophosphors, with a particular focus on their optical properties and how these properties change as their dimensionality is reduced. Rare earth (RE) ions are highly effective luminescent centers when incorporated into host lattices, often leading to high quantum efficiency in bulk phosphors. Unlike semiconductor quantum dots, where electronic states are spatially extended and quantum confined, the 4f electronic states of RE ions are inherently localized and remain largely unaffected by dimensional reduction.

However, the phonon levels in nanophosphors become delocalized as the material size decreases, and the phonon density of states (PDOS) is reduced in nanoparticles. This reduction in PDOS, particularly the cut-off of low-frequency acoustic phonon modes due to spatial confinement, plays a crucial role in altering the optical properties of nanophosphors compared to their bulk counterparts. These low-frequency phonons contribute significantly to non-radiative relaxation processes, meaning their reduction enhances the radiative efficiency and changes the luminescence behaviour in nanophosphors.

Additional factors influencing the optical properties of RE-doped nanophosphors include crystal field effects, spin-orbit coupling of 4f electrons, and the large surface-to-volume ratio of the nanostructured material. These combined factors provide valuable insights into how reduced dimensionality affects the optical performance of nanophosphors. Phosphors do play an integral role in modern technology - ranging from applications in fluorescent lighting and cathode ray tube displays to medical imaging technologies like positron emission tomography (PET) scanners and nuclear radiation detection. Hitherto, investigating the full potential of nanophosphor materials is immensely relevant for advancing both fundamental research and practical applications [18].

Nanophosphors are typically synthesized as powders, though some are prepared in matrixes or as films using various techniques. The materials produced are then characterized through a range of advanced techniques. Luminescence properties are assessed using specialized instruments designed to exceed current standards in terms of excitation and emission range, spectral resolution, nano- to picosecond time resolution, along with high-intensity, high-energy excitation sources. Other key characterization methods include X-ray diffraction (XRD), small angle X-ray scattering (SAXS), small angle neutron scattering (SANS), high-resolution electron microscopy (HRTEM), low-frequency Raman scattering, longitudinal-optic (LO) phonon Raman scattering, atomic force microscopy (AFM), time-of-flight secondary ion mass spectrometry (ToF-SIMS), and X-ray photoelectron spectroscopy (XPS). These techniques are crucial for advancing our understanding of nanophosphors and their potential applications [19].

Rare-earth-doped phosphors are renowned for their ability to emit light at distinct wavelengths across the electromagnetic spectrum, making them essential in a wide range of applications. These phosphors have been integral to technologies such as color cathode ray tubes (CRT), tri-phosphor fluorescent lamps, X-ray intensifying screens, and recently developed vacuum mercury-free lamps. They are also used in various types of displays, including plasma display panels (PDPs), field emission displays (FEDs), and projection televisions. Additionally, laser detection phosphors (LDPs) are employed to detect infrared lasers by converting infrared energy into visible light, while storage phosphors can capture a broad spectrum of infrared energy but require charging via daylight or ultraviolet light before releasing the stored energy. "Anti-Stokes" phosphors, on the other hand, directly convert infrared energy to visible light, providing continuous output but with a more limited response to infrared radiation.

The performance of these phosphors depends on several factors, such as the selection of the host lattice, suitable activators or coactivators, doping processes, and the underlying physics of nanophosphors, which include quantum confinement, quantum size effects, surface area, surface morphology, band gap variations, and shifts in excitation energy. Understanding these parameters is crucial for selecting the right materials and synthesizing nanophosphors with optimal properties [17].

With the increasing importance of phosphors in a multibillion-dollar industry, especially in the realm of display technologies, there is a pressing need to assess and enhance scientific knowledge and technological capabilities in this area. Multidisciplinary collaboration and research are essential to further advancements in nanophosphor synthesis and applications. For instance, phosphors used in displays must meet international analog video standards such as NTSC (National Television System Committee) and PAL (Phase Alternating Line), with distinct frame rate and resolution, to ensure color accuracy and consistency. Despite considerable progress, there are still relatively few phosphors that are fully suitable for display applications. The synthesis, characterization, and manufacturing of commercial phosphors are well-documented in the literature, but ongoing efforts to develop new materials and improve existing ones are critical to meet the evolving demands of modern display technologies and beyond [20].

The morphology (particle size and shape), particle size distribution (PSD), body color, and rheology are critical physical factors influencing the performance of display phosphors. Rheological properties of a paste or slurry are determined by the particle size, shape, and the binders and vehicles used. Display phosphors are typically manufactured using processes like settling, slurry deposition, dusting, screen printing, or inkjet techniques. The morphology, PSD, and thickness of the phosphor layer not only affect the manufacturing process but also play a significant role in display performance. For instance, incorporating flux materials during preparation can modify the phosphor's morphology and improve its luminescent properties. Spherical particles are advantageous as they reduce the need for excess binders and vehicles, while smaller particles improve packing density and overall display efficiency [17,18,21,22].

In addition to these structural factors, optical properties such as excitation, emission, brightness, afterglow decay (or persistence), color coordinates, saturation, and degradation must be optimized for optimal display performance. Other key parameters, such as the purity of raw materials, the blend ratio of raw materials, synthesis methods, processing atmosphere, particle size control, and firing conditions, also significantly impact the quality of the phosphors. Therefore, the optimization of all these factors is essential for producing high-performance display phosphors [23–25].

1.3 Luminescence

The term luminescence, derived from the Latin word *lumen* meaning "light," was first introduced as “luminescenz” by physicist and science historian Eilhardt Wiedemann in 1888. Unlike incandescence, luminescence is not caused by heat and is therefore often referred to as "cold light." It is defined as the spontaneous emission of non-thermal radiation from an electronically or vibrationally excited species that is not in thermal equilibrium with its surroundings. Luminescence is categorized based on the mode of excitation, with types including photoluminescence, electroluminescence, cathodoluminescence, chemiluminescence, sonoluminescence, triboluminescence, and many more [26].

1.3.1 Photoluminescence

Photoluminescence, which is the focus of this study, involves the emission of light following the absorption of photons with shorter wavelengths. The material that exhibits the phenomenon of photoluminescence is called a phosphor. A phosphor matrix generally comprises of a host lattice capable of incorporating activator ions, a deliberately added impurity that can modify the spectral output of the host. For efficient activator assimilation, it is ideal to have an exceptional match between the valency and ionic radii of the activator ion and the replaced host lattice cation. In case of any mismatch, charge compensation can be achieved intrinsically through creation of anion vacancies or extrinsically via charge compensating impurities referred to as the co-activator.

Photoluminescence can be classified into intrinsic or extrinsic luminescence. Intrinsic luminescence refers to that light emission which originates from within a pure material or crystal itself. It is of three types, band to band luminescence, cross luminescence and exciton luminescence. Band to band luminescence occurs when an electron in the conduction band (CB) recombines with a hole in the valence band (VB), creating a band-to-band transition. It is seen in pure materials at high temperatures but shifts to exciton luminescence at low temperatures. Examples include Si, Ge, and GaAs. Cross-luminescence occurs when an electron in the valence band recombines with a hole in the outermost core band. This type of luminescence is commonly observed in alkali and alkaline-earth halides, as well as double halides. An exciton is a bound electron-hole pair where an excited electron interacts with a hole, and as it moves through the crystal, it recombines to emit luminescence, which is the exciton luminescence. There are two types: the Wannier exciton, found in IIIb–Vb and IIb–VIb semiconductors, involves an electron in CB and a hole in VB bound by Coulomb interaction; the Frenkel exciton, found in organic crystals, inorganic complex salts, and uranyl salts, has smaller electron and hole wavefunction overlap than the lattice constant [26].

Extrinsic luminescence is caused by deliberately introducing impurities or defects into a phosphor, and in ionic crystals and semiconductors, it can be either unlocalized or localized. It is unlocalized when charge carriers, free electrons in CB and holes in the VB, of the host lattice contribute to luminescence. In contrast, localized luminescence occurs when both the excitation and emission processes are confined to a specific luminescent center.

Photoluminescence can be classified into fluorescence and phosphorescence based on the emission life time. Fluorescence is the emission of light with a characteristic time, τ less than 10^{-8} s, occurring from an excited singlet state, while phosphorescence ($\tau > 10^{-8}$ s) involves emission from an excited triplet state.

The photoluminescence of a molecular species differs from the emission observed in atomic species. In atomic emission, both excitation and emission typically occur at the same resonance wavelength. However, in the case of molecular species, excitation generally leads to emission at a longer wavelength than that of the excitation source.

Luminescence spectroscopy monitors luminophore emission and can record both emission and excitation spectra using spectrofluorometers, which can also measure phosphorescence with added accessories. In emission spectra, the excitation wavelength is fixed while emission is scanned; in excitation spectra, the emission wavelength is fixed while excitation is scanned. Excitation spectra typically resemble the absorption spectra of the luminophores.

1.3.2 Jablonski diagram

The radiative and non-radiative transitions responsible for molecular photoluminescence are commonly represented using an energy level diagram known as the Jablonski diagram. Figure 1.1 presents a Jablonski diagram illustrating the mechanism of light emission in the majority of organic and inorganic luminophores.

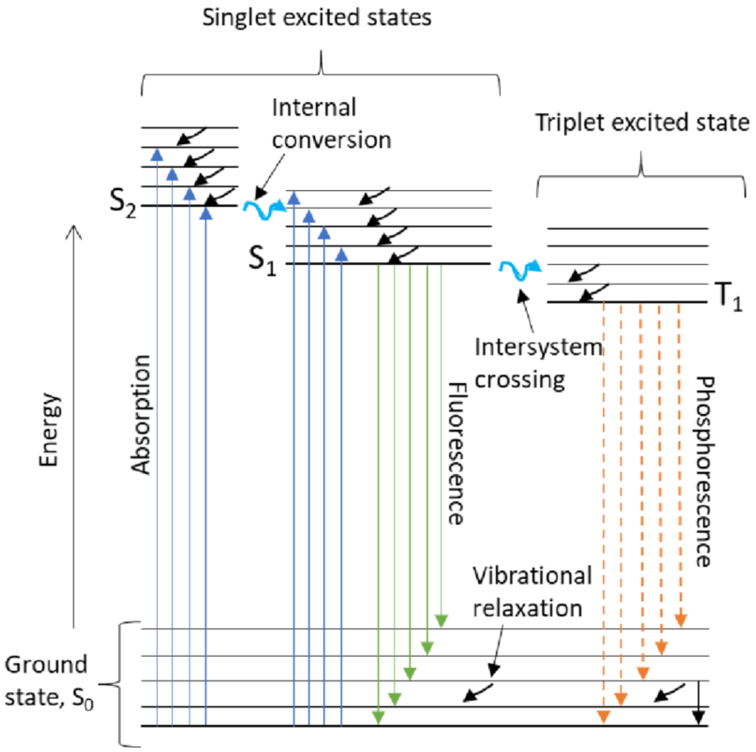

Fig 1.1 Jablonski diagram

The spin multiplicity of an electronic state can be classified as either singlet (with paired electrons) or triplet (with unpaired electrons). Typically, the ground electronic state is a singlet, labelled as S_0. Excited states may exist as either singlet states (S_1, S_2) or as a triplet state (T_1). Upon absorbing light, an electron moves from the ground electronic state to an excited state within approximately 10^{-14} to 10^{-15} seconds. The excited state must retain the same spin multiplicity as the ground state, meaning that direct excitation to a triplet state is forbidden. This is because the selection rules for electronic transitions require the spin state to remain unchanged during excitation [27].

The non-radiative relaxation processes are of different types – vibrational relaxation, internal conversion, intersystem crossing and non-radiative de-excitation. Excitation typically promotes the molecule to a higher vibrational level of the target excited state, after which it rapidly relaxes to the lowest vibrational level through a non-radiative process called vibrational relaxation. This relaxation occurs within 10^{-14} to 10^{-12} seconds - much faster than typical luminescence lifetimes - so it takes place before any luminescence is observed. When a molecule is excited to a higher singlet state (e.g., S_2), it rapidly undergoes non-radiative relaxation to the lowest singlet excited state (S_1) through a process called internal conversion, which typically occurs within 10^{-12} seconds. A process where relaxation occurs between excited states with different spin multiplicities is known as intersystem crossing. The transition from S_1 to T_1 serves as an example of intersystem crossing. Intersystem crossing is less probable and slower ($\sim 10^{-8}$ s) than internal conversion due to the non-conservation of spin multiplicity. Intersystem crossing becomes more prominent in molecules with heavy atoms (e.g., iodine, bromine) and metal ions in transition-metal complexes, due to enhanced spin–orbit coupling. In solution, paramagnetic species like molecular oxygen further promote intersystem crossing. Its significance also increases from 3d- to 4d- and 5d-block metal complexes. Following absorption, the stored excitation energy must be dissipated to satisfy energy conservation. Rapid non-radiative processes release only tiny, often undetectable amounts of heat, while the remaining energy is lost either through photon emission (luminescence) or as thermal energy. Non-radiative de-excitation — indicated experimentally by luminescence quenching — primarily occurs via energy transfer to solvents, non-luminescent solutes, or, in solids, to crystal vibrations (phonons).

Spin-allowed transitions are more probable than spin-forbidden ones because of the selection rule. Fluorescence involves light emission from an excited state to the ground state without a change in spin multiplicity, as shown by the $S_1 \rightarrow S_0$ transition. Being spin-allowed, fluorescence occurs rapidly, with excited-state lifetimes typically under microseconds. Spin-forbidden transitions become more likely with increased spin–orbit coupling. Factors that enhance intersystem crossing also promote phosphorescence, which is light emission from a triplet to a singlet ground state ($T_1 \rightarrow S_0$). Since phosphorescence involves a change in spin multiplicity, it is slow, with excited-state lifetimes ranging from 10^{-6} seconds to several seconds.

Luminescence spectroscopy provides insights into molecular geometry in excited states, revealing differences in bonding compared to the ground state. These transitions are best understood through ground and excited state potential surfaces. Because electronic absorption occurs in $\sim 10^{-15}$ s, nuclear motion is negligible, leading to 'vertical' transitions in energy diagrams according to the Franck-Condon principle. This is why the absorption was depicted to a higher vibrational level of the excited singlet states in the Jablonski diagram, and no direct excitation occurs to the triplet excited state T_1. In excited molecules, nuclei are often displaced from ground-state positions, leading to vibronic transitions involving both electronic and vibrational states. If excited-state distortion is minimal, the $\nu = 0$ to 0 transition is most probable; greater distortion favours $\nu = 0$ to higher ν transitions. Transition probability is proportional to the square of the Franck–Condon factor, the overlap of vibrational wavefunctions. When distortion is small, absorption and emission spectra follow the 'mirror image' rule. Excited-state distortion can be estimated from the luminescence spectra, either by identifying the most intense vibronic transition or by measuring the Stokes shift - the energy difference between absorption and emission peaks.

1.3.3 Energy transfer mechanisms

Energy transfer is a process in which an excited atom or molecule, known as the donor, passes its excitation energy to an acceptor atom or molecule during the lifetime of its excited state. This transfer causes the donor to return to its ground state while the acceptor is elevated to an excited state. If the acceptor is a luminescent species, it can emit light accepting the transferred energy — meaning the acceptor luminesces due to the donor's initial excitation. This type of emission is referred to as sensitized luminescence. The terms sensitizer and activator can be used in place of donor and acceptor, respectively. Energy transfer can occur through radiative or non-radiative mechanisms.

Radiative energy transfer: In the radiative energy transfer mechanism, a donor atom or molecule absorbs light, emits a photon, and the acceptor absorbs the emitted photon. The process is efficient when the acceptor absorbs strongly at the donor's emission wavelength, with its efficiency determined by the donor's quantum yield and the acceptor's absorbance. Since no direct interaction between donor and acceptor is needed, transfer can occur over large distances but is generally inefficient between similar molecules due to poor spectral overlap.

Non-radiative energy transfer: In this mechanism, the donor does not emit light. Instead, the excitation energy is transferred non-radiatively to the acceptor. Non-radiative energy transfer processes occur via two major mechanisms, the Forster resonance mechanism, and the Dexter exchange mechanism. The Forster resonance mechanism involves a long-range electrostatic interaction between a donor and an acceptor, allowing energy transfer over distances up to 50 - 100 Å without requiring direct contact. Efficient transfer requires that the energy levels of the donor and acceptor transitions be nearly identical, although small mismatches can be bridged by phonon-assisted processes, where vibrational quanta can facilitate energy transfer. However, if phonon energies are too high, they can promote non-radiative de-excitation before energy transfer occurs. The Dexter exchange mechanism requires direct contact between donor and acceptor molecules, involving a transition state where the donor to acceptor distance is approximately the sum of their collision radii. Structural studies can reveal the likely energy transfer mechanism based on the separation: short distances (typically < 5 Å) favor exchange, while longer distances (> 5 Å) favour resonance mechanisms. Thus, the nature of the interaction is closely tied to the spatial arrangement of the donor and acceptor.

Concentration quenching: In sensitised luminescence, a reduction in luminescence intensity or yield at higher activator concentrations is known as concentration quenching. Various research groups around the world have proposed explanations for this phenomenon. One of the earliest theories was put forward by Walter in 1889, who suggested a polymerisation mechanism for organic phosphors. According to this theory, as the concentration increases, the molecules tend to aggregate, forming larger, non-luminescent yet light-absorbing species, which in turn reduces the overall emission intensity.

Another proposed mechanism is collision quenching, where excited and non-excited molecules collide, resulting in non-radiative energy dissipation. This relaxation process occurs faster than radiative luminescent emission, thus lowering the observed luminescence. Additionally, the energy from an excited molecule may be transferred to a nearby unexcited molecule, which becomes excited in turn. This chain of energy transfers can continue across multiple molecules, leading to a diminished final luminescent output. These mechanisms are generally more applicable to organic liquid luminophores than to inorganic solids [28–30].

For inorganic phosphors, Johnson and Williams proposed that when activator ions are in proximity, their thermal activation energy decreases, promoting non-radiative transitions to the ground state. Furthermore, interactions with lattice vibrations in the solid matrix can also facilitate concentration quenching. Another explanation is the resonance mechanism, where the energy emitted by an excited activator is transferred to a neighbouring unexcited one, reducing the overall quantum yield of luminescence [28].

1.4 Oxide phosphors

Oxide phosphors have gained considerable attention for use in FPDs due to their excellent luminescent properties, high stability under vacuum conditions, and the absence of corrosive gas emissions under electron bombardment - advantages that set them apart from traditional sulphide-based screens. Persistent issues associated with conventional sulphide phosphors, such as limited primary colour emission and poor chemical stability, particularly moisture sensitivity, have been effectively addressed by oxide-based alternatives. In addition, oxide phosphors are atmospherically stable and easier to handle, with safer synthesis processes that do not require the use of hazardous reactive gases often involved in the production of other phosphor materials.

Despite these advantages, several challenges have hindered the widespread adoption of oxide phosphors as the dominant class in display devices. Oxide phosphors require high temperature processing - often above 1000 °C - to achieve the requisite polycrystalline structure for efficient luminescing. This restricts the use of conventional glass substrates for FPDs and necessitates inverted device architectures with heat-resistant substrates and insulating layers. In contrast, sulphide phosphors, due to their low melting points, high volatility and greater condensability compared to oxygen, can be deposited via simple thermal evaporation methods, without the need for supplementary gaseous compensation for anion loss. Also, prolonged and complex synthesis routes narrow down their usage for diverse applications. Henceforth, investigations in simple, economical, and environmentally benign techniques, that can cut down the synthesis temperature of oxide phosphors and their procedural extent, has been an area of research interest.

1.4.1 AB_2O_4 spinel oxide materials

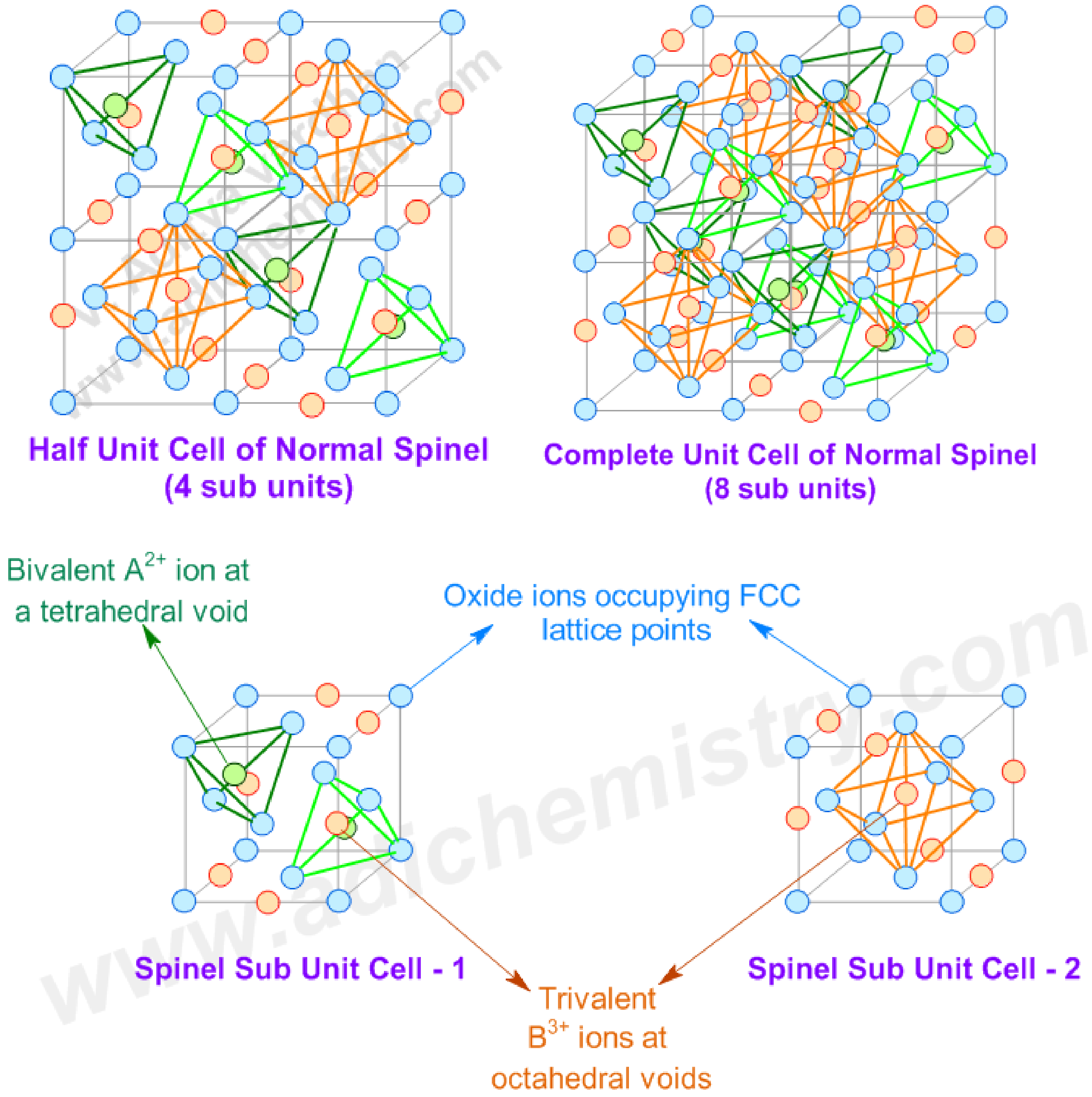

Fig 1.2 Normal AB_2O_4 spinel crystal structure

The ability to manipulate the magnetic, electronic, and optical properties of a compound, altering their composition, is vital for tailoring the response of a system for diverse as well as specific applications. Spinels, an excellent choice in this respect, generally exist in two distinct structural forms: normal and inverse. In a normal AB_2O_4 spinel, the bivalent A-site cations are coordinated to four oxygen atoms in a tetrahedral geometry, while the trivalent B-site cations are surrounded by six oxygen atoms arranged at the vertices of an octahedron [31]. A normal spinel is made up of 8 FCC formula units. The anions, here O^{2-}, lodge into the FCC lattice points, the divalent A^{2+} cations occupy one-eighth of its tetrahedral voids and trivalent B^{3+} half of its octahedral voids (Figure 1.2).

On the other hand, inverse spinels feature a rearranged ionic distribution, with the A-site ions and half of the B-site ions exchanging positions, i.e., the A^{2+} cations and half of the B^{3+} ions occupy octahedral sites, while the remaining B^{3+} ions are placed in tetrahedral sites. On manipulating the A- and B-site occupancy by various divalent and trivalent cations, one can modify the properties of a spinel.

At room temperature, spinel oxides typically adopt a cubic structure with a face-centered cubic (FCC) unit cell, exhibiting the Fd3m space group symmetry. However, certain spinels can crystallize in a tetragonal I4/amd phase under specific conditions. The lattice parameters, as well as the A-O and B-O bond lengths, gets modified with the atomic number of the A- and B-site cations. Interestingly, the relationship between the bond distances in the tetrahedral and octahedral sites exhibits complex behaviour.

The forbidden energy gap (or, bandgap) of a spinel compound differs significantly based on the choice of the A- and B-site cation. Spinels containing aluminium (Al) at the B-site are found to exhibit the largest bandgaps, while those with indium (In) demonstrates the least. As the atomic number of the B-site cation increases, the accompanied lattice expansion reduces the binding force between the valence electrons and their parent atoms. Now, electrons can freely move between the VB and CB, lowering the energy gap, mostly evident from the redshift in material's absorption spectrum. Hitherto, when a lattice contracts, electrons are more tightly held to their parent nucleus, widening the energy band gap. Additionally, band gap also gets modified when the number of d-electrons in the A-site cation increases. In short, both the size and electronic configuration of the cations play a crucial role in determining the electronic properties of spinels [32].

In the present work, the AB_2O_4 spinel oxide is carefully chosen as their properties can be tuned depending on the nature of the A- and B- site cations. The mostly discussed matrix is zinc aluminate in which A cation is Zn and B cation is Al. The synthesis procedures adopted also amends the properties of the investigated luminescent systems.

1.4.2 $ZnAl_2O_4$:

Zinc aluminate ($ZnAl_2O_4$), a spinel material with a wide bandgap of about 3.8 eV, inherently luminesces in the violet-blue spectral region. The transparency to wavelengths beyond 320 nm, makes it an excellent host lattice for ions that can induce luminescence, both transition metal ions and rare earth (RE) ions. $ZnAl_2O_4$ is widely studied as a potential material for reflective optical coatings in aerospace applications, as a phosphor material, and as an ultraviolet-transmitting electroconductive oxide. The spinel even finds usage for diverse applications in the field of optics and dielectric devices, and as catalyst supports, sensors, and lubricant additives. Recently, several studies have reported the synthesis of rare earth-doped zinc aluminate for use as high-efficiency phosphors in display technologies like FEDs and PDPs [33]. In a normal spinel $ZnAl_2O_4$ matrix, divalent Zn (Zn^{2+}) and trivalent Al (Al^{3+}) occupies, respectively, the tetrahedral and octahedral positions.

Combustion synthesis of spinel $ZnAl_2O_4$, at temperatures well above 1000 ºC, have been reported earlier. Robert Ianos *et al.* reported the synthesis of $ZnAl_2O_4$ powders using combustion method in a preheated electric furnace at 450 ºC, employing urea as the fuel and ammonium nitrate as the pore-forming agent. A notable drawback pointed out was the release of large volumes of gases during combustion accompanying the final product [34]. Diana Visinescu *et al.* prepared $ZnAl_2O_4$ using starch and N-methylurea as fuels in varying ratios, followed by heat treatment at 800 °C for 1 hour [35]. Megha Jain *et al.* employed fuel-blended combustion approach for $ZnAl_2O_4$ with the help of mixtures of urea and MEA (mono-ethanolamine) in different proportions at 550 ºC followed by annealing at 1000 ºC [36]. G. Buvaneswari *et al.* reported the combustion synthesis of Cu, Ni and Mn substituted zinc aluminate with urea as fuel at 500 ºC preheating accompanied by 12 hours of heating at 700 and 900 ºC [37].

Doping plays a crucial role in tailoring the structural and optical properties of self-blue luminescent $ZnAl_2O_4$. Ce doped $ZnAl_2O_4$ were prepared by Vijay Singh *et al.* at 500 °C with urea as fuel, tailed by annealing at 800 °C for 2 hours [38]. Vijay Singh *et al.* synthesized Cr doped $ZnAl_2O_4$ through combustion at 500 °C [39]. N.M. Gahane *et al.* reported the synthesis of cubic nanoparticles of Eu-doped zinc aluminate spinel ($ZnAl_2O_4$), synthesized via a combustion method, suitable for display and lighting applications [40]. Selective doping of spinel matrices for tunable NIR emission by melting evaporation technique has been reported by G. Yu *et al.* [41]. Similarly, combustion routes has been extensively employed for synthesising Eu^{3+} [40,42–44] and Sm^{3+} [40,42–44] doped $ZnAl_2O_4$. As elevated temperatures facilitate the effective incorporation of dopants into the host lattice, the drawbacks associated with such treatments are often overlooked.

Achieving high specific surface area, a requisite essential for efficient adsorbent materials, is challenging using traditional refractory methods due to the high temperatures involved, generally above 1000 °C, and long processing time. The extreme temperatures involved during synthesis may degrade the luminescent performance through non-radiative decay processes, termed as thermal quenching. Occasionally, luminescent materials and their dopants may exhibit phase change at high temperatures, upsetting their reliability and long-term performance. An additional drawback is the inability to maintain a controlled stoichiometry, especially while crafting luminescent nanomaterials. Alternative synthesis methods are recently being explored to overcome these limitations and improve the quality and reactivity of $ZnAl_2O_4$ spinels in the nano regime.

Chemical synthesis procedures, such as sol-gel, coprecipitation, hydrothermal and microwave techniques, noteworthy of their simplicity, short reaction times, low energy requirements, and ability to finely control the properties of the final products by adjusting reaction conditions, have emerged as promising alternative, enabling the production of zinc aluminate powders with tailored properties. These low-temperature synthesis methods present a significant advantage by enabling the production of materials with fine particle sizes, high surface area, and enhanced reactivity, making them more suitable for a wider range of applications.

Tomasz Strachowski *et al.* synthesized spinel $ZnAl_2O_4$ via a microwave-assisted hydrothermal method, resulting in high-quality, well-defined nanoparticles under controlled conditions [45–54]. P. Kumari *et al.* reported the luminescent response of $ZnAl_2O_4$:Dy synthesized via coprecipitation and hydrothermal routes [55]. The synthesis of single phase microporous nano $ZnAl_2O_4$ via microwave assisted hydrothermal method has been reported by M. Zawadzki [54]. A few reported hydrothermal assisted works probe into the optical properties [51,52] and magnetic response of Mn:$ZnAl_2O_4$ nanocrystals [49] and Co:$ZnAl_2O_4$ nanosheets [56]. There are works investigating the effect of synthesis parameters on the physical properties of nanosized $ZnAl_2O_4$ prepared via coprecipitation method [57][58]. Diverse methods for synthesising Cr:$ZnAl_2O_4$ nanoparticles and to enhance its reddish emission has been reported [59–63]. Xiaodan Huang *et al.* synthesized coral-like $ZnAl_2O_4$:Cr nanoparticles with tunable size and long NIR (near infra-red) afterglow luminescence via a methanol mediated wet-chemical method [64].

Zinc aluminate is increasingly used for photocatalysis of organic dyes, water purification and gas sensing applications. Zinc aluminate nanoparticles, synthesized from industrial aluminium and zinc sludges using solid-state reaction and molten salt synthesis at 1100 °C, was reported to achieve 94.5% degradation of brilliant cresyl blue dye under optimal conditions [65]. H. Filali *et al.* reported that co-doped $ZnAl_2O_4:Pb^{2+}$, La^{3+}, synthesized via citrate sol–gel method and post-annealed at 900 ºC for 2 hours, were effective photocatalysts and adsorbents for the degradation of hexamethyl crystallized violet dye in aqueous solutions [66]. Photocatalytic activity of pure as well as doped $ZnAl_2O_4$ nanomaterials were investigated towards methylene blue, reactive red 141, toluene and phenol hydroxylation [47,50,53,67]. L. Gildo-Ortiz *et al.* investigated the carbon monoxide and propane gas sensing capability of $ZnAl_2O_4$, synthesized via an aqueous sol-gel method using ethylenediamine as a chelating agent [68]. Emilio Huizar-Padilla *et al.* studied the synthesis of $ZnAl_2O_4$

particles employing a colloidal method used for detecting propane gas concentrations [69].

1.5. Objectives of the present work

Synthesis methods do play a crucial role in determining the material's purity, crystallinity, surface area, particle size, and morphology. Lowering the synthesis temperature well below 1000 °C shall significantly influence the optical, magnetic and catalytic properties in the nanometric dimension. The research, therefore, focusses on a comprehensive analysis of the luminescent response of RE doped ternary $ZnAl_2O_4$ phosphor matrix synthesized via simple non-ceramic routes - co-precipitation and hydrothermal – for primary color emissions. A plant-extract assisted auto-combustion technique towards synthesis of RE doped $ZnAl_2O_4$ system is also explored. Furthermore, the research probes into the possibility of generating a white emission, through rare earth ion co-doping in $ZnAl_2O_4$ matrix, thereby enhancing the material potential for use in lighting and display technologies. The viability of the green approach towards synthesis of other AB_2O_4 spinel oxides (A – Zn, Mg; B – Al, Cr) is checked. In addition, some initial investigations towards probing the photocatalytic, anti-microbial and cytotoxic functionality of pure $ZnAl_2O_4$ nano-matrix prepared via the three routes has also been presented.

References

[1] Boverhof, D. R., Bramante, C. M., Butala, J. H., Clancy, S. F., Lafranconi, W. M., West, J., & Gordon, S. C. (2015). Comparative assessment of nanomaterial definitions and safety evaluation considerations. *Regulatory Toxicology and Pharmacology, 73*(1), 137–150. https://doi.org/10.1016/j.yrtph.2015.06.001

[2] Chen, G., Seo, J., Yang, C., & Prasad, P. N. (2013). Nanochemistry and nanomaterials for photovoltaics. *Chemical Society Reviews, 42*(21), 8304–8338. https://doi.org/10.1039/c3cs60054h

[3] Louie, S. M., Ma, R., & Lowry, G. V. (2014). Transformations of nanomaterials in the environment. In *Frontiers of Nanoscience* (Vol. 7, pp. 55–87). Elsevier. https://doi.org/10.1016/B978-0-08-099408-6.00002-5

[4] Peralta-Videa, J. R., Zhao, L., Lopez-Moreno, M. L., de la Rosa, G., Hong, J., & Gardea-Torresdey, J. L. (2011). Nanomaterials and the environment: A review for the biennium 2008–2010. *Journal of Hazardous Materials, 186*(1), 1–15. https://doi.org/10.1016/j.jhazmat.2010.11.020

[5] Ramesh, K. T. (2009). *Mechanics and mechanisms: Nanomaterials*. Springer. https://doi.org/10.1007/978-0-387-09783-1

[6] Kaliva, M., & Vamvakaki, M. (2020). Nanomaterials characterization. In R. Narain (Ed.), *Polymer science and nanotechnology* (pp. 401–433). Elsevier. https://doi.org/10.1016/B978-0-12-816806-6.00017-0

[7] Sharma, V. P., Sharma, U., Chattopadhyay, M., & Shukla, V. N. (2018). Advance applications of nanomaterials: A review. *Materials Today: Proceedings, 5*(1), 6376–6380. https://doi.org/10.1016/j.matpr.2017.12.248

[8] Gajanan, K., & Tijare, S. N. (2018). Applications of nanomaterials. *Materials Today: Proceedings, 5*(1), 1093–1096. https://doi.org/10.1016/j.matpr.2017.11.187

[9] Barhoum, A., & García-Betancourt, M. L. (2018). Physicochemical characterization of nanomaterials: Size, morphology, optical, magnetic, and electrical properties. In A. Barhoum & A. S. H. Makhlouf (Eds.), *Emerging applications of nanoparticles and architecture nanostructures* (pp. 279–304). Elsevier. https://doi.org/10.1016/B978-0-323-51254-1.00010-5

[10] Baig, N., Kammakakam, I., & Falath, W. (2021). Nanomaterials: A review of synthesis methods, properties, recent progress, and challenges. *Materials Advances, 2*(6), 1821–1871. https://doi.org/10.1039/d0ma00807a

[11] Bissessur, R. (2020). Nanomaterials applications. In R. Narain (Ed.), *Polymer science and nanotechnology* (pp. 435–453). Elsevier. https://doi.org/10.1016/B978-0-12-816806-6.00018-2

[12] Saleh, T. A. (2020). Nanomaterials: Classification, properties, and environmental toxicities. *Environmental Technology & Innovation, 20,* 101067. https://doi.org/10.1016/j.eti.2020.101067

[13] Roduner, E. (2006). Size matters: Why nanomaterials are different. *Chemical Society Reviews, 35*(7), 583–592. https://doi.org/10.1039/b502142c

[14] Mitrano, D. M., Motellier, S., Clavaguera, S., & Nowack, B. (2015). Review of nanomaterial aging and transformations through the life cycle of nano-enhanced products. *Environment International, 77,* 132–147. https://doi.org/10.1016/j.envint.2015.01.013

[15] Sharifi, S., Behzadi, S., Laurent, S., Forrest, M. L., Stroeve, P., & Mahmoudi, M. (2012). Toxicity of nanomaterials. *Chemical Society Reviews, 41*(6), 2323–2343. https://doi.org/10.1039/c1cs15188f

[16] Hong, N. H. (2019). Introduction to nanomaterials: Basic properties, synthesis, and characterization. In N. H. Hong (Ed.), *Nano-sized multifunctional materials* (pp. 1–19). Elsevier. https://doi.org/10.1016/B978-0-12-813934-9.00001-3

[17] Chander, H. (2005). Development of nanophosphors: A review. *Materials Science and Engineering: R: Reports, 49*(5), 113–155. https://doi.org/10.1016/j.mser.2005.06.001

[18] Jacobsohn, L. G., Bennett, B. L., Muenchausen, R. E., Smith, J. F., & Cooke, D. W. (2007). Luminescent properties of nanophosphors. *Radiation Measurements, 42*(4–5), 675–678. https://doi.org/10.1016/j.radmeas.2007.01.066

[19] Chander, H. (2006). A review on synthesis of nanophosphors – Future luminescent materials. In *Proceedings of the International Conference on Advances in Semiconductor Devices (ASID)* (pp. 11–22). http://www.iitk.ac.in/asid06/proceedings/papers/MB1_4-C.pdf

[20] Kubrin, R. (2014). Nanophosphor coatings: Technology and applications, opportunities and challenges. *KONA Powder and Particle Journal, 31,* 22–52. https://doi.org/10.14356/kona.2014006

[21] Murthy, K. V. R. (2012). Nano phosphors for light emitting diodes (LEDs): Syntheses and characterization. *Recent Research in Science and Technology, 4*(4), 8–13. http://recent-science.com/

[22] Kortov, V. S. (2010). Nanophosphors and outlooks for their use in ionizing radiation detection. *Radiation Measurements, 45*(5), 512–515. https://doi.org/10.1016/j.radmeas.2009.11.009

[23] Cesaria, M., & Di Bartolo, B. (2019). Nanophosphors-based white light sources. *Nanomaterials, 9*(7), 1048. https://doi.org/10.3390/nano9071048

[24] Mishra, S., Rajeswari, R., Vijayan, N., Shanker, V., Dalai, M. K., Jayasankar, C. K., Babu, S. S., & Haranath, D. (2013). Probing the structure, morphology and multifold blue absorption of a new red-emitting nanophosphor for LEDs. *Journal of Materials Chemistry C, 1*(36), 5849–5855. https://doi.org/10.1039/c3tc31032a

[25] Sharma, R. K., Mudring, A. V., & Ghosh, P. (2017). Recent trends in binary and ternary rare-earth fluoride nanophosphors: How structural and physical properties influence optical behavior. *Journal of Luminescence, 189,* 44–63. https://doi.org/10.1016/j.jlumin.2017.03.062

[26] Murthy, K. V. R., & Virk, H. S. (2014). Luminescence phenomena: An introduction. *Defect and Diffusion Forum, 347,* 1–34. https://doi.org/10.4028/www.scientific.net/DDF.347.1

[27] Omary, M. A., & Patterson, H. H. (1999). Luminescence. *Comprehensive Coordination Chemistry II, 2,* 1372–1391.

[28] Dexter, D. L., & Schulman, J. H. (1954). Theory of concentration quenching in inorganic phosphors. *Journal of Chemical Physics, 22*(6), 1063–1070. https://doi.org/10.1063/1.1740265

[29] Baldacchini, G., Menchini, F., & Montereali, R. M. (2003). Concentration quenching of photoluminescence. *Journal of the Electrochemical Society, 150*(3), H124. https://doi.org/10.1149/1.1566964

[30] Barysaitė, S., Chmeliov, J., Valkunas, L., & Gelzinis, A. (2024). Concentration quenching of fluorescence decay kinetics of molecular systems. *Journal of Physical Chemistry B, 128*(12), 4887–4897. https://doi.org/10.1021/acs.jpcb.3c08254

[31] Candan, A., & Uɨur, G. (2016). First-principles study of structural, electronic, elastic and phonon properties of AB_2O_4 (A = Ge, Si; B = Mg, Zn, Cd) spinel oxides. *Modern Physics Letters B, 30,* 1650002. https://doi.org/10.1142/S0217984916500020

[32] Ka, S. K., Novak, P., & Wohlfarth, E. E. P. (1982). Oxide spinels. In *Comprehensive Treatise on Inorganic and Theoretical Chemistry* (Vol. 2, Chap. 4).

[33] Lahariya, V., & Pandey, K. K. (2021). A comprehensive review on Eu-doped zinc aluminate phosphor for solid-state lighting. *International Journal of Scientific Research in Science and Technology, 8*(5), 439–443. https://doi.org/10.32628/IJSRST.RAMAN2181

[34] Ianoş, R., Băbuţă, R., Păcurariu, C., Lazău, R., Istratie, R., & Butaciu, C. (2017). Combustion synthesis of $ZnAl_2O_4$ powders with tuned surface area. *Ceramics International, 43*(11), 8975–8981. https://doi.org/10.1016/j.ceramint.2017.04.038

[35] Visinescu, D., Jurca, B., Ianculescu, A., & Carp, O. (2011). Starch – A suitable fuel in new low-temperature combustion-based synthesis of zinc aluminate oxides. *Polyhedron, 30*(13), 2824–2831. https://doi.org/10.1016/j.poly.2011.08.006

[36] Jain, M., Manju, Gundimeda, A., Kumar, A., Kumar, S., Gupta, G., Won, S. O., Chae, K. H., Vij, A., & Thakur, A. (2019). Enhanced near-infrared luminescence in zinc aluminate bestowed by fuel-blended combustion approach. *Journal of Alloys and Compounds, 797,* 148–158. https://doi.org/10.1016/j.jallcom.2019.04.257

[37] Buvaneswari, G., Aswathy, V., & Rajakumari, R. (2015). Comparison of color and optical absorbance properties of divalent ion substituted Cu and Zn aluminate spinel oxides synthesized by combustion method towards pigment application. *Dyes and Pigments, 123,* 413–419. https://doi.org/10.1016/j.dyepig.2015.08.024

[38] Singh, V., Singh, N., Pathak, M. S., Dubey, V., & Singh, P. K. (2018). Annealing effects on the luminescence properties of Ce doped $ZnAl_2O_4$ produced by combustion synthesis. *Optik, 155,* 285–291. https://doi.org/10.1016/j.ijleo.2017.10.167

[39] Singh, V., Chakradhar, R. P. S., & Rao, J. L., & Kwak, H. Y. (2011). EPR and photoluminescence properties of combustion-synthesized $ZnAl_2O_4:Cr^{3+}$ phosphors. *Journal of Materials Science, 46*(8), 2331–2337. https://doi.org/10.1007/s10853-010-5078-z

[40] Gahane, N. M., Chaware, P. J., & Rewatkar, K. G. (2023). Structural, morphological, and photoluminescence study of Europium doped spinel $ZnAl_2O_4$ phosphors. *International Journal of Chemistry, Mathematics and Physics, 7*(1), 1–6. https://doi.org/10.22161/ijcmp.7.1.1

[41] Yu, G., Wang, W., & Jiang, C. (2021). Linear tunable NIR emission via selective doping of Ni^{2+} ion into ZnX_2O_4 (X = Al, Ga, Cr) spinel matrix. *Ceramics International, 47*(13), 17678–17683. https://doi.org/10.1016/j.ceramint.2021.03.087

[42] Priya, R., Negi, A., Singla, S., & Pandey, O. P. (2020). Luminescent studies of Eu doped $ZnAl_2O_4$ spinels synthesized by low-temperature combustion route. *Optik, 204,* 164173. https://doi.org/10.1016/j.ijleo.2020.164173

[43] Mahajan, R., Kumar, S., Prakash, R., & Kumar, V. (2018). Synthesis and luminescent properties of Sm^{3+} doped zinc aluminate phosphor. *AIP Conference Proceedings, 1953,* 2–6. https://doi.org/10.1063/1.5032544

[44] Hussain, T., Junaid, M., Atiq, S., Abbas, S. K., Ramay, S. M., Alrayes, B. F., & Naseem, S. (2017). Tunable dielectric behaviour and energy band gap range of $ZnAl_2O_4$ ceramics mediated by Mg substitution. *Journal of Alloys and Compounds, 724,* 940–950. https://doi.org/10.1016/j.jallcom.2017.07.104

[45] Dwibedi, D., Murugesan, C., Leskes, M., & Barpanda, P. (2018). Role of annealing temperature on cation ordering in hydrothermally prepared zinc aluminate ($ZnAl_2O_4$) spinel. *Materials Research Bulletin, 98,* 219–224. https://doi.org/10.1016/j.materresbull.2017.10.010

[46] Chen, Z., Zhao, X., & Wei, S. (2021). Comparative study on sol-gel combined with a hydrothermal synthesis of $ZnAl_2O_4$ and $ZnO/ZnAl_2O_4$ nanocomposites and its photoluminescence properties and antibacterial activity. *Optik, 242,* 167151. https://doi.org/10.1016/j.ijleo.2021.167151

[47] Zhang, W., Wang, Y., Shen, Y., Xie, M., & Guo, X. (2016). Mesoporous zinc aluminate ($ZnAl_2O_4$) nanocrystal: Synthesis, structural characterization and catalytic performance towards phenol hydroxylation. *Microporous and Mesoporous Materials, 226,* 278–283. https://doi.org/10.1016/j.micromeso.2016.02.001

[48] Quirino, M. R., Oliveira, M. J. C., Keyson, D., Lucena, G. L., Oliveira, J. B. L., & Gama, L. (2016). Synthesis of zinc aluminate with high surface area by microwave hydrothermal method applied in the transesterification of soybean oil (biodiesel). *Materials Research Bulletin, 74,* 124–128. https://doi.org/10.1016/j.materresbull.2015.10.027

[49] Zhang, D., Yin, Y., Liu, Y., Chao, W., & Zhai, Y. (2013). The photoluminescence and magnetic properties of $ZnAl_2O_4$:Mn nanocrystals. *Journal of Physics and Chemistry of Solids, 74*(8), 1131–1135. https://doi.org/10.1016/j.jpcs.2013.03.012

[50] Foletto, E. L., Battiston, S., Simões, J. M., Bassaco, M. M., Pereira, L. S. F., De Moraes Flores, É. M., & Müller, E. I. (2012). Synthesis of $ZnAl_2O_4$ nanoparticles by different routes and the effect of its pore size on the photocatalytic process.

Microporous and Mesoporous Materials, 163, 29–33. https://doi.org/10.1016/j.micromeso.2012.06.039

[51] Miron, I., Enache, C., & Grozescu, I. (2012). Doped zinc aluminate spinel synthesized by hydrothermal method. *Digest Journal of Nanomaterials and Biostructures, 7*, 967–972.

[52] Miron, I., Enache, C., Vasile, M., & Grozescu, I. (2012). Optical properties of $ZnAl_2O_4$ nanomaterials obtained by the hydrothermal method. *Physica Scripta, 2012*(T149), 014064. https://doi.org/10.1088/0031-8949/2012/T149/014064

[53] Zhu, Z., Zhao, Q., Li, X., Li, Y., Sun, C., Zhang, G., & Cao, Y. (2012). Photocatalytic performances and activities of $ZnAl_2O_4$ nanorods loaded with Ag towards toluene. *Chemical Engineering Journal, 203*, 43–51. https://doi.org/10.1016/j.cej.2012.07.035

[54] Zawadzki, M. (2006). Synthesis of nanosized and microporous zinc aluminate spinel by microwave-assisted hydrothermal method (microwave–hydrothermal synthesis of $ZnAl_2O_4$). *Solid State Sciences, 8*, 14–18. https://doi.org/10.1016/j.solidstatesciences.2005.08.006

[55] Kumari, P., & Dwivedi, Y. (2016). Structural and photophysical investigations of bright yellow emitting Dy: $ZnAl_2O_4$ nanophosphor. *Journal of Luminescence, 178*, 407–413. https://doi.org/10.1016/j.jlumin.2016.06.027

[56] Gurugubelli, T. R., Babu, B., & Yoo, K. (2021). Structural, optical, and magnetic properties of cobalt-doped $ZnAl_2O_4$ nanosheets prepared by hydrothermal synthesis. *Energies, 14*, 1–9. https://doi.org/10.3390/en14102869

[57] Mekprasart, W., Worasawat, S., & Pecharapa, W. (2015). Effect of pH and temperature on physical properties of zinc aluminate based nanostructure synthesized via co-precipitation method. *Advanced Materials Research, 1103*, 53–59. https://doi.org/10.4028/www.scientific.net/AMR.1103.53

[58] Mekprasart, W., Worasawat, S., Tangcharoen, T., & Pecharapa, W. (2015). Characterization and effect of calcination temperature on structural properties of spinel zinc aluminate synthesized via co-precipitation process. *Physica Status Solidi C, 627*, 624–627. https://doi.org/10.1002/pssc.201400292

[59] Menon, S. G., Choudhari, K. S., Shivashankar, S. A., Santhosh, C., & Kulkarni, S. D. (2017). Rapid annealing: A novel processing technique for Cr:$ZnAl_2O_4$ nanoparticles. *Journal of Alloys and Compounds, 728*, 484–489. https://doi.org/10.1016/j.jallcom.2017.09.026

[60] Zhang, D., Qiu, Y. H., Xie, Y. R., Zhou, X. C., Wang, Q. R., Shi, Q., Li, S. H., & Wang, W. J. (2017). The improvement of structure and photoluminescence properties of $ZnAl_2O_4:Cr^{3+}$ ceramics synthesized by using solvothermal method. *Materials & Design, 115*, 37–45. https://doi.org/10.1016/j.matdes.2016.11.034

[61] Zhang, D., Chen, J., Du, C., Zhu, B., Wang, Q., Shi, Q., Cui, S., & Wang, W. (2020). Enhancement of red emission assigned to inversion defects in $ZnAl_2O_4:Cr^{3+}$ hollow spheres. *Frontiers of Materials Science, 14*, 73–80. https://doi.org/10.1007/s11706-020-0487-7

[62] Rani, G. (2017). Annealing effect on the structural, optical and thermoluminescent properties of $ZnAl_2O_4:Cr^{3+}$. *Powder Technology, 312*, 354–359. https://doi.org/10.1016/j.powtec.2017.02.040

[63] Zhang, D., Ma, X., Zhang, Q., Xie, Y., Shi, Q., Wang, Q., & Wang, W. (2016). Influence of Zn/Al molar ratio on the structural and photoluminescence performances of $Zn_xAl_2O_4:Cr^{3+}$ phosphors. *Journal of Alloys and Compounds, 688*, 581–587. https://doi.org/10.1016/j.jallcom.2016.07.044

[64] Huang, X., Wei, X., Zeng, Y., Jing, L., Ning, H., Sun, X., Li, Y., Li, D., Yi, Y., & Gao, M. (2021). Turning-on persistent luminescence out of chromium-doped zinc aluminate nanoparticles by instilling antisite defects under mild conditions. *Nanoscale, 13*, 8514–8523. https://doi.org/10.1039/d0nr08267h

[65] Abd-Allah, A. A., Ahmed, Y. M. Z., El-Sheikh, S. M., Youssef, A. O., & Amin, A. M. M. (2022). Synthesis of zinc aluminate nanoparticles from aluminum/zinc sludge for degradation of brilliant cresyl blue under visible light irradiation. *Journal of Water and Environmental Nanotechnology, 7*, 288–305. https://doi.org/10.22090/jwent.2022.03.005

[66] Filali, H., Boukheit, N., Bouhroum, R., Chekirou, W., & Karaali, A. (2021). Citrate assisted synthesis of co-doped $ZnAl_2O_4$ with La^{3+} and Pb^{2+} ions and

applications: Adsorption–photocatalysis. *Acta Physica Polonica A, 140*, 379–388. https://doi.org/10.12693/APhysPolA.140.379

[67] Sumathi, S., & Kavipriya, A. (2017). Structural, optical and photocatalytic activity of cerium doped zinc aluminate. *Solid State Sciences, 65*, 52–60. https://doi.org/10.1016/j.solidstatesciences.2017.01.003

[68] Gildo-Ortiz, L., Rodríguez-Betancourtt, V. M., Ramírez Ortega, J. A., & Blanco-Alonso, O. (2023). An alternative approach for the synthesis of zinc aluminate nanoparticles for CO and propane sensing applications. *Chemosensors, 11*, 105. https://doi.org/10.3390/chemosensors11020105

[69] Huízar-Padilla, E., Guillén-Bonilla, H., Guillén-Bonilla, A., Rodríguez-Betancourtt, V. M., Sánchez-Martínez, A., Guillen-Bonilla, J. T., Gildo-Ortiz, L., & Reyes-Gómez, J. (2021). Synthesis of $ZnAl_2O_4$ and evaluation of the response in propane atmospheres of pellets and thick films manufactured with powders of the oxide. *Sensors, 21*, 2362. https://doi.org/10.3390/s21072362

Chapter 2

EXPERIMENTAL TECHNIQUES

The chapter discusses the various experimental and analytical techniques explored during the entire research work. The three nanoparticle synthesis routes, the synthesis strategies adopted, theory underlying the various structural, morphological, and optical characterization techniques employed for nanomaterial analysis, and the photocatalytic, anti-bacterial and anti-cancerous procedures used in the present study are outlined in detail.

2.1 Introduction

The high surface area-to-volume ratio of nanomaterials leads to their distinct properties such as reactivity, stability, and functionality. These unique features, quite different from their bulk counterparts, makes them suitable for diverse applications. This signifies the proper selection and optimization of nanoparticle synthesis methods, as they greatly influence the basic material properties. Nanomaterial synthesis techniques are broadly classified into two - the top-down and bottom-up approach (figure 2.1). In the former subtractive approach, a bulk material is sliced down to get the final product whereas, in the latter additive approach, the nanostructures are built from basic building units, the atoms.

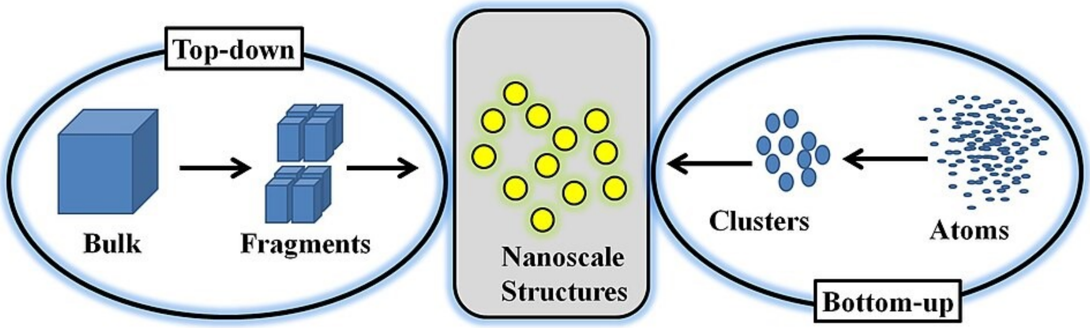

Fig 2.1 Synthesis strategies of nanomaterials

The ternary oxide spinel matrix chosen for the present study is $ZnAl_2O_4$. The research emphasizes on low-temperature, straightforward, and energy efficient synthesis procedures - co-precipitation, hydrothermal method, and plant extract-assisted auto-combustion. The chapter also outlines the various analytical tools and application specific photocatalytic, antibacterial, and anticancer procedures adopted in the present study.

2.2 Nanophosphor synthesis

2.2.1 Co-precipitation method

Co-precipitation is a recognized simple, cost-effective technique, effortlessly adaptable for large-scale industrial applications. This method produces nanomaterials with high purity through an eco-friendly approach, eliminating the need for hazardous organic solvents or conditions involving high pressure or temperature. Co-precipitation is particularly advantageous when high purity and precise stoichiometric control are essential [1].

In comparison to other techniques, co-precipitation is more accessible for synthesizing lanthanide-doped nanocrystals, as it does not require expensive equipment or complicated procedures. This technique involves the simultaneous precipitation of two or more metal ions as hydroxides or oxides in alkaline aqueous solutions. It is widely used for the rapid preparation of magnetite, functioning as a stepwise chemical synthesis where a metallo-organic precursor undergoes nucleation followed by aggregation to form metal oxides. Secondary processes, such as Ostwald ripening, help control the size of the resulting metallic oxide nanoparticles [2,3].

Co-precipitation is often aided by methods like microwave assistance or sonication to expedite the synthesis of metallic oxide nanoparticles, particularly in biofuel production. Among various preparation methods - including hydrothermal, solvothermal, microwave exfoliation, and reverse microemulsion - co-precipitation is considered the most common due to the ease of controlling reaction parameters such as solution pH, flow rate, and temperature. It has been recognized as one of the most durable and reproducible methods for synthesizing layered metal hydroxides [4].

In this work, co-precipitation technique was used to synthesize pure and doped ternary $ZnAl_2O_4$ spinel oxide. The synthesis procedure (figure 2.2) is detailed below:

- Selection of precursors: The nitrate precursors, of divalent and trivalent cations, were chosen for each type of matrices and the amounts of precursors is taken based on the requirement by calculating their concentration in molarities. The solvent used is distilled water.

$$Molarity\ (M) = \frac{Mass\ of\ solute\ to\ be\ taken\ (g) \times 1000}{Molar\ mass\ of\ solute\ (g) \times\ Volume\ of\ solution\ (mL)}$$

- Precursor mixing and material precipitation: The required amounts of respective precursors are mixed in the solvent, using a magnetic stirrer, for complete dissolution. The precursor solutions are then mixed, continuously stirring for 20 minutes. The precipitating agent, ammonia solution (Merck, 25%), was added to the homogeneous mixture, and left for 24 hours for complete precipitation. The residue is filtered, dried in a hot air oven for 12 hours and grinded to get fine powders.

- Calcination: Post-heat treatment of the synthesized powders was done using a high temperature programmable furnace.

Fig 2.2 Flow chart of co-precipitation method

2.2.2 Hydrothermal method:

Hydrothermal synthesis is utilized for fabricating single crystals exploiting the solubility of minerals in hot water under high pressure. This method offers considerable advantages over other approaches, particularly its capability to create crystalline phases that remain stable at temperatures exceeding their melting points. It excels in growing large, high-quality crystals while providing precise control over their composition. In sealed vessels, such as bombs or autoclaves, solvents are heated to temperatures well above their boiling points, due to the increased autogenous pressure. This technique is often referred to as solvothermal processing when carried out in solvents other than water, and as hydrothermal processing when water is used as the solvent [5].

The hydrothermal method enables the crystallization of materials directly from solutions through chemical reactions in aqueous environments under elevated temperatures and pressures. It can function under extreme conditions which promotes the dissolution of reactants and encourages the nucleation and growth of materials like carbon nanotubes, diamonds, or single oxide crystals. This technique effectively facilitates the dissolution and recrystallization of substances that are typically insoluble or weakly soluble. The reactants, known as precursors, are often provided in gels, suspensions, or solutions, making hydrothermal synthesis a preferred choice for producing nanomaterials while minimizing material loss [6].

Despite its advantages, hydrothermal synthesis presents certain limitations. The use of sealed pressure vessels complicates the measurement, monitoring, and control of the reaction process. Furthermore, this method typically produces only small yields per synthesis run, which can pose challenges for large-scale applications. While hydrothermal techniques can generate a diverse array of material morphologies and are generally more environment friendly than many other synthesis methods, the difficulties associated with understanding and managing the reaction dynamics can render it less suitable for fabricating high-quality up-conversion nanoparticles [7].

The hydrothermal procedure (figure 2.3) adopted in the present work is briefed below:

- Weighing the precursors: The appropriate nitrate precursors are selected for each matrix, and the quantities are calculated in terms of molarity. Distilled water is used as the solvent.
- Precursor mixing and heating: The adequate amounts of each precursor are mixed in distilled water and stirred, on a magnetic stirrer, until fully dissolved. The precursor solutions are then combined and stirred for 20 minutes. An alkaline pH is imparted to the homogeneous mixture on dropwise addition of ammonia solution (Merck, 25%), and subsequently transferred to a Teflon container placed in a tightly sealed steel autoclave. It is heated under high pressure in a hot air oven. The temperature and duration of heating for each matrix are determined through a trial-and-error approach. After the heating process, the solution is allowed to cool, then filtered, washed with water, and the residue is dried and ground to obtain the final products.

- Calcination: The synthesized powder is then subjected to heat treatment in a high-temperature furnace.

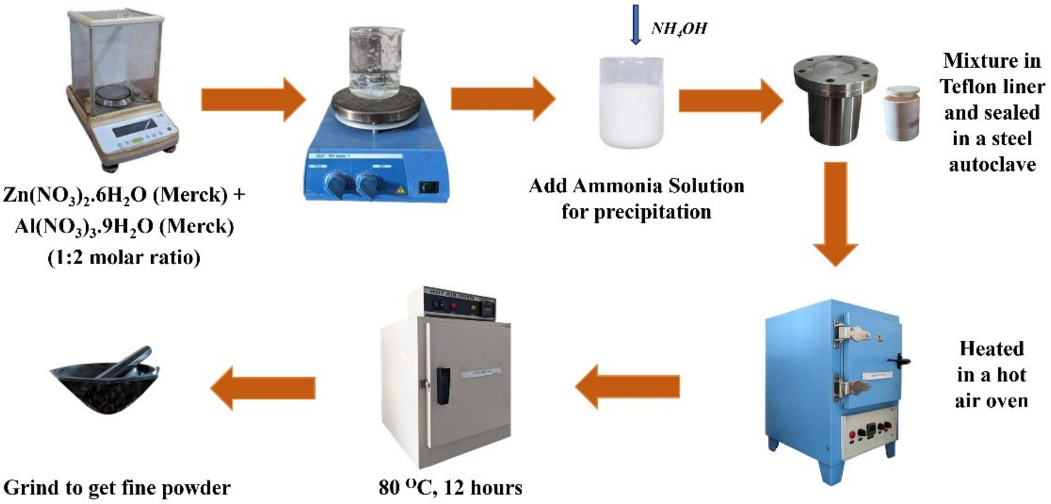

Fig 2.3 Flow chart of hydrothermal method

2.2.3 Auto-combustion method:

Self-combustion is a time-efficient and cost-effective approach for producing nanomaterials, particularly nanostructures of ceramics, composites, alloys, and inter-metallics. In this solution combustion technique, heating initiated via an exothermic reaction, later propagates in a self-sustaining manner until the final products are obtained. This method falls under wet chemical techniques that involve exothermic reactions between metal nitrates (oxidants) and organic fuels. An oxidant facilitates combustion by providing oxygen, while the fuel serves as a source of carbon and hydrogen, generating CO_2, H_2O, and heat during combustion. In this process, the fuel forms complexes with metal ions.

Most metal oxides produced via auto-combustion are synthesized by combining metal nitrates with a fuel source. Nitrates are the preferred metal precursors due to their ability to yield water-soluble metal ions, which enhances homogeneity. Key parameters in the solution combustion process include temperature, the fuel-to-oxidant ratio, and the chemical composition of the precursor. Commonly used fuels include urea, carbohydrazide, oxalyldihydrazide, glycine, citric acid, polyacrylic acid, and hydrazine. The fuel-to-oxidant ratio is particularly important, as it significantly affects the properties of the resulting nanostructured materials. The volume of gases produced during synthesis impacts particle size and agglomeration. Fuels with long molecular chains tend to generate larger amounts of gases during synthesis, resulting in less agglomeration of the final product. For example, urea, which contains two amino groups (NH_2), enhances the reactivity of the reaction, facilitating the formation of powders with nanosized crystallite dimensions [8–10].

The exothermic nature of the self-propagating combustion synthesis process eliminates the need for expensive equipment and complex facilities. The high reaction temperatures achieved can volatilize impurities with low boiling points, resulting in products of greater purity. The atomic-level mixing of reactants enhances the solubility of precursor materials, improving the synthesis quality. The release of non-toxic gases and excellent complexing between metal ions and fuels during the process leads to the formation of porous products with minimal agglomeration, making them easier to grind and enabling the creation of fine powders with superior homogeneity. When the solution is heated to a specific temperature, the water content evaporates, helping to stabilize the metal ions in the solution.

The various crucial factors for successful nanomaterial development via auto-combustion includes the coordination ability of the fuel, the selection and quantity of the fuel, the type of metal salt used, the heating rate, the synthesis environment, and the volume of gas released during the process. Recognizing the importance of fuel selection in combustion synthesis, this study focuses on plant extract-assisted combustion synthesis, where leaf extracts serve as the fuel. This approach not only eliminates the need for chemical fuels but also reduces environmental pollution by minimizing the release of toxic gases.

Phytochemical analysis: The primary and secondary metabolites found in the leaves, stems, and roots of different plants significantly contribute to nanoparticle synthesis. Secondary metabolites, which help the plant survive, serve as sources of anti-oxidant, anti-viral, anti-malarial, analgesic, diuretic, anti-bacterial, anti-cancerous, antiinflammatory, anti-fungal, anti-allergic, and anti-mutagenic properties. The phytochemicals in the extract vary based on the plant part used, climate, soil conditions, and the fertilizers used. Therefore, analysing the phytochemicals present in the plant extract is crucial [11].

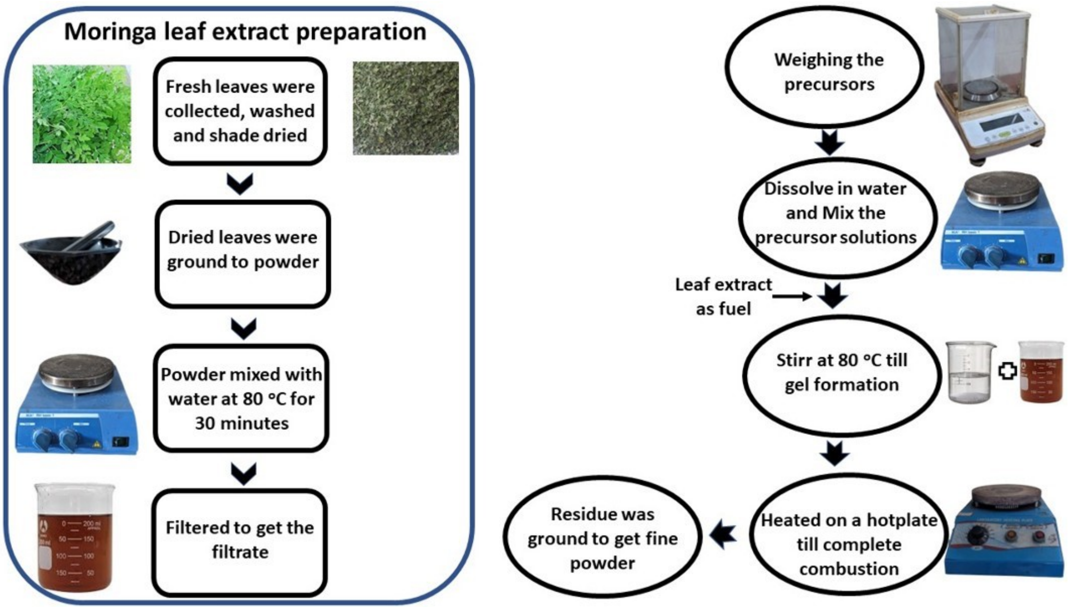

Fig 2.4 Flow chart of plant extract assisted combustion method

The synthesis procedure (figure 2.4) employed in the present study is as follows:

- Preparation of leaf extract: Leaves of the Moringa oleifera plant (commonly known as Moringa) were collected from Thrissur district of Kerala in the month of September. The leaves were thoroughly washed with water and shade-dried for four days. Once dried, they were ground into a fine powder using a mortar and pestle. This powder is then mixed with water in appropriate quantities and heated for 30 minutes. The resulting mixture is filtered, and the filtrate is used as the fuel for combustion synthesis.
- Calculating precursor concentration: The adequate amount of suitable nitrate precursors is chosen for each type of matrix, and their amounts are calculated in terms of molarity. Distilled water was used as the solvent.
- Heating: The necessary amounts of each precursor are stirred with a magnetic stirrer until completely dissolved. The precursor solutions are then mixed and

stirred for 20 minutes. Next, the mixture is heated to 80 °C while stirring until a gel-like formation occurs, after which it is placed on a hotplate. This mixture is further heated to produce a solid residue, which is then ground to obtain the final powder.

- Calcination: The as-prepared powder was then subjected to heat treatment in a high-temperature furnace post- synthesis.

2.3 Characterization techniques:

2.3.1 Structural characterization

2.3.1a X-ray diffraction (XRD) analysis:

When X-rays, with wavelength comparable to the spacing between atoms in the sample, are shined on a material, the angle of diffraction will be influenced by the atomic spacing. As the X-rays pass through the sample, they "bounce" off the atoms in the structure (figure 2.5), changing direction. Some of these diffracted beams may cancel each other out, but if their path difference is an integral multiple of the same wavelength, constructive interference occurs and a new beam with greater amplitude results.

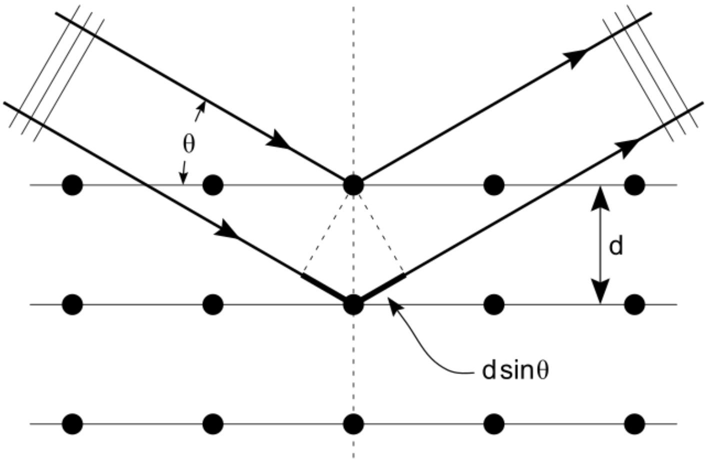

Fig 2.5 Schematic diagram of X-ray diffraction from crystal planes

The increased amplitude translates to a stronger signal at that specific angle of diffraction. This angle can then be used to determine the differences between atomic planes using Bragg's law,

$$2d\sin\theta = n\lambda ,$$

where, λ is the wavelength, θ is the glancing angle, and d is the distance between atomic planes. The distance between atomic planes can then be used to determine composition or crystalline structure [12,13].

An X-ray diffractogram displays the intensity of the signal across different angles of diffraction at their respective 2θ positions. These 2θ positions correspond to specific spacings between the atoms in the sample, determined by the angle of diffraction from the incident X-ray beam directed at the sample. The intensity of the peaks is indicative of the quantity of molecules in that phase or with a particular spacing. Thus, higher peak intensity corresponds to a greater number of crystals or molecules with that specific spacing.

The peak positions (2θ values in the XRD pattern) are compared with the International Centre of Diffraction Data card (JCPDS) and confirmed different phases in the prepared nanomaterial. The crystalline size was determined by Debye-Scherrer method. According to Scherrer's formula,

$$D = \frac{K\lambda}{\beta\cos\theta} ,$$

Here, K is the Scherrer constant with a value from 0.9 to 1, $\lambda = 1.5414$ Å (wavelength of Cu-K_{α}), β is the line broadening at half the maximum intensity (FWHM) in radians, and θ is the angle obtained from the 2θ value corresponding to the most intense peak of an XRD measurement for a specific sample. The crystalline size values obtained from XRD techniques are comparable to those from other characterization methods. The sharp peak in the XRD pattern confirms the crystallinity of the synthesized nanoparticles, while a broad peak in the spectrum indicates the material's amorphous nature. One advantage of XRD techniques, often conducted on powder samples after drying their corresponding colloidal solutions, is that they provide statistically representative, volume-averaged values [12,14]. Analysing a X-ray diffractogram, one can gather idea on the phase purity, orientation, crystallinity, lattice parameters, and size of the nanoparticles.

An X-ray apparatus (figure 2.6) consists of three main components: an X-ray source, a sample holder, and a detector. The X-rays generated by the source illuminate the sample, which then diffracts the rays before they enter the detector. By adjusting the position of the tube, sample, or detector to change the diffraction angle (2θ, the angle between the incident and diffracted beams), the intensity is measured and diffraction data are recorded.

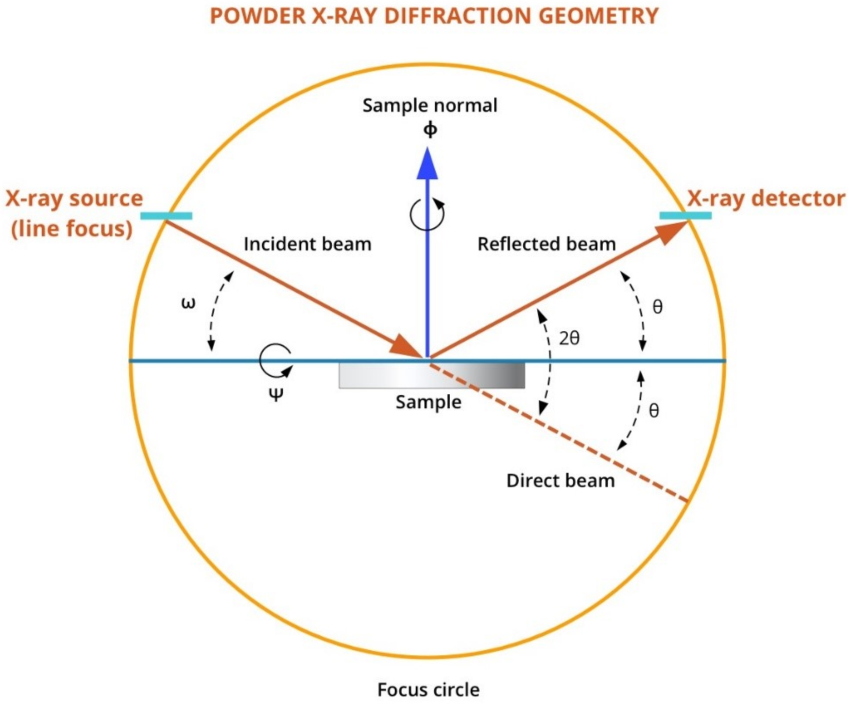

Fig 2.6 XRD Instrumentation

Fig 2.7 Panalytical AERIS X-ray diffractometer

Depending on the geometry of the diffractometer and the type of sample, the angle between the incident beam and the sample can be either fixed or variable, typically in conjunction with the angle of the diffracted beam.

The X-ray diffractometer used in this project is Panalytical AERIS X-ray diffractometer (figure 2.7).

2.3.1b Fourier-transform infrared spectroscopy

In Fourier Transform Infrared (FTIR) spectroscopy, infrared radiation is directed on a sample, where some of the radiation is absorbed while the rest is transmitted. The resulting spectrum reflects the molecular absorption and transmission, creating a unique molecular fingerprint of the sample. Just like fingerprints, no two distinct molecular structures produce the same infrared spectrum, making infrared spectroscopy valuable for various types of analysis [15].

FTIR spectral analysis can identify the bonds in unknown materials, determine the quality or consistency and the amounts of components of a sample. FTIR spectroscopy is preferred over other methods of IR spectral analysis, being a highly efficient and accurate non-invasive technique without any need for external calibration. It improves sensitivity, as multiple one-second scans can be combined to minimize random noise.

The method features increased optical throughput and its design consists of just one moving component.

FTIR instrumentation (figure 2.8) mainly includes a source in which infrared energy is emitted from a black body and it passes through an aperture to control the energy falling on the sample and detector. The interferometer is a device which generates a unique signal that encodes all infrared frequencies simultaneously, rather than one at a time, allowing extremely fast data acquisition - typically in about one second. Most interferometers utilize a beam splitter to divide the incoming infrared beam into two optical paths. One beam reflects off a fixed flat mirror, while the other reflects off a movable flat mirror that can shift a short distance (usually a few millimetres) away from the beam splitter. When the two beams are reflected and then recombined at the beam splitter, they interfere with each other due to the varying path lengths - one being constant and the other changing. This interference creates a signal known as an interferogram, which uniquely contains information about every infrared frequency from the source.

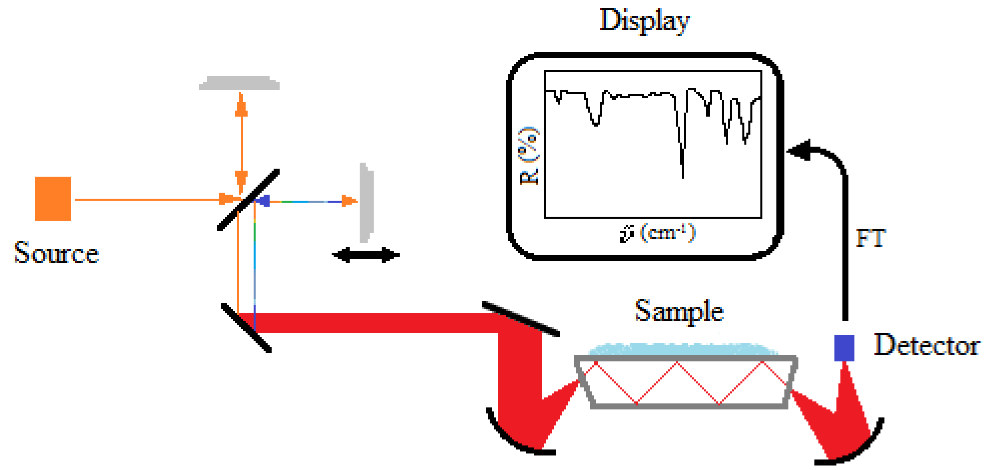

Fig 2.8 FTIR Instrumentation

From the beam splitter, the beam enters a sample compartment where specific frequencies were absorbed and a part of energy is being transmitted through or reflected. The detectors used are specially designed to measure the specific interferogram signal. On the monitor appears a frequency spectrum (a plot showing intensity at each individual frequency), which is "decoded" via a well-established mathematical technique known as Fourier transformation, providing the user with the required spectral information for analysis for structural identification [16,17].

Fig 2.9 Shimadzu IR Spirit FTIR spectrometer

The FTIR spectrometer instrument used in the present work is Shimadzu IR Spirit FTIR spectrometer (figure 2.9).

2.3.1c Transmission electron microscopy (TEM)

Transmission electron microscopy (TEM) is a technique to analyze the surface structure, surface imperfection, crystal structure of the atom, and the size of the particle. In this technique, an electron beam is passed through the sample and allowed to interact with the material. As a result of this interaction, an image is created with the help of an image recording device like fluorescent screen.

Generally, parts of a TEM microscope include electron Source, electromagnetic Lenses, specimen Holder and an imaging device (figure 2.10).

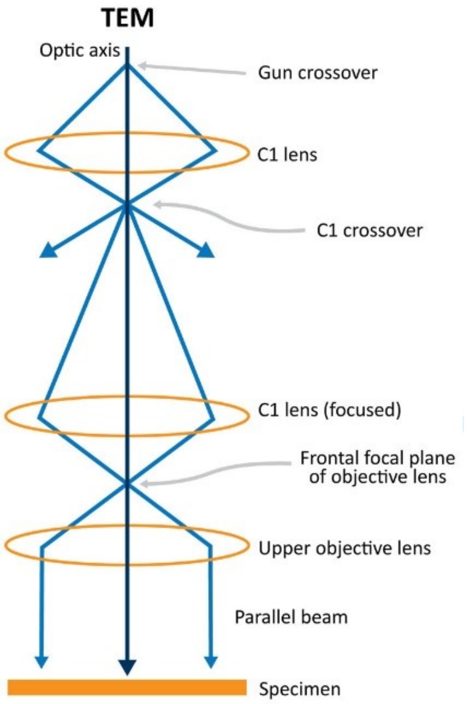

Fig 2.10 Transmission electron microscope

Electrons are generated through thermionic emission, where a heated filament releases them. The electromagnetic lens system, composed of copper wire coils and magnets, directs their path. By controlling the current passing through the coils, the electron trajectory can be precisely adjusted. In transmission electron microscopy (TEM), the specimen must be exceptionally thin to permit electron transmission and subsequent image formation, making careful sample preparation crucial. Thin sections are placed on copper grids, available in different materials and mesh sizes, which are then mounted in a holder and introduced into the TEM goniometer via a vacuum lock, since the instrument operates under high-vacuum conditions. Proper handling during preparation is vital to avoid deformation of the metallic specimen, as plastic deformation may introduce artificial structural defects in the TEM images. Common preparation methods include spark cutting and focused ion beam (FIB) techniques. The imaging system typically employs a phosphor or fluorescent screen to display the transmitted electron image.

2.3.2 Morphological and Compositional analysis

2.3.2a Scanning electron microscopy

The scanning electron microscope (SEM) employs a focused beam of high-energy electrons to produce various signals from the surfaces of solid specimens. These signals, resulting from interactions between the electrons and the sample, provide insights into the sample's external morphology (texture), chemical composition, and crystalline structure and orientation. In most applications, data are gathered from a chosen area on the sample's surface, generating a two-dimensional image that highlights spatial variations in these characteristics. Conventional SEM techniques can image areas ranging from approximately 1 cm to 5 microns in width, with magnifications from 20X to around 30,000X and spatial resolutions of 50 to 100 nm. Additionally, the SEM can analyze specific point locations on the sample, making it particularly useful for qualitatively or semi-quantitatively determining chemical compositions (using EDS), crystalline structures, and crystal orientations (using EBSD).

Unlike the Transmission Electron Microscope, which relies on transmitted electrons, the Scanning Electron Microscope (SEM) utilizes emitted electrons. The SEM operates on the principle of applying kinetic energy to generate signals based on electron interactions with the sample. These interactions produce secondary electrons, backscattered electrons, and diffracted backscattered electrons, which are essential for imaging crystallized elements and photons. Secondary electrons, emitted from the specimen, are primarily responsible for capturing the morphology and topography of the sample, while backscattered electrons provide contrast that reveals compositional differences among the elements within the specimen [18,19].

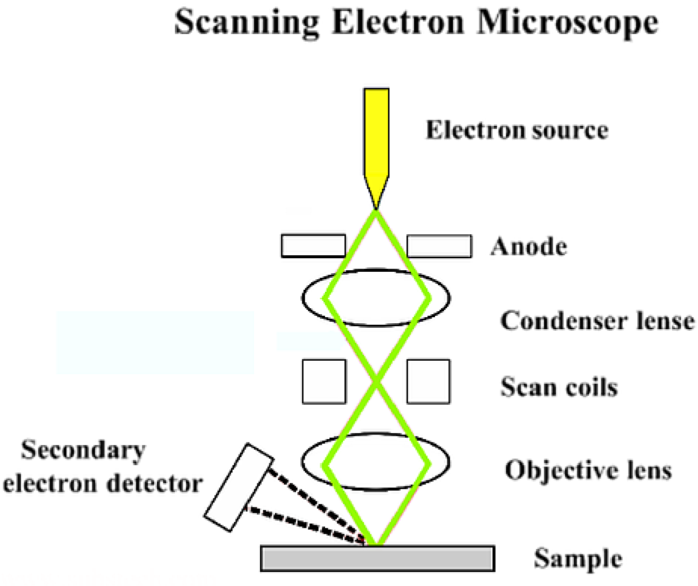

Fig 2.11 SEM Instrumentation

The parts of a SEM are depicted in figure 2.11. There are three types of electron sources that can be utilized: tungsten filament, lanthanum hexaboride, and field emission gun (FEG). There are several condenser lenses that focus the electron beam from the source as it travels through the column, resulting in a narrow beam that creates a spot known as the spot size. The scanning coil is used to scan the beam over the specimen surface. The detector consists of multiple detectors that can distinguish between secondary electrons, backscattered electrons, and diffracted backscattered electrons. The performance of these detectors is largely influenced by factors such as voltage speed and the density of the specimen.

The specimen does not require special preparation for visualization under the SEM; even air-dried samples can be examined directly. However, microbial specimens necessitate fixation, dehydration, and drying to preserve structural features and prevent collapse in the high vacuum environment of the microscope. Samples are mounted and typically coated with a thin layer of heavy metal to enhance spatial scattering of electric charges on the specimen's surface, resulting in clearer images.

Electrons are emitted after thermal energy is applied to the electron source, allowing them to accelerate rapidly towards the positively charged anode. The electron beam generates primary scattered electrons at high energy levels and secondary electrons at lower energy levels from the specimen's surface. This interaction produces signals that provide information about the surface topography and composition of the specimen.

Scanning is achieved by directing the electron beam back and forth over a thin section of the specimen. When the beam interacts with the surface, it emits secondary electrons, a process influenced by the specimen's topography: raised surfaces generate higher quantities of electrons, leading to brighter appearances on the screen, while depressed surfaces yield fewer electrons, resulting in darker images.

As the secondary electrons are captured by the detector, they strike a scintillator (a luminescent material that fluoresces upon impact with charged particles or high-energy photons). This produces flashes of light that are converted into an electric current by a photomultiplier, sending a signal to the cathode ray tube. The resulting image can be viewed and photographed.

2.3.2b EDAX

Energy dispersive X-ray analysis (EDAX), also referred to as energy dispersive spectroscopy (EDS), is widely used for the elemental or chemical characterization of various materials. The sample can be in various forms, including solid thin films, solid powders, liquid samples, or even pellets.

To generate characteristic X-rays from a sample, it is bombarded with a high-energy beam of charged particles (such as electrons or protons) or X-rays. The sample's atoms contain ground state electrons in distinct energy levels or electron shells bound to the nucleus. When an incident beam excites an electron from an inner shell, it is ejected, creating a vacancy. An electron from a higher-energy shell can then fill this vacancy, and the energy difference between the two shells is released as an X-ray. Quantitative analysis of the energy and quantity of these X-rays can be performed using energy-dispersive X-ray analysis. Since the energy of these X-rays is a characteristic feature of the energy difference between the two shells and reflects the atomic structure of the discharging element, EDAX is a valuable tool for identifying the elemental composition of a sample [20,21].

Since EDS is used in conjunction with SEM, the same electron gun serves as the source of incident electrons. Lenses and an aperture are used to focus the beam. The energy of the electron beam must be carefully chosen to balance the resolution requirements with the efficiency of X-ray production. The generated X-rays are detected by two crystal spectrometers. The EDS detector measures the count of X-rays (representing the abundance of emitted X-rays) against their energies. This detector is a solid-state device based on lithium-drifted silicon. When X-rays hit the detector's surface, they generate a charge pulse, which is directly proportional to the energy of the incident X-ray. A charge sensitive preamplifier is employed to convert the charge pulse to a voltage pulse. A multi-channel analyzer is employed to sort the pulses based on their voltage from the signals received. The energy of the X-rays is determined by measuring the voltage of these charge pulses, and the resulting data is then processed and displayed as a histogram of intensity versus voltage. Often, a Si (Li) detector, cooled with liquid nitrogen to cryogenic temperatures, is used. However, many modern systems also incorporate silicon drift detectors (SDD) with Peltier cooling systems.

EDAX is often integrated within the SEM system. The EDS spectrum generated from X-rays enables qualitative analysis to identify the elements present in the sample when it is exposed to a high-energy electron beam.

X-ray mapping helps to identify the distribution of specific elements within a sample. For analysis, the electron beam is scanned over a designated area, and the corresponding characteristic X-rays are collected. If the peak-to-background ratio is low, the X-ray map may not accurately represent the distribution of the desired element, instead displaying a continuous background of X-rays. Additionally, the map might fail to show the distribution of elements that are not of interest when their characteristic X-rays are similar to those of the elements of interest, especially if the energy difference between them falls within the spectrometer's energy resolution. Acquiring a single X-ray image takes longer because the intensities of X-rays are lower compared to those of secondary and backscattered electrons, and the resolution of X-ray mapping is constrained by "Area Analysis."

Since the intensities of characteristic X-rays are proportional to the concentration of specific elements, a quantitative analysis can also be conducted. The concentrations of unknown elements in a sample can be determined by comparing the intensities of the characteristic X-rays from a standard sample to those from the unknown sample. However, the X-rays generated within the sample may be absorbed by the sample itself or X-rays can be excited from other elements before being emitted into the vacuum. Therefore, corrections are necessary in this analysis method, and the following prerequisites must be met: i) The specimen surface should be flat, ii) The electron probe must enter the sample in a perpendicular direction, and iii) The distribution of elements in the X-ray generation area should be uniform.

2.3.3 Optical characterization

2.3.3a Diffuse reflectance spectroscopy (DRS)

When light hits a flat reflective surface, such as a mirror, it reflects at a specific angle in accordance with the law of reflection. In contrast, when light interacts with a powdered or porous material, it scatters in multiple directions due to the roughness of the surface and the variations in particle size and shape. This type of multi-directional scattering is referred to as diffuse reflectance.

In diffuse reflectance spectroscopy, a beam of light from a UV, visible, or IR spectrophotometer is directed at the sample, and the intensity of the diffusely reflected light is measured across a range of wavelengths. The absorption of light by the sample's components decreases the amount of light that is reflected. By applying suitable mathematical models to the diffuse reflected light measurements, it is possible to relate the reflectance to the absorbing and scattering properties of materials, thereby obtain a quantitative information about the composition and properties of powders, pastes, granules, fibres, and other materials.

Though Ultraviolet-Visible (UV-Vis) spectroscopy and diffuse reflectance spectroscopy are based on light-matter interaction, there are some differences between the two [22]. The former is primarily used for analysing liquid samples held in transparent cuvettes, whereas the latter is suitable for solids and powders. UV-Vis spectroscopy benefits from a well-defined light path through the liquid, allowing for quantitative analysis based on Beer's Law. In contrast, DRS requires complex mathematical modelling due to the scattering behaviour of light in solid samples. DRS can provide insights into layers beneath the surface of a material, while UV-vis spectroscopy is generally limited to surface analysis for opaque samples. Calibration in UV-vis spectroscopy typically relies on reference solutions, while DRS may use reference materials that are similar in composition to the sample being analyzed.

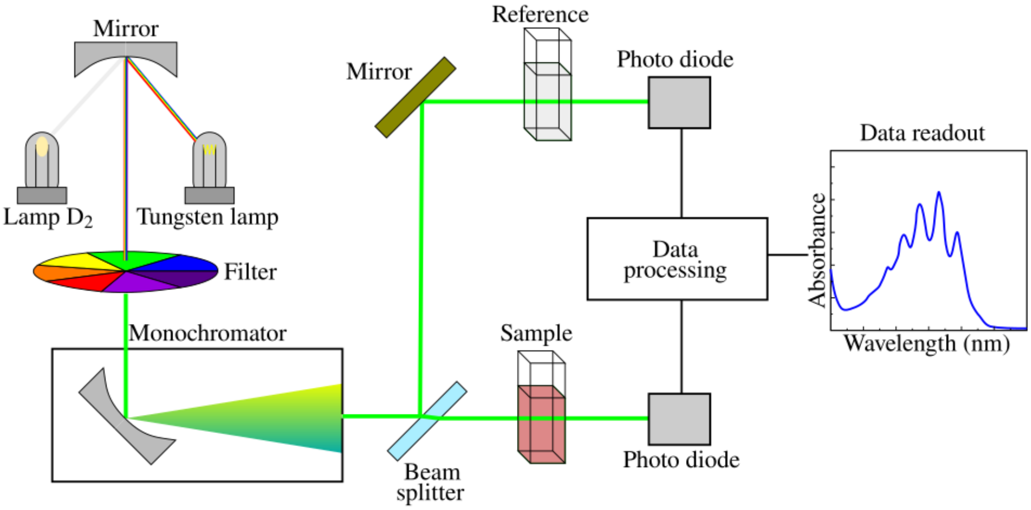

Fig 2.12 DRS instrumentation

The main parts of a DRS spectrophotometer are as follows (figure 2.12). The light Source provides a high-voltage spark to excite the atoms in the sample. Spectrophotometers use tungsten lamps for visible light or deuterium or hydrogen lamps for UV light. The monochromator generates a single wavelength of radiation. It features a fixed entrance slit, a dispersing element such as diffraction grating, and a moving exit slit. Collimator is an optical device that directs a light beam in a straight line. Wavelength Selector allows the transmission of a specific wavelength. Mirrors and Fibres guide the light beam through the optical path. Detector measures the intensity of light. And the photoelectric device, such as a photocell, converts light energy into electrical energy. The computer assembly of the spectrometer that converts the data from the detector into a digital display, also presenting the final output in a file format that can be processed for further use.

Dispersive elements separate the wavelength components of the light beam spatially, enabling simultaneous detection using an array detector, such as a CMOS (Complementary Metal Oxide Semiconductor) or CCD (Charge-Coupled Device) camera. The use of dispersive components in DRS spectroscopy simplifies the design of the instrument, facilitating miniaturization and reducing acquisition times. However, the data analysis in diffuse reflectance spectroscopy can be considerably more complex than in traditional transmission absorption measurements. Reflection geometries generally provide improved signal-to-noise ratios in measurements due to enhanced transmission through the spectrometer [23].

The theoretical framework for diffuse reflection lies on understanding how light propagates through inhomogeneous materials, although only approximate models are available. The frequently used model for diffuse reflection data analysis is Kubelka-Munk (K-M) model, a particularly straightforward solution for semi-infinite samples. In this case, all the geometric complexities of the inhomogeneous sample are encapsulated in a single parameter known as the scattering coefficient ‘s’. The familiar K-M transform, or the ‘k/s’ ratio, is expressed as:

$$\frac{k}{s} = \frac{(1 - R_\infty)^2}{2R_\infty}$$

where, ‘k’ is the absorption coefficient of the sample with a diffuse reflectance ‘R_∞’. The K-M transform of the measured spectroscopic observable is roughly proportional to the absorption coefficient, and in turn, on the concentration. The scattering coefficient, incorporated into the theoretical framework of diffuse reflection as a semi-empirical parameter to represent internal scattering processes, is primarily influenced by the particle size and refractive index of the sample rather than the wavelength or the absorption coefficient. More critically, it varies significantly with packing density, so it is important to ensure that powdered samples are packed as consistently as possible to achieve accurate quantitative results.

To evaluate the bandgap of the synthesized nanostructures, the reflectance data (R)recorded in the wavelength ranges of 200 - 800 nm, is then converted into f(R) by the K–M algorithm. From the $(f(R)h\nu)^n$ versus photon energy (hν) plot, on extrapolation of the linear region of the curve, one can obtain the indirect bandgap (n = ½) and direct bandgap (n = 2) values.

Fig 2.13 Shimadzu UV-2600 spectrophotometer

The instrument used in the present work is a Shimadzu UV-2600 spectrophotometer (figure 2.13).

2.3.3b Photoluminescence spectroscopy

Photoluminescence (PL) spectroscopy is a type of light emission spectroscopy that relies on a process known as photo-excitation. When light is directed at a sample, the electrons in the material are elevated to excited states. As these electrons return to their equilibrium states, the energy is released in the form of light. Like fluorescence spectroscopy, PL spectroscopy utilizes a fixed wavelength to excite electrons, resulting in the emission of light at different wavelengths. The intensity of this emitted light is plotted against the wavelength on a PL spectrum, that helps in determining the electronic structure and properties of materials.

Interpreting photoluminescence spectra is relatively straightforward. The PL excitation spectrum is obtained by fixing the emission wavelength while varying the excitation wavelength. The data obtained is essential for identifying the appropriate fixed excitation wavelength for the emission spectrum. Consequently, the emission spectrum is generated by exciting electrons at a fixed wavelength while detecting emissions at various wavelengths. The information obtained from the emission spectrum typically includes the peak emission intensity of the material, which is utilized to compare its electronic properties [24]. Key features o be noted in PL spectral analyze include:

- Peak Shift in PL Spectrum: By using the photon-energy equation, one can determine the transition energy from the wavelength of the emission maxima. If this peak shifts to a higher or lower wavelength than anticipated, it may indicate changes in the bulk material properties, such as the band gap. Movements in these emission peaks could also result from molecular aggregation, such as excimer formation, or increased conjugation in polymers.

- PL Intensity: The intensity of photoluminescence reveals much about the optical properties of your sample, including the balance between radiative and non-radiative processes, the extent of quenching, and any re-absorption occurring within the sample. In the absence of an integrating sphere, measurements of PL intensity should be considered comparative rather than quantitative. However, using an optical spectrometer allows you to detect significant changes in luminescent intensity relative to a control sample. Additionally, if photoluminescent materials are used to label specific molecules in the system, these molecules can be quantified during or after an event based on PL intensity, which will be linearly proportional to the concentration of fluorophores present.

- Full Width Half Maximum (FWHM): The FWHM of the sample provides insight into its homogeneity. A broader peak linewidth indicates that the fluorescing material is more polydisperse or inhomogeneous. In colloidal dispersions, such as luminescent quantum dots, increased polydispersity may suggest a wider range of particle sizes, shapes, or the presence of defects. In thin films, a broader linewidth could point to an increase in defects, trap states, or non-radiative recombination centres within the film.

- Evolving Peaks: There may be changes in photoluminescence intensity over time as the sample is continuously illuminated. Various factors can influence this. For instance, a decrease in intensity could indicate luminescence quenching. In thin films that are in contact with a transport layer, this measurement can provide insight into charge extraction efficiency from the absorbent layer. Conversely, PL intensity may increase over time in semiconductors due to interstitial vacancies. Initially, excited electrons fill these trap states, resulting in low radiative recombination. Over time, as these trap states become occupied, electrons can relax radiatively from the S_1 state, leading to an increase in radiative recombination. Depending on the time frame of these intensity changes, it can be measured using steady-state (lifetimes > 1s) or time-resolved photoluminescence (picoseconds to milliseconds) spectroscopy.

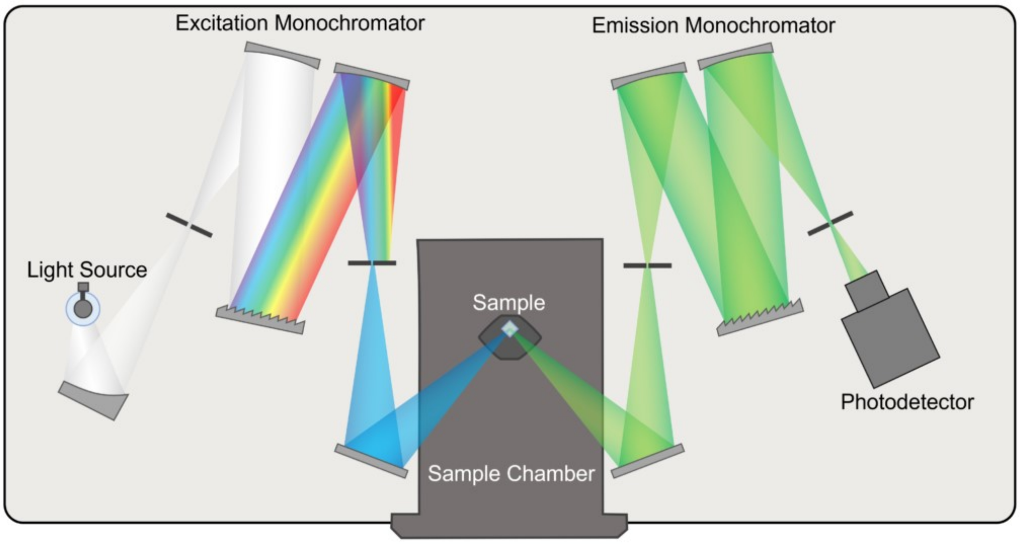

Fig 2.14 PL spectrometer instrumentation

The main parts of a PL spectrophotometer include (figure 2.14),

- Monochromator: A device that selects the specific excitation and emission wavelengths.
- Light Source: Provides illumination for the sample.
- Detector: Captures and records the fluorescence emitted by the sample.
- Sample Cell: Comparable to those used in molecular absorption experiments.

Fig 2.15 Shimadzu RF-5301PC spectrofluorometer

The PL measurements in this study were recorded using a Shimadzu RF-5301PC spectrofluorometer (figure 2.15).

2.3.3c Color characterization

In 1931, the Commission Internationale de l'Éclairage (CIE) introduced a universal color definition using a two-dimensional chromaticity diagram. The CIE system defines colors according to the human visual system, with each color specified by its CIE coordinates. Based on psychophysical data, the CIE established standard sensitivity curves for a “typical” observer, known as the color matching functions (CMFs), which represent derived responses rather than actual retinal pigment absorption. These color matching functions $x(\lambda)$, $y(\lambda)$, and $z(\lambda)$, give the relative contributions of the three CIE primaries X, Y, and Z, corresponding to wavelengths $\lambda x = 700$ nm, $\lambda y = 543.1$ nm, and $\lambda z = 435.8$ nm respectively. Each color is expressed as a mixture of three primaries - RGB (for CRT systems) or XYZ (for fundamental measurements) - with their proportions determining the perceived color. For convenience, color is often described in terms of luminance and chromaticity [25].

Any color in the diagram can thus be represented by the tristimulus values (x, y, z), corresponding respectively to the red, green and blue component in the luminescent emission. From the spectral power distribution (SPD) of light, one can calculate brightness (Y) and the chromaticity coordinates x, y and z, constrained under the condition x + y + z = 1. Since z = 1 – x – y, the color coordinate diagram (figure 2.16) can be visualised on a 2-D plot, and each colour corresponds to a point on the diagram. The process for determining chromaticity coordinates is:

- Measure the spectral power distribution of the object at each wavelength.
- Multiply by each colour matching function.
- Sum the results to obtain X, Y, and Z (with Y indicating brightness).
- The chromaticity coordinates (x, y) are $x = \frac{X}{X+Y+Z}$ and $y = \frac{Y}{X+Y+Z}$

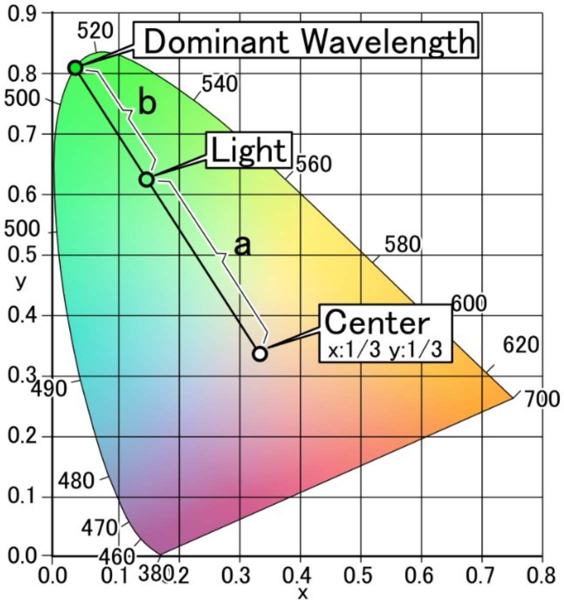

Fig 2.16 CIE chromaticity diagram

Once the color coordinates are calculated and plotted on a chromaticity diagram, one can calculate color purity using the procedure -

- Draw a line from the central white point (1/3,1/3) through the chromaticity coordinates of the sample to the boundary of the diagram.
- The intersection with the spectral locus gives the dominant wavelength.
- Purity is the ratio (a/(a+b)), where, ‘a’ is the distance from the white point to the sample’s chromaticity coordinate and ‘b’ is the distance from the sample’s chromaticity coordinate to the spectral locus at the dominant wavelength.

2.3.4 Photocatalytic Activity

Photocatalytic degradation of pollutants, is a major concern in a socially and industrially advanced society. Photocatalysis refers to the accelerated photo-reaction that occurs in the presence of a catalyst. A photocatalyst acts as a sensitizer for light-induced redox reactions, with the reaction rate depending on the catalyst's crystal structure and the energy of incoming photons.

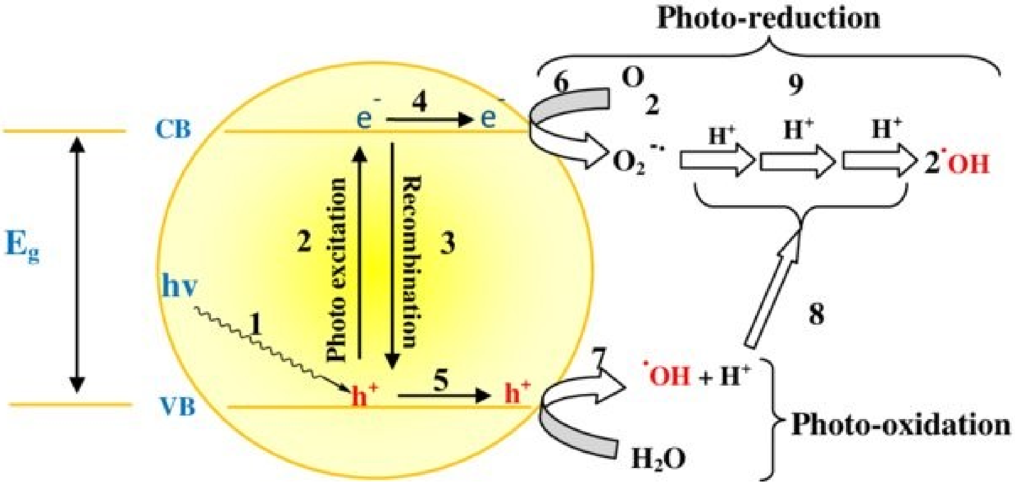

Fig 2.17 Mechanism of photocatalysis

When the catalyst's band gap is equal to or less than the photon energy, electrons in the valence band absorb the light and jump to the conduction band, leaving behind holes (figure 2.17). These holes oxidize donor molecules and react with water to produce hydroxyl radicals, while conduction band electrons reduce water to form superoxide ions. Together, these electron-hole pairs drive oxidation-reduction reactions, converting contacting materials into useful products [25]. The efficiency or activity of the catalyst largely depends on how effectively it can generate electron-hole pairs.

These electron-hole pairs further interact and generate free radicals, that undergo secondary reactions, typically with a reactant. The photocatalytic activity can be improved with nanoparticles instead of bulk semiconductor materials, since the nanomaterials have high surface to volume ratio and this will increase the surface adsorption of organic pollutants on the catalyst surface.

During the photocatalysis process, the sample being evaluated as a catalyst is introduced into an organic dye solution, which is continuously stirred under light exposure. At regular time intervals, aliquots of the solution are collected, and their absorbance spectra are measured. The degradation efficiency is then compared to that of the pure dye solution.

2.3.5 Anti-bacterial analysis

Agar diffusion-based assays, such as disk diffusion, well diffusion, agar plug, and agar spot assays, are widely used and cost-effective methods in antimicrobial research for assessing the antimicrobial activity of various test compounds. These techniques involve the diffusion of antimicrobial agents from paper discs, wells, or plugs into the surrounding agar medium, which inhibits the growth of the test microorganism inoculated on the agar surface. By measuring the resulting zone of inhibition, which indicates the area where microbial growth is prevented by the agent, researchers can evaluate the relative potency of the test compound against the microorganism being studied. The agar diffusion assay is a valuable tool in antimicrobial research, providing qualitative insights into the effectiveness of different substances against specific microorganisms [26].

The protocol for the agar diffusion assay involves several steps and typically takes 18–48 hours to complete, depending on the specific test microorganism. First, a culture of the test microorganism is prepared by inoculating it onto an appropriate growth medium and incubating it under optimal conditions. Once the culture reaches the desired growth phase, a sterile cotton swab is used to evenly distribute the microbial suspension across the surface of an agar plate, creating a uniform lawn. Next, wells of specific sizes are made in the agar using a sterile cork borer or pipette tip, into which the test substance is carefully added (well diffusion assay). Alternatively, the agar spot assay allows for the placement of filter paper disks (disk diffusion assay, also known as the Kirby-Bauer method) or agar plugs impregnated with the test compound on the agar surface. Another option involves spotting a small volume of the test compound directly onto the agar surface with a sterile inoculating loop (agar spot assay). The plate is then incubated at the appropriate temperature for a defined period to enable the compound to diffuse into the surrounding medium. After incubation, the plates are examined for inhibition zones, and the area or diameter of these zones is measured to evaluate the anti-microbial activity of the tested substances. Control plates containing only the solvent, culture filtrate, or buffer are included to account for any potential effects of the vehicle on microbial growth.

The agar diffusion assay offers several advantages that contribute to its popularity as a method for screening anti-microbial activity. It is a straightforward, cost-effective, and quick way of assessing microbial susceptibility to a test compound, that requires minimal specialized equipment, making it accessible to researchers with limited resources. This also allows for the simultaneous evaluation of multiple test substances against a single microorganism, facilitating comparative analysis of their antimicrobial effects. Additionally, the standardized protocol of the agar diffusion assay ensures consistency in results, which facilitates comparison across different studies and laboratories. This method is also highly versatile, allowing for the testing of a wide array of antimicrobial agents, including antibiotics, plant extracts, and synthetic compounds, against various microorganisms. The agar diffusion assay includes several variations, such as well, spot, plug, and paper disc methods, offering researchers additional flexibility. Finally, this assay has been extensively validated and is recognized as a reliable method by regulatory bodies, including the Clinical and Laboratory Standards Institute (CLSI).

The agar diffusion assay also has limitations that researchers should consider. The assay primarily provides qualitative results, indicating the presence or absence of antimicrobial activity through inhibition zones, rather than precise quantitative measurements or minimum inhibitory concentrations (MICs). Factors like temperature, humidity, and pH can influence the size of these zones, affecting the diffusion rate of the test compound. Variability may also arise from differences in molecular weight, solubility, and diffusion rates of the test substances, which can lead to uneven distribution of antimicrobial compounds. Additionally, the assay may struggle to assess the efficacy of volatile or heat-labile antimicrobial agents, and the subjective interpretation of inhibition zones can introduce bias, necessitating experienced judgment for accurate results. The agar diffusion method may not be as sensitive as other techniques, like the microdilution assay, in detecting low concentrations of antimicrobial agents, which could lead to missed weak activity. Despite these limitations, the agar diffusion assay remains a valuable tool for preliminary screening of antimicrobial activity [27].

2.3.6 Anti-cancerous measurements

In vitro cell viability and cytotoxicity assays using cultured cells are employed for assessing the toxic effects of chemicals and for drug screening. Interest in these assays has grown significantly in recent years, particularly in oncology research, where they are used to evaluate compound toxicity and tumour cell growth inhibition of a drug. These assays are rapid, cost-effective, and do not necessitate the use of any living species, making them suitable for testing large numbers of samples.

Cell viability and cytotoxicity assessments rely on various cellular functions, including cell membrane permeability, enzyme activity, cell adhesion, ATP (Adenosine Triphosphate) production, coenzyme production, and nucleotide uptake activity. Tests conducted using human cells may also provide more relevant results compared to some in vivo animal studies. These assays are currently utilized in toxicology and pharmacology, and the choice of assay method is critical for accurately assessing the nature of interactions [28].

These assays are categorized based on the types of endpoint measurements, such as color changes, fluorescence, and luminescence. In this work, the Trypan blue dye exclusion assay is employed to assess the number of viable and dead cells in a suspension. Trypan blue is a large negatively charged molecule that cannot penetrate intact cell membranes. Live cells exclude the dye, resulting in a clear cytoplasm, while dead cells take up the dye, appearing blue. In this assay, cells are treated with test compounds, washed, and then mixed with the dye for examination under a microscope to determine viability based on dye uptake. Although the staining process is straightforward, it becomes challenging to process many samples simultaneously, particularly when precise timing of cytotoxic effects is needed [29].

Procedure: The test compound was studied for short term in vitro cytotoxicity using Dalton's Lymphoma Ascites cells (DLA) or rat spleen cells. The tumour cells or spleen cells aspirated from the peritoneal cavity of tumour bearing mice were washed thrice with Phosphate-Buffered Saline (PBS) or normal cell line. Cell viability was determined by trypan blue exclusion method. Viable cells suspension (1×10^6 cells in 0.1 ml) was added to tubes containing various concentrations of the test compounds and the volume was made up to 1 ml using PBS. These assay mixtures were incubated for 3 hours at 37 ºC. further mixed with 0.1 ml of 1% trypan blue and kept for 2-3 minutes and loaded on a haemocytometer. Dead cells take up the blue colour of trypan blue while live cells do not take up the dye. The number of stained and unstained cells were counted separately.

$$\%\, cytotoxicity = \frac{No.of\ dead\ cells}{No.of\ live\ cells + No.of\ dead\ cells} \times 100$$

References

[1] Khalid, H., & Chaudhry, A. A. (2020). Basics of hydroxyapatite—Structure, synthesis, properties, and clinical applications. In A. S. Khan & A. A. Chaudhry (Eds.), *Handbook of ionic substituted hydroxyapatites* (pp. 85–115). Woodhead Publishing. https://doi.org/10.1016/B978-0-08-102834-6.00004-5

[2] Marciello, M., Luengo, Y., & Morales, M. del P. (2016). Iron oxide nanoparticles for cancer diagnosis and therapy. In *Nanoarchitectonics for smart delivery and drug targeting*. Elsevier. https://doi.org/10.1016/B978-0-323-47347-7.00024-0

[3] Zueva, S. B. (2018). Current legislation and methods of treatment of wastewater coming from waste electrical and electronic equipment processing. In F. Vegliò & I. Birloaga (Eds.), *Waste electrical and electronic equipment recycling* (pp. 213–240). Woodhead Publishing. https://doi.org/10.1016/B978-0-08-102057-9.00009-3

[4] Jamkhande, P. G., Ghule, N. W., Bamer, A. H., & Kalaskar, M. G. (2019). Metal nanoparticles synthesis: An overview on methods of preparation, advantages and disadvantages, and applications. *Journal of Drug Delivery Science and Technology, 53,* 101174. https://doi.org/10.1016/j.jddst.2019.101174

[5] Baig, N., Kammakakam, I., & Falath, W. (2021). Nanomaterials: A review of synthesis methods, properties, recent progress, and challenges. *Materials Advances, 2,* 1821–1871. https://doi.org/10.1039/d0ma00807a

[6] Sonawane, G. H., Patil, S. P., & Sonawane, S. H. (2018). Nanocomposites and its applications. In S. M. Bhagyaraj, O. S. Oluwafemi, N. Kalarikkal, & S. Thomas (Eds.), *Applications of nanomaterials* (pp. 1–22). Woodhead Publishing. https://doi.org/10.1016/B978-0-08-101971-9.00001-6

[7] Patil, N., Bhaskar, R., Vyavhare, V., Dhadge, R., Khaire, V., & Patil, Y. (2021). Overview on methods of synthesis of nanoparticles. *International Journal of Current Pharmaceutical Research, 13,* 11–16. https://doi.org/10.22159/ijcpr.2021v13i2.41556

[8] Sood, R., & Chopra, D. S. (2018). Metal–plant frameworks in nanotechnology: An overview. *Phytomedicine, 50,* 148–156. https://doi.org/10.1016/j.phymed.2017.08.025

[9] Parauha, Y. R., Sahu, V., & Dhoble, S. J. (2021). Prospective of combustion method for preparation of nanomaterials: A challenge. *Materials Science and Engineering: B, 267,* 115054. https://doi.org/10.1016/j.mseb.2021.115054

[10] Bhagwat, V. R., Humbe, A. V., More, S. D., & Jadhav, K. M. (2019). Sol-gel auto combustion synthesis and characterizations of cobalt ferrite nanoparticles: Different fuels approach. *Materials Science and Engineering: B, 248,* 114388. https://doi.org/10.1016/j.mseb.2019.114388

[11] Agarwal, H., Menon, S., Kumar, S. V., & Rajeshkumar, S. (2018). Mechanistic study on antibacterial action of zinc oxide nanoparticles synthesized using green route. *Chemico-Biological Interactions, 286,* 60–70. https://doi.org/10.1016/j.cbi.2018.03.008

[12] Sharma, R., Bisen, D. P., Shukla, U., & Sharma, B. G. (2012). X-ray diffraction: A powerful method of characterizing nanomaterials. *Recent Research in Science and Technology, 4,* 77–79. http://recent-science.com/

[13] Holder, C. F., & Schaak, R. E. (2019). Tutorial on powder X-ray diffraction for characterizing nanoscale materials. *ACS Nano, 13,* 7359–7365. https://doi.org/10.1021/acsnano.9b05157

[14] Abraham, J., Jose, B., Jose, A., & Thomas, S. (2020). Characterization of green nanoparticles from plants. In N. Thajuddin & S. Mathew (Eds.), *Phytonanotechnology* (pp. 21–39). Elsevier. https://doi.org/10.1016/B978-0-12-822348-2.00002-4

[15] Mallakpour, S., & Hussain, C. M. (2021). *Handbook of consumer nanoproducts*. Springer Singapore. https://doi.org/10.1007/978-981-15-6453-6

[16] Faghihzadeh, F., Anaya, N. M., Schifman, L. A., & Oyanedel-Craver, V. (2016). Fourier transform infrared spectroscopy to assess molecular-level changes in microorganisms exposed to nanoparticles. *Nanotechnology for Environmental Engineering, 1,* 1–9. https://doi.org/10.1007/s41204-016-0001-8

[17] Baudot, C., Tan, C. M., & Kong, J. C. (2010). FTIR spectroscopy as a tool for nano-material characterization. *Infrared Physics & Technology, 53,* 434–438. https://doi.org/10.1016/j.infrared.2010.09.002

[18] Akhtar, K., Khan, S. A., Khan, S. B., & Asiri, A. M. (2018). Scanning electron microscopy: Principle and applications in nanomaterials characterization. In *Handbook of materials characterization*. Springer International Publishing. https://doi.org/10.1007/978-3-319-92955-2_4

[19] Hodoroaba, V. D., Rades, S., Salge, T., Mielke, J., Ortel, E., & Schmidt, R. (2016). Characterization of nanoparticles by means of high-resolution SEM/EDS in transmission mode. *IOP Conference Series: Materials Science and Engineering, 109,* 012006. https://doi.org/10.1088/1757-899X/109/1/012006

[20] Hodoroaba, V.-D. (2020). Energy-dispersive X-ray spectroscopy (EDS). In V.-D. Hodoroaba, W. E. S. Unger, & A. G. Shard (Eds.), *Characterization of nanoparticles* (pp. 397–417). Elsevier. https://doi.org/10.1016/B978-0-12-814182-3.00021-3

[21] Sharma, V. (2019). A review on characterization of solid dispersion. *International Journal of Engineering Applied Sciences and Technology, 4,* 127–128. https://doi.org/10.33564/ijeast.2019.v04i06.021

[22] Bock, S., Kijatkin, C., Berben, D., & Imlau, M. (2019). Absorption and remission characterization of pure, dielectric (nano-)powders using diffuse reflectance

spectroscopy: An end-to-end instruction. *Applied Sciences, 9,* 4933. https://doi.org/10.3390/APP9224933

[23] Frei, R. W., & Zeitlin, H. (1971). Diffuse reflectance spectroscopy. *CRC Critical Reviews in Analytical Chemistry, 2*(2), 179–246. https://doi.org/10.1080/10408347108542764

[24] Matsuoka, M., Saito, M., & Anpo, M. (2012). Photoluminescence spectroscopy. In *Characterization of solid materials and heterogeneous catalysts: From structure to surface reactivity* (Vol. 1, pp. 149–184). Wiley-VCH. https://doi.org/10.1002/9783527645329.ch4

[25] Chen, J., Cranton, W., & Fihn, M. (2016). *Handbook of visual display technology* (J. Chen, W. Cranton, & M. Fihn, Eds.). Springer Cham. https://doi.org/10.1007/978-3-319-14346-0

[26] Tahir, M. B., Sohaib, M., Sagir, M., & Rafique, M. (2022). Role of nanotechnology in photocatalysis. In *Encyclopedia of smart materials* (pp. 578–589). Elsevier. https://doi.org/10.1016/B978-0-12-815732-9.00006-1

[27] Balouiri, M., Sadiki, M., & Ibnsouda, S. K. (2016). Methods for in vitro evaluating antimicrobial activity: A review. *Journal of Pharmaceutical Analysis, 6,* 71–79. https://doi.org/10.1016/j.jpha.2015.11.005

[28] Hossain, M. L., Lim, L. Y., Hammer, K., Hettiarachchi, D., & Locher, C. (2022). A review of commonly used methodologies for assessing the antibacterial activity of honey and honey products. *Antibiotics, 11,* 975. https://doi.org/10.3390/antibiotics11070975

[29] Riss, T., Niles, A., Moravec, R., et al. (2019). Cytotoxicity assays: In vitro methods to measure dead cells. In S. Markossian, A. Grossman, H. Baskir, et al. (Eds.), *Assay guidance manual*. Eli Lilly & Company & the National Center for Advancing Translational Sciences. https://www.ncbi.nlm.nih.gov/books/NBK540958/

[30] Aslantürk, Ö. S. (2018). In vitro cytotoxicity and cell viability assays: Principles, advantages, and disadvantages. InTech. https://doi.org/10.5772/intechopen.71923

Chapter 3

LUMINESCENT STUDIES IN PRISTINE AND RE (RE = Eu, Tb) DOPED $ZnAl_2O_4$ NANOPHOSPHOR SYNTHESIZED USING CO-PRECIPITATION TECHNIQUE

The chapter discusses the synthesis of pristine and RE doped (RE = Eu, Tb) zinc aluminate through co-precipitation technique. After optimising the synthesis conditions of pure $ZnAl_2O_4$*, the effect of RE dopant assimilation into the host matrix is thoroughly investigated. The structural characterization was done using XRD, TEM and FTIR measurements. SEM-EDAX was used for morphological and compositional analysis. The optical bandgap measurements were done by applying K-M theory on diffuse reflectance spectra. The photoluminescent response of the pure and doped samples were studied and the purity of the emission was gauged using CIE colorimetry.*

3.1 Introduction

Among the several methods for synthesis of zinc aluminate ($ZnAl_2O_4$) nanomaterials, the co-precipitation route stands out as a simple approach, with prominent distinctive features such as high product yield and purity, evasion of harmful chemicals, ease of reproducibility and low cost. In spite of the method being widely used to synthesise binary oxide phosphors, reports are rare in RE doped ternary oxides like $ZnAl_2O_4$.

Battiston *et al.* investigated the photocatalytic activity of $ZnAl_2O_4$, with a crystallite size of 25 nm, synthesized by co-precipitation method, followed by calcination at 750°C for 3.5 hours [1]. Cheng *et al.* synthesized porous $ZnAl_2O_4$ spinel nanorods using a homogeneous co-precipitation technique, followed by heat treatment at 900°C for 3 hours [2]. Syam sunder *et al.* synthesised $ZnAl_2O_4$ nanaoparticles with size 5-16 nm via chemical co-precipitation, post-calcination being done between 600-900 ºC for 4 hours [3]. Ciupina *et al.* reported the co-precipitation synthesis of zinc aluminate nanoparticles and observed the complete formation of nanoparticles only after calcination at 800 ºC [4]. Syam Sunder *et al.* also studied the thermal evolution of $ZnAl_2O_4$ spinel structure by varying the calcination temperature and concluded that the complete formation is only possible at 900 ºC for 4 hours [5,6]. Eka Angasa *et al.* tried the co-precipitation synthesis of zinc aluminate with and without the presence of water extract of Impatiens balsamina leaves for different amounts and concluded that uniform nanoparticle formation happens in the presence of the extract [7]. Parya *et al.* reported the action of ultra-fine $ZnAl_2O_4$ spinel hydrogel precursor, synthesized via co-precipitation of Zn^{2+} and Al^{3+} salts using ammonium hydroxide - hexamethylenetetramine, as a bonding material and sintering aid for pure alumina [8]. Valenzuela *et al*. reported a comparison between co-precipitation, sol-gel and wet mixing synthesis methods of $ZnAl_2O_4$ [9].

$ZnAl_2O_4$ is a proved wide bandgap material with inherent blue luminescence suitable for optoelectronic applications. The co-precipitation method, though simple, is less explored for making doped $ZnAl_2O_4$. Since various factors such as precursor ratio, pH, post-calcination temperature, etc. affect the formation of the final product, optimising the method for the formation of structurally good ternary oxide nanoparticles is an essential pre-requisite before probing the luminescent response of the material. Hence, exploring the synthesis of rare earth singly doped $ZnAl_2O_4$ via co-precipitation method stands as the prime aim of the present study.

3.2 Experiment

The precursors used for the synthesis of pristine and doped $ZnAl_2O_4$ were zinc nitrate ($Zn(NO_3)_2.6H_2O$; Merck), aluminium nitrate ($Al(NO_3)_3.9H_2O$; Merck), europium nitrate ($Eu(NO_3)_3.H_2O$; Sigma-Aldrich) and terbium nitrate ($Tb(NO_3)_3.H_2O$; Sigma-Aldrich). Adequate amounts of the chemical precursors of Zn and Al were weighed, added to distilled water and stirred separately till dissolution. The pH of the mixture was adjusted by adding ammonia solution (25%; Merck) dropwise with constant stirring. The mixture was kept for 24 hours at room temperature, then filtered and the precipitate was dried at 80 °C in a hot air oven for 12 hours and the ground fine powder was calcined between 300 - 750 °C.

$$Zn(NO_3)_2 + 2Al(NO_3)_3 \xrightarrow{NH_4OH} Zn(OH)_2.2Al(OH)_2 \xrightarrow[\Delta]{80^0C} ZnAl_2O_4 + H_2O$$

$ZnAl_{2-x}O_4{:}Eu_x$ (x = 0 - 0.15 M) and $ZnAl_{2-y}O_4{:}Tb_y$ (y = 0 - 0.09 M) nanophosphors were also prepared employing the same synthesis procedure, with the additional respective precursors of Eu^{3+} and Tb^{3+} ions.

The powder XRD patterns were recorded using the PANalytical Aeris X-ray diffractometer with Cu-K_α radiation (λ = 1.5406 Å, X-ray tube voltage = 40 kV and current = 15 mA). The TEM-SAED measurement was done using Joel-2100+ high resolution transmission electron microscope. The SEM-EDAX imaging was recorded by means of Jeol 6390LA/OXFORD XMX N scanning electron microscope. The FTIR spectra were taken using a Shimadzu IR Spirit FTIR spectrometer. The diffuse reflectance spectra were attained using a Shimadzu UV 2600 UV-Vis-NIR spectrophotometer. The photoluminescence (PL) spectra were recorded on a Shimadzu RF 5301 PC Spectrofluorophotometer and the color characterization of the samples were also done.

3.3 Results and discussions

3.3.1 Pristine $ZnAl_2O_4$

Figure 3.1 gives the XRD spectra of samples post-calcined at various temperatures, fixing the precursor molar ratio Zn:Al and pH at 1:2 and 8 respectively. As evident from the XRD spectra, the as-prepared sample does not exhibit any specific peak formation, which signifies the need for post-calcination for compound formation to occur.

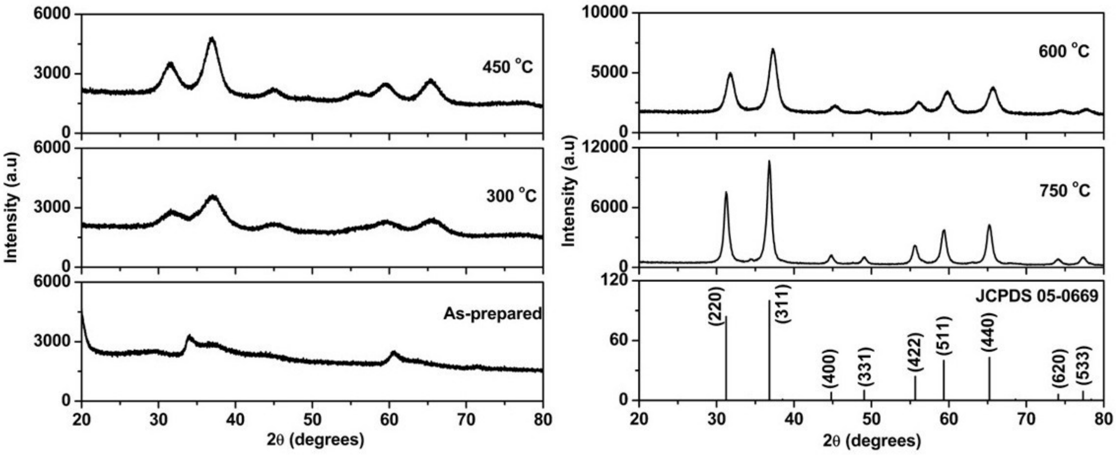

Fig 3.1 XRD spectra of $ZnAl_2O_4$ calcined at temperatures 300 - 750°C

The structural formation begins even at 300 °C, which is clear from the formation of peaks indexed to (220), (311), (400), (331), (511), (422), (440), (620) and (533) crystal planes of cubic spinel structure of $ZnAl_2O_4$ matrix according to the standard JCPDS file 05-0669 [10]. The growth of sharp, narrow and high intensity peaks with increase in temperature indicates improved crystallinity on calcination [11–13]. The structural parameters were calculated and given in table 3.1. As expected, crystallite size increases with temperature.

Parameter		**(311) peak diffraction angle 2θ (degrees)**	**FWHM (degrees)**	**Crystallite size (nm)**	**Lattice parameter (Å)**
Calcination temperature	**pH**				
300 °C	**8**	36.881	3.574	2.343	8.077
450 °C		36.905	2.212	3.786	8.072
600 °C		37.295	1.289	6.505	7.991
750 °C		36.809	0.745	11.239	8.093
JCPDS 05-0669					8.080

Table 3.1 Crystallite size and lattice parameter calculated for $ZnAl_2O_4$ synthesized at calcination temperatures 300 – 750 °C

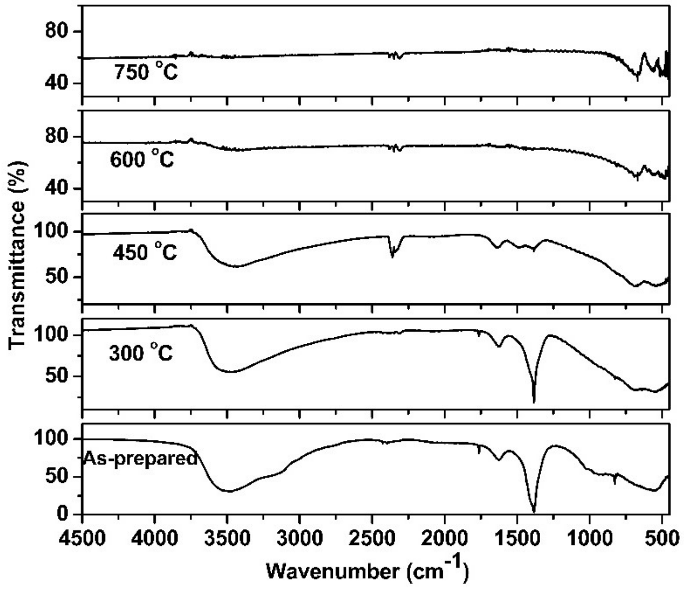

Fig 3.2 FTIR spectra of $ZnAl_2O_4$ calcined at temperatures 300 – 750 °C

The FTIR spectral results (figure 3.2) also agrees with the XRD analysis. The metal oxide peaks, that usually appear below 1000 cm^{-1}, becomes more intense and prominent with temperature, confirming the growth of the spinel lattice upon calcination. A broad band observed around 3500 cm^{-1}, attributed to the water content present in the samples, disappears gradually on heating and is completely absent on firing at 750 °C. The band at 2340 cm^{-1} represents the oxygen-oxygen bonds present in the FCC lattice. The existence of leftover NO_2 from the nitrate precursors explains the band at 1378 cm^{-1}, which decreases in intensity with calcination temperature. The FTIR measurements are well consistent with XRD results. The hydroxide groups present in the material showed infrared absorption bands at 1630 and 1380 cm^{-1} and are less prominent at higher temperatures [14,15].

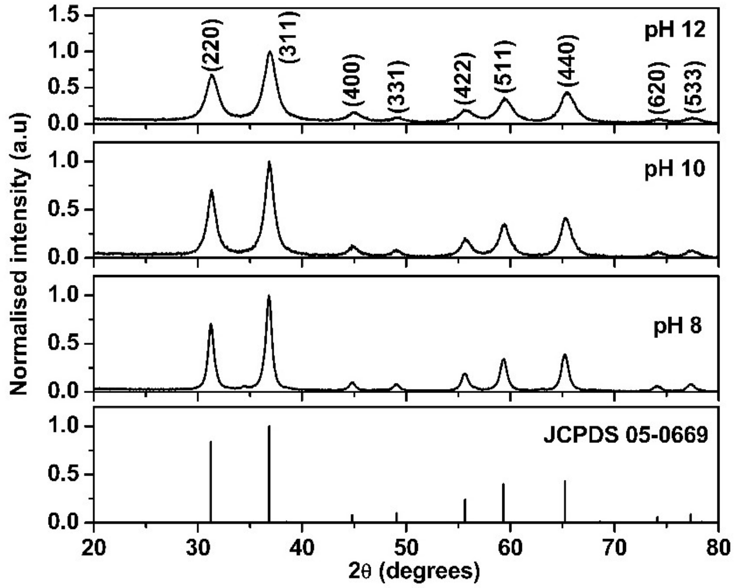

Fig 3.3 XRD spectra of $ZnAl_2O_4$ synthesized at pH values 8, 10 and 12

Samples were also prepared varying the pH of the precursor mixture, fixing the post-calcination temperature at 750 °C. Figure 3.3 shows the XRD spectra of particles formed at synthesis pH – 8, 10 and 12. All peaks could be indexed corresponding to spinel $ZnAl_2O_4$, in concurrence with JCPDS 05-0669.

Among the bands below 1000 cm^{-1} in the FTIR spectra, the band at 660 cm^{-1} could be attributed to the symmetric stretching of AlO_4 group. The band at 555 cm^{-1} represents the Zn-O symmetric stretching vibration and the band at 493 cm^{-1} represents the asymmetric stretching vibration of Al-O bond [15]. A closer look at the FTIR spectra (figure 3.4) revealed that all these bands are more clearly visible from pH 10.

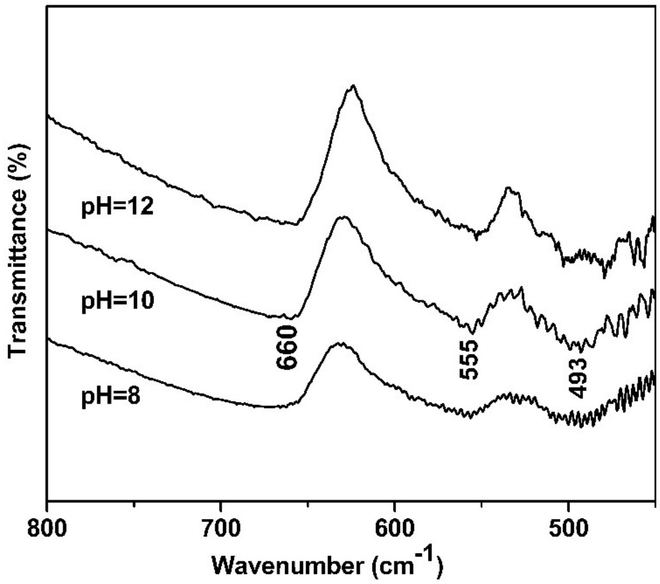

Fig 3.4 FTIR spectra of $ZnAl_2O_4$ synthesized at pH values 8, 10 and 12

The Debye-Scherrer method was used to determine the crystallite size of the synthesized nanoparticles, corresponding to the intense peak (311). The lattice parameter was also calculated using the diffraction equations [16,17]. The variation in crystallite size and lattice parameter with varying pH is presented in table 3.2.

Parameter		**(311) peak diffraction angle 2θ (degrees)**	**FWHM (degrees)**	**Crystallite size (nm)**		**Lattice parameter (Å)**
Calcination temperature	**pH**			**D-S method**	**W-H plot**	
750 °C	**8**	36.809	0.745	11.239	11.305	8.093
	10	36.871	1.149	7.288	8.077	8.080
	12	36.928	1.465	5.717	5.611	8.068
JCPDS 05-0669						8.080

Table 3.2 Crystallite size and lattice parameter values of $ZnAl_2O_4$ synthesized at pH values 8, 10 and 12

The results obtained using Scherrer formula were substantiated using Williamson-Hall (W-H) plot (figure 3.5) analysis, where the intercept of the straight-line graph gives the crystallite size. The lattice constant of the sample synthesized at pH 10, 8.08 Å, matched well with the standard value from JCPDS. The crystallite size calculations reflected the peak broadening effect, that can be explained based on the pressure effect induced by the surrounding particle [18]. The observed deviation in lattice parameter may be due to change in distribution of cations or a change in oxygen supply with pH. As pH of the precursor mixture is raised, nucleation will be high due to higher degrees of supersaturation, resulting in smaller crystallite formation, as observed. Also, pH affects the surface charge and solubility of precursors thus varying the aggregation of particles.

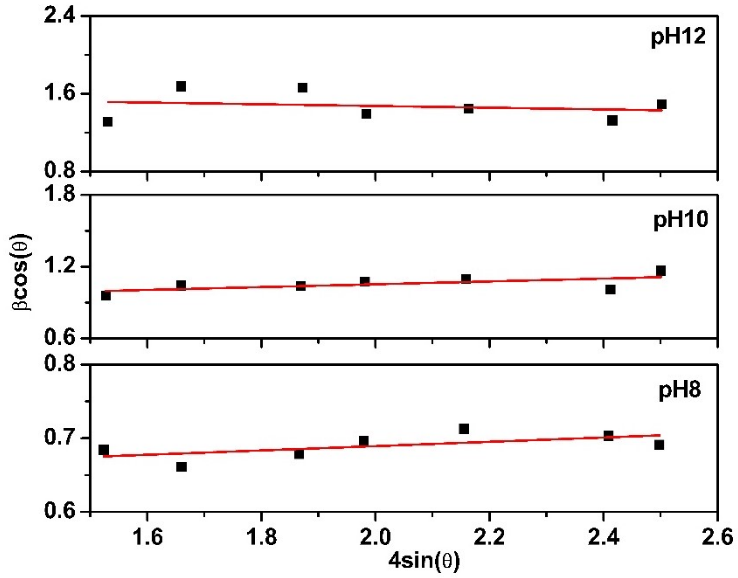

Fig 3.5 W-H plot of $ZnAl_2O_4$ synthesized at pH 8, 10 and 12

The TEM analysis of synthesized pristine $ZnAl_2O_4$ (pH 10 and calcined at 750 °C) is presented in figure 3.6. From the SAED pattern, d-spacing of the crystal planes is measured and compared with that obtained from the XRD spectral analysis (table 3.3). The excellent agreement between the two further affirms the spinel formation at these optimized conditions.

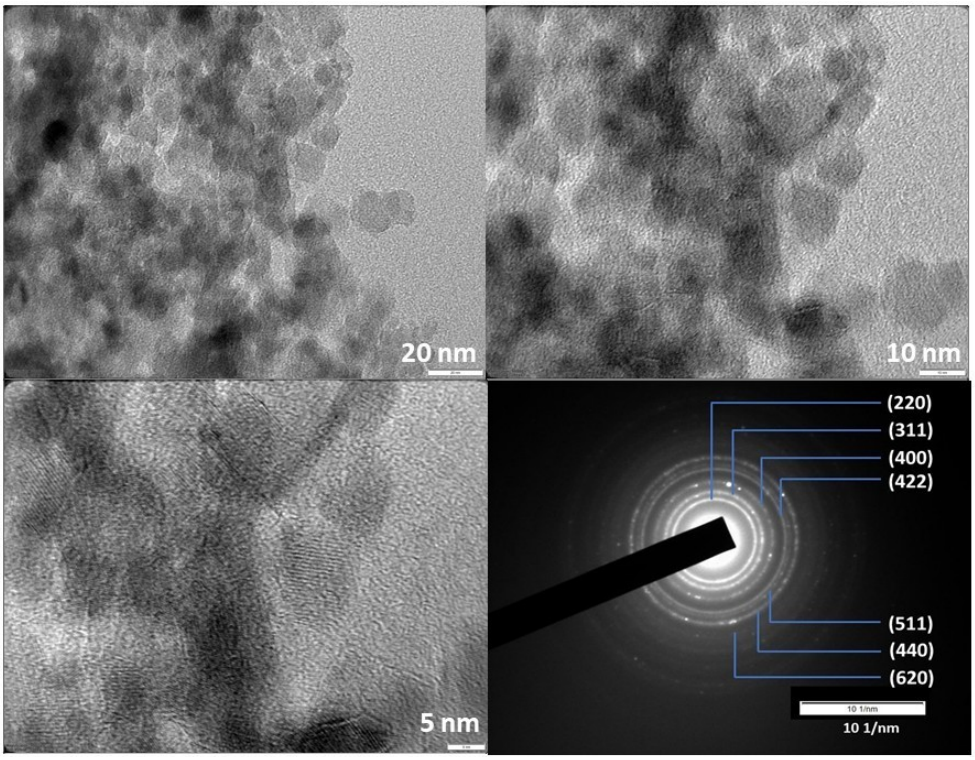

Fig 3.6 TEM images and SAED pattern of pure $ZnAl_2O_4$ (pH 10; calcined at 750 ºC)

Miller indices of crystal plane (hkl)	d-spacing (nm) from	
	XRD	SAED
(220)	2.839	2.872
(311)	2.425	2.439
(400)	2.009	2.042
(422)	1.644	1.672
(511)	1.550	1.568
(440)	1.424	1.442
(620)	1.275	1.278

Table 3.3 Miller indices and d-spacing of crystal planes of $ZnAl_2O_4$

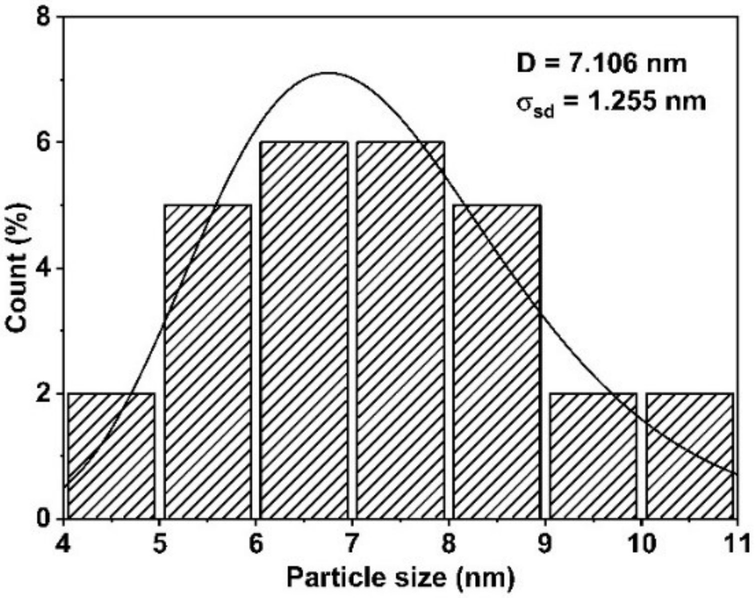

Fig 3.7 Histogram of pure $ZnAl_2O_4$ (pH 10; calcined at 750 °C)

The particle size, determined from the TEM image using the corresponding histogram (figure 3.7), is found to be 7.106 ± 1.255 nm, that closely aligns with the crystallite size obtained from Scherrer formula and W-H plot of the sample.

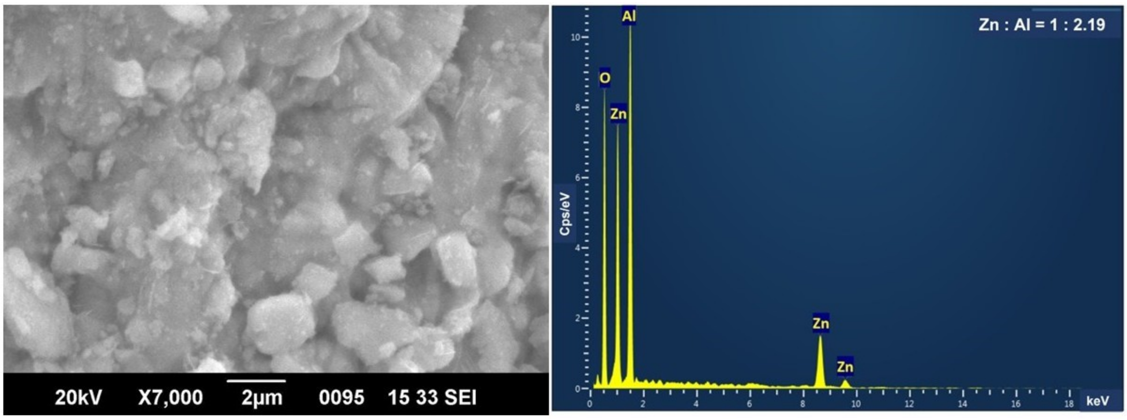

Fig 3.8 SEM image (left) and EDAX spectrum (right) of $ZnAl_2O_4$ synthesized at pH 10 and calcined at 750 °C

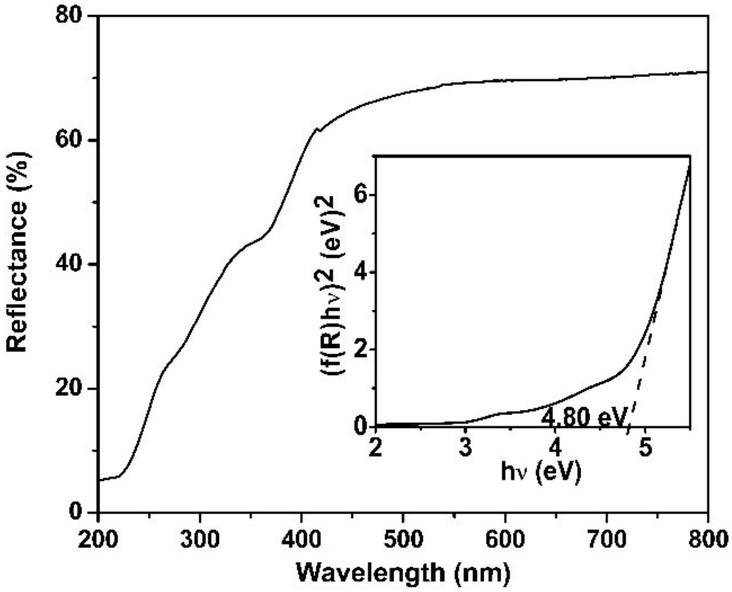

Fig 3.9 DRS spectrum and K-M plot (inset) of $ZnAl_2O_4$ synthesized at pH 10 and calcined at 750 °C

Figure 3.8 shows the SEM image of the co-precipitated $ZnAl_2O_4$ synthesized at the optimum conditions. The EDAX spectra (figure 3.8) gives the elemental composition present in the zinc aluminate sample as Zn:Al = 1:2.19, which is very near to expected value 1:2.

The diffuse reflectance spectrum of the sample synthesized at pH 10 and calcined at 750 °C exhibited a reflectance of ~ 80 % above 400 nm (figure 3.9), in the visible region. The bandgap was calculated to be 4.80 eV, applying K-M theory (inset of figure 3.9) and by extrapolating the linear portion of the curve onto the abscissa. It was high compared to the bulk value of 3.8 eV, as expected in nano-regime.

Based on all the observations made, the pH of precursor mixture and post-calcination temperature for the co-precipitation synthesis of doped zinc aluminate nanoparticles were optimized at 10 and 750 °C respectively. Also, the wide bandgap makes zinc aluminate a suitable host for lanthanide ion doping.

3.3.2 $ZnAl_{2-x}O_4:Eu_x$

The XRD spectra of the Eu^{3+} doped zinc aluminate phosphors prepared via co-precipitation method is given in figure 3.10. The XRD peaks align well with the standard JCPDS data, confirming the formation of a pure cubic $ZnAl_2O_4$ phase with Fd3m (227) symmetry.

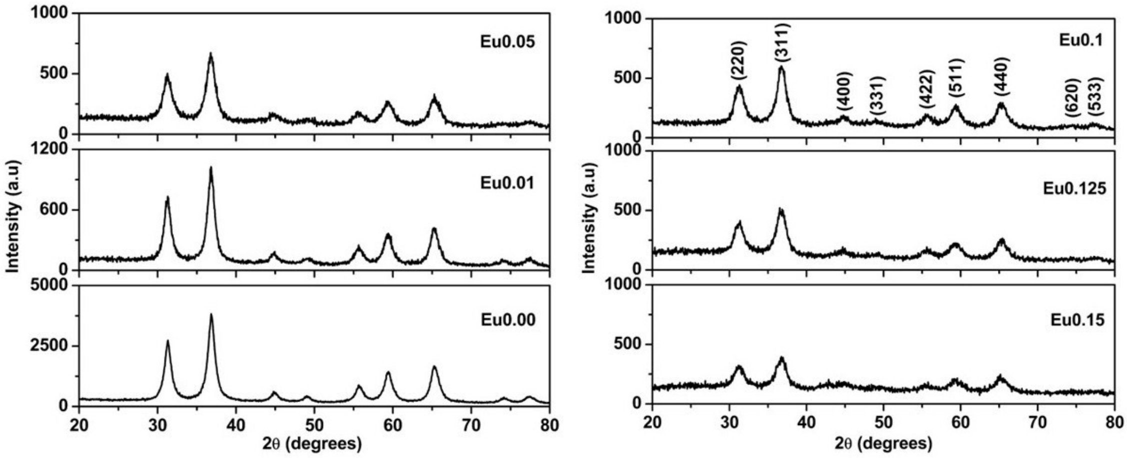

Fig 3.10 XRD spectra of $ZnAl_{2-x}O_4:Eu_x$

Molar concentration of Eu (x)	(311) Peak diffraction angle 2θ (degrees)	FWHM (degrees)	Crystallite size (nm)	Lattice parameter (Å)
0	36.870	1.126	7.288	8.080
0.01	36.824	1.109	7.550	8.089
0.05	36.795	1.362	6.147	8.095
0.1	36.77	1.353	6.187	8.101
0.125	36.717	1.482	5.648	8.112
0.15	36.704	1.505	5.562	8.115

Table 3.4 Crystallite size and lattice parameter of $ZnAl_{2-x}O_4:Eu_x$

The primary XRD peaks observed in the diffractograms at 31.2°, 36.8°, 44.8°, 49.1°, 55.6°, 59.3°, 65.2°, 74.1°, and 77.3°, correspond to the (111), (220), (311), (400), (331), (422), (511), (440), (620), and (533) reflections of zinc aluminate spinel, respectively. No additional peaks indicating impurity phases from the nitrate precursors were detected. A shift in the diffraction peaks to lower angles, with Eu^{3+} concentration, was noted in comparison to the pure sample. This observation confirms the lattice expansion in doped samples, which is expected on incorporation of large dopant ions - ionic radius of Eu^{3+} ions being 95 pm in a 6-coordinate structure - compared to the cations, Zn^{2+} and Al^{3+}, in the host matrix. The broadening of the XRD peaks and subsequent enhancement in the calculated lattice parameter also confirm the successful incorporation of Eu^{3+} ions into the host lattice. The average crystallite size of the phosphors, as calculated from Sherrer formula, is given in table 3.4.

The room temperature PL emission spectrum (figure 3.11) displays a distinct, intense red emission band with a peak maximum at 615 nm, when excited at a wavelength of 250 nm. The UV-blue emission at 360 nm, indicative of the characteristic charge-transfer band (CTB) emission of the host, has significantly dropped in the doped sample. At the same time, the primary emission bands of Eu^{3+} dopant ion, attributed to the transition between its $^5D_0 \rightarrow {}^7F_j$ energy levels in a crystal field environment, has become more prominent. The intensity of the $^5D_0 \rightarrow {}^7F_2$ transition of Eu^{3+} ion is found to be the maximum at 615 nm, imparting redness to the PL emission of the sample.

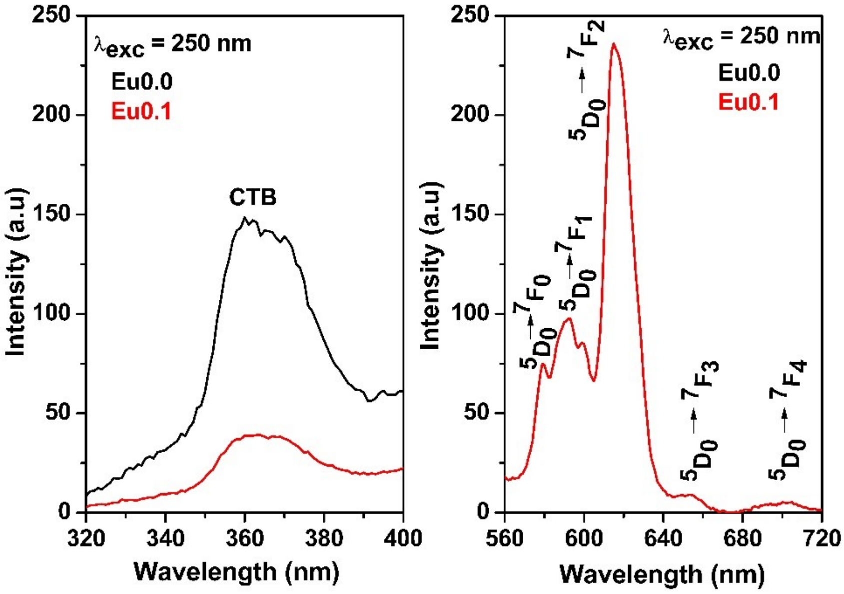

Fig 3.11 PL emission spectra of $ZnAl_{2-x}O_4:Eu_x$ at λ_{exc}=250 nm

The emission spectra, characterized by transitions $^5D_0 \rightarrow {}^7F_j$ (j = 1,2,3,4), indicate the multiple bands depending on the number of stark components of Eu^{3+} in $ZnAl_2O_4$ crystal adhering to the 2J+1 rule [19]. Specifically, bands corresponding to the transition $^5D_0 \rightarrow {}^7F_0$ appear at 580 nm, $^5D_0 \rightarrow {}^7F_1$ at 590 and 599 nm, $^5D_0 \rightarrow {}^7F_3$ at 650 nm and $^5D_0 \rightarrow {}^7F_4$ at 701 nm. The hypersensitive band observed at 615 nm is linked to the electric dipole transition $^5D_0 \rightarrow {}^7F_2$ of Eu^{3+} ions, which is highly sensitive to structural changes and crystal field effects at the vicinity of the Eu^{3+} ion. The presence of the highly prominent $^5D_0 \rightarrow {}^7F_2$ transition of Eu^{3+} ion at 615 nm, compared to all additional shoulder bands, indicates a large transition probability in the crystal field at sites with inversion antisymmetry. The meagre presence of the forbidden $^5D_0 \rightarrow {}^7F_0$ transition doesn't rule out the possibility of the presence of some of the Eu^{3+} ions at a low-symmetry site [19,20].

The luminescence intensity ratio of $^5D_0 \rightarrow {}^7F_2$ to $^5D_0 \rightarrow {}^7F_1$ transitions, commonly referred to as the asymmetry ratio, provides an indication of the degree of distortion in the local environment surrounding the Eu^{3+} ion within the matrix. Here the value of asymmetric ratio is found to be very much greater than 1 (from figure 3.11), which indicates a highly non-symmetric environment around Eu^{3+} ions [21,22]. All the above observations – highly intense $^5D_0 \rightarrow {}^7F_2$ transition, high assymmetry ratio, splitting of the $^5D_0 \rightarrow {}^7F_1$ transition - points at the fact that crystal field effects are so prominent in the matrix and Eu^{3+} ions, replaces the Al^{3+} ions due to lesser charge imbalance and preference for higher coordination environment, though the site is highly distorted due to the size mismatch.

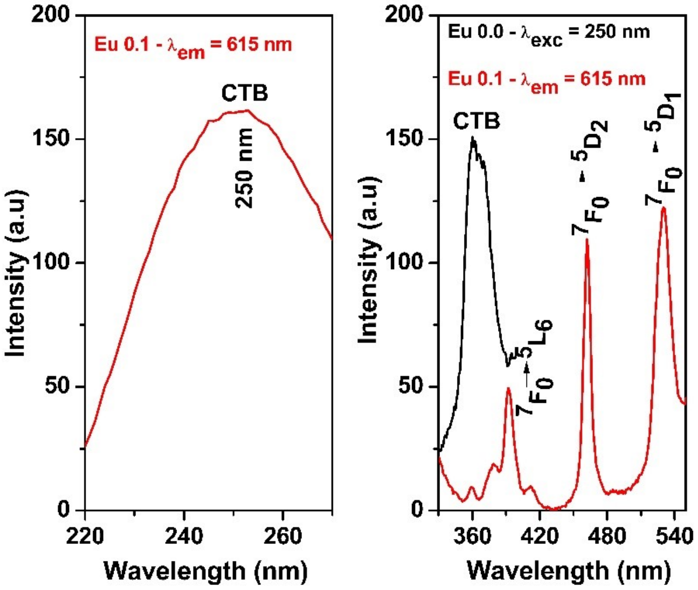

Fig 3.12 PL excitation spectrum of $ZnAl_{1.9}O_4:Eu_{0.1}$ at $\lambda_{em} = 615$ nm

Figure 3.12 gives the excitation spectrum of Eu^{3+} doped zinc aluminate recorded at an emission wavelength, $\lambda_{em} = 615$ nm. The peaks observed at 390, 460 and 530 nm corresponding to $^7F_0 \rightarrow {}^5L_6$, $^7F_0 \rightarrow {}^5D_2$ and $^7F_0 \rightarrow {}^5D_1$ absorptions respectively. However, the peak at 250 nm is more predominant over the dopant absorptions for the $ZnAl_{1.9}O_4:Eu_{0.1}$ sample. This broad band in the UV region around 250 nm arises from the charge-transfer transition ($O^{2-} \rightarrow Al^{3+}$) from surrounding anions to Al^{3+} [23].

A luminescent emission results when a sensitizer S (here, the host) and an activator A (here, the dopant ion) can exhibit either a radiative or a nonradiative energy transfer. For intrashell transitions, due to the low magnitude of the oscillator strength for absorption (as observed in figure 3.12), radiative energy transfer shall not be very efficient. Hitherto, a nonradiative resonance transfer rate depends both on the spectral overlap of the S emission band and the A absorption band and on the proximity (the distance R) between S and A energy levels. As evident from figure 3.12, there is an overlap between the host emission and the spectral absorption levels of the dopant ion, affirming a host-sensitizing phenomenon to occur in the matrix.

The 'R' dependence is exponential for exchange interactions and varies by a R^{-n} factor for electric multipolar interactions. A thorough analysis of the entire scenario - the enhanced reddish emission and the simultaneous reduction in bluish host emission (as evident from figure 3.11) – can therefore be attributed to nonradiative resonance energy transfer from the host to activator sites mediated by exchange interactions. This observation further supports the fact that Eu^{3+} ions replaces Al^{3+} ions, enabling a proximity between S and A energy levels facilitating host-sensitized emission. A model of the energy band diagram based on these observtions is depicted in figure 3.13.

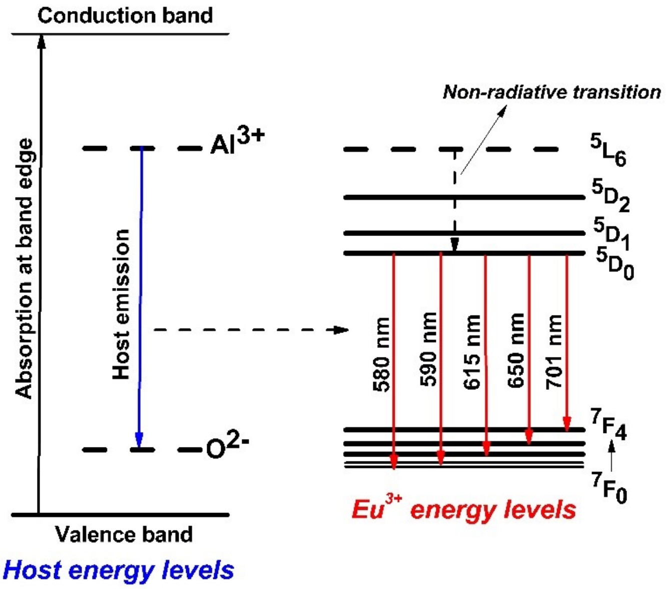

Fig 3.13 The energy band diagram of $ZnAl_{2-x}O_4:Eu_x$

A comparison of the PL emission spectra for various dopant concentrations is depicted in figure 3.14. The highest PL intensity at 615 nm was observed for the sample with 0.1 M concentration of Eu^{3+} ions (see figure 3.15), beyond which concentration quenching occurs. This phenomenon may be attributed to the development of impure phases due to excessive doping of Eu^{3+} ions. Additionally, non-radiative energy transfer among the Eu^{3+} ions, via exchange and multipole-multipole interactions, enhances on reduction in the distance between activator ions, serving as another contributing factor [22].

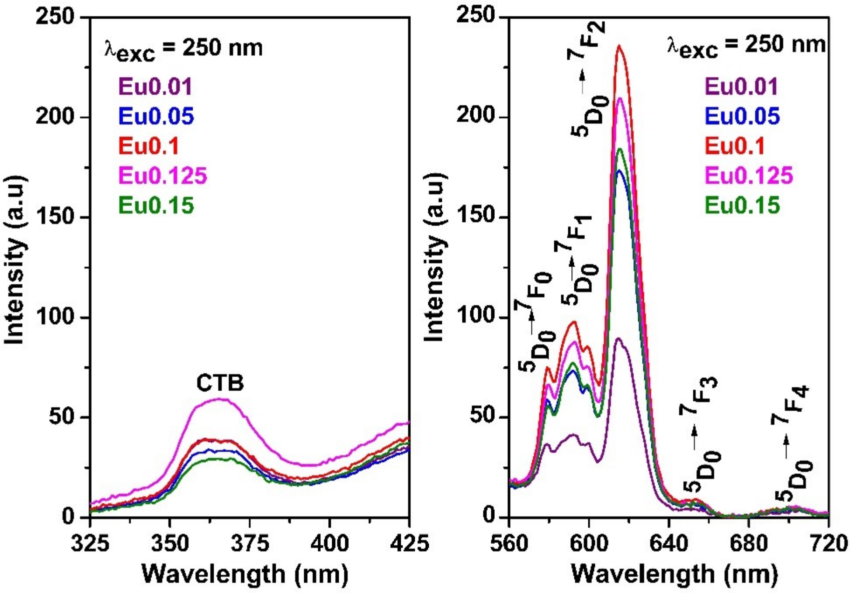

Fig 3.14 PL emission spectra of $ZnAl_{2-x}O_4:Eu_x$ at $\lambda_{exc} = 250$ nm for various dopant concentrations

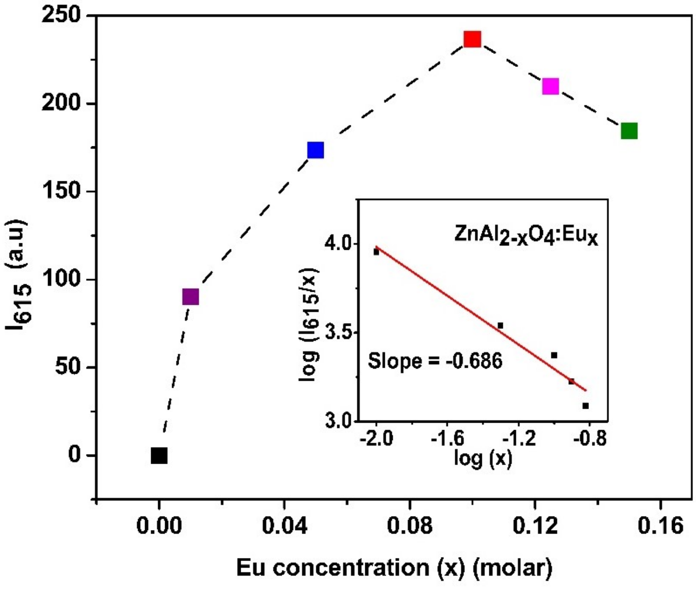

Fig 3.15 Intensity versus dopant ion concentration of $ZnAl_{2-x}O_4:Eu_x$ at $\lambda_{exc} = 250$ nm

The dependence of luminous intensity, I, on dopant concentration, x, can be described using Dexter's theory,

$$\frac{I}{x} = K[1 + \beta x^{\theta/3}]^{-1} ,$$

where the term (I/x) represents the peak emission intensity to the activator concentration ratio, and K and β are the constants corresponding to a given host crystal under the same excitation wavelength. The parameter θ is associated with multipole–multipole interactions. By plotting log(I/x) against log(x), given in the inset of figure 3.15, the slope was determined to be -0.686, that yields a corresponding θ value 2.058. This parameter, being close to 3, again confirms the occurrence of exchange interaction between the host matrix and the activator ions Eu^{3+} [24].

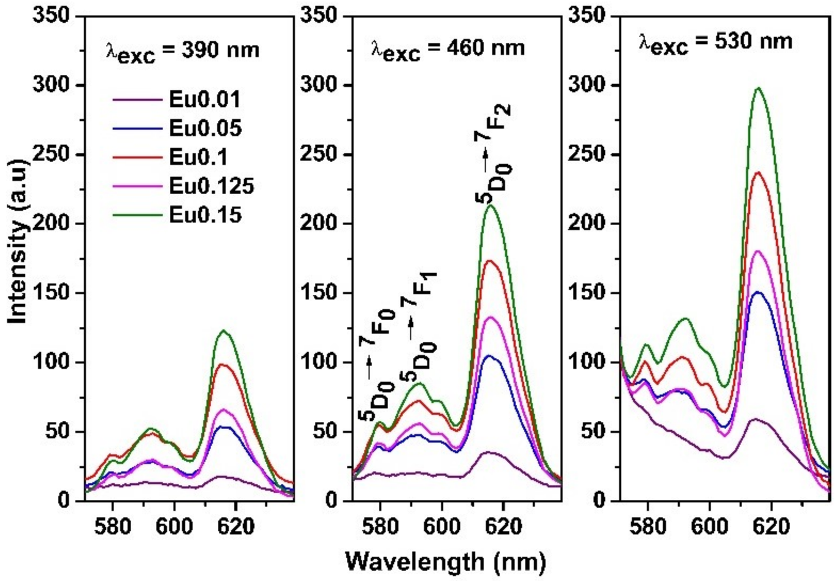

Fig 3.16 PL emission spectra of $ZnAl_{2-x}O_4:Eu_x$ at λ_{exc}= 390, 460 and 530 nm

The intensity of the emission bands, when excited at the dopant absorption peaks 390, 460 and 530 nm for various dopant concentrations are depicted in figure 3.16. A comparison of the emission intensity has been done to that at 250 nm band absorption of the host matrix in figure 3.17. The luminescent emission, corresponding to the CTB of the host i.e., at an excitation wavelength of 250 nm is found to be the predominant one, which once again affirms the host-sensitization process.

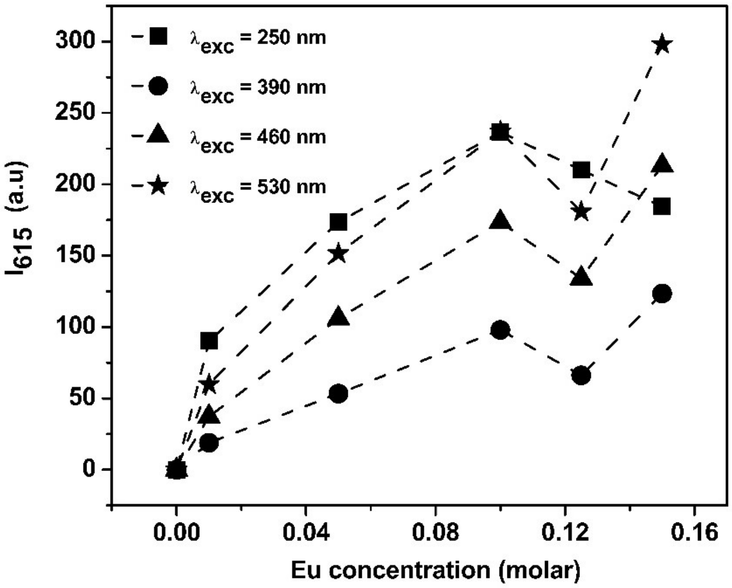

Fig 3.17 Intensity versus dopant concentration of $ZnAl_{2-x}O_4:Eu_x$ at various excitation wavelegths

Now at the excitation wavelength of 530 nm, an almost equal luminescent emission intensity is observed as that when excited at 250 nm. Since there is no overlap between the host emission and the 530 nm excitation band of Eu^{3+} (as evident from figure 3.12), one cannot totally exclude the possibility of absorption directly at the activator sites at 530 nm. This also might be the reason for the increase in emission intensity observed beyond 0.125 M dopant concentration.

3.3.3 $ZnAl_{2-y}O_4:Tb_y$

Figure 3.18 shows the XRD patterns of Tb^{3+} doped zinc aluminate for different concentrations (y = 0 – 0.09 M) over the 2θ range 20 to 80°. All the samples possessed the cubic spinel structure of $ZnAl_2O_4$. The absence of any additional peaks asserts that the Tb^{3+} ions are well incorporated in to the lattice without destroying the crystalline nature. However, the peaks were found to be broadened compared to pure zinc aluminate sample, owing to the strain [23] due to the incorporation of large Tb^{3+} ions at octahedral sites of Al^{3+} ions. To avoid charge imbalance, Tb^{3+} dopant ions are considered to occupy Al^{3+} sites. Also, the ionic radius of Tb^{3+} ions, 92 pm, is quite comparable to that of Al^{3+} ions, 54 pm at the octahedral site of the spinel.

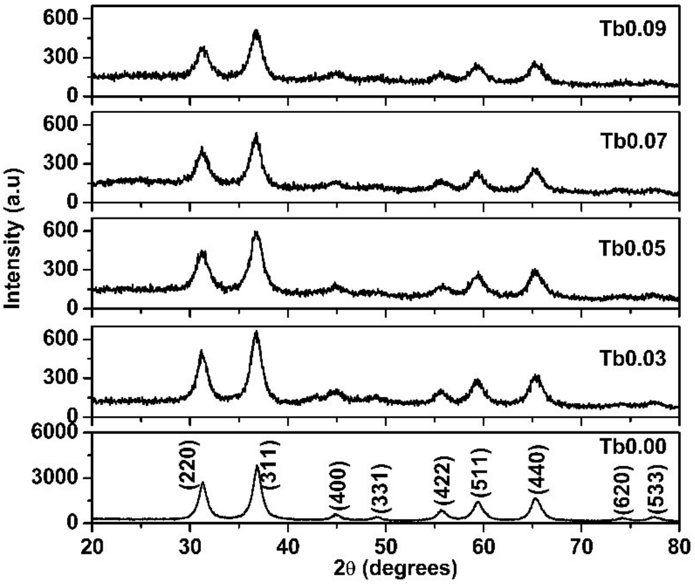

Fig 3.18 XRD spectra of $ZnAl_{2-y}O_4:Tb_y$

The average crystallite size is calculated from Sherrer formula (Table 3.5), corresponding to the (311) peak. A blue shift in the (311) peak is observed for all doped samples, in comparison to the undoped sample, eventually contributing to an increase in lattice parameter, generally expected when a RE ion of larger ionic radius replaces an equivalent host cation.

Molar concentration of Tb (y)	(311) peak diffraction angle 2θ (degrees)	FWHM (degrees)	Crystallite size (nm)	Lattice parameter (Å)
0	36.870	1.119	7.288	8.080
0.03	36.764	1.319	6.346	8.102
0.05	36.783	1.518	5.516	8.098
0.07	36.707	1.338	6.256	8.114
0.09	36.749	1.433	5.842	8.105

Table 3.5 Crystallite size and lattice parameter of $ZnAl_{2-y}O_4:Tb_y$

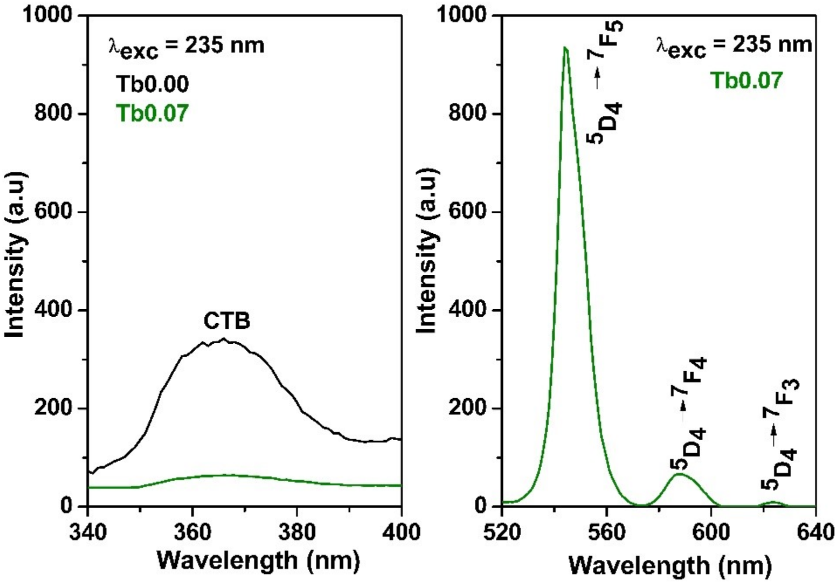

Fig 3.19 PL emission spectra of $ZnAl_{2-y}O_4:Tb_y$ (y = 0.00 and 0.07) at λ_{exc} = 235 nm

The room temperature PL emission spectra of pure and $ZnAl_{2-y}O_4:Tb_y$ (y = 0.07 M) recorded at an excitation wavelength of 235 nm is shown in figure 3.19. The characteristic emission bands at 544 nm, 588 nm and 623 nm correspond to the electronic transitions $^5D_4 \rightarrow {}^7F_j$ (j = 5, 4, and 3 respectively) of Tb^{3+} ions. The maximum emission peak at 544 nm is attributed to the magnetic dipole $^5D_4 \rightarrow {}^7F_5$ transition. The stronger magnetic dipole transition indicates a symmetrical environment around Tb^{3+} ions, which is another evidence of the fact that Tb^{3+} ions are predominantly substituted into the Al^{3+} octahedral sites.

The PL excitation spectra of Tb^{3+} doped zinc aluminate was recorded at an emission wavelength of 544 nm in figure 3.15. The spectrum reveals the charge transfer band of the host at 235 nm and three absorption peaks at 348, 367 and 374 nm, much lesser in intensity than host absorption, that correspond to the spin allowed f-d transition of the Tb^{3+} ions [25,26].

On comparing figures 3.11 and 3.19, it is quite evident that the characteristic 365 nm violet-blue emission of the host zinc aluminate matrix reduced significantly in intensity on doping with Tb^{3+} ions, rather than with Eu^{3+} ions. Moreover, the host emission significantly overlaps with Tb^{3+} dopant excitation levels (as depicted in figure 3.20), a phenomenon less pronounced in the case of Eu doped $ZnAl_2O_4$ (figure 3.12).

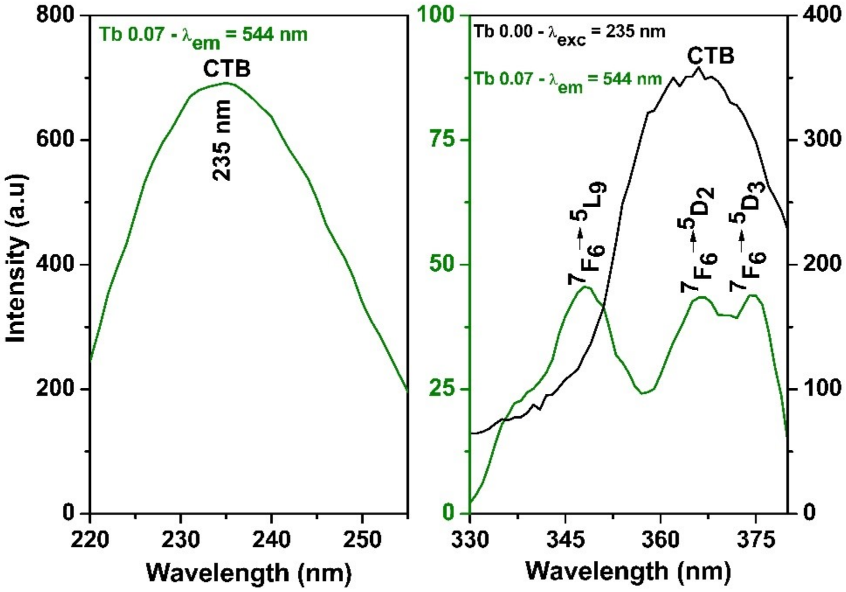

Fig 3.20 PL excitation spectrum of $ZnAl_{2-y}O_4$:Tb_y (y = 0.07 M) at λ_{em} = 544 nm

A schematic model of the energy band diagram of the $ZnAl_{2-y}O_4$:Tb_y matrix is given in figure 3.21.

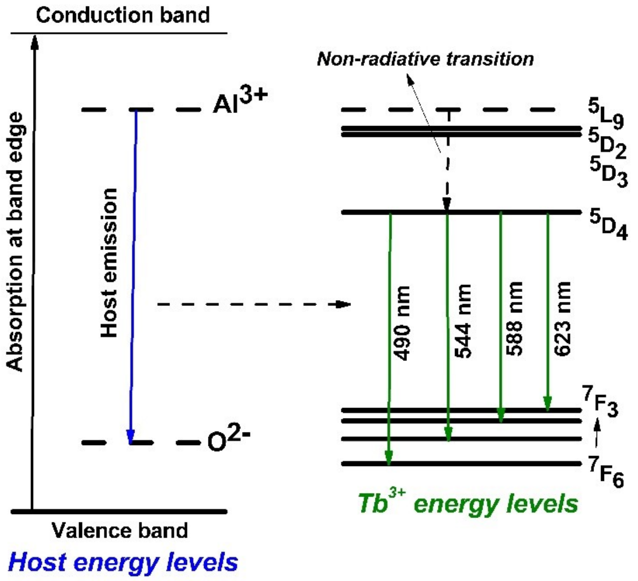

Fig 3.21 A model of energy band level diagram of $ZnAl_{2-y}O_4$:Tb_y

A detailed study of the emission and excitation spectra undoubtedly attributes the green luminescent emission of the $ZnAl_{2-y}O_4:Tb_y$ to a nonradiative resonance energy transfer from the host to activator sites mediated by exchange interactions [27]. The enhanced proximity between S and A energy levels in the Tb doped aluminate matrix leads to a much more dominant host-sensitization effect (almost four times) on Tb doping rather than Eu doping in $ZnAl_2O_4$. The intensity of the green emission, hence, has increased manifold in comparison to the reddish one emanated by the Eu doped sample.

Figure 3.22 gives the PL emission spectrum at λ_{exc} = 348 nm of Tb^{3+} doped samples and compares the corresponding I_{544} PL emission intensity with that of at λ_{exc} = 235 nm. The intensity drastically falls at 348 nm, which rules out the direct excitation at the dopant site, further ratifying the incorporation of dopant Tb^{3+} ions into the lattice. Also, the characteristic emission band at 490 nm corresponding to $^5D_4 \rightarrow {}^7F_6$ transition appears at 348 nm excitation, which was absent at 235 nm because of the very high intense emission peak at 544 nm.

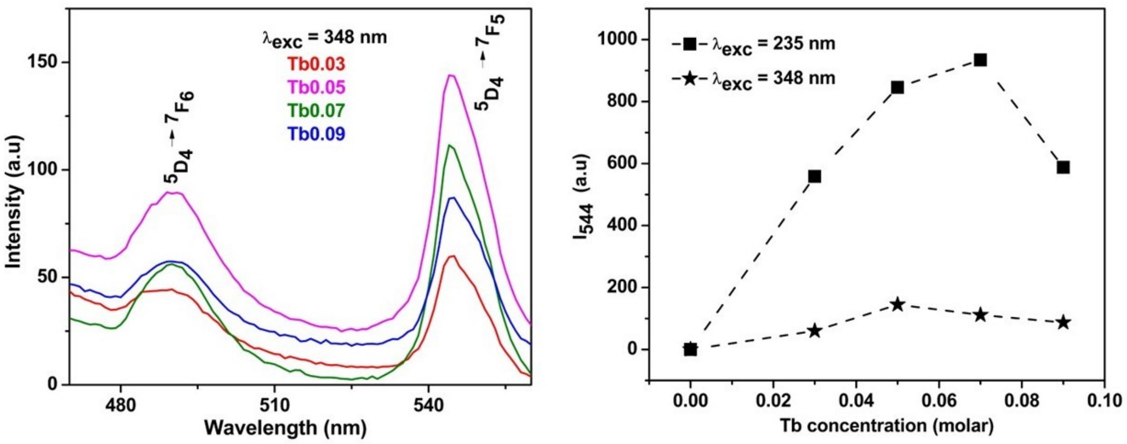

Fig 3.22 PL emission spectrum at λ_{exc} = 348 nm (left) and PL emission intensity versus Tb concentration at λ_{exc} = 235 nm and 348 nm (right) of $ZnAl_{2-y}O_4:Tb_y$

On varying the Tb concentration in the host matrix, the highest PL intensity at 544 nm was observed for the sample with 0.07 M concentration of Tb^{3+} ions (refer figure 3.23 and 3.24). As the concentration of activator ions increases, the distance between adjacent Tb^{3+} ions decreases, strengthening their interactions and leading to mutual non-radiative transitions, which diminishes the luminous intensity beyond 0.07 M. On increasing the Tb^{3+} concentration in the lattice, the proximity of energy levels in Tb^{3+} increases considerably, enhancing the cross-relaxation phenomena, eventually leading to concentration quenching [27].

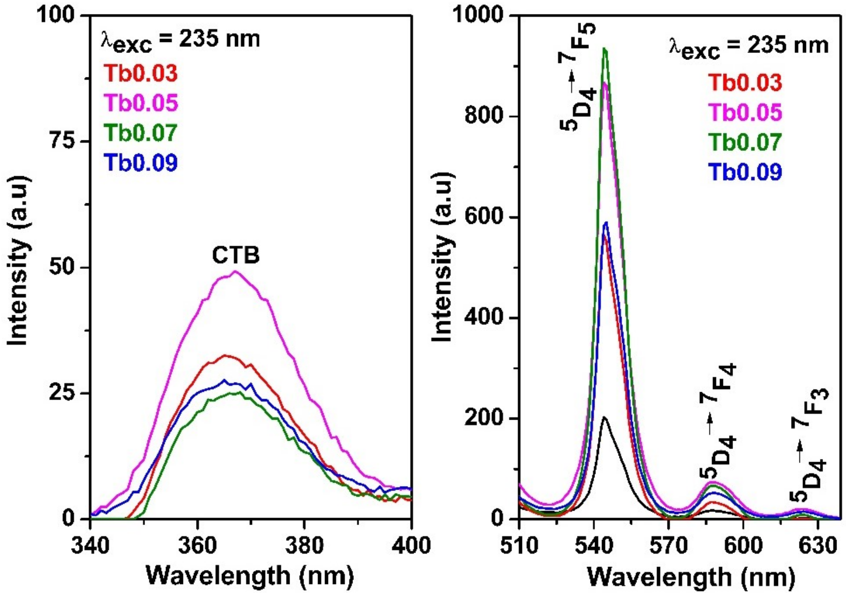

Fig 3.23 PL emission versus dopant concentration of $ZnAl_{2-y}O_4:Tb_y$ at $\lambda_{exc} = 235$ nm

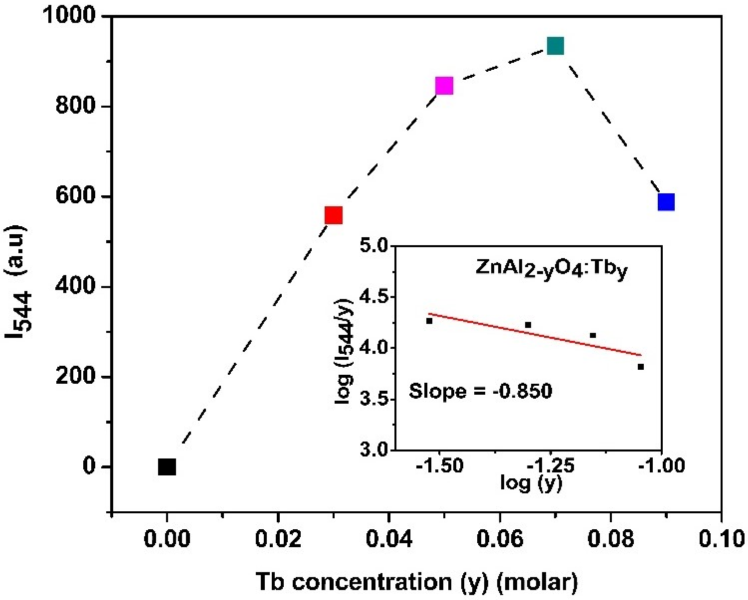

Fig 3.24 Intensity versus dopant concentration of $ZnAl_{2-y}O_4:Tb_y$ at $\lambda_{exc} = 235$ nm

The log(I/y) versus log(y), plotted in the inset of figure 3.24 applying Dexter's theory, gives a slope of -0.850, that yields a corresponding θ value 2.55. This parameter, again being close to 3, confirms the occurrence of exchange interaction between the host matrix and the activator ions Tb^{3+} .

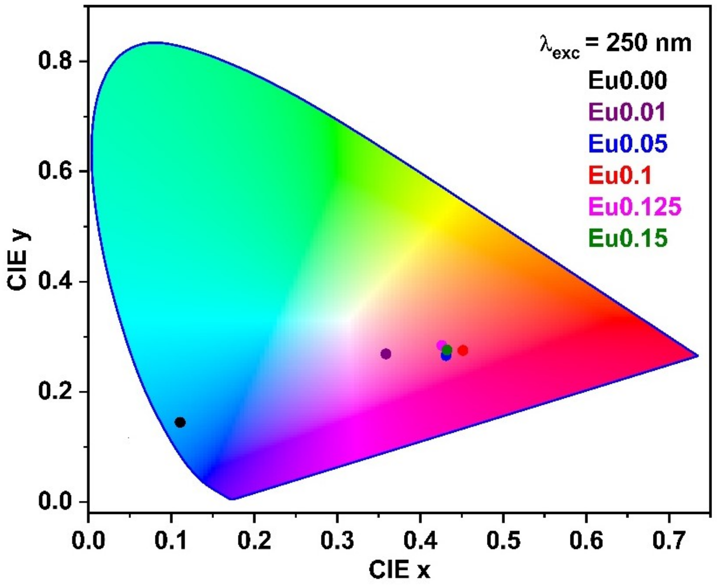

Fig 3.25 CIE color chromaticity diagram of $ZnAl_{2-x}O_4:Eu_x$

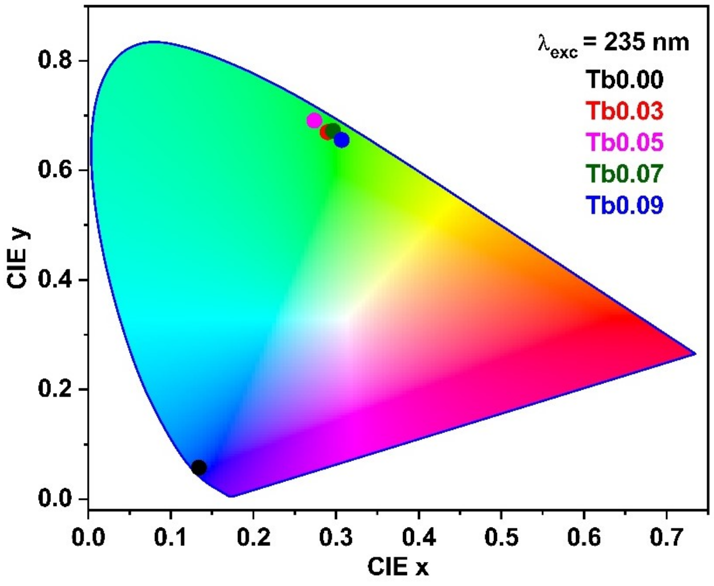

Fig 3.26 CIE color chromaticity diagram of $ZnAl_{2-y}O_4:Tb_y$

The PL emission purity of all the systems synthesized via co-precipitation method were gauged using CIE chromaticity diagram. The colorimetric evaluation of $ZnAl_{2-x}O_4:Eu_x$ and $ZnAl_{2-y}O_4:Tb_y$ are presented in figure 3.25 and figure 3.26 respectively. The chromaticity cordinates of the doped samples are presented in table 3.6. The dominant wavelength of each emission is taken as the intersecting point, when a line drawn from the achromatic white point through the CIE (x, y) of the sample hits the locus. Color purity was calculated from the ratio of the distance between the achromatic point (0.33, 0.33) and the sample CIE value to that between the white point and the dominant wavelength on the locus.

Sample	Dopant concentration (M)	CIE coordinates		Color purity (%)
		x	y	
$ZnAl_{2-x}O_4$:Eu_x	**Eu0.00**	0.111	0.145	91.72
	Eu0.01	0.359	0.269	29.51
	Eu0.05	0.431	0.266	43.67
	Eu0.1	0.451	0.275	44.45
	Eu0.125	0.426	0.284	36.57
	Eu0.15	0.432	0.276	40.41
$ZnAl_{2-y}O_4$:Tb_y	**Tb0.00**	0.134	0.058	96.96
	Tb0.03	0.290	0.670	90.30
	Tb0.05	0.274	0.691	92.66
	Tb0.07	0.296	0.672	93.29
	Tb0.09	0.307	0.656	90.57

Table 3.6 CIE color coordinates and purity of $ZnAl_{2-y}O_4:Tb_y$ and $ZnAl_{2-x}O_4:Eu_x$

The CIE colorimetric coordinates of pure $ZnAl_2O_4$ were found to be (0.111, 0.145) and (0.134, 0.058) at λ_{exc} = 250 nm and λ_{exc} = 235 nm respectively. All the Eu incorporated samples gave a purplish pink emission. The color coordinate of $ZnAl_{1.99}O_4:Eu_{0.1}$ sample, that showed the maximum red emission, was found to be (0.451, 0.275), the color purity being 44 %. The green emission from Tb^{3+} doped zinc aluminate samples lie so close to the horse-shoe shaped spectral locus, affirming the purity of these samples, in comparison to the Eu doped ones. The CIE (x, y) of

$ZnAl_{1.93}O_4$:$Tb_{0.07}$ sample, that gave the best 544 nm green emission with a color purity of 93 %, was calculated as (0.296, 0.672).

3.4 Conclusions

Pure and RE doped $ZnAl_2O_4$ (RE = Eu, Tb) nanophosphors could be effectively synthesized using the non-ceramic co-precipitation method. The standard single-phased cubic spinel structure formation of pure $ZnAl_2O_4$ initiated at a post-calcination temperature of 300 °C itself. The optimum conditions for pristine sample were determined to be - synthesis pH 10 and calcination at 750 °C - from XRD, FTIR, TEM and SAED measurements. The particle size, determined from TEM data, was found to be 7.106 ± 1.255 nm, that closely aligns with the crystallite size obtained from Scherrer formula (7.288 nm) and W-H plot (8.077 nm) analysis of the optimized sample. EDAX analysis showed a Zn:Al ratio of 1:2.19 and DRS spectral data, on applying K-M theory, gave a bandgap of 4.8 eV.

The incorporation of RE dopants into the host $ZnAl_2O_4$ lattice was investigated. Dopant incorporation was ensured from the lattice expansion and the luminescent emissions of the doped samples. The PL emission and excitation spectral intensity variations and spectral overlap confirmed a host-sensitized emission in the doped samples. The non-radiative resonant energy transfer from the host to the dopant ion was mediated by exchange interaction, confirmed by Dexter theory. The effect of concentration quenching was visible beyond 0.1 M and 0.07 M of Eu and Tb incorporation respectively.

Pure $ZnAl_2O_4$ emitted in the violet-blue region of the electromagnetic spectrum whereas Eu^{3+} and Tb^{3+} doped $ZnAl_2O_4$ luminesced in the red and green regions respectively. The CIE colorimetric coordinates of pristine $ZnAl_2O_4$ were found to be (0.111, 0.145) and (0.134, 0.058) at $\lambda_{exc} = 250$ nm and $\lambda_{exc} = 235$ nm respectively. On doping the host with Eu^{3+} ion, the dominant emission at 615 nm results, attributed to the crystal field enhanced electric dipole $^5D_0 \rightarrow {}^7F_2$ transition at non-centrosymmetric sites. All the Eu incorporated samples gave a purplish pink emission. The color coordinate of $ZnAl_{1.99}O_4$:$Eu_{0.1}$ sample, that showed the maximum red emission, was found to be (0.451, 0.275), the color purity being 44 %. The green emission from Tb^{3+} doped zinc aluminate samples, with a peak maximum at 544 nm, was attributed to the magnetic dipole $^5D_4 \rightarrow {}^7F_5$ transition at symmetric sites. These green emissions lie so close to the monochromatic spectral locus, affirming the purity of these samples, in comparison to the Eu doped ones. A 93% pure green emission could be attained on incorporating 0.07 M Tb into the host matrix, color cordinates determined to be (0.296, 0.672).

References

1. Battiston, S., Rigo, C., Da Cruz Severo, E., Mazutti, M. A., Kuhn, R. C., Gündel, A., & Foletto, E. L. (2014). Synthesis of zinc aluminate ($ZnAl_2O_4$) spinel and its application as photocatalyst. *Materials Research, 17*(3), 734–738. https://doi.org/10.1590/S1516-14392014005000073
2. Cheng, B., Ouyang, Z., Tian, B., Xiao, Y., & Lei, S. (2013). Porous $ZnAl_2O_4$ spinel nanorods: High sensitivity humidity sensors. *Ceramics International, 39*(6), 7379–7386. https://doi.org/10.1016/j.ceramint.2013.02.077
3. Sunder, S., Rohilla, S., Kumar, S., & Aghamkar, P. (2011). Structural characterization of spinel zinc aluminate nanoparticles prepared by coprecipitation method. *AIP Conference Proceedings, 1349*(1), 123–125. https://doi.org/10.1063/1.3653640
4. Ciupina, V., Carazeanu, I., & Prodan, G. (2004). Characterization of $ZnAl_2O_4$ nanocrystals prepared by coprecipitation and microemulsion techniques. *Journal of Optoelectronics and Advanced Materials, 6*(4), 1317–1322. https://doi.org/10.1566/j.joam.2004.1317-1322
5. Sunder, S., & Singh, W. (2017). Thermal evolution of zinc aluminate spinel nanoparticles prepared by coprecipitation technique. *International Journal of Scientific Research in Science, Engineering and Technology (IJSRSET)*, *3*(8), 1302-1315. Print ISSN : 2395-1990, Online ISSN : 2394-4099
6. Sunder, S., Rohilla, S., & Kumar, S. (2011). Structural characterization of spinel zinc aluminate nanoparticles prepared by coprecipitation method. *AIP Conference Proceedings, 1349*(1), 1–4. https://doi.org/10.1063/1.3653640

7. Angasa, E., Sari, I. N., Wardani, P. K., Yudha, S. P., & Gustian, I. (2015). Synthesis of zinc aluminate ($ZnAl_2O_4$) by using water extract of *Impatiens balsamina* L. *Journal of Chemical and Pharmaceutical Research, 7*(2), 518–521. Retrieved from http://www.jocpr.com
8. Parya, T. K., Bhattacharyya, R. K., Banerjee, S., & Adhikari, U. B. (2010). Co-precipitated $ZnAl_2O_4$ spinel precursor as potential sintering aid for pure alumina system. *Ceramics International, 36*(1), 1211–1215. https://doi.org/10.1016/j.ceramint.2010.01.013
9. Valenzuela, M. A., Jacobs, J., Bosch, P., Reijne, S., Zapata, B., & Brongersma, H. H. (1997). The influence of the preparation method on the surface structure of $ZnAl_2O_4$. *Applied Catalysis A: General, 148*(1), 315–324.
10. Sunder, S., & Kumar, A. (2015). Study of $ZnAl_2O_4$ prepared by co-precipitation method. *International Journal of Engineering and Education, 7*(2), 54–56. Retrieved from http://www.csjournalss.com
11. Kumar, K. V., & Bhavani, S. D. (2023). Effect of calcination temperature on structural and optical properties of nickel aluminate nanoparticles. *East European Journal of Physics, 2023*(3), 355–362. https://doi.org/10.26565/2312-4334-2023-3-37
12. Puspitasari, P., Rizkia, U. A., Sukarni, S., Permanasari, A. A., Taufiq, A., & Putra, A. B. N. R. (2021). Effects of various sintering conditions on the structural and magnetic properties of zinc ferrite ($ZnFe_2O_4$). *Materials Research, 24*(1), e20200300. https://doi.org/10.1590/1980-5373-MR-2020-0300
13. Sangeetha, A., Kumar, K. V., & Kumar, G. N. (2017). Effect of annealing temperature on the structural and magnetic properties of $NiFe_2O_4$ nanoferrites. *Advances in Materials Physics and Chemistry, 7*(2), 19–27. https://doi.org/10.4236/ampc.2017.72003
14. Wang, S. F., Sun, G. Z., Fang, L. M., Lei, L., Xiang, X., & Zu, X. T. (2015). A comparative study of $ZnAl_2O_4$ nanoparticles synthesized from different aluminum salts for use as fluorescence materials. *Scientific Reports, 5*, 12849. https://doi.org/10.1038/srep12849

15. Nawle, A. C., Humbe, A. V., Babrekar, M. K., Deshmukh, S. S., & Jadhav, K. M. (2017). Deposition, characterization, magnetic and optical properties of Zn-doped $CuFe_2O_4$ thin films. *Journal of Alloys and Compounds, 695*, 1573–1582. https://doi.org/10.1016/j.jallcom.2016.10.301
16. Sharma, R., Bisen, D. P., Shukla, U., & Sharma, B. G. (2012). X-ray diffraction: A powerful method of characterizing nanomaterials. *Recent Research in Science and Technology, 4*(1), 77–79. Retrieved from https://updatepublishing.com/journal/index.php/rrst/article/view/933
17. Autonomous, V. C. (2020). Characterization of green nanoparticles from plants. In *Green Synthesis, Characterization and Applications of Nanoparticles* (pp. 25–48). Elsevier. https://doi.org/10.1016/B978-0-12-822348-2.00002-4
18. Ghahfarokhi, S. E. M., & Shobegar, E. M. (2020). Influence of pH on the structural, magnetic and optical properties of $SrFe_2O_4$ nanoparticles. *Journal of Materials Research and Technology, 9*(6), 12177–12186. https://doi.org/10.1016/j.jmrt.2020.08.063
19. Gahane, N. M., Chaware, P. J., & Rewatkar, K. G. (2023). Structural, morphological, and photoluminescence study of europium doped spinel $ZnAl_2O_4$ phosphors. *International Journal of Chemistry, Mathematics and Physics, 7*(1), 1–6. https://doi.org/10.22161/ijcmp.7.1.1
20. Swapna, K., Mahamuda, S., Rao, A. S., Sasikala, T., Packiyaraj, P., Moorthy, L. R., & Prakash, G. V. (2014). Luminescence characterization of Eu^{3+} doped zinc alumino bismuth borate glasses for visible red emission applications. *Journal of Luminescence, 156*, 80–86. https://doi.org/10.1016/j.jlumin.2014.07.022
21. Vengala Rao, B., Rambabu, U., & Buddhudu, S. (2006). Photoluminescence spectral analysis of Eu^{3+}: Phosphors. *Physica B: Condensed Matter, 382*(1), 86–91. https://doi.org/10.1016/j.physb.2006.02.003
22. Priya, R., Negi, A., Singla, S., & Pandey, O. P. (2020). Luminescent studies of Eu-doped $ZnAl_2O_4$ spinels synthesized by low-temperature combustion route. *Optik, 204*, 164173. https://doi.org/10.1016/j.ijleo.2020.164173

23. Silva, D., Abreu, A., Davolos, M. R., & Rosaly, M. (2011). Determination of the local site occupancy of Eu^{3+} ions in $ZnAl_2O_4$ nanocrystalline powders. *Optical Materials, 33*(7), 1226–1233. https://doi.org/10.1016/j.optmat.2011.02.014
24. Dexter, D. L., & Schulman, J. H. (1954). Theory of concentration quenching in inorganic phosphors. *The Journal of Chemical Physics, 22*(6), 1063–1070. https://doi.org/10.1063/1.1740265
25. Kumar, M., & Gupta, S. K. (2015). An insight into optical spectroscopy of intense green emitting $ZnAl_2O_4:Tb^{3+}$ nanoparticles: Photo, thermally stimulated luminescence and EPR study. *Journal of Luminescence, 168*, 151–157. https://doi.org/10.1016/j.jlumin.2015.07.021
26. Kaur, S., Rao, A. S., Jayasimhadri, M., Jaiswal, V. V., & Haranath, D. (2020). Tb^{3+} ion induced colour tunability in calcium aluminozincate phosphor for lighting and display devices. *Journal of Alloys and Compounds, 826*, 154212. https://doi.org/10.1016/j.jallcom.2020.154212
27. Fernández-Osorio, A., Rivera, C. E., Vázquez-Olmos, A., & Chávez, J. (2015). Luminescent ceramic nano-pigments based on terbium-doped zinc aluminate: Synthesis, properties and performance. *Dyes and Pigments, 119*, 22–29. https://doi.org/10.1016/j.dyepig.2015.03.021

Chapter 4

LUMINESCENT STUDIES IN PRISTINE AND RE (RE = Eu, Tb) DOPED $ZnAl_2O_4$ NANOPHOSPHOR SYNTHESIZED USING HYDROTHERMAL ROUTE

This chapter presents the hydrothermal synthesis of pure and RE doped (RE = Eu, Tb) zinc aluminate. The synthesis conditions of pristine sample were optimized for structural purity. The effect of rare-earth doping in the host matrix was also studied. The structural, morphological and compositional investigations were done using XRD, FTIR and SEM-EDAX measurements. Diffuse reflectance data helped in determining the optical bandgap of the prepared samples, using K-M theory. The PL emission and excitation spectra, along with CIE colorimetrical analysis probed the luminescent response of the synthesized samples.

4.1 Introduction

Among the significant efforts made by research groups worldwide to lower the synthesis temperature of ternary $ZnAl_2O_4$ nanophosphor, hydrothermal technique stands out as a promising method for making nanoparticles with high structural purity. Compared to co-precipitation synthesis, this method requires higher temperature (100 – 280 °C) for longer durations in an autoclave under high pressure.

Zhang *et al.* synthesized zinc aluminate nanocrystals through hydrothermal treatment at 453 K for 24 hours and studied its catalytic response [1]. Miron *et al.* studied the optical and luminescent properties of zinc aluminate synthesized hydrothermally at 220 °C for 8 hours, followed by calcination at 800-1000 °C for 5 hours [2]. Strek *et al.* synthesized Eu^{3+} doped $ZnAl_2O_4$ hydrothermally at 430 K temperature for 4 hours and reported that crystalline structure formation required a post-calcination treatment ~ 1000 °C [3]. D. Dwibedi *et al.* reported the hydrothermal synthesis of pristine $ZnAl_2O_4$ at 240 °C in 24 hours [4]. F. F. Alharbi *et al.* employed hydrothermal treatment at 180 °C for 10 hours followed by calcination to make $ZnAl_2O_4$ for enhancing the photocatalytic reduction of hexavalent chromium to trivalent chromium [5]. Heloisa Pimenta de Macedo *et al.* prepared zinc aluminate via hydrothermal treatment at 180 °C for 24 hours with the precursors mixed with urea and compared it with the microwave method [6]. $ZnAl_2O_4$: Cr^{3+} (Co^{2+}) powder was synthesized by Le Hong Ha *et al.* by mixing the precursors with NaOH and C_2H_5OH via hydrothermal route at 200 °C for 96 hours [7]. T. Strachowski *et al.* reported a microwave assisted hydrothermal synthesis of $ZnAl_2O_4$ with the help of a computer controlled microwave reactor followed by vaccum drying at 70 °C for 24 hours [8]. Also, the ternary matrix has been probed to investigate its catalytic, antibacterial and luminescent properties [9–11].

The prime aim of the present work was to check the possibility of synthesising nanosized $ZnAl_2O_4$ from its nitrate precursors, varying the temperature of synthesis, duration of hydrothermal treatment and synthesis pH of the precursor mixture. Also, the investigations in hydrothermally synthesized luminescent RE (Eu, Tb) doped ternary oxides are also illustrated.

4.2 Experiment

The precursors used for pure and doped $ZnAl_2O_4$ synthesis were zinc nitrate ($Zn(NO_3)_2.6H_2O$; Merck), aluminium nitrate ($Al(NO_3)_3.9H_2O$; Merck), europium nitrate ($Eu(NO_3)_3.H_2O$; Sigma-Aldrich) and terbium nitrate ($Tb(NO_3)_3.H_2O$; Sigma-Aldrich).

The Zn:Al precursor molar ratio was fixed for all samples at 1:2. Appropriate amounts of zinc and aluminium precursors were weighed and dissolved separately in distilled water with continuous stirring. The pH of the combined solution was adjusted by the dropwise addition of 25% ammonia solution (Merck) under constant stirring. The resulting mixture, transferred to a Teflon vessel and tightly sealed in a steel autoclave, was subjected to hydrothermal treatment in a hot-air oven under high pressure. After the reaction, the solid product was filtered, dried at 80 °C for 15 hours, and ground into a fine powder. The powder was subsequently calcined for 2 hrs at different temperatures (300 °C, 450 °C, 600 °C, and 750 °C) using a high-temperature programmable furnace. $ZnAl_{2-x}O_4:Eu_x$ (x - 0.01 - 0.1 M) and $ZnAl_{2-x}O_4:Tb_y$ (y - 0.01 - 0.08 M) were prepared using the same synthesis procedure with the respective precursors of Eu^{3+} and Tb^{3+} ions.

The structural (XRD, FTIR), morphological (SEM-EDAX) and optical (DRS, PL) characterizations were done. Also, the luminescent emissions were gauged using CIE colorimetry.

4.3 Results and discussions

4.3.1 Pure $ZnAl_2O_4$

Spinel zinc aluminate synthesis under hydrothermal conditions were checked varying the temperature and duration of synthesis, pH of the precursor mixture fixed at 10. The spinel peaks were less pronounced at synthesis temperatures below 250 °C and at lower durations of hydrothermal treatment. However, the compound formation could be successfully achieved at 250 °C combined with a 4 hour heat treatment, confirmed from the XRD spectra (figure 4.1) that matches well with the standard JCPDS 05-0669. It is noteworthy that the cubic spinel structure of $ZnAl_2O_4$ matrix is formed in the as-prepared stage, even without any calcination. This one-step procedure makes the hydrothermal route adopted more easy, cheap and less-time consuming compared with the previous work discussed.

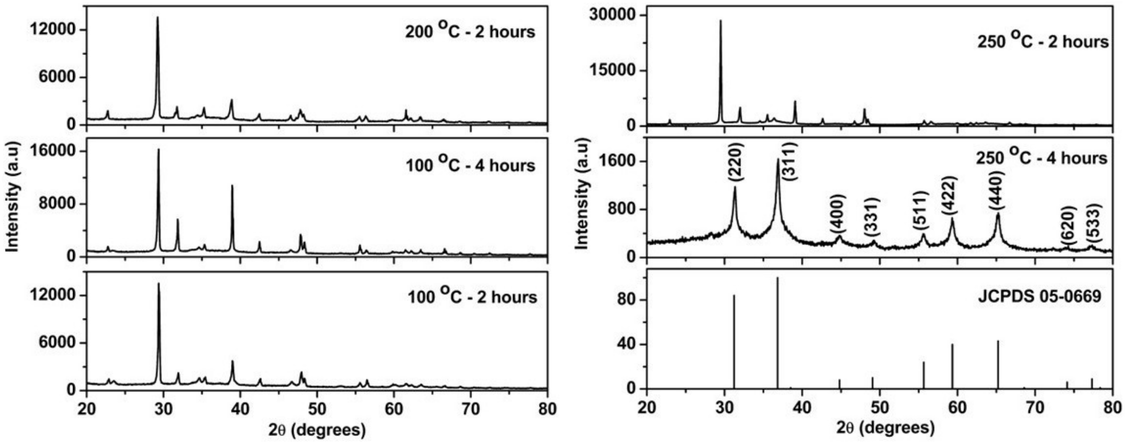

Fig 4.1 XRD spectra of $ZnAl_2O_4$ synthesized hydrothermally for different temperatures and duration of synthesis

But the powder had a sticky nature and was not easy to handle. So, to better the physical nature of the powder, the sample underwent calcination at four different temperatures, chosen well below 1000 °C.

From the XRD spectra shown in figure 4.2, it is evident that the (311) peak grow in intensity, as expected, as the temperature of calcination increases, confirming improved crystallinity on thermal treatment post-synthesis.

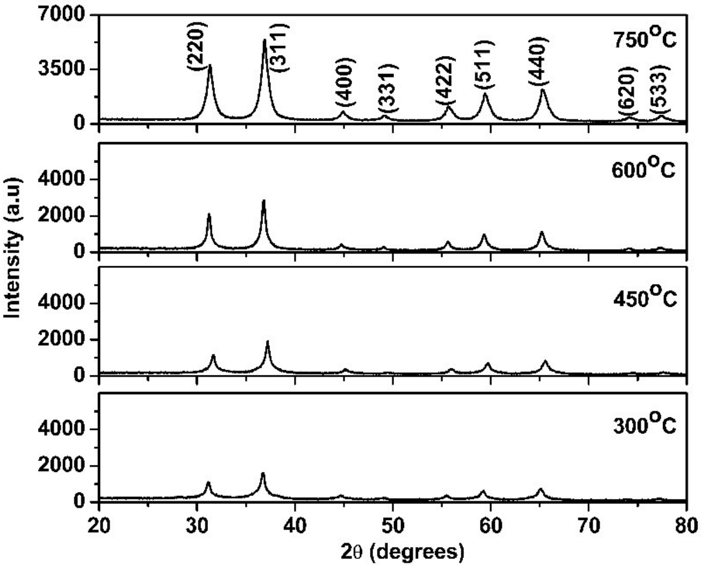

Fig 4.2 XRD spectra of $ZnAl_2O_4$ calcined at temperatures 300-750 °C

Parameter		(311) peak diffraction angle 2θ (degrees)	FWHM (degrees)	Crystallite size (nm)	Lattice parameter (Å)
Calcination temperature	pH				
As-prepared	**10**	36.862	0.669	12.518	8.081
300 °C		36.715	0.699	11.969	8.118
450 °C		37.203	0.766	10.951	8.015
600 °C		36.806	0.644	13.002	8.093
750 °C		36.720	0.899	9.315	8.087
JCPDS					8.080

Table 4.1 Crystallite size and lattice parameter of hydrothermally synthesized $ZnAl_2O_4$ for calcination temperature 0 – 750 °C

Now, the synthesis pH of the precursor mixture was varied, fixing all other variables. XRD spectra of the samples synthesized hydrothermally, after calcination at 750 °C for 2 hours, are shown in figure 4.3. All peaks could be indexed corresponding to spinel $ZnAl_2O_4$ and there are no impurity peaks appeared in either of the diffraction patterns. The crystallite size and lattice parameter were calculated by applying Debye-Scherrer method on (311) peak and diffraction formula respectively. The W-H plot analysis (figure 4.4) of the samples was also done and the results presented in table 4.1.

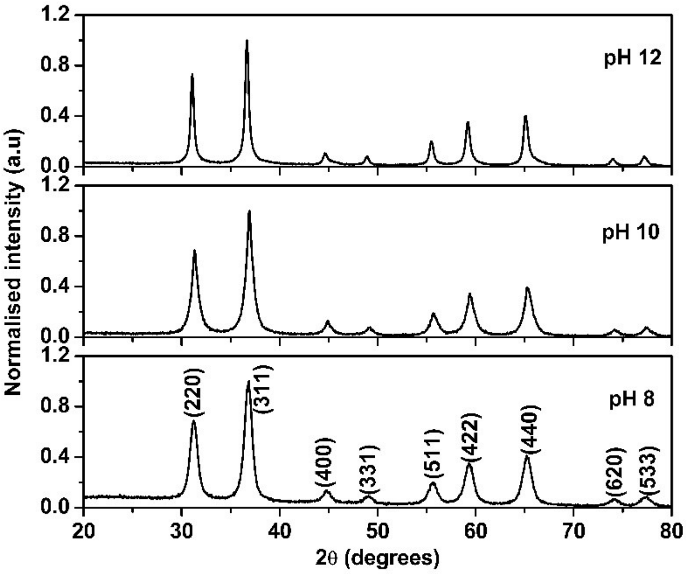

Fig 4.3 XRD spectra of $ZnAl_2O_4$ varying the synthesis pH (8 – 12)

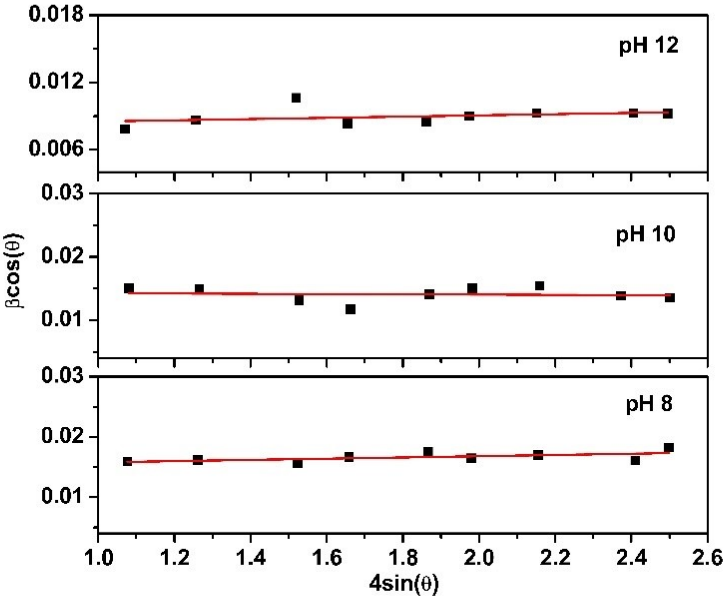

Fig 4.4 W-H plots of $ZnAl_2O_4$ for different values of synthesis pH

Parameter		**(311) peak diffraction angle 2θ (degrees)**	**FWHM (degrees)**	**Crystallite size (nm)**		**Lattice parameter (Å)**
Calcination temperature	**pH**			**D-S method**	**W-H plot**	
750 °C	**8**	36.804	0.977	8.567	9.384	8.095
	10	36.720	0.899	9.315	9.585	8.087
	12	36.651	0.522	16.028	14.288	8.132
JCPDS 05-0669						8.080

Table 4.2 Crystallite size and lattice parameter of hydrothermally synthesized $ZnAl_2O_4$ for different values of synthesis pH

From table 4.2, it is seen that the crystallite size increases with pH different from that of co-precipitated samples, since the effect of pH is dependent on the synthesis method too. The temperature treatment different in hydrothermal method, may hinders the effect of pH on the nucleation and growth of particles. Here also, very similar to co-precipitation method, lattice parameter shows a better match with the standard value for pH = 10.

The FTIR band transmittance below 1000 cm^{-1} drops severely, i.e., absorptions increase correspondingly at pH value of 10 (figure 4.5). These bands could be attributed to the metal-oxygen stretching vibrations in the host matrix.

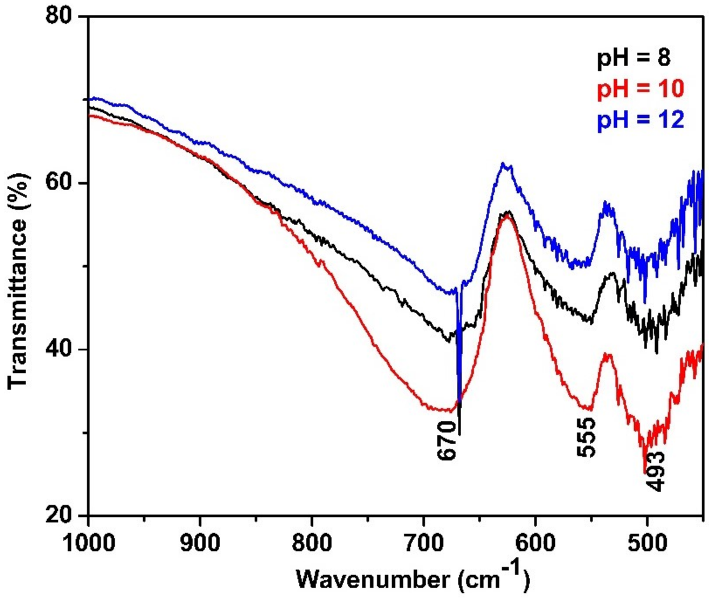

Fig 4.5 FTIR spectra of $ZnAl_2O_4$ at various synthesis pH

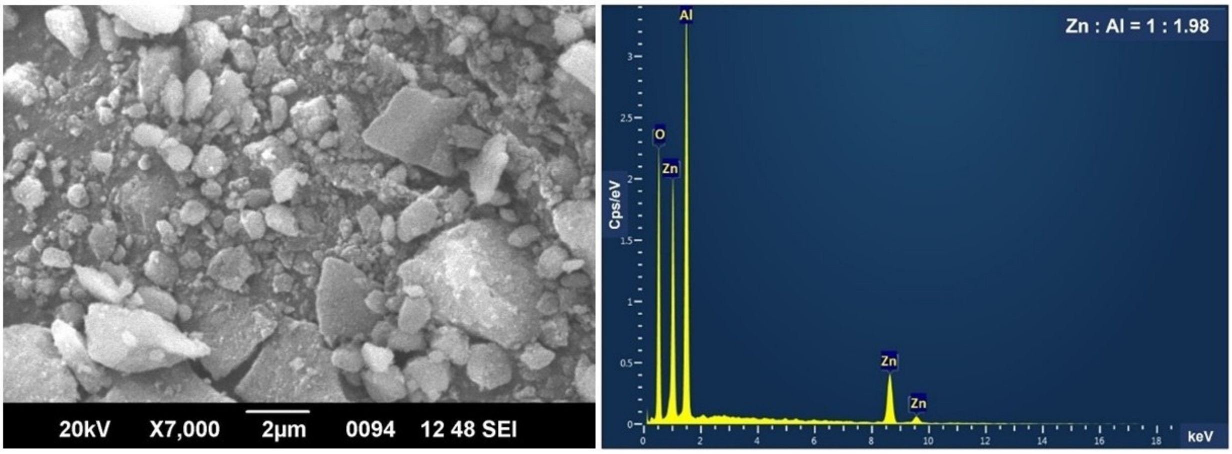

Fig 4.6 SEM image (left) and EDAX spectrum (right) of $ZnAl_2O_4$ synthesized at pH 10 and calcined at 750 °C

Hence, zinc aluminate nanoparticles can be synthesized hydrothermally by subjecting the precursor mixture, at pH 10, to heat treatment in a steel autoclave at 250 °C for 4 hours, followed by calcination at 750 °C for 2 hours.

The SEM image of hydrothermally synthesized $ZnAl_2O_4$ at the optimal conditions is shown in figure 4.6. From the EDAX spectra (figure 4.6), the elemental composition is obtained as Zn:Al = 1:1.98, very close to the expected 1:2 Zn:Al ratio.

The bandgap of the sample is determined from the DRS data, applying Kubelka-Munk theory (figure 4.7). The reflectance is lower compared to the sample prepared via co-precipitation. On extrapolating the linear portion of the $(f(R)h\nu)^2$ versus hν plot (shown in the inset of figure 4.7), the energy gap is found to be 4.73 eV, higher than its bulk counterpart as expected in nanomaterials.

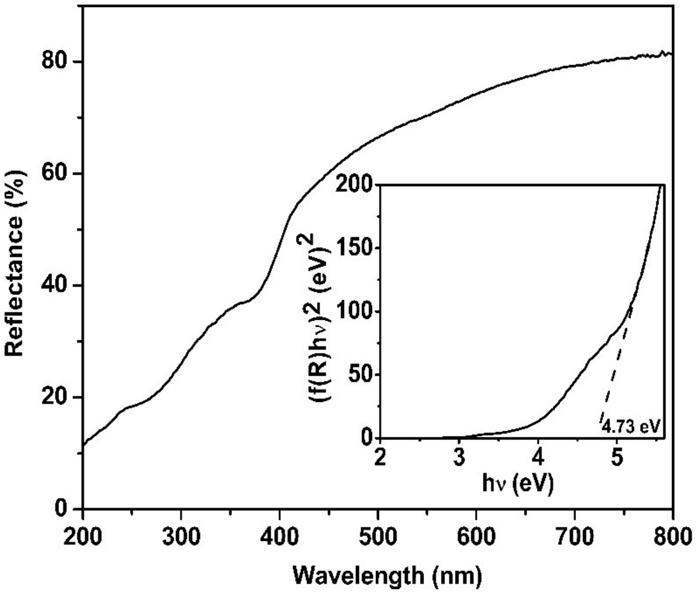

Fig 4.7 DRS spectrum and K-M plot (inset) of $ZnAl_2O_4$ synthesized at pH 10 and calcined at 750 °C

4.3.2 $ZnAl_{2-x}O_4:Eu_x$

The luminescent response of the synthesized pristine zinc aluminate nanoparticles was probed by doping Tb^{3+} and Eu^{3+} into the host matrix during preparation. The XRD spectra of the Eu^{3+} doped zinc aluminate is shown in figure 4.8. The XRD peaks obtained closely align with the standard JCPDS card number 05-0669, confirming the formation of a pure cubic $ZnAl_2O_4$ phase with Fd3m (227) symmetry. The primary XRD peaks in the diffractograms are observed at 31.2°, 36.8°, 44.8°, 49.1°, 55.6°, 59.3°, 65.2°, 74.1°, and 77.3°, corresponding to the (111), (220), (311), (400), (331), (422), (511), (440), (620), and (533) reflections of zinc spinels, respectively. No additional peaks indicating impurity phases from the initial nitrate precursors or fuel were detected.

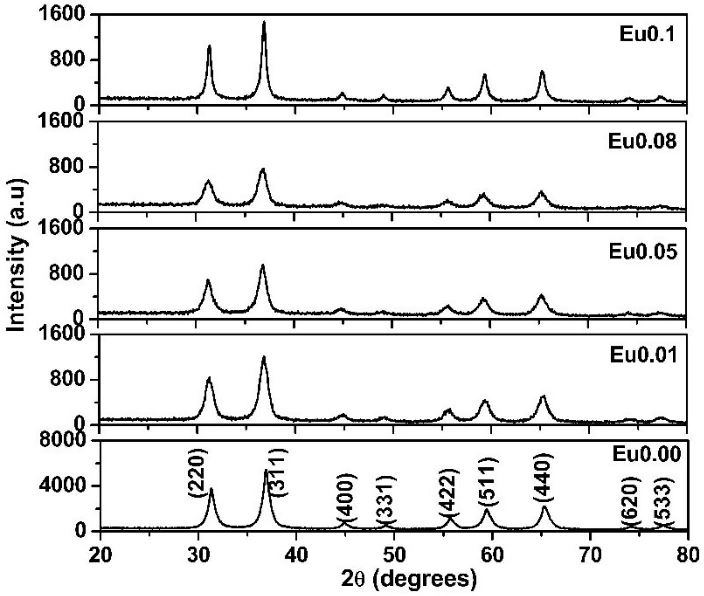

Fig 4.8 XRD spectra of $ZnAl_{2-x}O_4:Eu_x$

Molar concentration of Eu (x)	(311) Peak diffraction angle 2θ (degrees)	FWHM (degrees)	Crystallite size (nm)	Lattice parameter (Å)
0	36.720	0.899	9.315	8.087
0.01	36.805	1.047	7.997	8.094
0.05	36.793	1.032	8.113	8.096
0.08	36.782	1.058	7.913	8.098
0.1	36.808	0.589	14.215	8.093

Table 4.3 Crystallite size and lattice parameter of $ZnAl_{2-x}O_4:Eu_x$

A shift in the (311) diffraction peak maxima to lower angles is observed with Eu^{3+} concentration, which reflects the lattice distortion, or more correctly the lattice expansion, due to incorporation of dopant ions. This is expected as the ionic size of Eu^{3+} exceeds the host cations it replaces. The crystallite size of the phosphors was calculated applying Sherrer formula to the maximum intensity peak (table 4.3). The blueshift of the (311) peak, along with the increase in FWHM with dopant concentration, contributes to the decrease in crystallite size, compared to the pure sample. This is quite similar to that observed with co-precipitated Eu^{3+} doped samples [12].

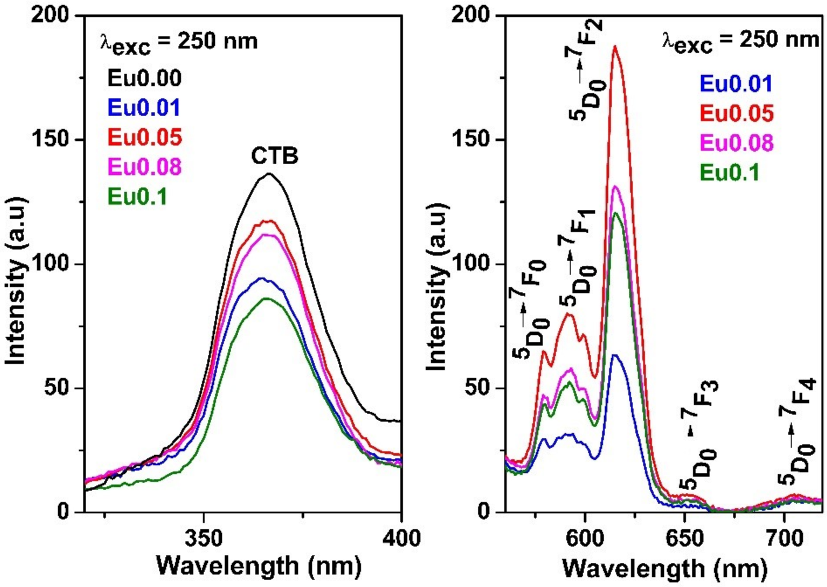

Fig 4.9 Room temperature PL emission spectra of $ZnAl_{2-x}O_4:Eu_x$ at $\lambda_{exc} = 250$ nm

The PL emission spectrum recorded at $\lambda_{exc} = 250$ nm (figure 4.9) displays a distinct, intense emission at 615 nm, accompanied by several smaller emission bands. Bands corresponding to the $^5D_0 \rightarrow {}^7F_j$ transitions, j = 1, 2, 3 and 4 respectively appear at 591, 615, 652 and 704 nm.

The hypersensitive band maxima observed at 615 nm, linked to the electric dipole transition $^5D_0 \rightarrow {}^7F_2$ of Eu^{3+} ions, indicates the presence of dopant ions at non-centrosymmetric sites in the strong crystal field. Though only slightly visible, the presence of the $^5D_0 \rightarrow {}^7F_0$ transition at 580 nm, reflects the fact that Eu^{3+} ions occupy low-symmetry sites in the host matrix. Also, the asymmetric ratio (intensity ratio of the $^5D_0 \rightarrow {}^7F_2$ to $^5D_0 \rightarrow {}^7F_1$ transitions), that is very much greater than 1 (as evident from figure 4.9), further confirms a highly non-symmetric environment around Eu^{3+} ions, confirming the incorporation of Eu^{3+} ions into the host lattice [12,13]. However, Eu^{3+} ions generally replaces the Al^{3+} ions, due to lesser charge imbalance and preference for higher coordination environment, though the site is highly distorted due to the size mismatch.

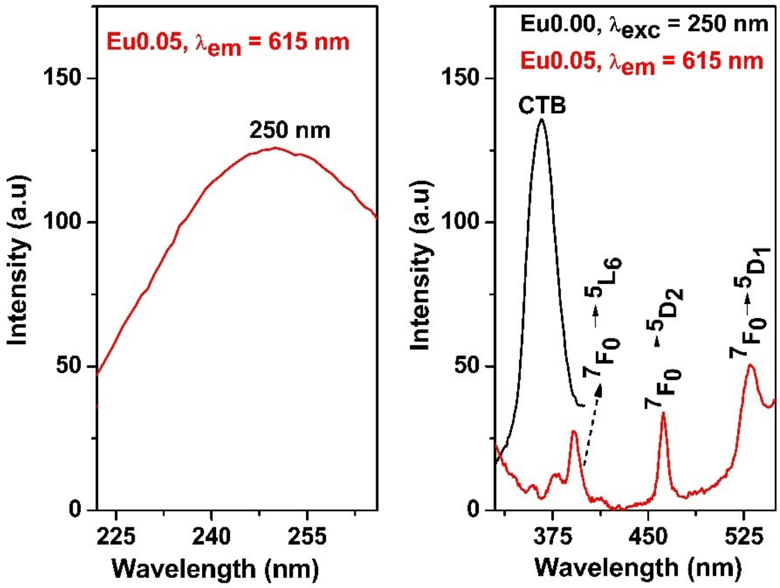

Fig 4.10 PL excitation spectrum of $ZnAl_{1.95}O_4:Eu_{0.05}$ at $\lambda_{em} = 615$ nm

Figure 4.10 gives the excitation spectrum of Eu^{3+} doped zinc aluminate (0.05 M doped sample) at $\lambda_{em} = 615$ nm. The broad band in the UV region around 250 nm, arising from the charge-transfer transition $O^{2-} \rightarrow Al^{3+}$ [14], is found to be more predominant over the dopant excitations observed at 390, 460 and 530 nm corresponding to $^7F_0 \rightarrow {}^5L_6$, $^7F_0 \rightarrow {}^5D_2$ and $^7F_0 \rightarrow {}^5D_1$ absorptions respectively. As evident from figure 4.10, the overlap between the host emission and the absorption levels of the dopant ion affirms a host-sensitising phenomenon to occur in the matrix.

As the activator concentration ‘x’ increases, the intensity of the emission at 615 nm ‘I’ gets more than the host emission. The dopant emission was even more pronounced in co-precipitated samples than the hydrothermally grown samples. The concentration quenching was found to occur at 0.05 M concentration of Eu (figure 4.11), may be attributed to the development of impure phases due to excessive doping of Eu^{3+} ions and also to the non-radiative energy transfer between activator ions through exchange and multipole-multipole interactions [12].

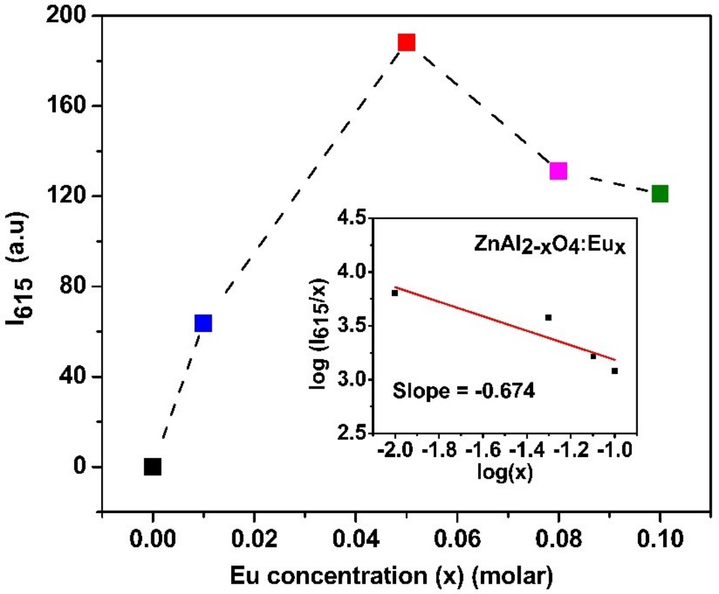

Fig 4.11 Intensity versu dopant concentration of $ZnAl_{2-x}O_4:Eu_x$ at λ_{exc} = 250 nm. The Inset shows the log(I/x) against log(x) plot of $ZnAl_{2-x}O_4:Eu_x$

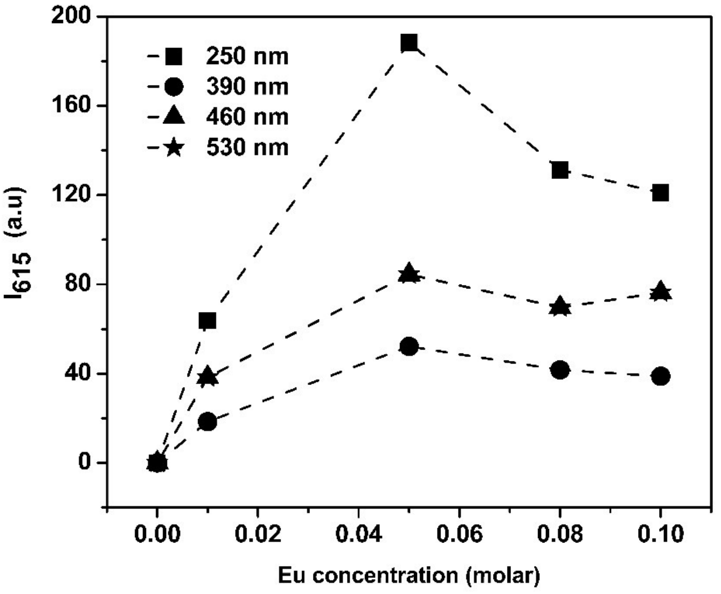

Fig 4.12 PL emission Intensity Vs Eu concentration of $ZnAl_{2-x}O_4$:Eu_x at λ_{exc} = 390, 460 and 530 nm

The inset depicts the log(I/x) against log(x) plot, the slope of the straight line was found to be -0.674, that yields a corresponding θ value 2.022. This parameter, being close to 3, again confirms the occurrence of exchange interaction between the host matrix and the activator ions Eu^{3+}.

The emission intensity at excitation wavelengths 390, 460 and 530 nm is less compared with the emission at host excitation 250 nm (figure 4.12), which affirms the fact that light absorption happens at the main band edge of the host rather than directly at the dopant ion levels.

4.3.3 $ZnAl_{2-y}O_4:Tb_y$

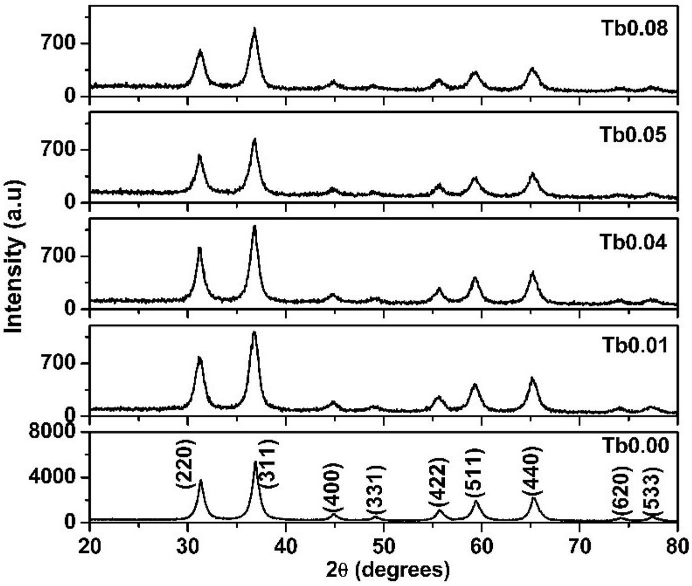

Fig 4.13 XRD spectra of $ZnAl_{2-y}O_4:Tb_y$ (y = 0.01, 0.04, 0.05, 0.08)

The XRD spectra of Tb^{3+} doped zinc aluminate prepared via hydrothermal method is shown in figure 4.13. The appearance of all diffraction peaks as in the standard JCPDS spectra of cubic spinel $ZnAl_2O_4$ structure and the absence of impurity phases confirms that Tb^{3+} ions are well incorporated into the lattice at all dopant concentrations, just like co-precipitated samples [10]. The diffraction peaks get broadened with increase in dopant addition into the host. In addition, the blue shift of the (311) peak maximum, compared to the pure sample prepared via hydrothermal method, contributes to the lowering of crystallite size. The lattice expansion observed, as evident from the increase in lattice parameter, also assures dopant assimilation into the spinel lattice (Table 4.3).

Molar concentration of Tb (y)	(311) Peak diffraction angle 2θ (degrees)	FWHM (degrees)	Crystallite size (nm)	Lattice parameter (Å)
0	36.720	0.899	9.315	8.087
0.01	36.771	1.092	7.667	8.101
0.04	36.791	1.019	8.216	8.096
0.05	36.786	1.086	7.709	8.097
0.08	36.775	1.101	7.604	8.099

Table 4.4 Crystallite size and lattice parameter of $ZnAl_{2-y}O_4$:Tb_y

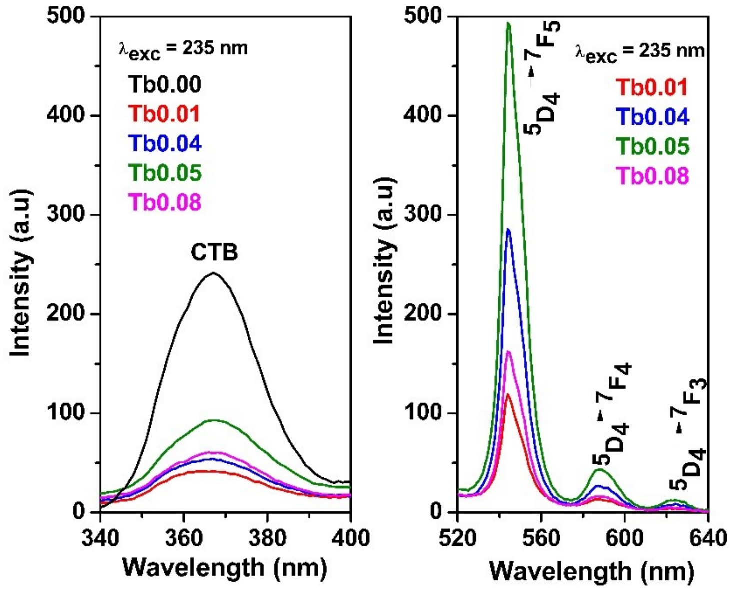

Fig 4.14 PL emission spectra of $ZnAl_{2-y}O_4$:Tb_y at λ_{exc}=235 nm

The PL emission is recorded for the Tb^{3+} doped samples. The emission spectra of Tb^{3+} doped $ZnAl_2O_4$ are shown in figure 4.14, which displays the characteristic emission bands at 544 nm, 590 nm and 621 nm corresponding to the electron transitions $^5D_4 \rightarrow {}^7F_j$ (j = 5, 4, and 3 respectively) of Tb^{3+} ions. The characteristic emission peak at 544 nm belongs to the magnetic dipole $^5D_4 \rightarrow {}^7F_5$ transition. The stronger magnetic dipole transition indicates a symmetrical environment around Tb^{3+} ions and that the Tb^{3+} ions are predominantly substituted into the Al^{3+} octahedral sites [15]. The phenomenon of host-sensitised emission is again observed here, as is evident from the reduction in intensity of host blue emission and appearance of pronounced dopant emissions, in the doped sample.

Though the emission peaks appear at the same position, intensity falls by half, when compared to the co-precipitated samples. The two-step heat treatment, one during the hydrothermal synthesis and the other during post-calcination, might be the reason for such a lowering in emission intensity. This may suppress the luminescent output due to many reasons, formation of new defect sites or modification of existing ones that can act as non-radiative recombination centers, migration of luminescent ions to other sites etc.

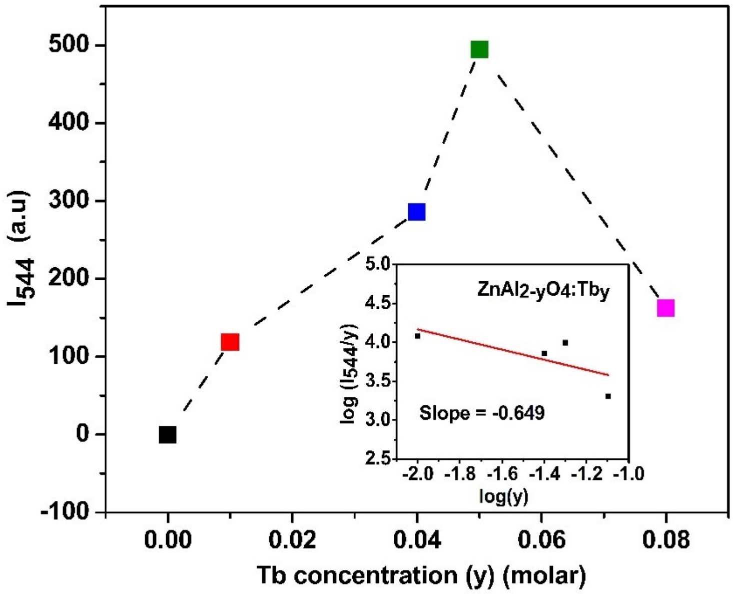

Fig 4.15 PL intensity I_{544} versus Tb concentration in $ZnAl_{2-y}O_4:Tb_y$ at λ_{exc} = 235 nm

The maximum PL intensity was observed at 0.05 M concentration of Tb^{3+} ions (figure 4.15). The decrease in luminescent intensity after 0.05 M is termed as concentration quenching. The inset shows the straight-line plot of log(I/y) versus log(y), slope of which calculated as –0.649 corresponds to a θ value of 1.947, a value close to 3, confirming the presence of exchange interaction between the host matrix and the activator ions (Tb^{3+}). However, the extent of these interactions in hydrothermally synthesized samples are generally less than that in co-precipitated ones, evident from the drop in intensity of the former compared to the latter.

The PL excitation spectrum is recorded at λ_{em}=544 nm (figure 4.16) and the most intense peak is observed at 235 nm, which is the charge-transfer band of the host. The less intense peaks at 348, 367 and 375 nm corresponds to the activator ion absorptions [16].

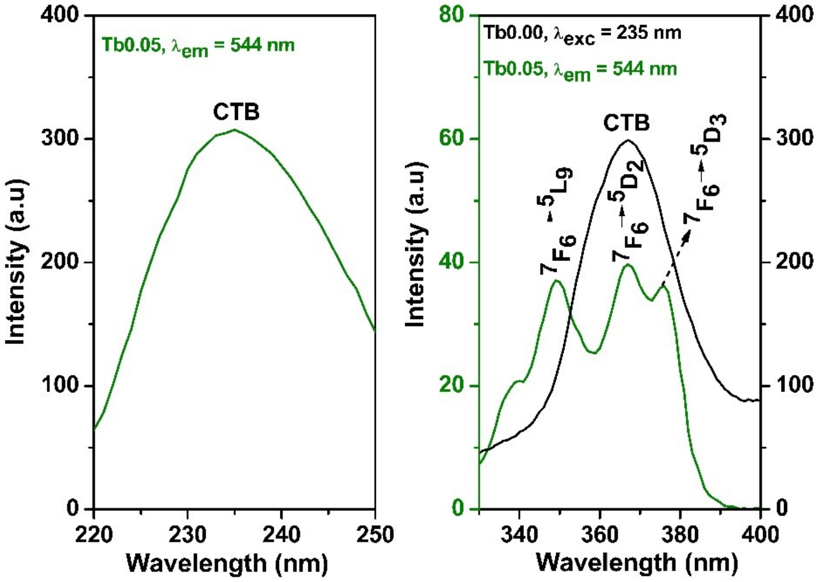

Fig 4.16 PL excitation spectrum of $ZnAl_{2-y}O_4:Tb_y$ (y = 0.05) at λ_{em} = 544 nm

Hence the emission is also checked at 348 nm and the corresponding PL intensity is less compared with that at 235 nm (figure 4.17), indicating that the photon absorption do take place predominantly at the charge transfer band of the host and subsequently energy is transferred to the dopant ions [16].

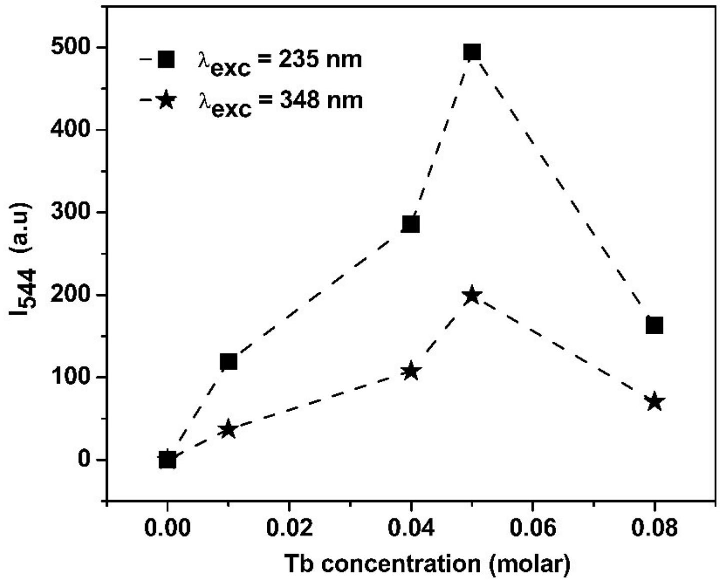

Fig 4.17 PL emission Intensity Vs Tb concentration of $ZnAl_{2-y}O_4:Tb_y$

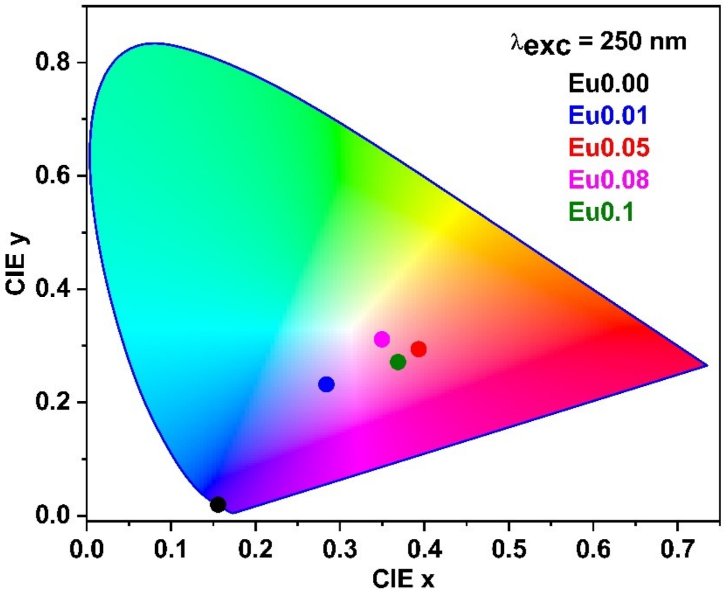

Fig 4.18 Color chromaticity diagram of $ZnAl_{2-x}O_4:Eu_x$

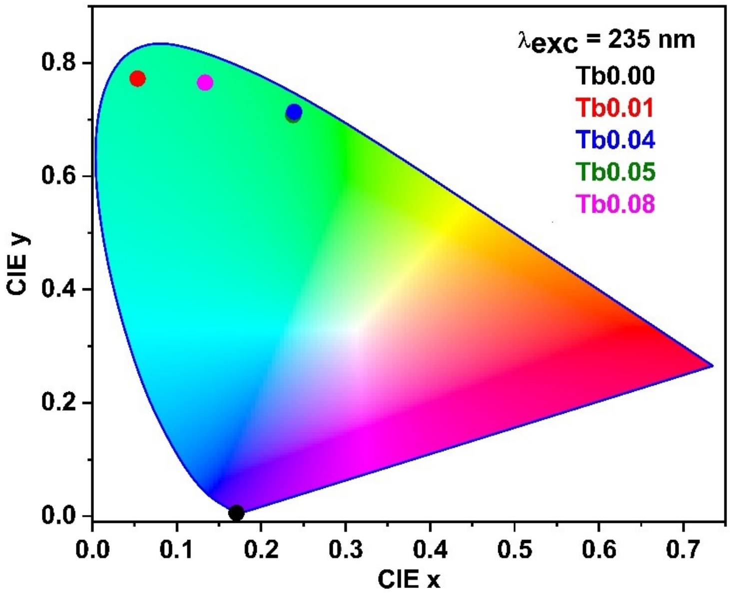

Fig 4.19 Color chromaticity diagram of $ZnAl_{2-y}O_4:Tb_y$

Sample	Dopant concentration (M)	CIE coordinates		Color purity (%)
		x	y	
$ZnAl_{2-x}O_4:Eu_x$	**Eu0.00**	0.156	0.020	98.58
	Eu0.01	0.284	0.232	29.96
	Eu0.05	0.393	0.294	25.71
	Eu0.08	0.350	0.311	10.80
	Eu0.1	0.369	0.271	30.22
$ZnAl_{2-y}O_4:Tb_y$	**Tb0.00**	0.171	0.006	99.96
	Tb0.01	0.053	0.773	93.48
	Tb0.04	0.238	0.708	88.40
	Tb0.05	0.239	0.714	91.14
	Tb0.08	0.133	0.766	87.18

Table 4.5 Color coordinates of $ZnAl_{2-x}O_4:Eu_x$ and $ZnAl_{2-y}O_4:Tb_y$

The color coordinates corresponding to luminescent emissions have been calculated from the CIE chromaticity diagram. Except for 0.01 M concentration of Eu, that emits in the blue region, all the others give a purplish pink emission (figure 4.18). However, the CIE (x, y) of the sample with 0.08 M Eu content was determined to be (0.350, 0.311), with a purity of 10.8 %, indicative of a near-white emission. A tuning in different shades of green is possible on varying the Tb dopant concentration (figure 4.19). The green emissions lie so close to the spectral locus, affirming a purity ~ 90 %, significantly close to their dominant wavelengths. The color coordinates (x, y) of pure $ZnAl_2O_4$ at λ_{exc} = 250 nm and λ_{exc} = 235 nm was found to be (0.156, 0.020) and (0.171, 0.006) respectively, lying almost near to the monochromatic spectral locus.

4.4 Conclusions

Pure and RE doped $ZnAl_2O_4$ (RE = Eu,Tb) nanophosphors can be effectively synthesized using hydrothermal method. The as-prepared sample itself showed the cubic spinel structure of zinc aluminate, and the crystallinity enhanced further on post-calcination. The FTIR, SEM-EDAX and DRS measurenents confirmed the optimum conditions (pH 10 and calcination at 750 °C for 2 hours), compositional ratio of 1:1.98 (Zn:Al) and a band gap of 4.73 eV. The crystallite size, calculated using Scherrer equation and W-H plot analysis, showed a value, higher than that of co-precipitated counterparts.

The incorporation of RE dopants into the host $ZnAl_2O_4$ lattice was investigated. The shift in diffraction angle and FWHM of (311) peak affirms the lattice expansion of the samples on dopant incorporation into the host matrix. The drop in intensity of the bluish host emission, the subsequent enhancenmene of dopant emissions and Dexter theory assessment confirms host-sensitised luminescent emission between the host and the activator mediated by exchange interaction.

Pure $ZnAl_2O_4$ emits in the violet-blue region, color coordinates (x, y) being (0.156, 0.020) and (0.171, 0.006) at λ_{exc} = 250 nm and λ_{exc} = 235 nm respectively, lying almost on the monochromatic spectral locus. On doping the host with Eu^{3+} ion, a dominant emission at 615 nm results. The maximum emission intensity was observed for the sample $ZnAl_{1.95}O_4{:}Eu_{0.05}$ whose (x, y) coordinates were found to be (0.393, 0.294). However, the sample with 0.08 M Eu content exhibited a color purity of 10.8 % (x,y) = (0.350, 0.311), indicative of a near-white emission. Green fluorescence, with peak maxima at 544 nm, results on incorporating Tb^{3+} ion into $ZnAl_2O_4$. These emissions lie so close to the spectral locus, affirming a color purity of

~ 90 %. The color coordinates of $ZnAl_{1.95}O_4$:$Tb_{0.05}$, that showed the maximum emission intensity, were found to be (0.239, 0.714).

References

[1] Zhang, W., Wang, Y., Shen, Y., Xie, M., & Guo, X. (2016). Mesoporous zinc aluminate ($ZnAl_2O_4$) nanocrystal: Synthesis, structural characterization and catalytic performance towards phenol hydroxylation. *Microporous and Mesoporous Materials, 226,* 278–283. https://doi.org/10.1016/j.micromeso.2016.02.001

[2] Miron, I., Enache, C., Vasile, M., & Grozescu, I. (2012). Optical properties of $ZnAl_2O_4$ nanomaterials obtained by the hydrothermal method. *Physica Scripta, 2012*(T149), 014064, 2–5. https://doi.org/10.1088/0031-8949/2012/T149/014064

[3] Strek, W., Dereń, P., Bednarkiewicz, A., Zawadzki, M., & Wrzyszcz, J. (2000). Emission properties of nanostructured Eu^{3+} doped zinc aluminate spinels. *Journal of Alloys and Compounds, 300,* 456–458. https://doi.org/10.1016/S0925-8388(99)00696-9

[4] Dwibedi, D., Murugesan, C., Leskes, M., & Barpanda, P. (2018). Role of annealing temperature on cation ordering in hydrothermally prepared zinc aluminate ($ZnAl_2O_4$) spinel. *Materials Research Bulletin, 98,* 219–224. https://doi.org/10.1016/j.materresbull.2017.10.010

[5] Alharbi, F. F., Aman, S., Abdullah, M., Abid, A. G., Manzoor, S., Khosa, R. Y., Farid, H. M. T., Silibin, M. V., Trukhanov, S. V., Zubar, T. I., & Trukhanov, A. V. (2024). Development of Mn doped $ZnAl_2O_4$ via hydrothermal method as photocatalyst for Cr(VI) reduction under visible light. *Ceramics International, 50,* 24177–24185. https://doi.org/10.1016/J.CERAMINT.2024.04.149

[6] de Macedo, H. P., Medeiros, R. L. B., de Araújo, A. L., de Medeiros, Â. A. S., de Oliveira, G. P. F., Antônio, M., Melo, F., & de Araújo Melo, D. M. (2017). Characterization of $ZnAl_2O_4$ spinel obtained by hydrothermal and microwave assisted

combustion method: A comparative study. *Materials Research, 20*(Suppl. 2), 29–33. https://doi.org/10.1590/1980-5373-MR-2016-0977

[7] Ha, L. H., Lanh, P. T., Long, N. N., & Loan, T. T. (2009). Some physical properties of $ZnAl_2O_4$:Cr^{3+}(Co^{2+}) powders prepared by hydrothermal method. *Journal of Physics: Conference Series, 187,* 012053. https://doi.org/10.1088/1742-6596/187/1/012053

[8] O, Z. S. Z., Strachowski, T., Grzanka, E., Mizeracki, J., Chlanda, A., Baran, M., Małek, M., & Niedziałek, M. (2022). Microwave-assisted hydrothermal synthesis of zinc-aluminium spinel $ZnAl_2O_4$. *Materials, 15*(1), 245. https://doi.org/10.3390/ma15010245

[9] Wrzyszcz, J., Zawadzki, M., Trawczy, J., Grabowska, H., & Mi, W. (2001). Some catalytic properties of hydrothermally synthesized zinc aluminate spinel. *Applied Catalysis A: General, 210*(1), 263–269. https://doi.org/10.1016/S0926-860X(00)00821-8

[10] Strek, W., Dereń, P., Bednarkiewicz, A., Zawadzki, M., & Wrzyszcz, J. (2000). Emission properties of nanostructured Eu^{3+} doped zinc aluminate spinels. *Journal of Alloys and Compounds, 300,* 456–458. https://doi.org/10.1016/S0925-8388(99)00696-9

[11] Miron, I., Enache, C., & Grozescu, I. (2012). Doped zinc aluminate spinel synthesized by hydrothermal method. *Digest Journal of Nanomaterials and Biostructures, 7,* 967–972.

[12] Priya, R., Negi, A., Singla, S., & Pandey, O. P. (2020). Luminescent studies of Eu doped $ZnAl_2O_4$ spinels synthesized by low-temperature combustion route. *Optik, 204,* 164173. https://doi.org/10.1016/j.ijleo.2020.164173

[13] Vengala Rao, B., Rambabu, U., & Buddhudu, S. (2006). Photoluminescence spectral analysis of Eu^{3+}: Phosphors. *Physica B: Condensed Matter, 382,* 86–91. https://doi.org/10.1016/j.physb.2006.02.003

[14] Silva, D., Abreu, A., Davolos, M. R., & Rosaly, M. (2011). Determination of the local site occupancy of Eu^{3+} ions in $ZnAl_2O_4$ nanocrystalline powders. *Optical Materials, 33,* 1226–1233. https://doi.org/10.1016/j.optmat.2011.02.014

[15] Fernández-Osorio, A., Rivera, C. E., Vázquez-Olmos, A., & Chávez, J. (2015). Luminescent ceramic nano-pigments based on terbium-doped zinc aluminate: Synthesis, properties and performance. *Dyes and Pigments, 119,* 22–29. https://doi.org/10.1016/j.dyepig.2015.03.021

[16] Kumar, M., & Gupta, S. K. (2015). An insight into optical spectroscopy of intense green emitting $ZnAl_2O_4:Tb^{3+}$ nanoparticles: Photo, thermally stimulated luminescence and EPR study. *Journal of Luminescence, 168,* 151–157. https://doi.org/10.1016/j.jlumin.2015.07.021

Chapter 5

EXPLORING THE POSSIBILITY OF WHITE LUMINESCENCE IN RE (RE = Eu, Tb) CO-DOPED $ZnAl_2O_4$ NANOPHOSPHORS SYNTHESIZED VIA CO-PRECIPITATION AND HYDROTHERMAL ROUTES

This chapter discusses the co-precipitation and hydrothermal synthesis of RE co-doped (RE = Eu, Tb) zinc aluminate. The possibility of white luminescence on co-doping the $ZnAl_2O_4$ *host matrix is explored in detail, employing the structural investigations using XRD and luminescent studies using PL spectra.*

5.1 Introduction

White light emitting devices are extensively under research due to their energy efficiency, durability and eco-friendly virtues over conventional light sources. Besides, they find applications in general illumination, medical fields, photography, specialised lighting and microscopy. Normally, white light is extracted from a display merging the primary colours red, green and blue, generated from various layers of inorganic materials, arranged in a sophistcated manner. This makes the device fabrication more complex and costly. The compatibility between the chosen materials for primary color emission may also significantly influence the luminescent output of the device. In this scenario, the advent of a single host matrix capable of emitting all the primary colours is a much sought after strategy.

Co-doping of lanthanide ions in binary oxide systems have been reported for fabricating LEDs, to improve light harvesting capacity or for attaining color tuning capability [1-5]. Several groups have explored white light generation from Eu^{3+} and Tb^{3+} codoped binary oxides such as Y_2O_3, In_2O_3 and Gd_2O_3 [4-6]. Promising nanophosphor systems based on mixed aluminates and phosphates for LEDs have been reported [7, 8]. K.G. Tshabalala *et al.* investigated the luminescent properties of green emitting (Ce^{3+}, Tb^{3+}) co-activated $ZnAl_2O_4$ [9]. Naveen Verma *et al.* reported an enhanced luminescence of Eu^{3+} emission with Tb^{3+} ion incorporation in $ZnAl_2O_4$ matrix via solution-combustion method through tunable coupling [6]. Rusu *et al.* demonstrated the colr tuning possiblity from red to green through (Tb, Eu) co-doping in $ZnAl_2O_4$ and $ZnGa_2O_4$ [7]. Strategies adopted to achieve white light emission from doubly and triply doped ternary $ZnAl_2O_4$ via various synthesis techniques are also available [10,11].

In the previous chapters, the successful synthesis of RE doped $ZnAl_2O_4$ via simple non-refractory co-precipitation and hydrothermal techniques had been demonstrated. It was observed that in addition to the material's inherent bluish luminescence, incorporation of terbium (Tb^{3+}) and europium (Eu^{3+}) ions into the host matrix could extract green and red emissions, respectively. The emission intensity varied with dopant concentration, suggestive of a tunable optical behaviour. These observations opened the possibility of exploring white light emission through co-doping the host material with Tb^{3+} and Eu^{3+}, as the combined emissions of blue, green, and red - the primary colours - can produce visible white light.

5.2 Experiment

The precursors used were zinc nitrate ($Zn(NO_3)_2.6H_2O$; Merck), aluminium nitrate ($Al(NO_3)_3.9H_2O$; Merck), europium nitrate ($Eu(NO_3)_3.H_2O$; Sigma-Aldrich) and terbium nitrate ($Tb(NO_3)_3.H_2O$; Sigma-Aldrich).

Eu^{3+} and Tb^{3+} co-doped zinc aluminate samples; $ZnAl_{2-(x+y)}O_4{:}Eu_xTb_y$ were prepared by weighing the precursors in molar ratio, fixing the total dopant concentration (x + y) at 0.05 M.

Co-precipitation method:

The weighed amounts of precursors were added to distilled water, stirred separately till dissolution and finally assorted together. pH of the mixture was maintained at 10 by adding ammonia solution (25%, Merck) dropwise with constant stirring. The mixture was kept for 24 hours at room temperature for precipitation. Then, it was filtered and dried at 80 °C in a hot air oven for 12 hours and the ground fine powder was calcined at 750 °C for 2 hours.

Hydrothermal method:

The adequate amounts of the chemical precursors were weighed, added to distilled water, stirred separately till dissolution and finally mixed. By dropwise addition of ammonia solution (25%, Merck), the pH of the mixture was kept at 10. The mixture was transferred into a Teflon beaker, and then placed in a tightly sealed steel autoclave at high pressure in a hot-air oven at 250 °C for 4 hours. The residue was filtered, dried at 80 °C and grinded to get powder. Then, it was calcined using a high-temperature furnace at 750 °C for 2 hours.

The samples were structurally analyzed using X-ray diffractograms and optically evaluated via PL spectral data. Quality of the fluorescent emissions were gauged using CIE color coordinates.

5.3 Results and discussions

5.3.1 $ZnAl_{2-(x+y)}O_4:Eu_xTb_y$ matrix – co-precipitation method

The XRD spectra of Eu and Tb co-doped $ZnAl_{2-(x+y)}O_4:Eu_xTb_y$ nanophosphors synthesised via co-precipitation are shown in figure 5.1. The spectra of all the samples matched well with the standard JCPDS pattern (Card No. 05-0669), confirming that all samples crystallised in cubic spinel structure of $ZnAl_2O_4$. No additional peaks are found to grow with dopant incorporation into the host, which shows that the crystalline structure is not affected by the presence of dopants.

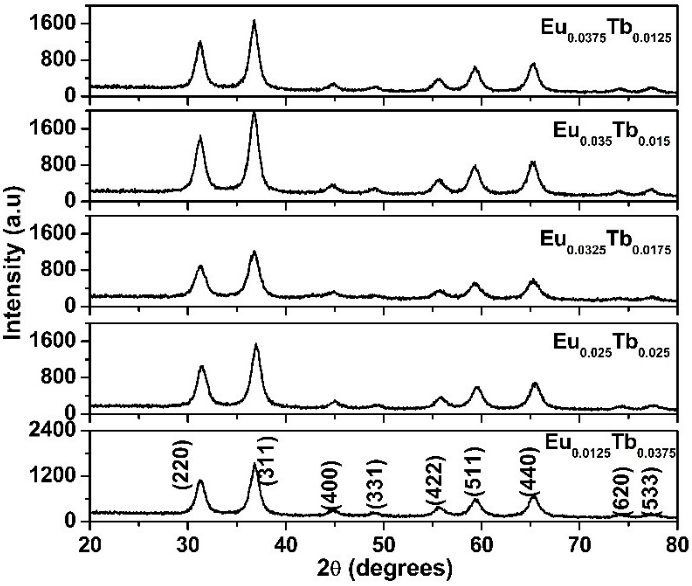

Fig 5.1 XRD spectra of $ZnAl_{2-(x+y)}O_4:Eu_xTb_y$ synthesised via co-precipitation

From table 5.1, one can note that on co-doping the host matrix, the (311) peak position shifts in comparison to the undoped sample (36.87°), which may be attributed to the distortion of crystal lattice due to the incorporation of dopant ions [8,9,11]. This results in an increase in lattice parameter from 8.08 Å of pure $ZnAl_2O_4$. The lattice expansion is a clear indication of effective incorporation of dopant ions into the host lattice. Morever, Eu^{3+} ions and Tb^{3+} ions, with an ionic radius of 0.95 Å and 0.92 Å respectively, larger than Zn^{2+} (0.74 Å) and Al^{3+} (0.50 Å), leads to lattice strain and expansion of the unit cell volume. The crystallite sizes were estimated from Scherrer equation for the most intense peak (311). The irregular shift in 2θ alongwith variations in FWHM of the (311) peak is reflected in the fluctuation in crystallite size for various Eu/Tb ratios.

Sample	(311) Diffraction angle 2θ (degrees)	FWHM (degrees)	Crystallite size (nm)	Lattice parameter (Å)
$Eu_{0.0375}$ $Tb_{0.0125}$	36.788	1.015	8.249	8.097
$Eu_{0.035}$ $Tb_{0.015}$	36.759	1.127	7.425	8.103
$Eu_{0.0325}$ $Tb_{0.0175}$	36.751	1.299	6.445	8.105
$Eu_{0.025}$ $Tb_{0.025}$	36.983	1.153	7.266	8.056
$Eu_{0.0125}$ $Tb_{0.0375}$	36.839	1.161	7.212	8.086

Table 5.1 Crystallite size and lattice parameter of $ZnAl_{2-(x+y)}O_4:Eu_xTb_y$ nanophosphors synthesised via co-precipitation

The luminescent emission of the co-doped samples, $ZnAl_{2-(x+y)}O_4:Eu_xTb_y$, were checked at both 230 nm (figure 5.2), and 250 nm (figure 5.3).

The magnetic dipole $^5D_4 \rightarrow {}^7F_5$ transition of Tb^{3+}, with emission peak at 544 nm, is more significant when $\lambda_{exc} = 230$ nm (figure 5.2), than the $^5D_0 \rightarrow {}^7F_j$ transitions of Eu^{3+}. But on the contrary, though less intense than the 544 nm Tb^{3+} emission, the hypersensitive $^5D_0 \rightarrow {}^7F_2$ transition at 615 nm, along with other $^5D_0 \rightarrow {}^7F_j$ Stark splittings, is more evident when excited at $\lambda_{exc} = 250$ nm and even dominates the spectrum at higher Eu/Tb ratios (figure 5.3).

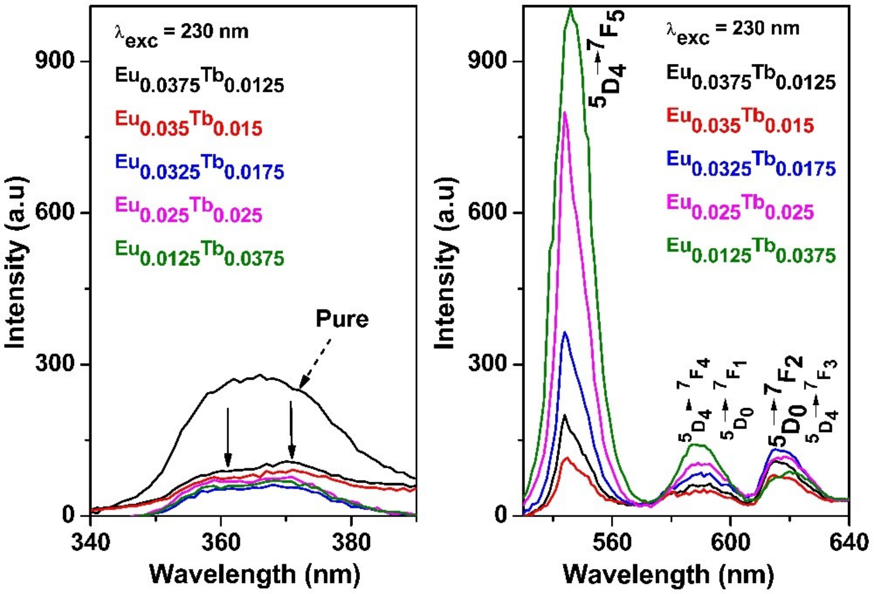

Fig 5.2 PL emission spectra of $ZnAl_{2-(x+y)}O_4:Eu_xTb_y$ samples at $\lambda_{exc} = 230$ nm (co-precipitation synthesis)

The UV-blue emission of the host is less in intensity compared to the dopant emissions in most cases, when excited at 230 nm as well as 250 nm. Host emission, though less in intensity, presents a peak splitting, in either case. The arrows (marked in the PL emission spectra at both excitations), indicate these two sites, whose peak wavelengths shift between 361 and 372 nm respectively. The variations in PL emission intensities confirm the host sensitised luminescent emission, where the energy is resonantly transferred from the host to the activator ions. The intensity of the two peak emissions, at 544 nm and 615 nm, varies with doping concentration of Eu^{3+} and Tb^{3+}.

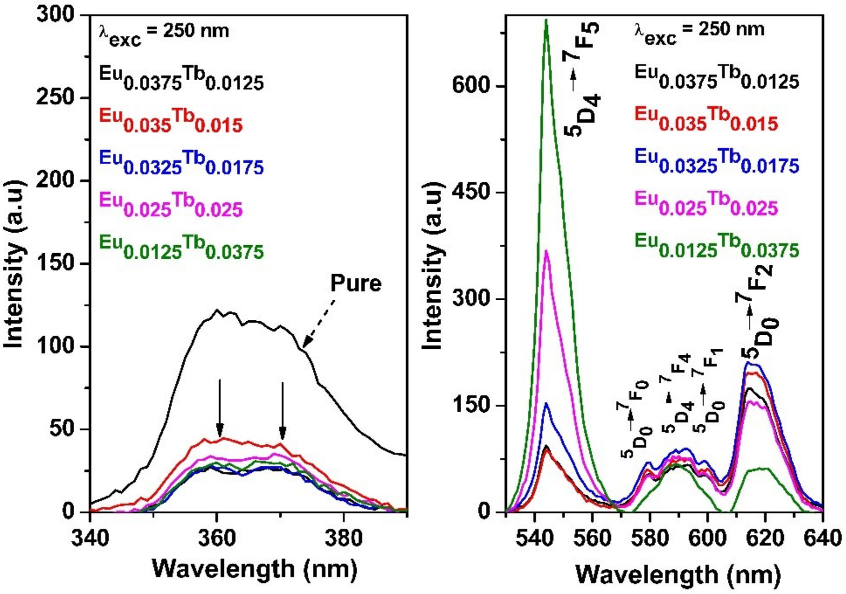

Fig 5.3 PL emission spectra of ZnAl$_{2-(x+y)}$O$_4$:Eu$_x$Tb$_y$ samples at λ_{exc} = 250 nm (co-precipitation synthesis)

An energy band level diagram is proposed based on the observations from the PL emission spectrum (figure 5.4).

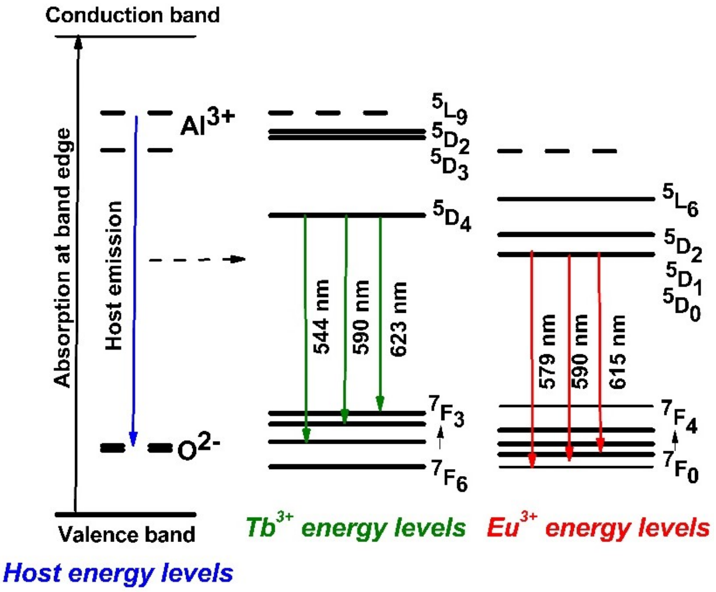

Fig 5.4 Energy band diagram model of ZnAl$_{2-(x+y)}$O$_4$:Eu$_x$Tb$_y$

When the concentration of Eu^{3+} is less, the green Tb^{3+} emission band at 544 nm dominates over the entire spectral output, along with its less intense transitions $^5D_4 \rightarrow {}^7F_4$ and $^5D_4 \rightarrow {}^7F_3$. As the Eu^{3+}/Tb^{3+} ratio increases, the intensity of the green emission drops, as expected. The crystal field splittings, corresponding to the Eu^{3+} transitions $^5D_0 \rightarrow {}^7F_j$ (j = 0, 1, 2), becomes more evident at higher concentrations of Eu^{3+}. A closer look at higher concentrations of Tb^{3+}, reveals that the band at 615 nm makes a slight red shift indicating the emission $^5D_4 \rightarrow {}^7F_3$ of Tb^{3+} ions. These effects are more pronounced at λ_{exc} = 250 nm. In other words, all the $^5D_4 \rightarrow {}^7F_j$ and $^5D_0 \rightarrow {}^7F_j$ transitions, corresponding to Tb^{3+} and Eu^{3+}respectively, appear in mixed proportions with dopant ratio.

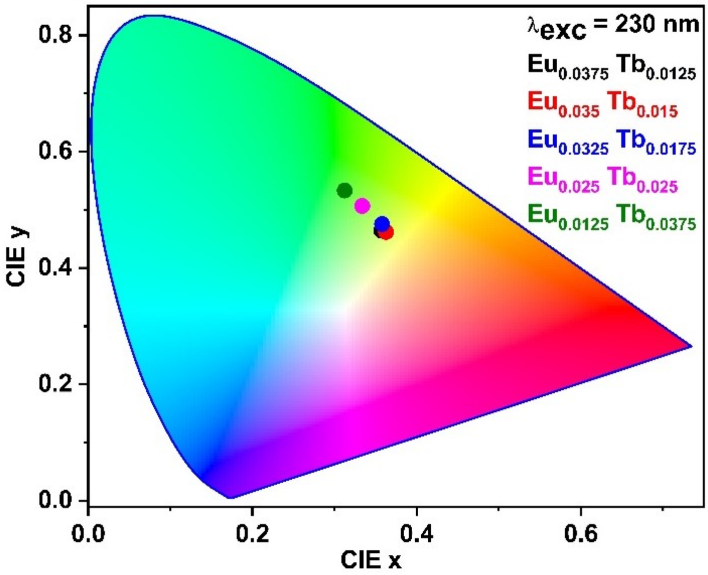

Fig 5.5 CIE color chromaticity diagram of $ZnAl_{2-(x+y)}O_4{:}Eu_xTb_y$ excited at wavelength 230 nm (co-precipitation method)

The quality of the emissions were further gauged using color cordinates, and are presented in table 5.2 [6]. The CIE chromaticity diagram of $ZnAl_{2-(x+y)}O_4{:}Eu_xTb_y$ for the two excitation wavelengths, 230 nm and 250 nm, are depicted in figure 5.5 and 5.6 respectively. As evident from the color coordinates tabulated (table 5.2), it is found that the bluish contribution is meagre at 230 nm. Henceforth, the emissions from the co-doped samples lie in the yellowish region. The value of color purity around 50 % also confirms the yellowish nature of the emission.

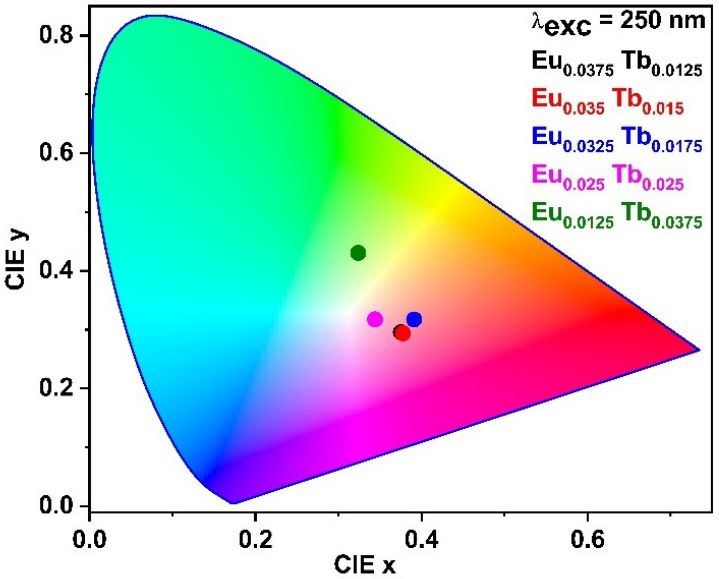

Fig 5.6 CIE color chromaticity diagram of $ZnAl_{2-(x+y)}O_4:Eu_xTb_y$ excited at wavelength 250 nm (co-precipitation method)

But when excited at 250 nm, the intensities of the primary color emissions draw nearer, so does the CIE coordinate values. A near-white emission is obtained for the $ZnAl_{1.95}O_4:Eu_{0.025}Tb_{0.025}$ sample for which (x, y) = (0.344, 0.318) at 250 nm excitation, which is very close to the standard value (0.33, 0.33) of white emission. The value of color purity was found to be 7 % for this sample, as expected from the observation.

	Eu/Tb	**CIE**					
		230 nm			**250 nm**		
		x	**y**	**Color Purity (%)**	**x**	**y**	**Color Purity (%)**
$Eu_{0.0375}$ $Tb_{0.0125}$	3	0.357	0.465	48.16	0.375	0.296	21.33
$Eu_{0.035}$ $Tb_{0.015}$	2.33	0.363	0.462	49.02	0.378	0.294	22.72
$Eu_{0.0325}$ $Tb_{0.0175}$	1.86	0.358	0.476	51.42	0.391	0.318	16.13
$Eu_{0.025}$ $Tb_{0.025}$	1	0.334	0.507	53.38	0.344	0.318	7.13
$Eu_{0.0125}$ $Tb_{0.0375}$	0.33	0.312	0.533	55.83	0.324	0.431	28.31

Table 5.2 CIE color coordinates of $ZnAl_{2-(x+y)}O_4:Eu_xTb_y$ (co-precipitation method) at the two excitation wavelengths

At 230 nm, the PL emission spectra reveals that as the Eu^{3+} concentration increases, the reddish emission gets intensified and comparable to green emission of Tb^{3+}, opening the possibility of yellowish white emissions. For near-white emission, the system must be excited at 250 nm, corresponding to the CTB of Eu^{3+} 615 nm emission, rather than at 230 nm.

5.3.2 $ZnAl_{2-(x+y)}O_4:Eu_xTb_y$ matrix – hydrothermal method

The XRD spectra of $ZnAl_{2-(x+y)}O_4:Eu_xTb_y$ samples synthesised via hydrothermal method are shown in figure 5.7. For all the samples, the spectra match with the standard JCPDS pattern and it could be confirmed that the cubic spinel structure was formed. The average crystallite size and lattice parameter calculated are given in table 5.3.

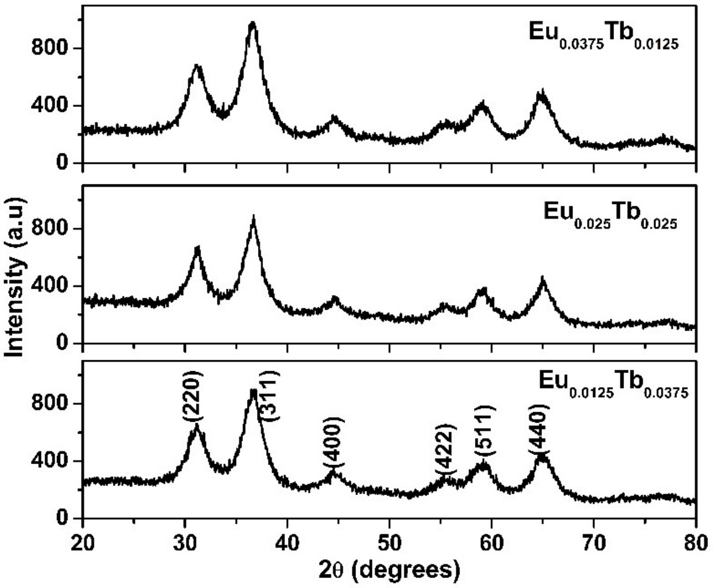

Fig 5.7 XRD spectra of $ZnAl_{2-(x+y)}O_4:Eu_xTb_y$ synthesised via hydrothermal method

In the co-doped samples synthesised via hydrothermal method, the broadening of the (311) peak and its shift to lower angles (compared to 36.72° for pure $ZnAl_2O_4$) is more pronounced, both contributing significantly to the reduction in crystallite size. Accordingly, the lattice parameter was high compared to the pure one; 8.087 Å, the lattice expansion is more obvious than that in the co-precipitated samples.

Sample	(311) Diffraction angle 2θ (degrees)	FWHM (degrees)	Crystallite size (nm)	Lattice parameter (Å)
Eu$_{0.0375}$ Tb$_{0.0125}$	36.595	2.261	3.701	8.138
Eu$_{0.025}$ Tb$_{0.025}$	36.588	1.964	4.260	8.139
Eu$_{0.0125}$ Tb$_{0.0375}$	36.611	2.324	3.601	8.135

Table 5.3 Crystallite size and lattice parameter of ZnAl$_{2-(x+y)}$O$_4$:Eu$_x$Tb$_y$ synthesised via hydrothermal method

The PL emission spectra, recorded at excitation wavelengths 230 nm and 250 nm, are shown in figure 5.8 and 5.9 respectively. A lot of deviations were noted in this set of hydrothermally prepared samples, compared to all other co-precipitated and auto-combustion synthesised (to be discussed in chapter 6) sample sets. The spectra mostly displayed the high intense emission band at 544 nm attributed to Tb^{3+} ions, accompanied by other smaller bands. The $^5D_4 \rightarrow {}^7F_j$ transitions of Tb^{3+} ion and $^5D_0 \rightarrow {}^7F_j$ transitions of Eu^{3+} ion appear in mixed proportions with dopant ratio and excitation wavelengths. The $^5D_4 \rightarrow {}^7F_5$ transition of Tb^{3+} ion was dominant in all cases, except for the sample ZnAl$_{1.95}$O$_4$:Eu$_{0.0375}$Tb$_{0.0125}$ excited at 250 nm (figure 5.9).

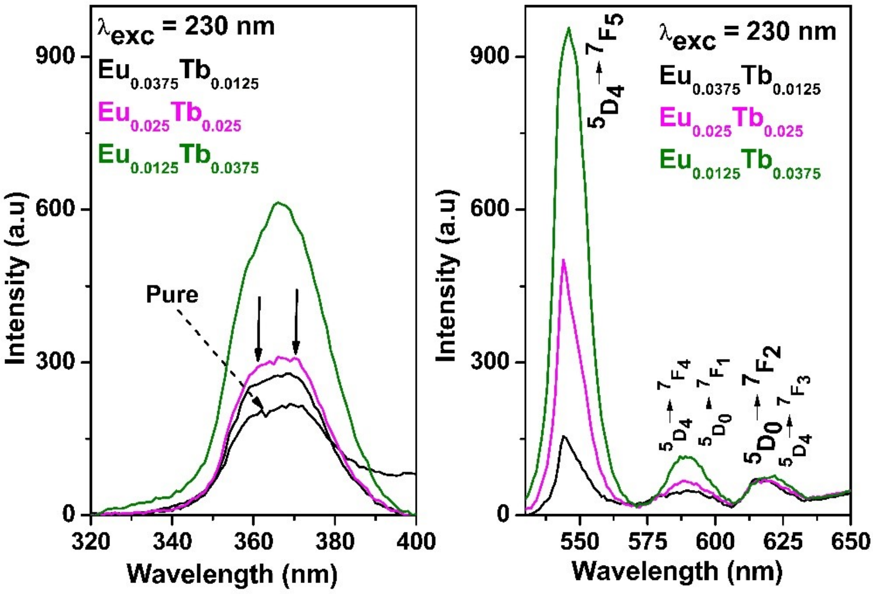

Fig 5.8 PL emission spectra of ZnAl$_{2-(x+y)}$O$_4$:Eu$_x$Tb$_y$ (hydrothermal method) recorded at an excitation wavelegth of 230 nm

In contrary to the other co-doped samples, the intensity of the charge transfer band of the host increases considerably than the pure matrix on co-doping in hydrothermally synthesised samples, though still less intense than the 544 nm emission of Tb^{3+}, irrespective of the excitation wavelength. This effect is more pronounced at 230 nm than at 250 nm. Additionally, the host emissions also exhibit the peak splitting, indicated by arrows in figure 5.8 and 5.9, the peak wavelengths shifting between 361 and 372 nm with dopant concentration. But as the Eu/Tb ratio increases to 3:1, the host emission of the co-doped sample has a trend to dominate even the activator emissions at both excitations, in addition to energy transfer between host and activator ions.

The hydrothermal method involves a unique two-step heat treatment compared to other methods discussed in this work. This might create beneficial defects such as oxygen vacancies, thereby altering the band structure and modifying the host for improved light absorption and emission. Such synergistic effects cannot be totally excluded here.

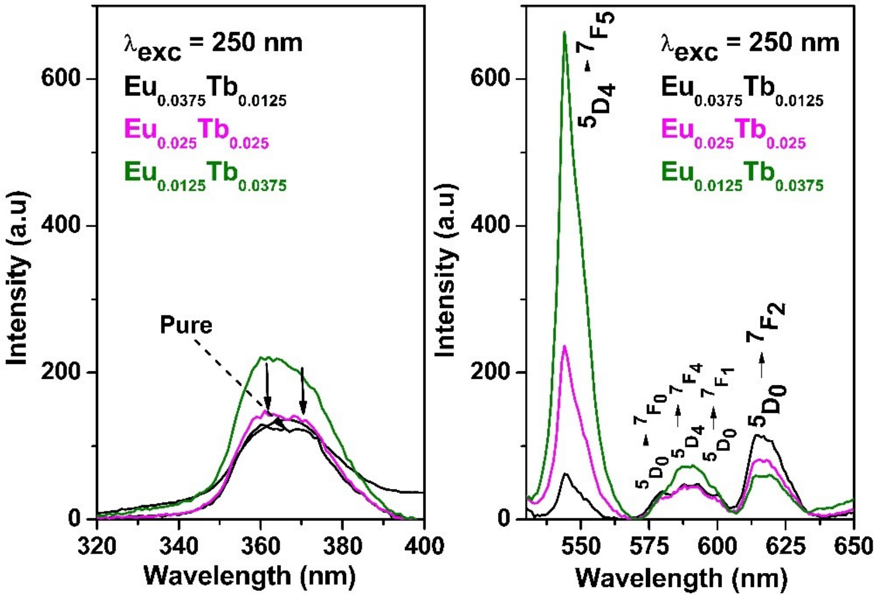

Fig 5.9 PL emission spectra of $ZnAl_{2-(x+y)}O_4:Eu_xTb_y$ (hydrothermal method) recorded at an excitation wavelegth of 250 nm

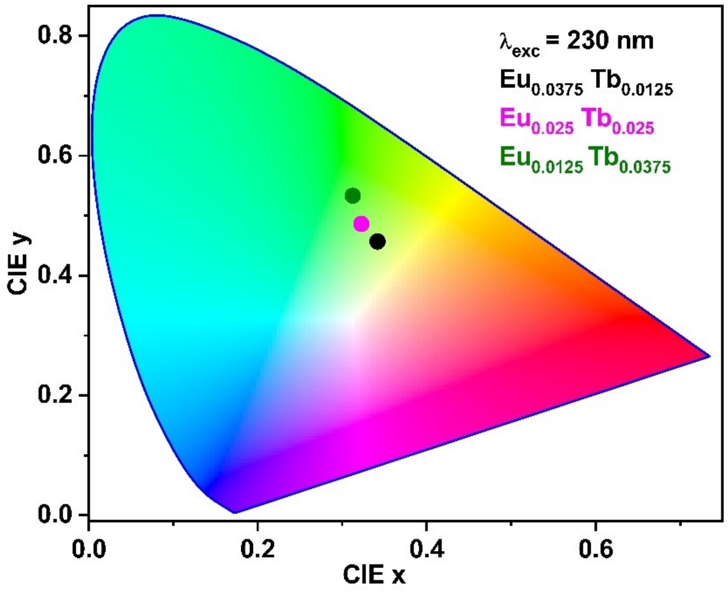

Fig 5.10 CIE color chromaticity diagram of $ZnAl_{2-(x+y)}O_4:Eu_xTb_y$ at λ_{exc} = 230 nm synthesised via hydrothermal method

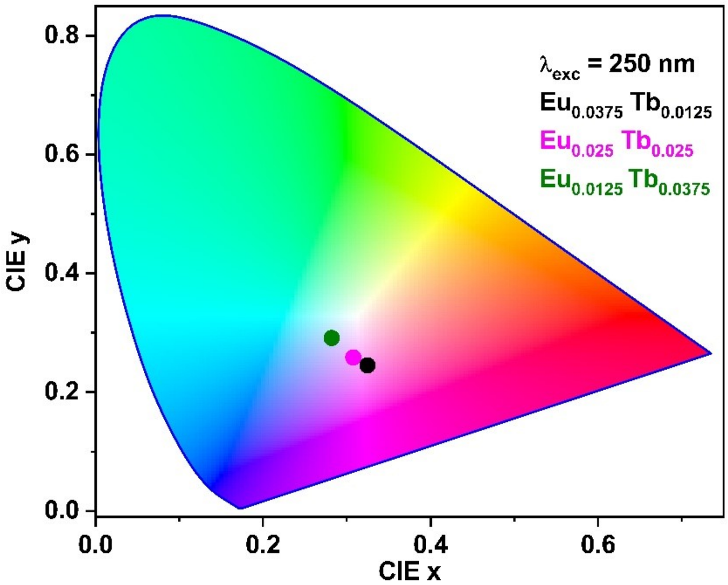

Fig 5.11 CIE color chromaticity diagram of $ZnAl_{2-(x+y)}O_4:Eu_xTb_y$ at λ_{exc} = 250 nm synthesised via hydrothermal method

	Eu/Tb	CIE					
		230 nm			250 nm		
		x	y	Color purity	x	y	Color purity
$Eu_{0.0375}$ $Tb_{0.0125}$	3	0.3417	0.4568	40.79	0.3248	0.2454	32.42
$Eu_{0.025}$ $Tb_{0.025}$	1	0.3226	0.4863	44.40	0.3078	0.2588	24.39
$Eu_{0.0125}$ $Tb_{0.0375}$	0.33	0.3124	0.5332	55.86	0.2819	0.2915	19.98

Table 5.4 CIE color coordinates of $ZnAl_{2-(x+y)}O_4$:Eu_xTb_y (hydrothermal method)

In-order to check the purity of PL emission, color chromaticity diagram was employed and the calculated values are given in table 5.4. When excited at 230 nm, as Eu^{3+} concentration increases, the co-doped sample showed a yellowish emission (figure 5.10). At 250 nm, near-white emissions could be obtained, but with a color purity of only 20 % (figure 5.11). To obtain a color purity less than 10 %, one can try varying the Eu dopant concentration, fixing the Tb^{3+} content (say, at 0.025 M). In the present work, the co-precipitation method gave a better luminescent response towards acquiring a white emission than the hydrothermal method.

5.4 Conclusions

Eu^{3+} and Tb^{3+} co-doped $ZnAl_2O_4$ was successfully prepared through co-precipitation and hydrothermal method and checked for white luminescence. The incorporation of dopants into the host lattice was evident from the variations in structural parameters like lattice parameter, and shift in (311) diffraction peak. The PL spectra of the co-doped samples were recorded at two excitation wavelengths, 230 and 250 nm, they being the host excitation peaks corresponding to the respective intense emissions, 544 and 615 nm, in Tb^{3+} and Eu^{3+} doped samples. In all the co-doped samples, it was found that the $^5D_4 \rightarrow {}^7F_j$ transitions of Tb^{3+} ion and $^5D_0 \rightarrow {}^7F_j$ transitions of Eu^{3+} ion appear in mixed proportions with dopant ratio and excitation wavelengths. The color coordinate analysis confirmed the possibility of a yellowish-white emission at 230 nm excitation and a near-white emission at 250 nm absorption. A near-white emission with

7% color purity could be attained for the co-precipitated co-doped $ZnAl_{1.95}O_4:Eu_{0.025}Tb_{0.025}$ sample for which CIE (x, y) was found to be (0.344, 0.318) at 250 nm excitation.

References

[1] Guillaume, C., Frieiro, J. L., Blázquez, O., Labbé, C., López-Vidrier, J., Garrido, B., Hernández, S., Liu, B., Khomenkova, L., Frilay, C., Lemarié, F., Leroux, C., Pelloquin, D., & Portier, X. (2021). Influence of post annealing treatments on the luminescence of rare earth ions in ZnO:Tb,Eu/Si heterojunction. *Applied Surface Science, 556,* 149754. https://doi.org/10.1016/j.apsusc.2021.149754

[2] Wang, W., Wang, R., Ge, Y., & Wu, B. (2018). Color tuning and white light emission by codoping in isostructural homochiral lanthanide metal-organic frameworks. *RSC Advances, 8,* 42100–42108. https://doi.org/10.1039/c8ra06793g

[3] Motloung, S. V., Tshabalala, K. G., Kroon, R. E., Hlatshwayo, T. T., Mlambo, M., & Mpelane, S. (2019). Effect of Tb^{3+} concentration on the structure and optical properties of triply doped $ZnAl_2O_4$:1% Ce^{3+}, 1% Eu^{3+}, x% Tb^{3+} nano-phosphors synthesized via citrate sol-gel method. *Journal of Molecular Structure, 1175,* 241–252. https://doi.org/10.1016/j.molstruc.2018.08.002

[4] Akman, E., Akin, S., Ozturk, T., Gulveren, B., & Sonmezoglu, S. (2020). Europium and terbium lanthanide ions co-doping in TiO_2 photoanode to synchronously improve light-harvesting and open-circuit voltage for high-efficiency dye-sensitized solar cells. *Solar Energy, 202,* 227–237. https://doi.org/10.1016/j.solener.2020.03.108

[5] Yang, J., Wang, X., Song, L., Luo, N., Dong, J., Gan, S., & Zou, L. (2018). Tunable luminescence and energy transfer properties of $GdPO_4:Tb^{3+}$, Eu^{3+} nanocrystals for warm-white LEDs. *Optical Materials, 85,* 71–78. https://doi.org/10.1016/j.optmat.2018.08.043

[6] Verma, N., Marí, B., Singh, K. C., Jindal, J., Yadav, S., & Mittal, A. (2019). Enhanced luminescence by tunable coupling of Eu^{3+} and Tb^{3+} in $ZnAl_2O_4:Eu^{3+}:Tb^{3+}$ phosphor synthesized by solution combustion method. *Journal of the Australian Ceramic Society, 55,* 179–185. https://doi.org/10.1007/s41779-018-0223-2

[7] Rusu, E., Ursaki, V., Novitschi, G., Vasile, M., Petrenco, P., & Kulyuk, L. (2009). Luminescence properties of $ZnGa_2O_4$ and $ZnAl_2O_4$ spinels doped with Eu^{3+} and Tb^{3+} ions. *Physica Status Solidi (C), 6,* 1199–1202. https://doi.org/10.1002/pssc.200881172

[8] Hernández-Pérez, C. D., Baéz-Rodríguez, A., Ramos-Brito, F., Barrera-Calva, E., González, F., Martinez-Martinez, R., Alvarez-Fregoso, O., García-Hipólito, M., & Falcony, C. (2021). Strategy to achieve the emission of white light and other colors from $ZnAl_2O_4$:(Eu^{3+} + Tb^{3+}) films deposited by the USP technique. *Applied Physics A: Materials Science & Processing, 127,* 1–9. https://doi.org/10.1007/s00339-021-04274-6

[9] Tshabalala, K. G., Cho, S. H., Park, J. K., Pitale, S. S., Nagpure, I. M., Kroon, R. E., Swart, H. C., & Ntwaeaborwa, O. M. (2012). Luminescence properties of Ce^{3+} and Tb^{3+} co-activated $ZnAl_2O_4$ phosphor. *Physica B: Condensed Matter, 407,* 1489–1492. https://doi.org/10.1016/j.physb.2011.09.068

[10] Liu, Z., Yu, L., Wang, Q., Tao, Y., & Yang, H. (2011). Effect of Eu, Tb codoping on the luminescent properties of Y_2O_3 nanorods. *Journal of Luminescence, 131,* 12–16. https://doi.org/10.1016/j.jlumin.2010.08.012

[11] Li, F., Liu, H., Wei, S., Sun, W., & Yu, L. (2013). Photoluminescent properties of Eu^{3+} and Tb^{3+} codoped Gd_2O_3 nanowires and bulk materials. *Journal of Rare Earths, 31,* 1063–1068. https://doi.org/10.1016/S1002-0721(12)60404-9

Chapter 6

GREEN SYNTHESIS OF AB_2O_4 TERNARY SYSTEMS USING AUTO-COMBUSTION

The present chapter discusses a plant extract mediated green auto-combustion synthesis procedure for pure, singly doped and co-doped $ZnAl_2O_4$. XRD data, FTIR, TEM and SEM-EDAX measurements were used for structural and morphological characterization of the synthesised nanoparticles. Optical measurements were done using DRS data, luminescent spectral studies and colorimetric analysis. The possibility for green synthesis of other AB_2O_4 (A = Zn, Mg; B = Al, Cr) systems were also explored.

6.1 Introduction

Spinel nanoparticle synthesis using conventional approaches often involve expensive and environmentally harmful chemicals, along with energy-intensive heating steps that contribute to pollution. Recently, researchers focus on more cost-effective and environmentally benign synthesis techniques that leaves behind biodegradable and non-toxic spin-offs, unlike the hazardous waste from traditional methods. Moreover, green synthesis procedures are designed such that waste production is minimized, reducing pollution of the ecosystem we thrive in.

Literature highlights that metal nanoparticles can be effectively synthesized from metal salt solutions using plant extracts as natural reducing agents - eliminating the need for hazardous chemicals [1–4]. Many works report that phytochemicals in plant extracts can act as capping as well as stabilizing agents during nanoparticle formation, giving stable final yields [5–7]. While the green synthesis approach has been widely employed to produce metal nanoparticles, its viability towards synthesis of ternary spinel nanoparticles remains largely unexplored.

R. Yuvasravana *et al.* has reported a green synthesis of $ZnAl_2O_4$ using pomegranate peel extract at 750 °C for 3 hours [8]. D. S Bobade *et al.* synthesised Ce^{3+} doped $ZnAl_2O_4$ using aloe-vera gel in a muffle furnace at 500 °C, followed by calcination at 800 °C for 3 hours [9]. The rarity of reported works was the key factor behind the present work.

Green synthesis of zinc aluminate using a moringa (Scientific name - Moringa Oleifera) leaf extract-assisted combustion method is detailed in the present chapter. Works are reported where Moringa Oleifera is used to synthesise metal nanoparticles and investigated for antibacterial as well as cytotoxic applications [10][11]. Also, the work focusses on the RE (RE = Eu, Tb) doping into the zinc aluminate host matrix through green synthesis route and investigates the possibility of white light emission from green synthesised RE co-doped $ZnAl_2O_4$. Also, the feasibility of other AB_2O_4 systems with A = Zn^{2+}, Mg^{2+} and B = Al^{3+}, Cr^{3+} are also checked.

6.2 Experiment

The precursors used for synthesis were zinc nitrate ($Zn(NO_3)_2.6H_2O$; 96%, Merck), aluminium nitrate ($Al(NO_3)_3.9H_2O$; 95%, Merck), europium nitrate ($Eu(NO_3)_3.H_2O$; 99.9%, Sigma-Aldrich) and terbium nitrate ($Tb(NO_3)_3.H_2O$; 99.99%, Sigma-Aldrich).

Preparation of leaf extract: Fresh moringa leaves were collected from Thrissur, Kerala, washed well and shade-dried for 4 days. The dried leaves were grinded to powder and dissolved in distilled water. The solution was heated at 60 °C for half an hour and filtered to obtain the extract.

Synthesis of pure $ZnAl_2O_4$: The chemical precursors of Zn and Al were weighed in the molar ratio Zn:Al = 1:2, added to distilled water and stirred separately till dissolution. 10 ml of moringa leaf extract was added to the precursor mixture, heated at 80 °C till gel formation and later placed on a hotplate for combustion. The residue was then collected, powdered and calcined at various tmperatures (300 – 750 °C) for 2 hours.

The precursor ratio chosen for singly doped $ZnAl_{2-x}O_4:RE_x$ (RE = either Eu or Tb) was Zn:Al:RE = 1:1.95:0.05. Three samples of Eu and Tb co-doped $ZnAl_2O_4$ were prepared and labelled as $ZnAl_{2-(x+y)}O_4:Eu_xTb_y$, varying x and y, the molar concentrations of Eu and Tb respectively, such that $x + y = 0.05$.

The viability of the procedure was tested with other AB_2O_4 systems - A = Zn / Mg and B = Al / Cr. The precursors used for the synthesis were zinc nitrate ($Zn(NO_3)_2.6H_2O$; 96%, Merck), magnesium nitrate ($Mg(NO_3)_2.6H_2O$; 96%, Merck), chromium nitrate ($Cr(NO)_3$) and aluminium nitrate ($Al(NO_3)_3.9H_2O$; 95%, Merck) adopting a similar synthesis procedure keeping the precursor ratio A:B at 1:2.

Diffractions patterns, TEM and FTIR studies were used for structural analysis. SEM-EDAX imaging aided morphological and compositional characterization. Optical studies include diffuse reflectance spectral analysis, luminescent studies and colorimetric characterization.

6.3 Results and discussions

6.3.1 Phytochemical analysis of moringa leaf extract

Moringa Oleifera (moringa) leaves were selected for the procedure owing to ease of its natural access and biodegradable nature. Plant extracts can act as non-toxic reducing agents for the extraction of nanoparticles [10,11], the phytochemical content assists as binders and stabilising agents for the synthesised nanoparticles.

Phytochemical test	Observed result	Inference
Saponins (Form test)	2 cm layer of foam observed	Present
Phenols ($FeCl_3$ test)	Dark green colour	Present
Steroids	Reddish brown ring at the interphase	Present
Carbohydrates (Fehling's test)	Orange precipitate	Present
Amino acid (Millon's test)	Brick red precipitate	Present
Tannins ($FeCl_3$ test)	Brownish green or blue black formation	Present
Proteins	Violet colour	Present
Alkaloids	Orange red precipitate	Present
Flavonoids (NaOH test)	Yellow colour disappears	Present
Cardiac glycosides (Keller Killani test)	Brown ring formed	Present
Sugars	No precipitate	Absent
Starch	No color change	Absent
Terpenoids	No color change	Absent
Phlobetannin	No precipitate	Absent
Coumarins	No color change	Absent

Table 6.1 Phytochemical analysis of the aqueous extract of dried moringa leaves

Table 6.1 presents the phytochemical analysis of raw moringa leaf extract [12]. Negative results affirm the absence of such phytochemical content in the extract.

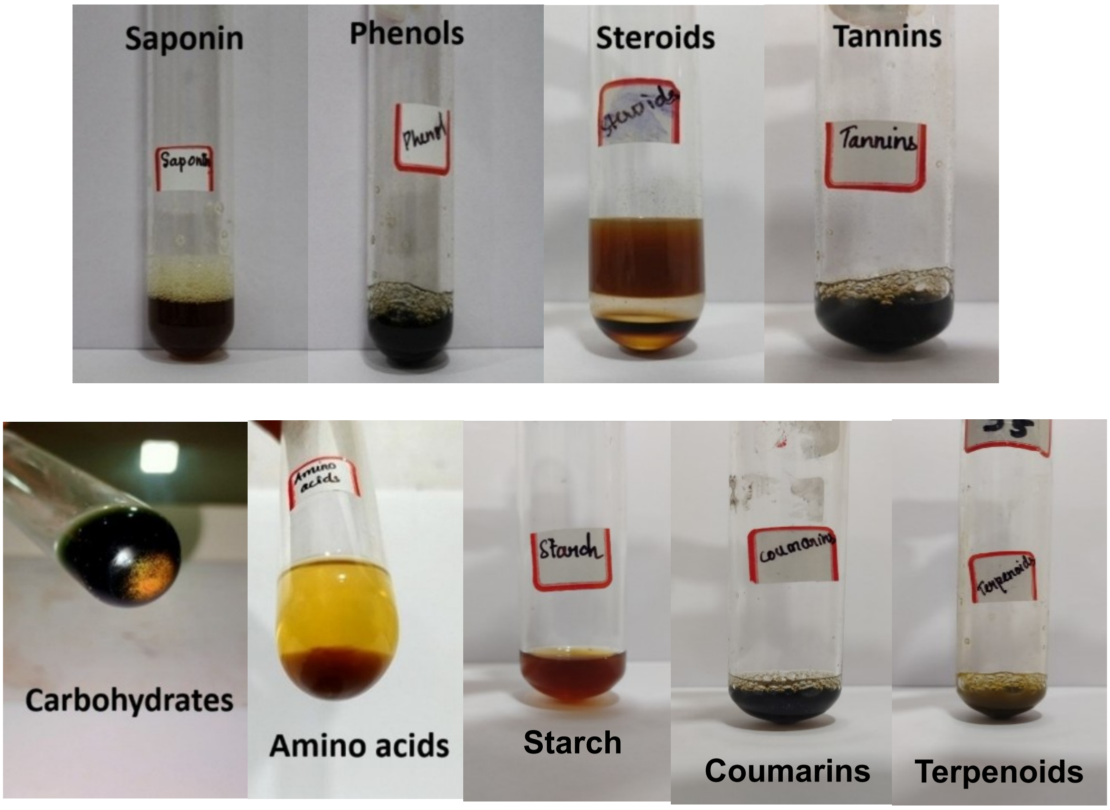

Fig 6.1 Phytochemical analysis of the aqueous extract of dried moringa leaves

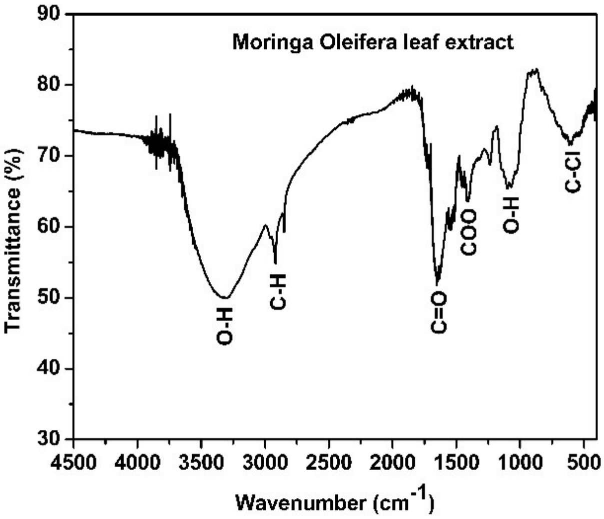

Fig 6.2 FTIR spectrum of the extract of dried moringa leaves

Some excerpts from the phytochemical analysis of the aqueous extract of dried moringa leaves are shown in figure 6.1. From the analysis, it is observed that phytochemicals such as saponins, phenols, tannins etc. were present in the aqueous extract, that in-turn helps in nanoparticle synthesis.

The FTIR spectrum of moringa leaf extract is taken (figure 6.2) and is observed that the organic bonds corresponding to the phytochemicals are present.

6.3.2 Green synthesis of pure $ZnAl_2O_4$

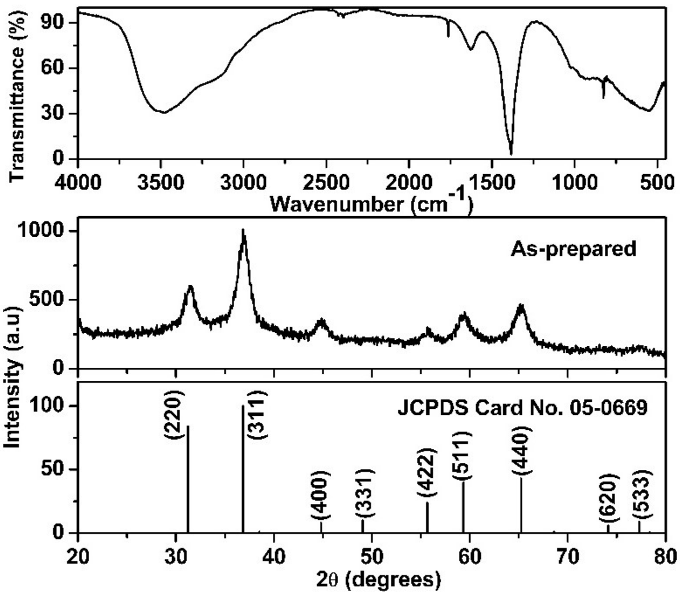

Fig 6.3 XRD and FTIR spectrum (top) of green synthesised $ZnAl_2O_4$

The XRD and FTIR spectra of as-prepared $ZnAl_2O_4$ via auto-combustion technique in the presence of moringa leaf extract is given in figure 6.3. The sample shows all the diffraction peaks corresponding to the planes of cubic $ZnAl_2O_4$. This affirms the possibility of ternary $ZnAl_2O_4$ spinel nanoparticle synthesis employing leaf extract assisted auto-combustion method, without the use of harmful chemical fuels.

The FTIR spectrum (figure 6.3) showed low intense bands below 1000 cm^{-1} corresponding to the vibration of metal-oxygen bonds. The existence of leftover NO_2 from the nitrate precursors explains the band at 1378 cm^{-1}, and the band at 1630 cm^{-1}

correspond to the OH group. The high intense band at 3500 cm^{-1} attributed to hydroxyl groups indicates the presence of moisture in the as-prepared sample, necessitating the need for post-heat treatments.

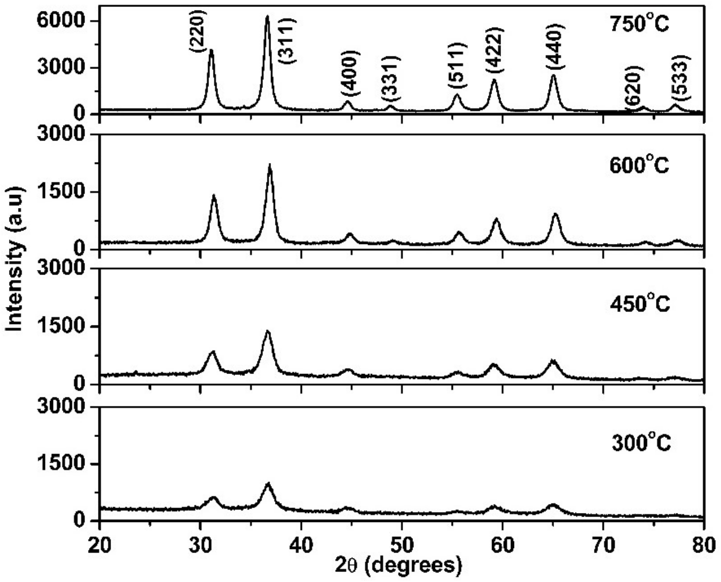

Fig 6.4 XRD patterns of pure ZnAl$_2$O$_4$ calcined between 300 – 750 °C

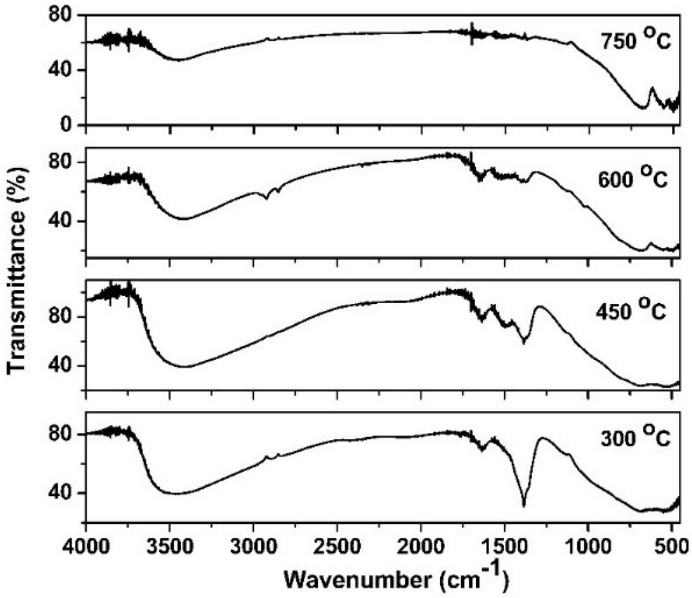

Fig 6.5 FTIR spectra of pure ZnAl$_2$O$_4$ calcined between 300 – 750 °C

On calcination at temperatures 300 – 750 ºC, the (311) peak intensity improves and becomes more sharper, as evident from the XRD spectra (figure 6.4). The bands between 1250 – 1750 cm^{-1} disappear on post-calcination. Also, the increase in intensity of the FTIR vibrational bands below 1000 cm^{-1} with calcination temperature (figure 6.5) correlates with the XRD results, affirming the improvement in crystallinity.

The crystallite size was calculated for all the samples from the FWHM of the main XRD peak (311) using Debye-Scherrer method, and compared with that obtained from Williamson-Hall analysis (table 6.2). The increase in crystallite size with post-calcination temperature could be due to the agglomeration of particles on heat treatment [13–15]. The lattice parameter of the sample calcined at 750 ºC, 8.078 Å, matches quite well with that of JCPDS data, 8.08 Å.

Sample	**(311) peak diffraction angle 2θ (degrees)**	**FWHM (degrees)**	**Crystallite size (nm)**		**Lattice parameter (Å)**
			D-S method	**W-H plot**	
As-prepared	36.894	1.369	6.118	6.754	8.072
300 ºC	36.691	1.260	6.643	6.699	8.108
450 ºC	36.659	1.219	6.866	7.122	8.112
600 ºC	36.635	0.766	10.925	11.021	8.118
750 ºC	36.887	0.918	9.124	10.267	8.078
JCPDS 05-0669					8.080

Table 6.2 Crystallite size, lattice parameter of green synthesised $ZnAl_2O_4$ before and after calcination

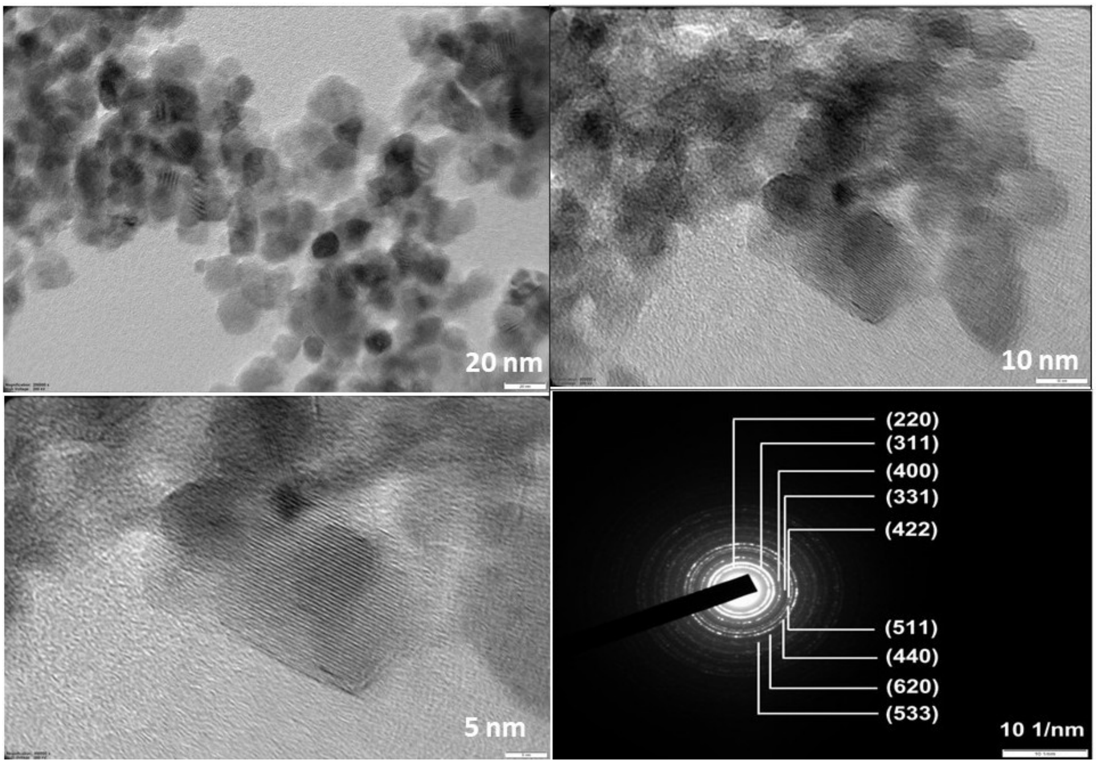

Fig 6.6 TEM images and SAED pattern of green sythesised $ZnAl_2O_4$ calcined at 750 ºC

The TEM analysis of $ZnAl_2O_4$ synthesised with moringa leaf extract, calcined at 750 ºC is presented in figure 6.6. From the SAED pattern, d-spacing of the crystal planes is measured and compared with that obtained from the XRD spectral analysis (table 6.3), showing excellent agreement. Hence, the structural purity is confirmed through TEM-SAED analysis. The particle size determined from the TEM image using the corresponding histogram (figure 6.7), is found to be 10.062 ± 1.152 nm. This value closely aligns with the crystallite size obtained from Scherrer formula and W-H plot, confirming the successful formation of $ZnAl_2O_4$ nanoparticles.

Miller indices of crystal plane (hkl)	d-spacing (Å)	
	From XRD	From SAED
(220)	2.850	2.859
(311)	2.435	2.445
(400)	2.019	2.037
(331)	1.854	1.846
(422)	1.649	1.668
(511)	1.555	1.561
(440)	1.429	1.444
(620)	1.277	1.285
(533)	1.233	1.234

Table 6.3 Comparison of interplanar spacing between crystal planes from XRD and SAED data of green sythesised $ZnAl_2O_4$ calcined at 750 °C

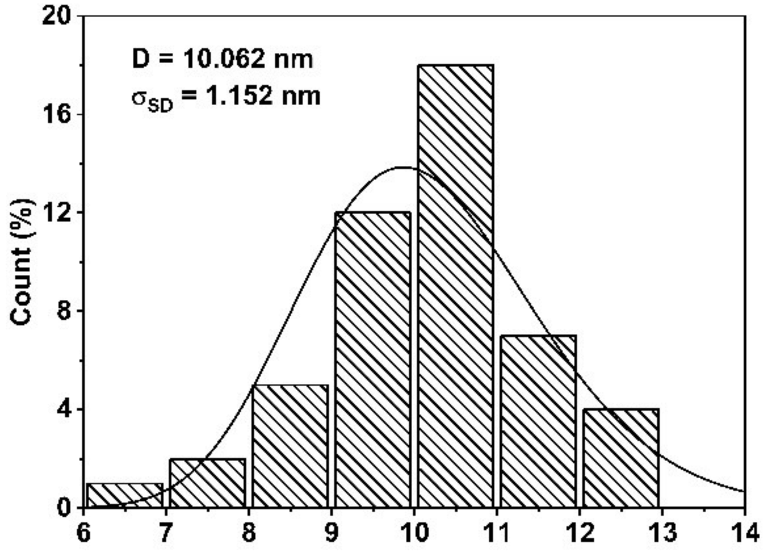

Fig 6.7 Histogram of green sythesised $ZnAl_2O_4$ calcined at 750 °C

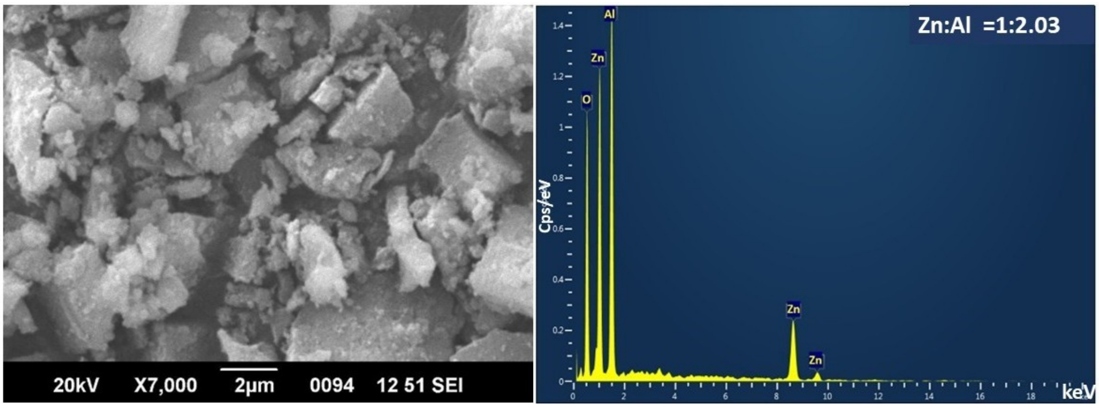

Fig 6.8 SEM and EDAX images of $ZnAl_2O_4$ after calcination at 750 °C

Figure 6.8 gives the SEM image and EDAX spectra of leaf extract assisted auto-combusted $ZnAl_2O_4$ calcined at 750 °C. The elemental composition obtained from the EDAX measurement is Zn:Al = 1:2.03, in well agreement with the expected ratio 1:2.

The DRS spectra and K-M plot is shown in figure 6.9, and the bandgap is obtained as 4.95 eV. A subbandgap at 3.22 eV may be attributed to defects or presence of binary oxides. The latter may be ruled out as XRD spectra (figure 6.4) doesn't reveal any indication of component oxide presence in the synthesised sample.

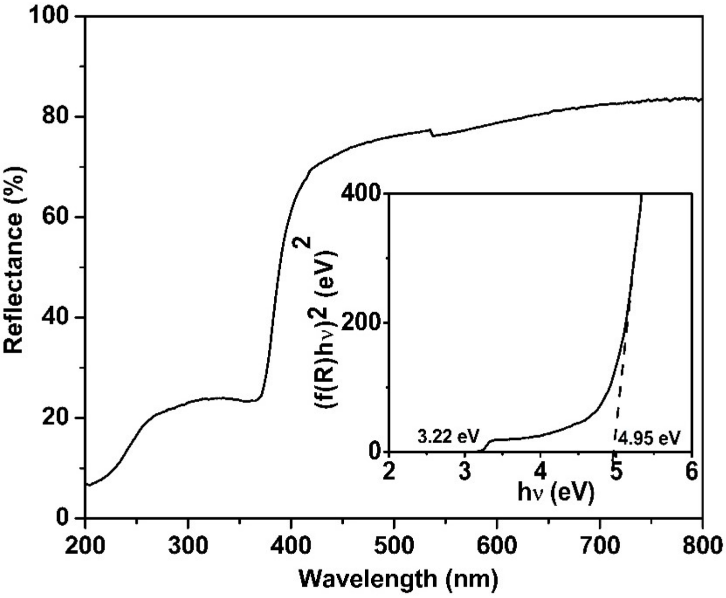

Fig 6.9 DRS spectrum and K-M plot (inset) of green synthesised $ZnAl_2O_4$ after calcination at 750 °C

6.3.3 Green synthesis of RE doped $ZnAl_2O_4$

After optimising the synthesis conditions of pure $ZnAl_2O_4$ via the green auto-combustion route, RE doping was tested in the host. The XRD spectra of 0.05 M concentrations of Eu^{3+} and Tb^{3+} singly doped zinc aluminate, $ZnAl_{1.95}O_4:Eu_{0.05}$ and $ZnAl_{1.95}O_4:Tb_{0.05}$ is depicted in figure 6.10. The intense and sharp diffraction peaks, indicative of the high crystallinity of the samples, exactly match with the standard JCPDS spectra of cubic $ZnAl_2O_4$ spinel. Though no additional or impure peaks are present in the diffraction graphs, doping is found to drop the intensity of the peaks (compared to figure 6.4). Additionally, the blue-shift of the peak maxima also confirms the incorporation of dopants into the zinc aluminate lattice.

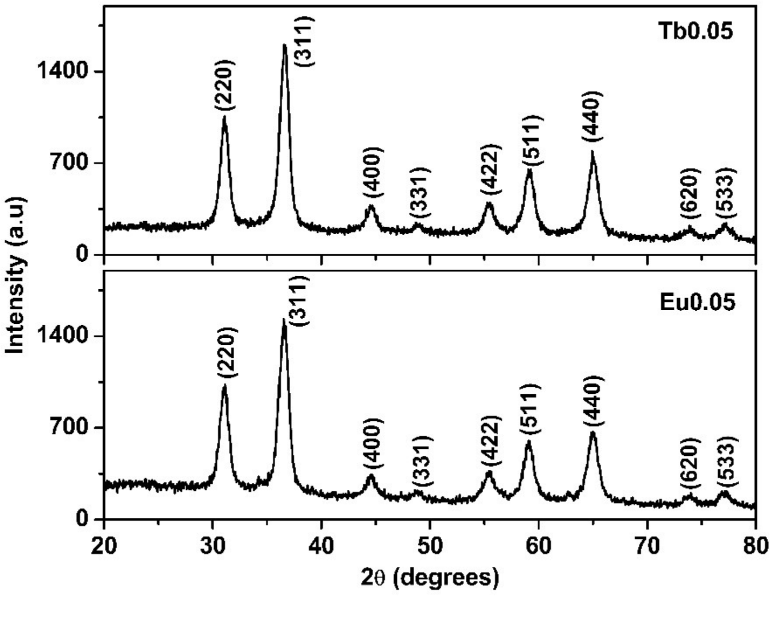

Fig 6.10 XRD sepctra of green synthesised $ZnAl_{1.95}O_4:RE_{0.05}$ (RE = Eu and Tb) calcined at 750 °C

Sample	**(311) diffraction peak 2θ (degrees)**	**FWHM (degrees)**	**Crystallite size (nm)**	**Lattice parameter (Å)**
Pure $ZnAl_2O_4$	36.887	0.918	9.124	8.078
$ZnAl_{1.95}O_4$:$Tb_{0.05}$	36.608	0.971	8.622	8.135
$ZnAl_{1.95}O_4$:$Eu_{0.05}$	36.548	1.056	7.920	8.148

Table 6.4 Crystallite size, FWHM and lattice parameter of pure and doped samples

The average crystallite size was calculated using Scherrer formula for the (311) peak and compared with that of the undoped matrix (table 6.4). The broadening of the (311) peak along with the shift to lower angles contributes to the decrease in crystallite size on doping. Lattice parameter, obtained from the first order diffraction formula, shows an increase on doping. This lattice expansion, expected due to the larger ionic size of dopant ions than the host cations, also indicates the successful incorporation of dopant ions into the host matrix.

Figure 6.11 depicts the room temperature PL emission spectra of pure $ZnAl_2O_4$ and $ZnAl_{1.95}O_4$:$Eu_{0.05}$ recorded at an excitation wavelength of 250 nm. The sample fluoresces in the red region of the em spectrum, attributed to the the crystal field enhanced $^5D_0 \rightarrow {}^7F_j$ (j = 0 – 4) transitions of Eu^{3+} ions. The lowering of the bluish host emission and subsequent increase in dopant emission confirms the host-sensitised luminescent response of the sample, as observed in co-precipitated and hydrothermally synthesized Eu doped samples. The presence of the highly intense crystal field enhanced electric dipole $^5D_0 \rightarrow {}^7F_2$ peak at 615 nm further confirms the Eu^{3+} ion incorporation at the highly distorted octahedral Al^{3+} sites of the spinel lattice.

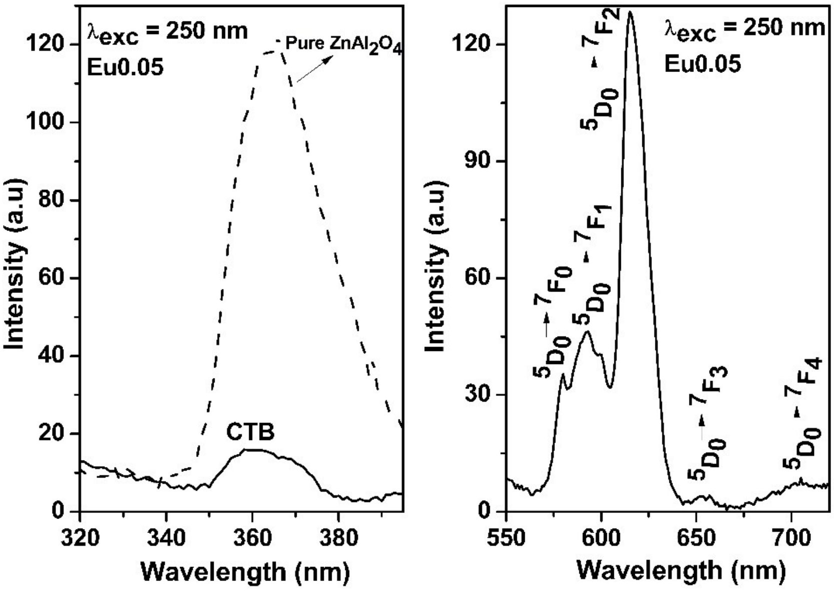

Fig 6.11 PL emission spectra of green synthesised $ZnAl_{1.95}O_4:Eu_{0.05}$

The Tb^{3+} doped sample emits in the green region, peak maximum at 544 nm, when excited at 235 nm (figure 6.12). The intense magnetic dipole $^5D_4 \rightarrow {}^7F_5$ transition approves of the fact that Tb^{3+} ions are predominantly substituted into the Al^{3+} octahedral sites. The drop in the intensity of the host emission and subsequent increase in dopant emission confirms the host-sensitised energy transfer to the activator ions. In contrary to earlier methods, in auto-combustion method, the red emission is more intense compared to the green emission.

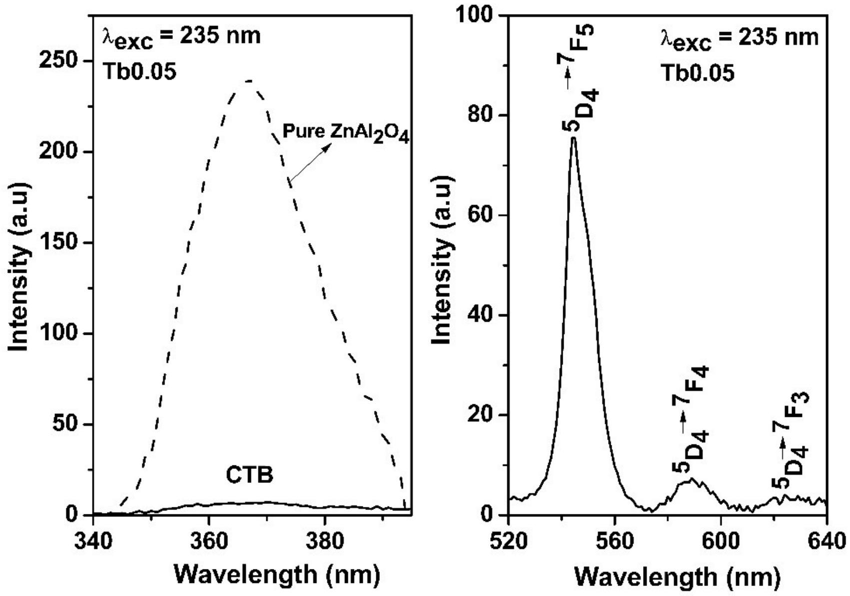

Fig 6.12 PL emission spectrum of green synthesised $ZnAl_{1.95}O_4:Tb_{0.05}$

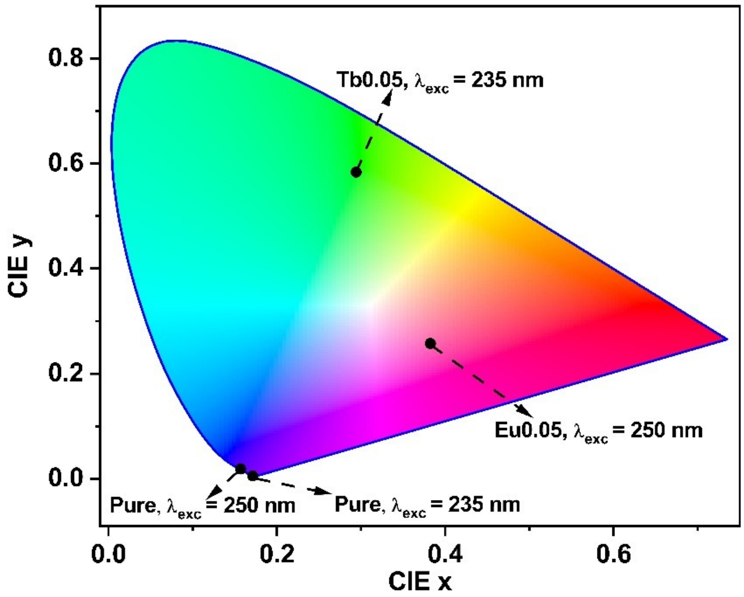

Fig 6.13 CIE chromaticity diagram of green synthesised $ZnAl_{1.95}O_4:Eu_{0.05}/Tb_{0.05}$

The colorimetric cordinates corresponding to the emissions of pure and doped samples were calculated and depicted on a CIE diagram (figure 6.13). The pure sample emits in blue region with CIE coordinates (0.171,0.006) and (0.157,0.019) respectively for 235 and 250 nm excitations, with 99 % of color purity. The CIE (x, y) for the green and red emissions were determined to be (0.294, 0.584) and (0.382, 0.258) with color purities 65.44 and 38.25 % respectively.

Both the undoped and doped zinc aluminate matrices were successfully prepared using the moringa leaf extract assisted green combustion route. Now, the co-doped effect of RE dopants into the zinc aluminate matrix was investigated. Three samples of $ZnAl_2O_4$, simultaneously doped with Eu^{3+} and Tb^{3+}, were synthesized via the auto-combustion route, with x:y = 1:3, 1:1 and 3:1. XRD patterns are shown in figure 6.14. The spectra for all samples align with the standard JCPDS pattern of cubic $ZnAl_2O_4$. The absence of additional peaks indicates that the crystalline structure remains intact.

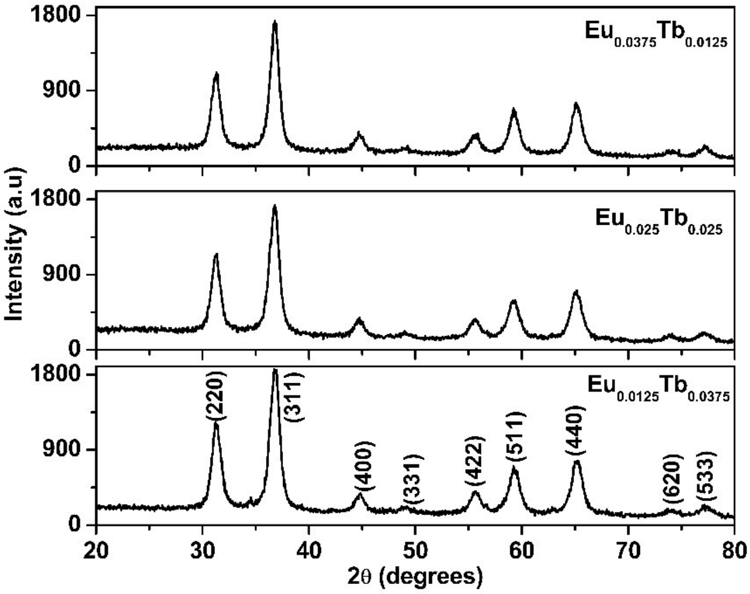

Fig 6.14 XRD spectra of green synthesised $ZnAl_{1.95}O_4:Eu_xTb_y$

Sample	(311) Peak diffraction angle (degrees)	FWHM (degrees)	Crystallite size (nm)	Lattice parameter (Å)
$Eu_{0.0375}$ $Tb_{0.0125}$	36.783	0.998	8.389	8.112
$Eu_{0.025}$ $Tb_{0.025}$	36.732	1.102	7.593	8.100
$Eu_{0.0125}$ $Tb_{0.0375}$	36.779	1.070	7.822	8.091

Table 6.5 Crystallite size and lattice parameter of green $ZnAl_{2-(x+y)}O_4:Eu_xTb_y$

The broadened diffraction peaks justify the incorporation of the dopants into the lattice, eventually leading to lattice expansion. Crystallite sizes and lattice parameters were calculated and tabulated (see table 6.5).

The PL emission spectra of $ZnAl_{2-(x+y)}O_4:Eu_xTb_y$, as for singly doped samples, were recorded for two exciation wavelengths 230 and 250 nm as shown in figure 6.15 and 6.16 respectively. The peak splitting of the host emission is more evident in these samples, peak wavelengths shifting between 361 and 372 nm.

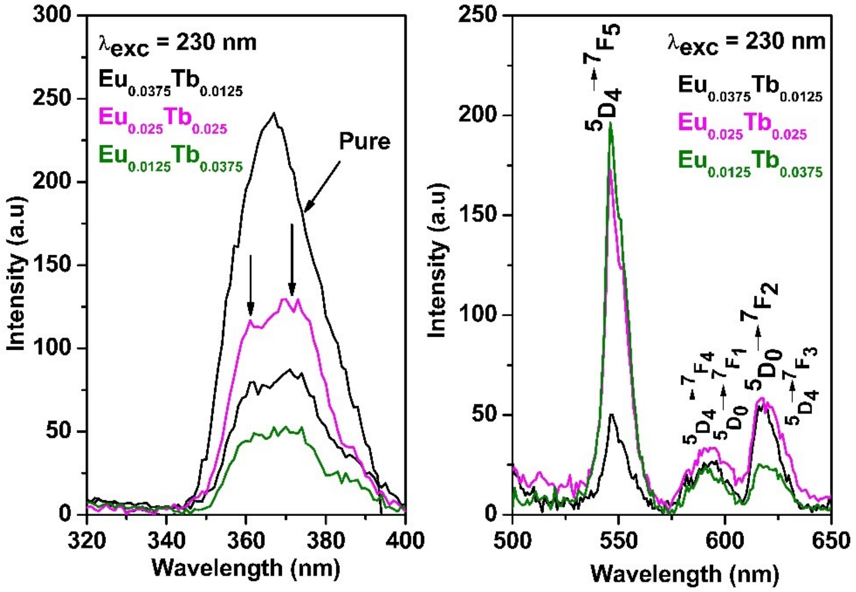

Fig 6.15 PL emission spectra of $ZnAl_{2-(x+y)}O_4:Eu_xTb_y$ recorded at $\lambda_{exc} = 230$ nm

The high intense bands, corresponding to $^5D_4 \rightarrow {}^7F_5$ transition of Tb^{3+} ion (544 nm) and $^5D_0 \rightarrow {}^7F_2$ transition of Eu^{3+} ion (618 nm), appear in mixed proportions along with the smaller bands, which alters in intensity with dopant ratio and excitation wavelengths. Only the sample with Eu/Tb ratio 3:1 at 230 nm shows a deviation in its luminescent response, for which the host emission overdoes the activator emissions. In all other cases, compared to the charge transfer band of the host, the bluish emissions reduced in intensity with a simultaneous increase in dopant ion emission. This reflects the host-sensitised emission in these samples.

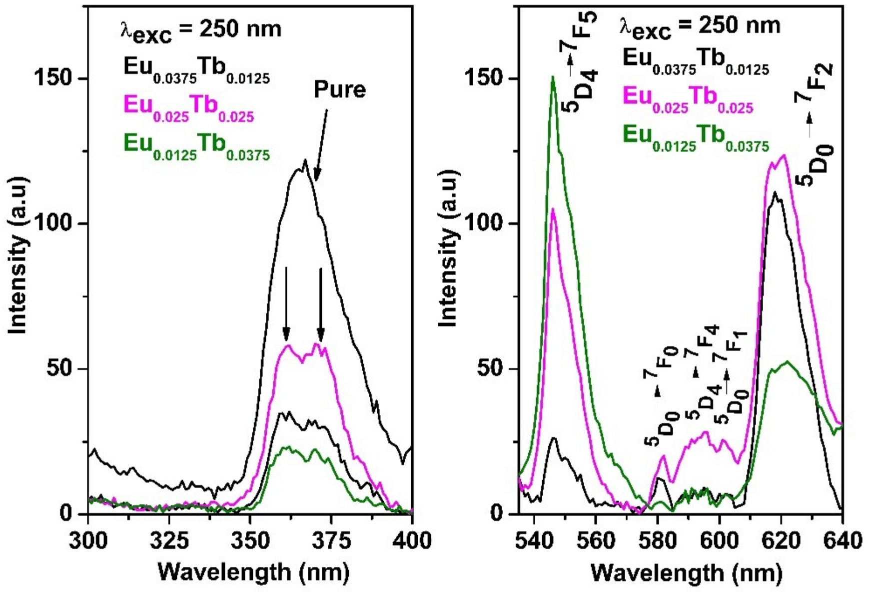

Fig 6.16 PL emission spectra of $ZnAl_{2-(x+y)}O_4:Eu_xTb_y$ recorded at $\lambda_{exc} = 250$ nm

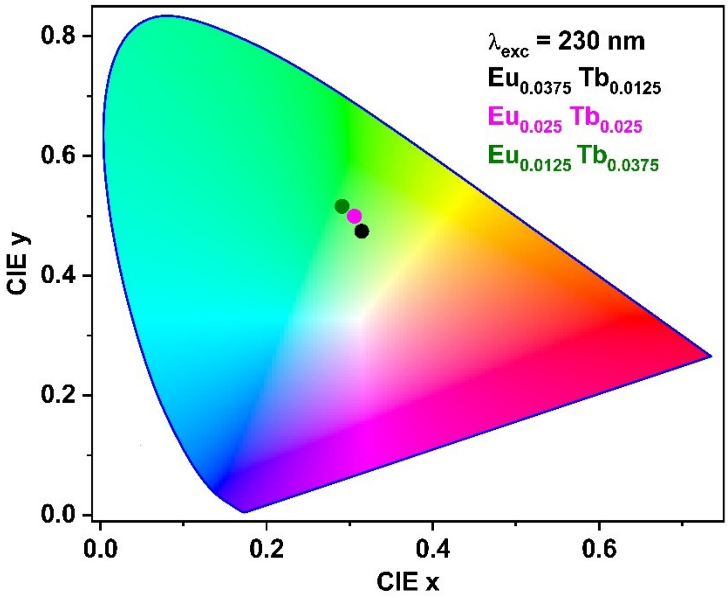

Fig 6.17 CIE color chromaticity diagram at 230 nm excitation for various Eu/Tb concentration ratio of green synthesised $ZnAl_{2-(x+y)}O_4:Eu_xTb_y$

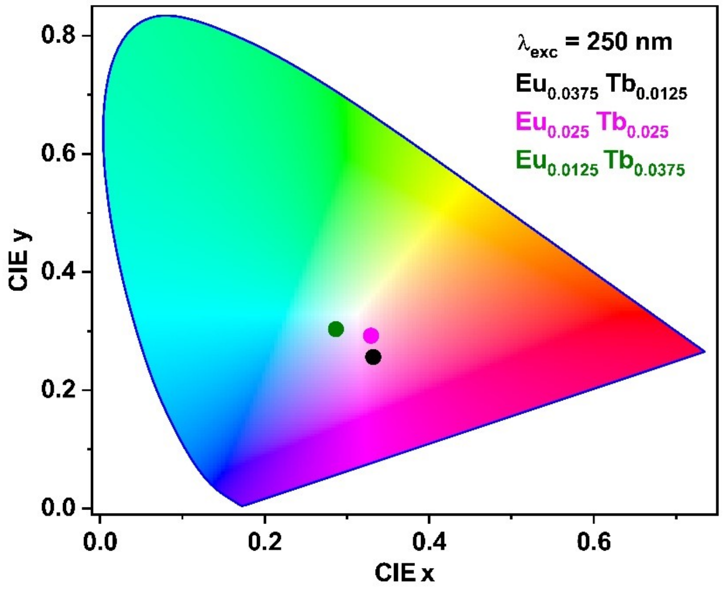

Fig 6.18 CIE color chromaticity diagram at 250 nm excitation for various Eu/Tb concentration ratio of green synthesised $ZnAl_{2-(x+y)}O_4:Eu_xTb_y$

Sample	CIE					
	230 nm			250 nm		
	x	y	Color purity	x	y	Color purity
Eu0.0375 Tb0.0125	0.314	0.474	38.68	0.332	0.256	29.62
Eu0.025 Tb0.025	0.306	0.499	43.97	0.329	0.292	15.13
Eu0.0125 Tb0.0375	0.291	0.516	44.94	0.286	0.304	17.39

Table 6.6 CIE color coordinates of green synthesised $ZnAl_{2-(x+y)}O_4:Eu_xTb_y$

To know the color purity of emissions, chromaticity diagram was plotted at the different excitation wavelengths, 230 nm (figure 6.17) and 250 nm (figure 6.18). Table 6.6 presents the calculated colorimetric coordinates. The emissions turn yellowish as Eu/Tb ratio increases at 230 nm. But at 250 nm, near-white emission is obtained at 1:1 and 1:3 Eu/Tb ratios, with 15 % and 17 % color purity respectively.

6.3.4 Green synthesis of other AB_2O_4 spinel systems

The successful synthesis of zinc aluminate spinel using the green synthesis route opens a new method of synthesis for ternary spinel oxides. Hence, the feasibility of the same is checked for the other spinel systems, namely $MgAl_2O_4$, $ZnCr_2O_4$ and $MgCr_2O_4$. Several groups have used the sol-gel synthesis route for preparing $MgCr_2O_4$ [16–18] and $ZnCr_2O_4$ [19,20]. N. Mayedwa et al. reported an aqueous synthesis of $ZnCr_2O_4$ mixed oxide nanoparticulate growth using Hibiscus Rosa Sinensis leaf extract [21]. Sanjay R. Thakare et al. reported the green synthesis of $ZnCr_2O_4$ nanosheets for degradation of methylene blue [19].

XRD patterns of $MgAl_2O_4$, prepared using the moringa leaf extract via auto-combustion technique, was monitored in the range of 20−80° angle is shown in figure 6.19. It can be noted that the nucleation could be initiated even under as-prepared conditions, and the sample exhibited the major spinel diffraction peaks indexed to (220), (311), (400), (422), (511), and (440) crystal planes, on post-calcination at 750 °C for 2 hours. The pattern was in agreement to the standard pattern of cubic $MgAl_2O_4$ spinel JCPDS file No. 21-1152 [22].

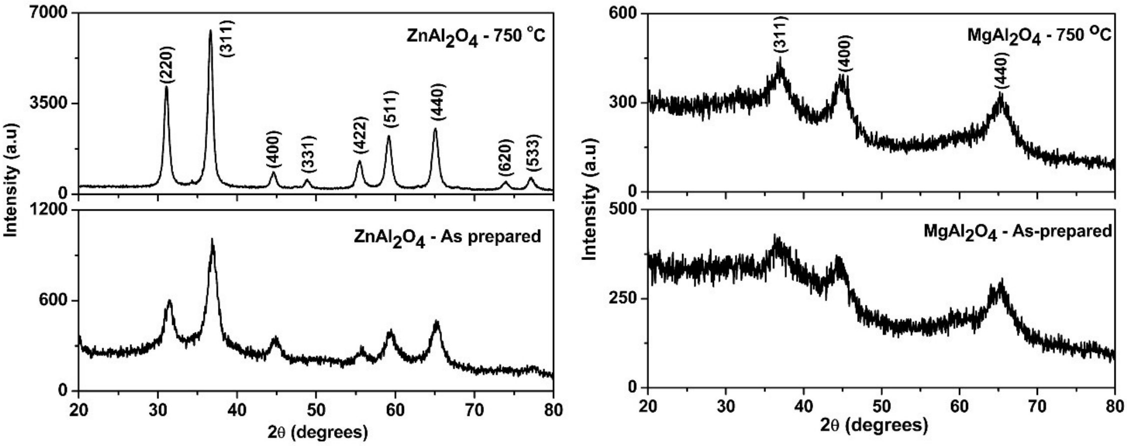

Fig 6.19 XRD spectra of as-synthesised and 750 °C post-calcined $ZnAl_2O_4$ and $MgAl_2O_4$

Compared to $ZnAl_2O_4$, a shift in 2θ value (table 6.7) could be attributed to the development of strain in the c-axis orientation on the account of Mg^{2+} ions substitution in the place of Zn^{2+} ions. The broadness of the peaks also increases compared with $ZnAl_2O_4$ lattice indicative of lattice distortion and subsequent fall in crystallinity. The crystallite size and lattice parameter of the matrix is also given in table 6.7.

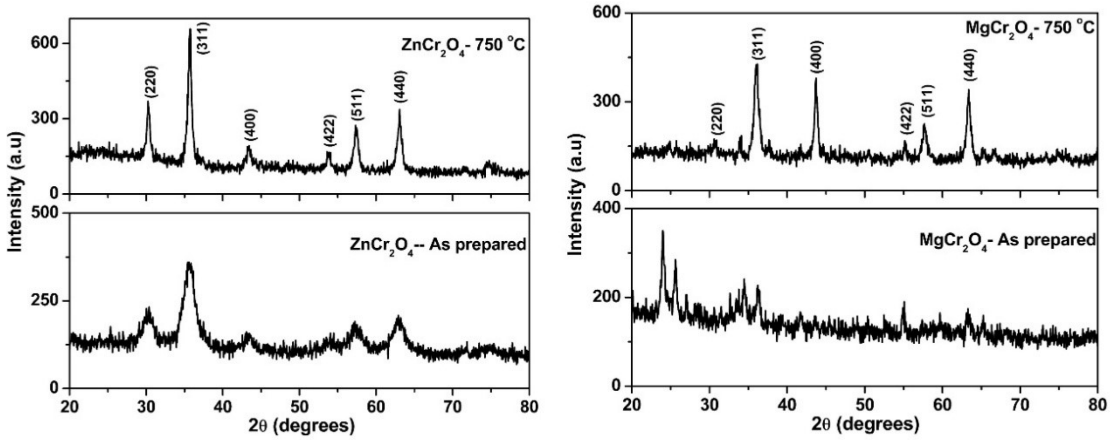

Fig 6.20 XRD spectra of as-prepared and 750 ºC post-calcined $ZnCr_2O_4$ and $MgCr_2O_4$

The XRD spectra of as-prepared $ZnCr_2O_4$ and $MgCr_2O_4$ via auto-combustion method are depicted in figure 6.20. The method is successful in growing $ZnCr_2O_4$ even without any post-calcination, but only nucleation could be initiated for $MgCr_2O_4$. Upon calcination at 750 ºC, the structure becomes more crystalline which is visible from the increase in X-ray diffraction intensity. The patterns could be indexed to the respective (hkl) planes, as per standard JCPDS Card No. 22-1107 for $ZnCr_2O_4$ and JCPDS Card No. 82-1529 for $MgCr_2O_4$ [16,17].

Crystallite size increases on replacing Al^{3+} with Cr^{3+} due to larger ionic radius of Cr^{3+} ions (62 pm) than Al^{3+} ions (53 pm) and decreases on replacing Zn^{2+} ions (74 pm) with Mg^{2+} ions (72 pm)., since the ionic radius of Zn^{2+} is larger than that of Mg^{2+}. This is because larger ions cause greater strain and distortion at a lattice site, leading to expansion of the crystal structure, which in turn facilitates growth of larger crystallites during synthesis. The crystallite size and lattice parameter of these matrices are determined and listed in table 6.7.

Sample	(311) peak diffraction angle (degrees)	Crystallite size (nm)	Lattice parameter (Å)
$ZnAl_2O_4$	36.887	9.124	8.078
$MgAl_2O_4$	36.988	2.514	8.118
$ZnCr_2O_4$	35.691	14.798	8.337
$MgCr_2O_4$	36.049	11.669	8.257

Table 6.7 Crystallite size and lattice parameter of $ZnAl_2O_4$, $MgAl_2O_4$, $ZnCr_2O_4$ and $MgCr_2O_4$

The FTIR spectra (Figure 6.21) shows vibrational bands between 700 and 400 cm^{-1}, which indicates the metal-oxygen bands in the materials [19]. Generally, ternary aluminates exhibit the 3300 – 3500 cm^{-1} wide absorption band corresponding to hydroxyl group, indicative of water content in these samples than chromates. Also, there is a presence of C=C and C=O bond vibrations at 1630 and 1650 cm^{-1} in samples other than zinc aluminate, indicating a small amount of left over plant extract. The presence of band at 1120 cm^{-1} only in the case of chromates indicates the Cr-O vibrations which may be due to the impurities present in the spinel associated with the chromium precursors. However, FTIR analyses confirm that ternary AB_2O_4 systems can be effectively synthesised using this green approach mediated by moringa plant extract.

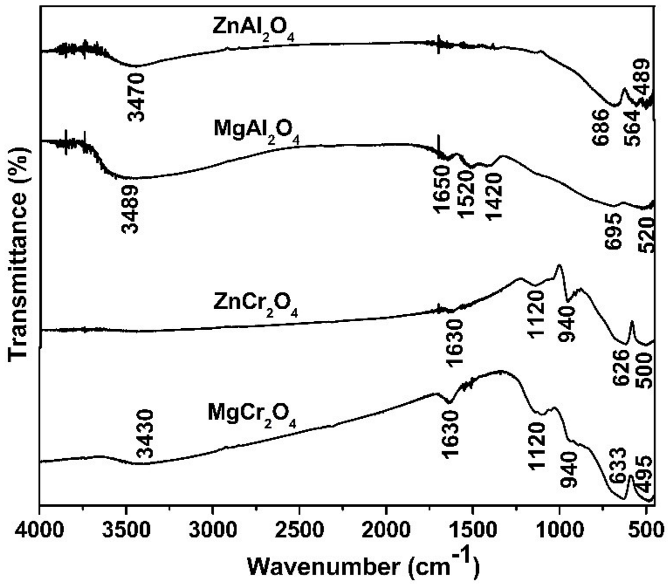

Fig 6.21 FTIR spectra of 750 °C calcined $ZnAl_2O_4$, $MgAl_2O_4$, $ZnCr_2O_4$ and $MgCr_2O_4$

The optical bandgap of these samples was calculated from DRS data analysis. For $MgAl_2O_4$, the bandgap was obtained as 5.25 eV (figure 6.22), which is more than zinc aluminate, proving the theory of quantum confinement in which less crystallites have higher bandgaps.

Unlike aluminates, it was observed that the reflectance decreased for chromate samples (figure 6.22), which was quite evident from their colored appearance. The bandgap was calculated using the Kubelka-Munk function, resulting in values of 3.07 eV for $ZnCr_2O_4$ and 3.77 eV for $MgCr_2O_4$, the smaller bandgap values may be attributed to higher density of defect levels in these samples [18,20].

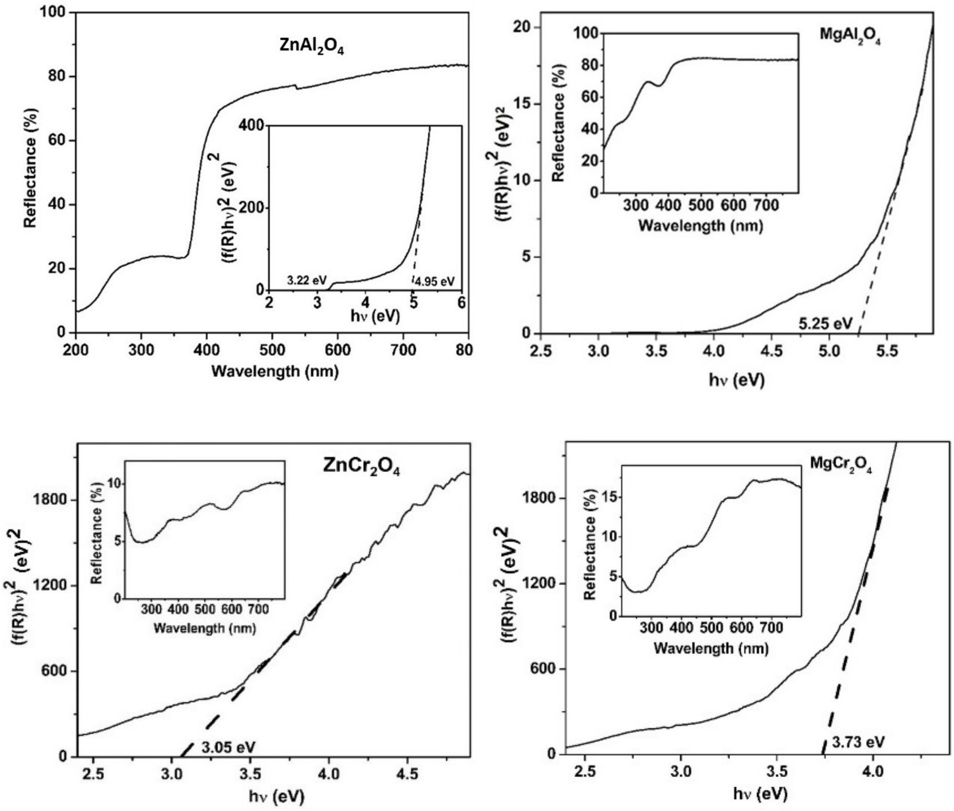

Fig 6.22 DRS spectra and K-M plot (inset) of green synthesised AB_2O_4 systems

6.4 Conclusions

Pure, singly doped, and co-doped $ZnAl_2O_4:RE^{3+}$ (RE = Eu, Tb) nanophosphors could be successfully synthesized using a novel Moringa leaf extract-assisted auto-combustion method. Phase formation could be seen in as-synthesised samples. Post-synthesis heat treatments need be done only to improve crystallinity and performance. The green synthesis approach is environment friendly, with low hazardous waste and eliminates the need for toxic chemical fuels. TEM measurements were in excellent match with the average crystallite size, calculated from the (311) diffraction peak using Scherrer equation and W–H analysis.

Doping with rare-earth ions resulted in reduced crystallite size and increased lattice parameter compared to the pure sample. The PL spectrum revealed the inherent violet-blue luminescence of the host. The green emission for Tb^{3+} doped, and red emission for Eu^{3+} doped $ZnAl_2O_4$, was attributed to arise from a host-sensitised energy transfer to the activator site. Co-doping with Eu^{3+} and Tb^{3+} led to structural changes visible in the XRD patterns and resulted in photoluminescence with chromaticity coordinates confirming near-white luminescent emission, when excited at 250 nm. This indicates the potential for achieving white-light-emitting phosphors from a single $ZnAl_2O_4$ host using the novel green synthesis route.

Using the same synthesis route, other AB_2O_4 spinel systems such as $MgAl_2O_4$, $ZnCr_2O_4$, and $MgCr_2O_4$ could also be prepared. XRD and FTIR analyses confirmed the formation of phase-pure crystalline materials.

References

[1] Al-Radadi, N. S. (2019). Green synthesis of platinum nanoparticles using Saudi's dates extract and their usage on the cancer cell treatment. *Arabian Journal of Chemistry, 12*(3), 330–349. https://doi.org/10.1016/j.arabjc.2018.05.008

[2] Ahmed, S., Saifullah, Ahmad, M., Swami, B. L., & Ikram, S. (2016). Green synthesis of silver nanoparticles using *Azadirachta indica* aqueous leaf extract. *Journal of Radiation Research and Applied Sciences, 9*(1), 1–7. https://doi.org/10.1016/j.jrras.2015.06.006

[3] Kora, A. J., & Rastogi, L. (2018). Green synthesis of palladium nanoparticles using gum ghatti (*Anogeissus latifolia*) and its application as an antioxidant and catalyst. *Arabian Journal of Chemistry, 11*(7), 1097–1106. https://doi.org/10.1016/j.arabjc.2015.06.024

[4] Aziz, W. J., & Jassim, H. A. (2018). A novel study of pH influence on Ag nanoparticles size with antibacterial and antifungal activity using green synthesis. *World Scientific News, 97*, 139–152. http://www.worldscientificnews.com

[5] Kuppusamy, P., Yusoff, M. M., Maniam, G. P., & Govindan, N. (2016). Biosynthesis of metallic nanoparticles using plant derivatives and their new avenues in pharmacological applications – An updated report. *Saudi Pharmaceutical Journal, 24*(4), 473–484. https://doi.org/10.1016/j.jsps.2014.11.013

[6] Zhang, D., Ma, X. L., Gu, Y., Huang, H., & Zhang, G. W. (2020). Green synthesis of metallic nanoparticles and their potential applications to treat cancer. *Frontiers in Chemistry, 8*, 799. https://doi.org/10.3389/fchem.2020.00799

[7] Kharissova, O. V., Dias, H. V. R., Kharisov, B. I., Pérez, B. O., & Pérez, V. M. J. (2013). The greener synthesis of nanoparticles. *Trends in Biotechnology, 31*(4), 240–248. https://doi.org/10.1016/j.tibtech.2013.01.003

[8] Yuvasravana, R., George, P. P., & Devanna, N. (2017). Synthesis and characterization of spinel metal aluminate by a simple microwave assisted green synthesis. *Materials Today: Proceedings, 4*(11), 10664–10671. https://doi.org/10.1016/j.matpr.2017.08.012

[9] Bobade, D. S., & Undre, P. B. (2020). Synthesis and characterization of nanomaterials. *Journal of Physics: Conference Series, 1644*, 012032. https://doi.org/10.1088/1742-6596/1644/1/012032

[10] Haris, Z., & Ahmad, I. (2024). Green synthesis of silver nanoparticles using *Moringa oleifera* and its efficacy against gram-negative bacteria targeting quorum sensing and biofilms. *Journal of Umm Al-Qura University for Applied Sciences, 10*(2), 156–167. https://doi.org/10.1007/s43994-023-00089-8

[11] Mohammed, G. M., & Hawar, S. N. (2022). Green biosynthesis of silver nanoparticles from *Moringa oleifera* leaves and its antimicrobial and cytotoxicity activities. *International Journal of Biomaterials, 2022*, 4136641. https://doi.org/10.1155/2022/4136641

[12] Gangula, A., Podila, R., M., R., Karanam, L., Janardhana, C., & Rao, A. M. (2011). Catalytic reduction of 4-nitrophenol using biogenic gold and silver nanoparticles derived from *Breynia rhamnoides*. *Langmuir, 27*(24), 15268–15274. https://doi.org/10.1021/la2034559

[13] Kumar, K. V., & Bhavani, S. D. (2023). Effect of calcination temperature on structural and optical properties of nickel aluminate nanoparticles. *East European Journal of Physics, 2023*(3), 355–362. https://doi.org/10.26565/2312-4334-2023-3-37

[14] Puspitasari, P., Rizkia, U. A., Sukarni, S., Permanasari, A. A., Taufiq, A., & Putra, A. B. N. R. (2021). Effects of various sintering conditions on the structural and magnetic properties of zinc ferrite ($ZnFe_2O_4$). *Materials Research, 24*(1), e20200300. https://doi.org/10.1590/1980-5373-MR-2020-0300

[15] Sangeetha, A., Kumar, K. V., & Kumar, G. N. (2017). Effect of annealing temperature on the structural and magnetic properties of $NiFe_2O_4$ nanoferrites.

Advances in Materials Physics and Chemistry, 7(2), 19–27. https://doi.org/10.4236/ampc.2017.72003

[16] Ghotekar, S., Pansambal, S., Nguyen, V. H., Bangale, S., Lin, K. Y. A., Murthy, H. C. A., & Oza, R. (2023). Spinel $ZnCr_2O_4$ nanorods synthesized by facile sol-gel auto combustion method with biomedical properties. *Journal of Sol-Gel Science and Technology, 105*(1), 176–185. https://doi.org/10.1007/s10971-022-05964-0

[17] Jafarnejad, E., Khanahmadzadeh, S., Ghanbary, F., & Enhessari, M. (2016). Synthesis, characterization and optical band gap of pirochromite ($MgCr_2O_4$) nanoparticles by stearic acid sol-gel method. *Current Chemistry Letters, 5*(4), 173–180. https://doi.org/10.5267/j.ccl.2016.7.001

[18] Mykhailovych, V., Kanak, A., Cojocaru, Ş., Chitoiu-Arsene, E. D., Palamaru, M. N., Iordan, A. R., Korovyanko, O., Diaconu, A., Ciobanu, V. G., Caruntu, G., Lushchak, O., Fochuk, P., Khalavka, Y., & Rotaru, A. (2021). Structural, optical, and catalytic properties of $MgCr_2O_4$ spinel-type nanostructures synthesized by sol–gel auto-combustion method. *Catalysts, 11*(12), 1476. https://doi.org/10.3390/catal11121476

[19] Thakare, S. R., & Gawande, S. B. (2020). Green synthesis of novel $ZnCrO_4$ nanosheets for photocatalytic degradation: A new catalyst. *Materials Science for Energy Technologies, 3*, 719–727. https://doi.org/10.1016/j.mset.2020.08.003

[20] Dumitru, R., Manea, F., Păcurariu, C., Lupa, L., Pop, A., Cioablă, A., Surdu, A., & Ianculescu, A. (2018). Synthesis, characterization of nanosized $ZnCr_2O_4$ and its photocatalytic performance in the degradation of humic acid from drinking water. *Catalysts, 8*(5), 210. https://doi.org/10.3390/catal8050210

[21] Mayedwa, N., Mulaudzi-Masuku, T., Matinise, N., & Nkosi, M. (2019). Biosynthesis and characterization of multifunctional mixed oxides of $ZnCr_2O_4$/$ZnCrO_4$ nanoparticulate from natural leaf extracts of *Hibiscus rosa-sinensis*. *Materials Today: Proceedings, 36*, 309–312. https://doi.org/10.1016/j.matpr.2020.04.108

[22] Goswami, B., Rani, N., Vats, R., Bhukkal, C., & Ahlawat, R. (2021). Highly crystalline and narrow bandgap $MgAl_2O_4$: Synthesis and characterization. *AIP Conference Proceedings, 2352*(1), 050019. https://doi.org/10.1063/5.0052473

Chapter 7

PHOTO-CATALYTIC, CYTOTOXIC AND ANTI-BACTERIAL RESPONSES OF SELECTED SYSTEMS

This chapter discusses the photocatalytic activity of $ZnAl_2O_4$ *synthesized via co-precipitation against methylene blue dye, the effect of catalyst concentration and pH on catalytic degradation, in particular. Also, the activity of* $ZnAl_2O_4$ *synthesized via hydrothermal and Moringa leaf extract assisted auto-combustion methods towards the dye under similar conditions are compared. The in-vitro cytotoxic response of* $ZnAl_2O_4$ *synthesized via the three methods against normal spleen cells and Dalton's lymphoma ascites cells from the peritoneal cavity of tumour bearing mice is presented. The anti-bacterial activity against E-Coli bacteria and in-vitro cytotoxic response of* AB_2O_4 *(A = Zn, Mg and B = Al, Cr) matrices synthesized via auto-combustion is also compared.*

The ternary spinel oxide nanoparticles are viable candidates for diverse applications in the fields of photo-electronics, catalysis, biomedicine, sensors etc. The wide and tunable bandgap, along with the possibility of doping with different RE elements at A or B cationic sites, make them perfect as luminescent materials. Alternately, the high chemical and thermal stability, high surface to volume ratio, enhanced surface properties of spinel nanoparticles find applications in various other fields. The present chapter discusses the photo-catalytic, cytotoxic, and anti-bacterial responses of selected spinel aluminate and chromate systems, luminescent responses of singly and co-doped systems being discussed in previous chapters.

7.1 Pristine $ZnAl_2O_4$ as a photo-catalyst

Zinc aluminate in its bulk form, with a wide bandgap in the range 3.8 - 4 eV, and good thermal and chemical stability, is expected to have a good response to light [1–5]. In our work, we have successfully synthesized nano - zinc aluminate matrix via co-precipitation (ZAO-CP), hydrothermal (ZAO-HY) and green auto-combustion (ZAO-AU) routes. This chapter discusses the photocatalytic activity of pure $ZnAl_2O_4$ towards the catalytic degradation of methylene blue (MB) dye. Methylene blue is an organic dye commonly used in textile industries, and is a major contributor to water pollution. Photocatalysis is a green and cost-effective approach for pollutant removal, hence the potential of synthesized $ZnAl_2O_4$ is evaluated in this context.

2 ppm concentration of methylene blue dye solution was prepared in distilled water. Prior to photo irradiation under sunlight, the suspension was stirred for 45 minutes in dark to establish adsorption equilibrium. Subsequently in every 45 minutes, 3 ml of the aliquots were centrifuged and the UV- visible absorption spectrum was recorded (figure 7.1). From the absorption spectra of all the samples, degradation (%) was calculated.

$$Degradation\ (\%) = \frac{(A_0 - A)}{A_0} \times 100,$$

where A_0 is the absorbance maximum before illumination and A is the absorbance maximum at regular time intervals after illumination.

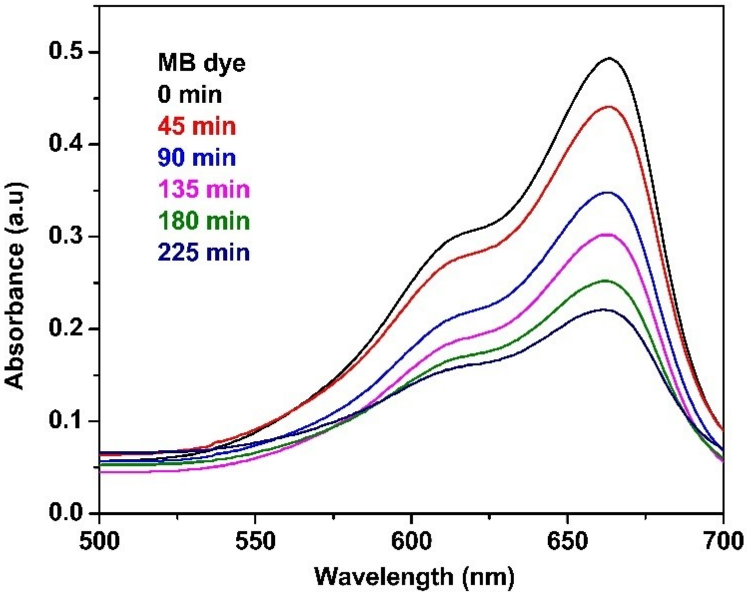

Fig 7.1 Absorbance spectra of methylene blue (MB) dye

The procedure was repeated with 2 ppm of dye solution mixed with the sample as a photocatalyst. The concentration of zinc aluminate (ZAO-CP), prepared via co-precipitation method, was varied from 0.04 - 0.13 grams. The absorbance spectra are shown in figure 7.2.

The degradation (%) obtained from the absorbance spectra was plotted as a function of time in figure 7.3. Figure 7.3 also depicts the degradation (%) versus catalyst concentration after light exposure for 225 minutes. It was observed that as the concentration of $ZnAl_2O_4$ catalyst increases, the photocatalytic activity initially improves, reaching a maximum of 74.89 % at 0.1 g, after which it declines. The initial rise in degradation (%) is attributed to the increased availability of active sites on the catalyst surface, leading to more hydroxyl radicals generated through light interaction. However, beyond 0.1 g, the % of degradation drops significantly due to reduced hydroxyl radical formation. This decline is likely caused by limited light penetration in the suspension due to the shielding effect at higher catalyst loadings. Catalyst concentration influences both the number of active sites and the ability of light to reach them. While more catalyst provides additional active sites, excessive amounts can block light, diminishing photocatalytic performance [6,7]. It's also important to note that the optimal catalyst loading depends on the choice of the dye, its initial concentration, and the operating conditions of the photoreactor.

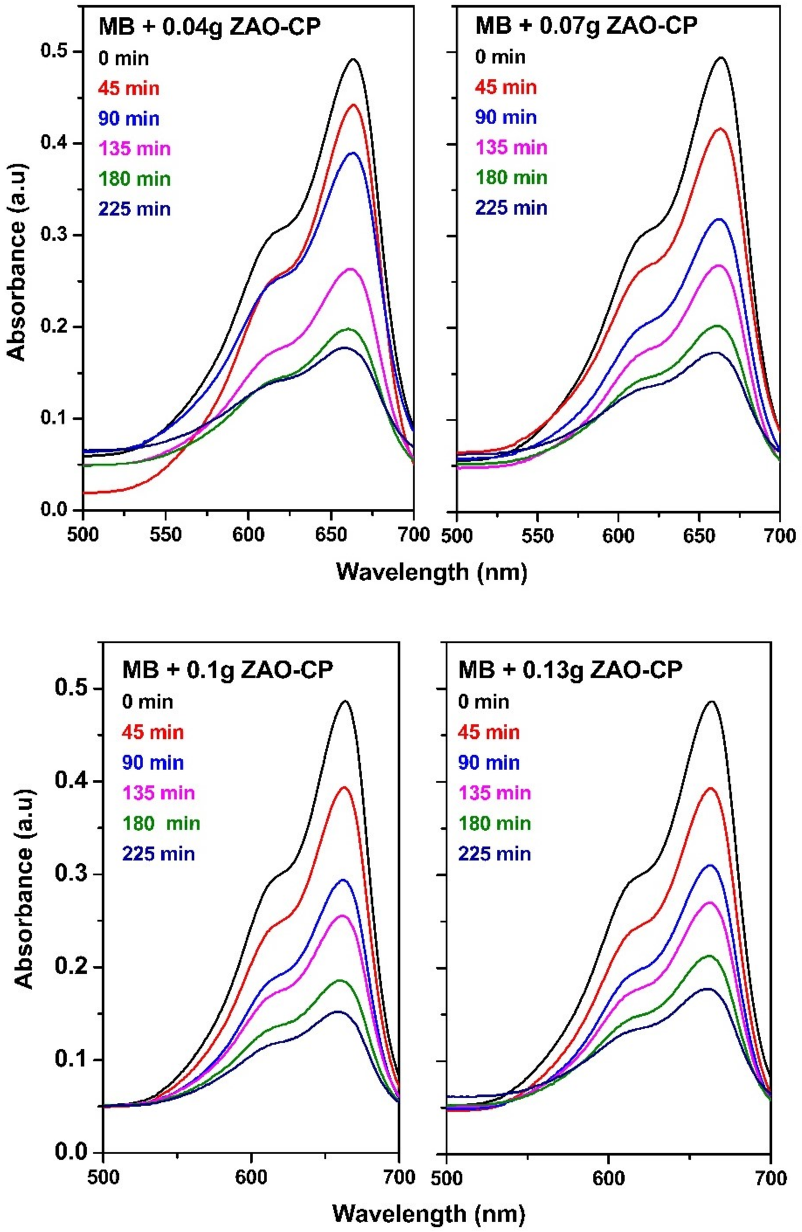

Fig 7.2 Absorbance spectra of methylene blue (MB) dye with ZAO-CP at various catalyst concentrations

However, in the presence of the synthesized ZAO-CP, a decrease in absorbance of MB dye is always noted, confirming that the material's presence effectively accelerates the photocatalytic degradation process. The degradation for the dye alone is 60.79%, while it increases to 74.89% in the presence of the catalyst at 225 minutes (figure 7.3).

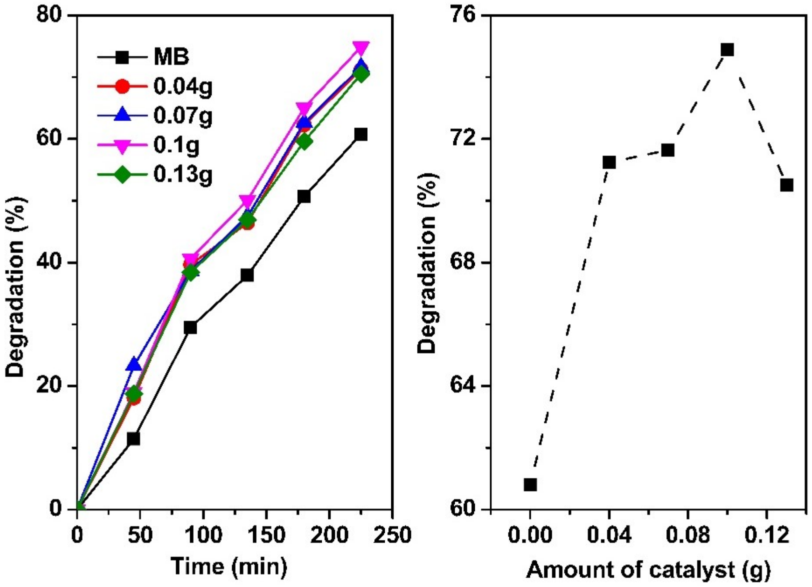

Fig 7.3 Degradation (%) versus time for 0.04 – 0.13 g of catalyst ZAO-CP (left) Degradation (%) versus amount of catalyst at 225 minutes (right)

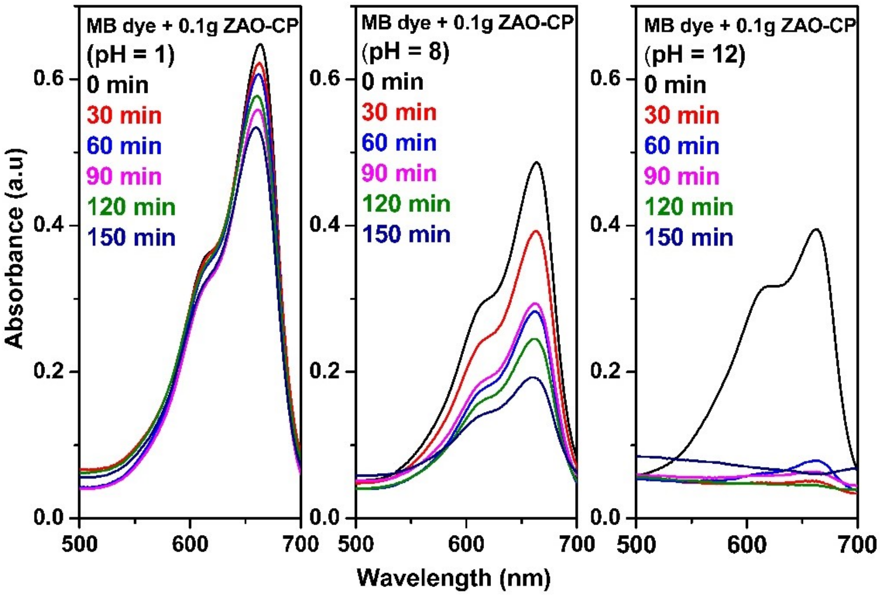

Fig 7.4 Absorbance spectra of MB dye with ZAO-CP for varying pH

In-order to understand the effect of pH on the catalytic activity, the experiment was carried out in acidic (pH = 1) and alkaline (pH = 12) conditions with 0.1g of ZAO-CP. The absorbance spectrum (figure 7.4) shows that in acidic conditions, absorbance decreases slowly, and in alkaline conditions it drops at a faster rate.

As the pH increases from acidic to alkaline, the % of degradation at 150 minutes, say, increases from 17.69 (pH = 1) to 59.6 % at pH = 8 and further to 89.85 % at pH = 12 (figure 7.5). This behaviour is attributed to the influence of pH on the surface charge and ionization state of the catalyst. In acidic environments, the catalyst surface becomes positively charged due to hydronium ions, whereas in alkaline conditions, it becomes negatively charged due to hydroxyl groups, thereby affecting dye molecule adsorption and surface reactions.

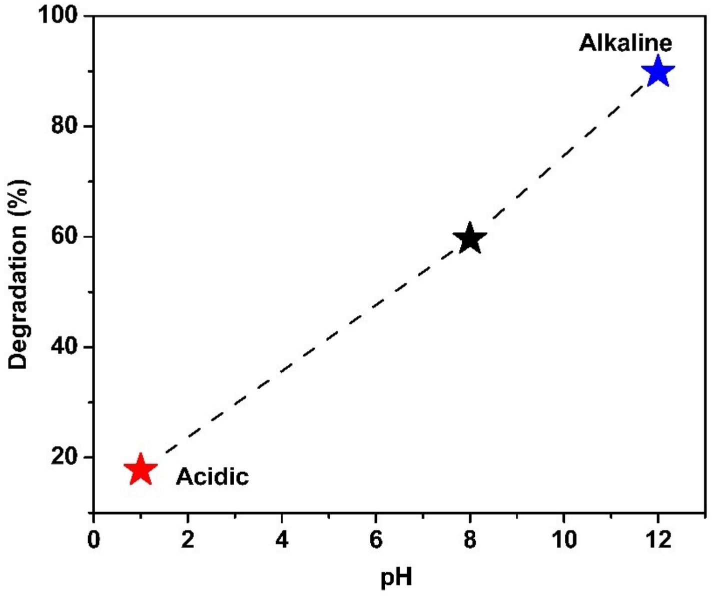

Fig 7.5 Effect of pH on the degradation efficiency of MB dye after 150 minutes with ZAO-CP as the photocatalyst

Based on the above observations, the photocatalytic activity of pure $ZnAl_2O_4$ synthesized via hydrothermal, ZAO-HY (figure 7.6), and auto-combustion methods, ZAO-AU (figure 7.7), was checked fixing the catalyst concentration at 0.1 g and pH at 8.

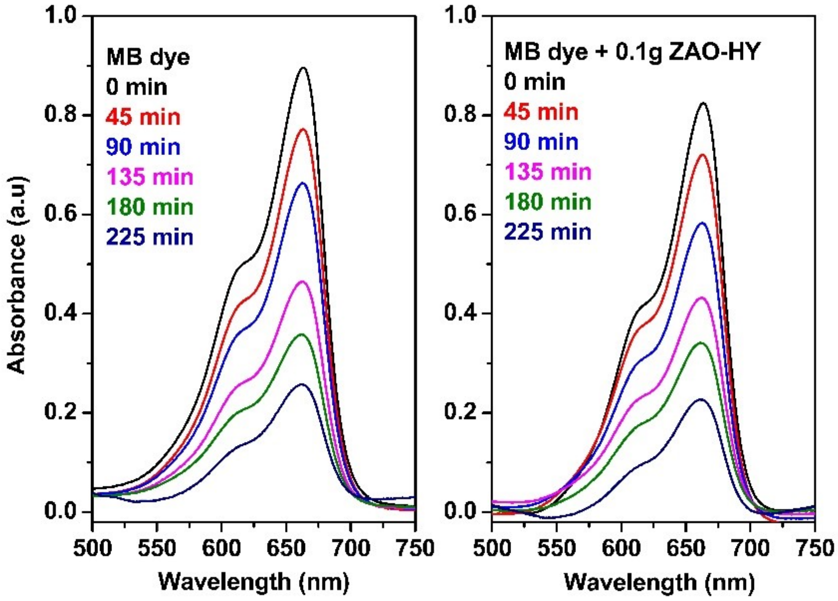

Fig 7.6 Absorbance spectra of MB dye with ZAO-HY (hydrothermal method)

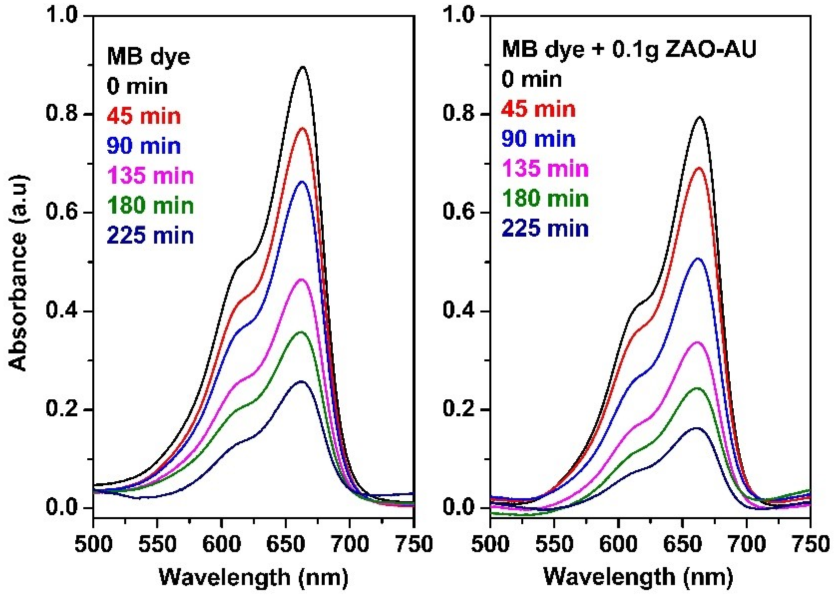

Fig 7.7 Absorbance spectra of MB dye with ZAO-AU (auto-combustion method)

A comparison of degradation efficiencies of all pure samples is depicted in figure 7.8. The hydrothermally synthesized $ZnAl_2O_4$ did not significantly enhance dye degradation, the efficiencies with and without the catalyst were found nearly the same (71.01 and 72.22 % respectively), demonstrating only a 1.21 % increase on adding the catalyst. Pristine $ZnAl_2O_4$ synthesized via leaf extract assisted auto-combustion method demonstrated a better performance with 71.01 and 79.648 % of degradation respectively with and without catalyst, exhibiting 8.638 % increase in degradation efficiency on catalyst addition to MB dye. However, the highest photocatalytic activity was obtained for co-precipitated $ZnAl_2O_4$, that showed a 14.1 % overall increase in catalytic degradation of MB dye. This trend correlates with crystallite size: smaller crystallites provide greater surface area, enhancing adsorption and thereby improving catalytic performance.

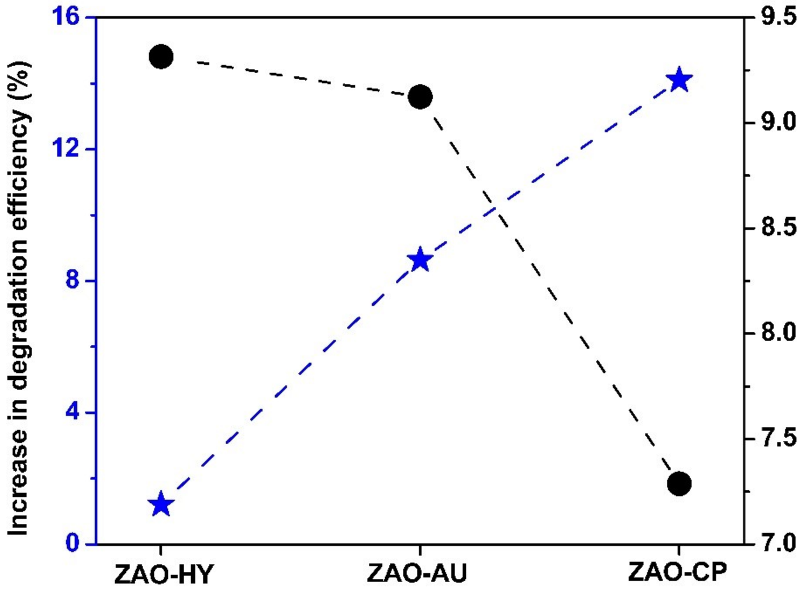

Fig 7.8 Increase in degradation (%) and crystallite size of pure $ZnAl_2O_4$ prepared by various synthesis routes

7.2 In-vitro cytotoxicity against normal and cancer cells:

Nanoparticles show significant role in biomedicine due to their large surface to volume ratio and better physical and chemical properties. They can be applied in targeted drug delivery, bioimaging and therapy. Binary oxides like ZnO were reported to show anti-microbial and anti-cancerous properties [8–11]. But ternary nanoparticles were less explored in this field. Therefore, this study investigates the anti-cancerous activity of the synthesized pure $ZnAl_2O_4$.

$ZnAl_2O_4$ synthesized via the three techniques were studied for short term in vitro cytotoxicity using Dalton's Lymphoma Ascites cells (DLA) or rat spleen cells. The tumour cells or spleen cells aspirated from the peritoneal cavity of tumour bearing mice were washed thrice with phosphate buffered cell line (PBS) or normal cell line. Cell viability was determined by trypan blue exclusion method. Viable cell suspension (1×10^6 cells in 0.1 ml) was added to tubes containing various concentrations of the test compounds and the volume was made up to 1 ml using PBS. Control tube contained only cell suspension. These assay mixtures were incubated for 3 hours at 37 °C. Further, the cell suspension was mixed with 0.1 ml of 1% trypan blue and kept for 2-3 minutes and loaded on a haemocytometer. Dead cells take up the blue colour of trypan blue while live cells do not take up the dye. The number of stained and unstained cells were counted separately.

$$\%\ cytotoxicity = \frac{No.of\ dead\ cells}{No.of\ live\ cells + No.of\ dead\ cells} \times 100$$

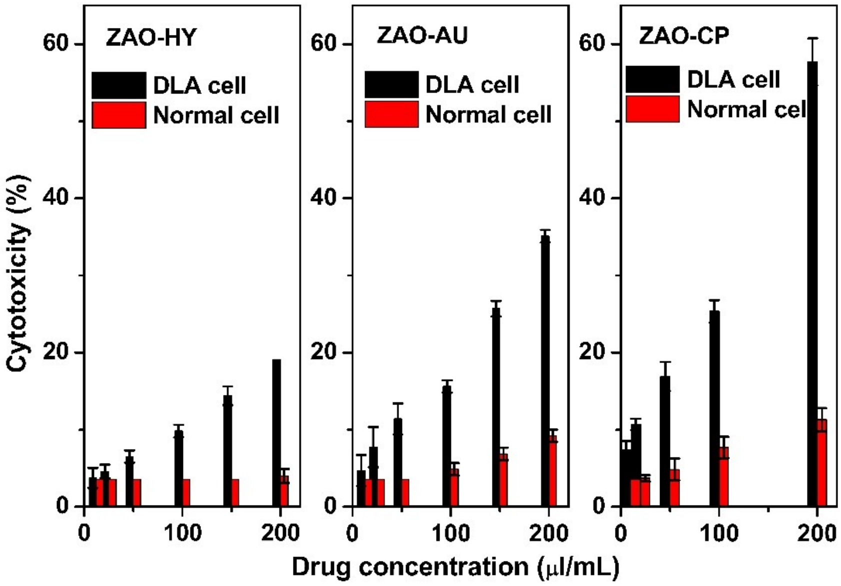

Fig 7.9 Cytotoxicity (%) versus drug concentration of ZAO-HY, ZAO-AU and ZAO-CP

Figure 7.9 gives the percentage of cytotoxicity of pure zinc aluminate synthesized via the three methods against normal and cancer cells. The co-precipitated sample exhibited the highest cytotoxic response of 57.69 % against DLA cells, whereas the samples prepared via the auto-combustion and hydrothermal techniques showed a respective 35.1 % and 19.2 % cytotoxic activity towards tumour cells. However, the activity of ZAO-CP, ZAO-AU and ZAO-HY samples against normal cells were found to be 11.2 %, 9.2 % and 4.01 % respectively. Quite similar to photocatalytic response, the co-precipitated $ZnAl_2O_4$ showed the highest cytotoxicity owing to its comparably low crystallite size. Size reduction increases the surface area and favours more surface interaction with the spleen cells. However, the biocompatibility of the synthesized nanoparticles is quite evident from the comparatively lesser toxicity towards normal cells.

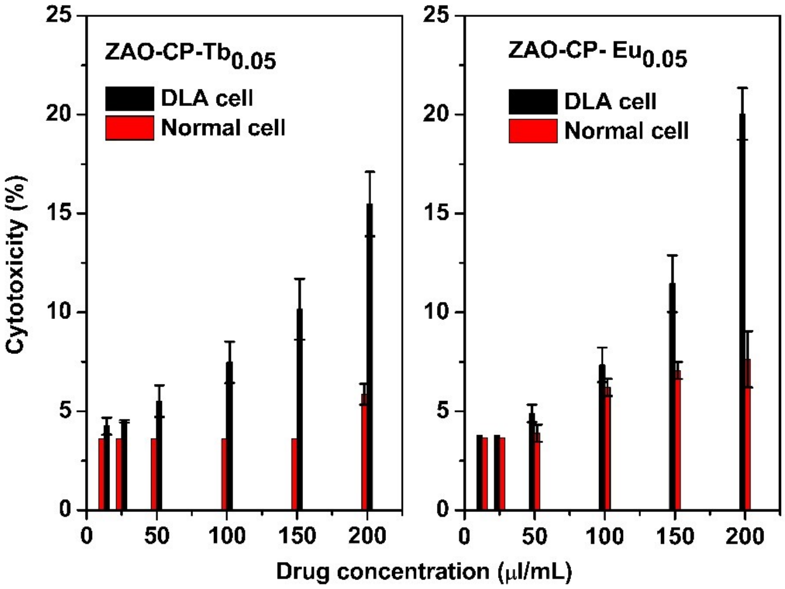

Fig 7.10 Cytotoxicity (%) versus drug concentration of RE doped ZAO-CP

Since, the greater cytotoxic response was from the co-precipitated $ZnAl_2O_4$, the Eu^{3+} and Tb^{3+} doped $ZnAl_2O_4$ (labelled as ZAO-CP-$Eu_{0.05}$ and ZAO-CP-$Tb_{0.05}$ respectively) were also investigated for the in-vitro cytotoxic response against DLA and normal cells. The observations are depicted in figure 7.10. ZAO-CP-$Eu_{0.05}$ and ZAO-CP-$Tb_{0.05}$ samples displayed a respective 20.03 % and 15.48 % cytotoxic activity towards tumour cells. The activity against normal cells was better for ZAO-CP-$Eu_{0.05}$ (7.63 %) whereas it was 5.86 % for ZAO-CP-$Tb_{0.05}$ sample. Overall, the cytotoxic response was commendable, for a rather small dopant concentration, expanding the applicability of the material as a luminescent marker drug.

7.3 Study of green synthesized AB_2O_4 systems

AB_2O_4 spinel nanoparticles with lower bandgap (< 4 eV) are said to owe applications in biomedical fields. Hence, in this study, the ternary chromates synthesized via the novel green route were checked for anti-bacterial and cytotoxic responses.

7.3.1 Anti-bacterial analysis against E-Coli bacteria: Well-diffusion method

Muller Hinton agar (MHA) is a type of growth medium used in microbiology to culture bacterial isolates and test their susceptibility to antibiotics. This medium is nutrient rich and free of inhibitors that could interfere with bacterial growth. Well diffusion is widely used to evaluate antimicrobial activity of plants or microbial extracts. In this method, the agar plate surface was inoculated by spreading a volume of the microbial inoculum over the entire agar surface. A hole with a diameter 6 to 8mm was punched and a volume of 20 to 100 μl of the antimicrobial solution was introduced into the well. The petri dishes were incubated under suitable conditions. Generally, antimicrobial agent diffuses into the agar and inhibits the growth of the test microorganism. The diameter of the inhibition growth zones was then measured and compared with that of the antibiotic that was used as the control.

Fig 7.11 Inhibition zone against E-Coli bacteria

MHA plate was prepared and the bacterial culture, Escherichia coli, was spread on the plate. Four wells (7 mm) were punched and the 100 µl of each sample was pipetted in to the well and Ampicillin disc was placed as a positive control. The plate was incubated for 24 hours and the zone of inhibition was observed (figure 7.11). Here, the green synthesized chromates, zinc chromate (ZCO-AU) and magnesium chromate (MCO-AU) were subjected to the analysis and compared with zinc aluminate (ZAO-AU) and magnesium aluminate (MAO-AU). The ternary chromate samples, ZCO-AU and MCO-AU, showed 20 mm and 18 mm zone of inhibition against E-Coli respectively whereas neither of the aluminate samples exhibited any zone of inhibition. This clearly indicates that the strain Escherichia coli was sensitive towards ternary chromate samples, whereas resistant towards aluminate samples. This is because commonly chromium ions or compounds are toxic to microbial stains, compared to aluminium compounds and have the potential to damage the DNA by entering into the cell [12,13].

7.3.2 In-vitro cytotoxicity against DLA and normal spleen cells of rats:

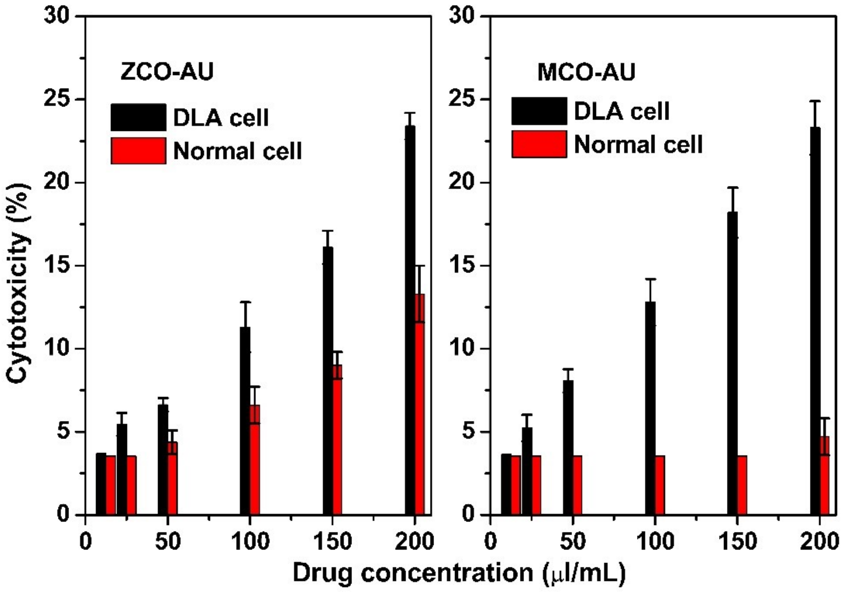

Fig 7.12 Cytotoxicity versus drug concentration of ZCO-AU and MCO-AU

Due to the toxic nature of chromates, they are considered as environmental pollutants and reduced with the help of chromate resistant organisms [14]. For this reason, even though ZCO-AU and MCO-AU were found to be bacterial resistant, their toxicity towards animal cells and biocompatibility had to be checked. Short-term in vitro cytotoxicity of ZCO-AU and MCO-AU was assessed using Dalton's Lymphoma Ascites (DLA) cells and rat spleen cells, with the results presented in figure 7.12. The cytotoxic response of ZCO-AU and MCO-AU were found to be 23.4 % and 23.3 % respectively, slightly lesser when compared to that of the zinc aluminate sample (35.1%). However, the MCO-AU sample exhibited lesser toxicity because of its smaller size, 4.7 %, towards normal cells than ZCO-AU (13.3 %), opening the possibility of bettering their performance in the field of biomedicine in the prospective future works.

7.4 Conclusions

$ZnAl_2O_4$ nanoparticles successfully synthesized using optimised co-precipitation, hydrothermal and auto-combustion routes were subjected to photocatalytic study against methylene blue under sunlight irradiation. The co-precipitated $ZnAl_2O_4$ showed the best performance, presenting a 14.1 % increase in catalytic degradation of MB dye compared to others, confirming the inverse relation between the crystallite size and photocatalytic activity. A similar trend was observed for the in-vitro cytotoxic response against DLA and normal cells, with the highest activity for the co-precipitated $ZnAl_2O_4$, that exhibited a cytotoxicity value of 57.69 %. Though the anti-cancerous response of the sample prepared via the novel moringa leaf extract assisted auto-combustion synthesis was lesser (35.1 %), both the aluminates and chromates prepared via the plant extract mediated process were found to be more biocompatible towards normal cells, revealing an activity less than 10 %. The ternary chromates, ZCO-AU and MCO-AU, demonstrated good inhibition zones in the well-diffusion method, unveiling their anti-bacterial activity against E-Coli bacteria. The simultaneous presence of antimicrobial and in-vitro cytotoxic response in chromate systems opens the possibility of further research in green synthesis for multi-functional ternary nanoparticles with diverse biomedical applications.

References

[1] Foletto, E. L., Battiston, S., Simões, J. M., Bassaco, M. M., Pereira, L. S. F., De Moraes Flores, É. M., & Müller, E. I. (2012). Synthesis of $ZnAl_2O_4$ nanoparticles by different routes and the effect of its pore size on the photocatalytic process. *Microporous and Mesoporous Materials, 163*(1), 29–33. https://doi.org/10.1016/j.micromeso.2012.06.039

[2] Filali, H., Boukheit, N., Bouhroum, R., Chekirou, W., & Karaali, A. (2021). Citrate assisted synthesis of co-doped $ZnAl_2O_4$ with La^{3+} and Pb^{2+} ions and applications: Adsorption–Photocatalysis. *Acta Physica Polonica A, 140*(4), 379–388. https://doi.org/10.12693/APhysPolA.140.379

[3] Pradeev Raj, K., Sadaiyandi, K., Kennedy, A., Sagadevan, S., Chowdhury, Z. Z., Bin Johan, M. R., Aziz, F. A., Rafique, R. F., Thamiz Selvi, R., & Rathina Bala, R. (2018). Influence of Mg doping on ZnO nanoparticles for enhanced photocatalytic evaluation and antibacterial analysis. *Nanoscale Research Letters, 13*(229), 1–12. https://doi.org/10.1186/s11671-018-2643-x

[4] Sumathi, S., & Kavipriya, A. (2017). Structural, optical and photocatalytic activity of cerium doped zinc aluminate. *Solid State Sciences, 65*, 52–60. https://doi.org/10.1016/j.solidstatesciences.2017.01.003

[5] Abd-Allah, A. A., Ahmed, Y. M. Z., El-Sheikh, S. M., Youssef, A. O., & Amin, A. M. M. (2022). Synthesis of zinc aluminate nanoparticles from aluminum/zinc sludge for degradation of brilliant cresyl blue under visible light irradiation. *Journal of Water and Environmental Nanotechnology, 7*(3), 288–305. https://doi.org/10.22090/jwent.2022.03.005

[6] Bazargan, A. (Ed.). (2022). *Photocatalytic water and wastewater treatment*. IWA Publishing. https://doi.org/10.2166/9781789061932

[7] Ayyar, D., Elayaperumal, M., Sethumathavan, V., Kumaravel, M., Duraisamy, M., & Ganesh, H. (2018). Photocatalysis: Present, past and future. *In* Advances in Photocatalysis (pp. 127–148). Arcler Press. https://doi.org/10.21741/9781945291630-7

[8] Zadeh, F. A., Bokov, D. O., Salahdin, O. D., Abdelbasset, W. K., Jawad, M. A., Kadhim, M. M., Qasim, M. T., Kzar, H. H., Al-Gazally, M. E., Mustafa, Y. F., &

Khatami, M. (2022). Cytotoxicity evaluation of environmentally friendly synthesis of copper/zinc bimetallic nanoparticles on MCF-7 cancer cells. *Rendiconti Lincei, 33*(2), 441–447. https://doi.org/10.1007/s12210-022-01064-x

[9] Saranya, S., Vijayaranai, K., Pavithra, S., Raihana, N., & Kumanan, K. (2017). *In vitro* cytotoxicity of zinc oxide, iron oxide and copper nanopowders prepared by green synthesis. *Toxicology Reports, 4*, 427–430. https://doi.org/10.1016/j.toxrep.2017.07.005

[10] Agarwal, H., Menon, S., Kumar, S. V., & Rajeshkumar, S. (2018). Mechanistic study on antibacterial action of zinc oxide nanoparticles synthesized using green route. *Chemico-Biological Interactions, 286*, 60–70. https://doi.org/10.1016/j.cbi.2018.03.008

[11] Kalra, K., Chhabra, V., & Prasad, N. (2022). Antibacterial activities of zinc oxide nanoparticles: A mini review. *Journal of Physics: Conference Series, 2267*(1), 012049. https://doi.org/10.1088/1742-6596/2267/1/012049

[12] Mala, J. G. S. M., Takeuchi, S., Sujatha, D., & Mani, U. (2020). Microbial chromate reductases: Novel and potent mediators in chromium bioremediation—A review. *Applied Microbiology: Theory & Technology, 2*(2), 32–44. https://doi.org/10.37256/amtt.112020222

[13] Herrera, K. M. S., Ferreira, L. S., Braga, A. V., Souza, J. P., Andrade, J. T., Soares, A. C., Soares, L. F., Chagas, R. C. R., & Ferreira, J. M. S. (2019). Synthesis, characterization and antimicrobial activity of Cr(III), Co(II) and Ni(II) complexes with 2-thiazoline-2-thiol derivative ligands against bacteria and yeasts of clinical importance. *Anais da Academia Brasileira de Ciências, 91*(1), e20180777. https://doi.org/10.1590/0001-3765201 81077

[14] Liu, Z., Wu, Y., Lei, C., Liu, P., & Gao, M. (2012). Chromate reduction by a chromate-resistant bacterium, *Microbacterium* sp. *World Journal of Microbiology and Biotechnology, 28*(4), 1585–1592. https://doi.org/10.1007/s11274-011-0962-5

Chapter 8

SUMMARY AND FUTURE RECOMMENDATIONS

The summary of the entire work along with significant conclusions are presented in this chapter. A comparison between the three synthesis routes adopted and the findings are outlined. The luminescent and biomedical applications are also discussed.

8.1 Summary

The chapter focusses on the inferences made from the preceding chapters and the prospects of the present work. The aim of the work was to optimize the three chosen non-ceramic routes - co-precipitation, hydrothermal and auto-combustion – to check its viability to facilitate nanophosphor synthesis at temperatures well below 1000 °C, generally preferred for solid state synthesis of oxide systems. The luminescent response of the synthesized singly-doped and co-doped AB_2O_4 ternary spinel oxide systems are detailed. Some initial investigations into the photocatalytic, cytotoxic, and anti-bacterial response of selected systems are also presented.

The cost-effective and energy-efficient non-ceramic techniques - co-precipitation and hydrothermal – were optimized for synthesising pure and RE (RE = Eu, Tb) doped ternary $ZnAl_2O_4$ spinel oxide. The precursors used in both methods were nitrate solutions of cations of appropriate molarity and pH of the final homogenous solution was maintained using ammonia.

Parameter	Co-precipitation method	Hydrothermal route
Zn:Al	1:2	1:2
pH	10	10
Temperature of synthesis procedure	No heating required	250 °C for 4 hours (As-prepared sample itself showed spinel peaks)
Post-calcination temperature	750 °C for 2 hours (Spinel formed at 300 °C itself)	750 °C for 2 hours
Crystalline size (nm)	• Scherrer formula: 7.288 nm • W-H plot: 8.077 nm • TEM: 7.106 ± 1.255 nm	• Scherrer formula: 9.315 nm • W-H plot: 9.585 nm
EDAX raio	Zn:Al = 1:2.19	Zn:Al = 1: 1.98
Bandgap	4.8 eV	4.73 eV
Pure $ZnAl_2O_4$	Color: violet-blue	Color: violet-blue

Table 8.1 A comparison of the optimized synthesis parameters and properties of pure $ZnAl_2O_4$

A comparison of the optimized synthesis parameters and optical bandgap of pristine samples are summarized in table 8.1. RE doping in host $ZnAl_2O_4$ was done with Eu^{3+} and Tb^{3+} ions. Dopant incorporation was evident from the shift in peak position of the (311) plane and FWHM variations. All samples showed a lattice expansion since dopant ions of larger ionic radius replaces the host cations. A comparison of the luminescent response of the singly- and co-doped samples by either method is presented in table 8.2.

On doping the host with Eu^{3+} ion, the dominant emission at 615 nm results, attributed to the crystal field enhanced electric dipole $^5D_0 \rightarrow {}^7F_2$ transition at non-centrosymmetric sites. When doped with Tb^{3+} ion, the dominant emission at 544 nm results, owing to its magnetic dipole $^5D_4 \rightarrow {}^7F_5$ transition. Beyond a specific value, concentration quenching effects were observed in the doped systems. The major luminescent response could be attributed to host-sensitized non-radiative resonant energy transfer from host to activator ions mediated by exchange interactions, confirmed by Dexter theory. A model of the energy band diagram was also proposed for each system.

Parameter	Co-precipitation method	Hydrothermal route
Doping concentration	• Eu: x = 0.01 – 0.15 M • Tb: y = 0.03 – 0.09 M	• Eu: x = 0.01 – 0.1 M • Tb: y = 0.01 – 0.08 M
Phenomenon	Non-radiative resonant energy transfer from host to activator ions at non-centrosymmetric sites mediated by exchange interactions	Non-radiative resonant energy transfer from host to activator ions at symmetric sites mediated by exchange interactions
Exchange interaction parameter θ (Dexter theory)	• Eu: 2.058 • Tb: 2.55	• Eu: 2.022 • Tb: 1.947
$ZnAl_{2-x}O_4:Eu_x$	• Peak wavelength: 615 nm • Color: Purplish pink • Max. PL intensity: 0.1 M • CIE (x, y) = (0.451, 0.275) • Color purity: 44.45 %	• Peak wavelength: 615 nm • Color: Purplish pink • Max. PL intensity: 0.05 M • CIE (x, y) = (0.393, 0.294) • Color purity: 25.71 %
$ZnAl_{2-y}O_4:Tb_y$	• Peak wavelength: 544 nm • Color: Green • Max. PL intensity: 0.07 M • CIE (x, y) = (0.296, 0.672) • Color purity: 93.29 %	• Peak wavelength: 544 nm • Color: Green • Max. PL intensity: 0.05 M • CIE (x, y) = (0.239, 0.714) • Color purity: 91.14 %
$ZnAl_{2-(x+y)}O_4:Eu_xTb_y$ (λ_{exc} = 230 nm)	Green to yellowish white	Green to yellowish white
$ZnAl_{2-(x+y)}O_4:Eu_xTb_y$ (λ_{exc} = 250 nm)	• Near-white • Best sample showed CIE (x, y) = (0.344, 0.318) and color purity – 7.13 %	• Near-white • Best sample showed CIE (x, y) = (0.282, 0.292) and color purity – 19.98 %

Table 8.2 A comparison of the luminescent response of the singly- and co-doped samples by co-precipitation and hydrothermal method

The study discusses a novel green synthesis route to prepare ternary aluminate spinels - moringa leaf extract assisted auto-combustion method. This eco-friendly approach avoids toxic fuels and the plant extract acts the role of the binder and the stabiliser.

The nucleation of most of the AB_2O_4 (A = Zn, Mg and B = Al, Cr) systems initiated in the as-prepared stage itself. Crystallinity was improved through post-synthesis heat treatment. EDAX validated an elemental composition of 1:2.03, while a bandgap of 4.95 eV was observed for pure $ZnAl_2O_4$. PL studies revealed the self-luminescent violet-blue emission from pure $ZnAl_2O_4$, and the host-sensitised green and red emissions on doping with Tb^{3+} and Eu^{3+} ions, respectively. Co-doping led to structural changes visible in the XRD patterns and resulted in a near-white luminescent emission, when excited at 250 nm, confirmed by chromaticity coordinates. A color purity of 15.13 % was obtained for the sample with 1:1 Eu/Tb ratio and CIE coordinate (x, y) = (0.329, 0.392).

To summarize, ternary aluminate spinel systems was successfully synthesized via three non-refractory methods - co-precipitation method, hydrothermal method and moringa leaf extract assisted auto-combustion. Auto-combustion was the fastest route, since the overall process ended up in 2 ½ hours, heating being done on a hot plate. Co-precipitation method was time consuming, that needed 24 hours for the precipitate to settle down, but required no prior heating other than post-calcination. Hydrothermal treatment was less time consuming compared to co-precipitation, which required 4 hours of heat treatment at 250 °C in an autoclave under high pressure prior to calcination. The ratio of the product yield from all the three methods - co-precipitation: hydrothermal: auto-combustion was determined to be 2:1:3.

The structural parameters, crystallite size and lattice parameter for the zinc aluminate nano powders prepared via the three methods are compared in figure 8.1.

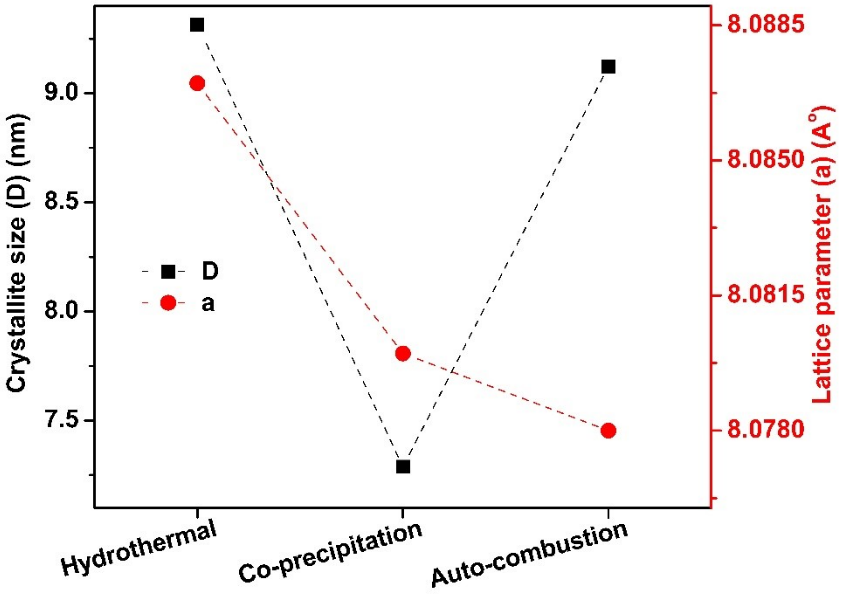

Fig 8.1 Crystallite size and lattice parameter variation with respect to synthesis method adopted for $ZnAl_2O_4$

On comparison, it was observed that the method of co-precipitation is optimum since, it gives particles with least crystallite size and the most comparable lattice parameter with the standard data (JCPDS 05-0669). The photoluminescent performance was also better for the co-precipitated $ZnAl_2O_4$ in the pure as well as doped matrices compared to the other two methods. The plant extract assisted green approach stands out as a novel approach for synthesising ternary nanoparticles, excluding toxic precipitating agents or fuels, being less time consuming providing highest yield with minimum equipment support.

Chapter 7 discussed the photocatalytic, anti-cancerous and anti-bacterial investigations done in selected systems synthesized in the present work. The photocatalytic investigations in co-precipitated sample were done in more detail. It was found that the best performance could be observed at an alkaline pH of 8 on adding an optimum 0.1 gram of catalyst to the dye. Table 8.3 summarizes the results of the studies carried out.

Property	ZAO-CP	ZAO-AU	ZAO-HY
Degradation efficiency of methylene blue increased by	14.10 %	8. 64 %	1.21 %
In-vitro cytotoxicity towards tumour cells	57.69 %	35.10 %	19.20 %
In-vitro cytotoxicity towards normal cells	11.20 %	9.20 %	4.01 %

Table 8.3 Summary of photocatalytic and anti-cancerous studies using pure $ZnAl_2O_4$

The co-precipitated sample showed superior photocatalytic capability and highest cytotoxicity against DLA cells, and a good response towards normal cells, all associated to its least crystallite size (figure 8.2).

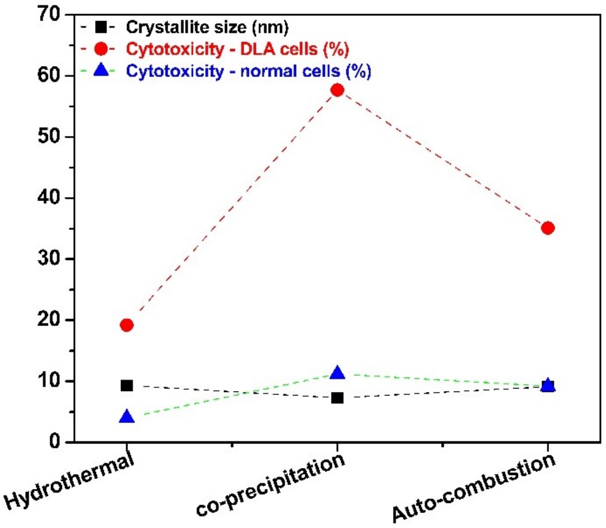

Fig 8.2 Effect of crystallite size on cytotoxic response of pure $ZnAl_2O_4$

After doping with 0.05 M of Eu and Tb, the co-precipitated $ZnAl_2O_4$ displayed a respective 20.03 % and 15.48 % cytotoxic activity towards tumour cells, and a respective 7.63 % and 5.86 % activity against normal cells – a commendable response for a rather small dopant concentration, expanding the applicability of the material as a luminescent marker drug. The sample prepared via the plant extract assisted auto-combustion method also gave a biocompatible result, next to the co-precipitated sample.

On conducting anti-bacterial studies in the samples synthesized via the green auto-combustion approach, ZCO-AU and MCO-AU showed a 20 mm and 18 mm zone of inhibition against E-Coli respectively, whereas neither of the aluminate samples exhibited any zone of inhibition. Also, the cytotoxic response of ZCO-AU and MCO-AU were found to be 23.4 % and 23.3 % respectively towards tumour cells, slightly lesser when compared to that of the corresponding pure sample (35.1%). Their response towards normal cells were respectively determined to be 13.3 % and 4.7 %, opening the possibility of bettering their performance in the field of biomedicine in the prospective works. The combined antimicrobial and in-vitro cytotoxic effects observed in chromate systems suggest promising potential for green synthesis approaches in developing multifunctional ternary nanoparticles for various biomedical applications.

8.2 Future recommendations

While the present study has successfully met its primary objectives, there remains scope for further exploration. Future work may include refining the co-precipitation, hydrothermal, and auto-combustion methods using various combinations of rare-earth and transition metal dopants. In addition to co-doping, the possibility of attaining white luminescence can be explored with single dopants like Dysprosium or enhanced tunable responses can be checked by incorporating ions such as Cerium into the host matrix. Since the synthesized AB_2O_4 spinels present strong cytotoxic effects against tumour cells, their potential use as luminescent drug marker warrants further investigation. Additionally, fabricating thin films from these powders using techniques such as spray pyrolysis and spin coating could open new application areas. The green auto-combustion method using moringa leaf extract could also be extended by experimenting with other plant parts or sources or integrating microwave-assisted combustion.

UNIVERSITY OF CALICUT
CERTIFICATE ON PLAGIARISM CHECK

1.	Name of the Research Scholar	VINITHA N	
2.	Title of thesis / dissertation	SYNTHESIS AND CHARACTERIZATION OF RARE EARTH DOPED TERNARY SPINEL MATRICES USING NON-CERAMIC ROUTES FOR LUMINESCENT AND BIOMEDICAL APPLICATIONS	
3.	Name of the Supervisor	DR MINI KRISHNA K	
4.	Department/Institution	DEPARTMENT OF PHYSICS, VIMALA COLLEGE (AUTONOMOUS), THRISSUR	
5.	Similar content (%) identified	Non Core	Core
		Introduction/ Theoretical overview/Review of literature/ Materials & Methods/ Methodology	**Analysis/Result/Discussion / Summary/Conclusion/ Recommendations**
		6	**3**
	Acceptable maximum limit (%)	10	10
6.	Software used	iThenticate	
7.	Date of verification	19.09.2025	

**Report on plagiarism check, specifying included/excluded items with % of similarity to be attached.*

Dr. Nasirudheen. T
Assistant Librarian
University of Calicut, Kerala.

Checked by (with name , designation & signature)

Name and signature of the Researcher VINITHA N Vinitha

Name and signature of the Supervisor. Dr. Mini Krishna K

The Doctoral Committee* has verified the report on plagiarism check with the contents of the thesis, as summarized above and appropriate measures have been taken to ensure originality of the Research accomplished herein.

Name & Signature of the HoD/HoI (Chairperson of the Doctoral Committee)

PRINCIPAL-IN-CHARGE
VIMALA COLLEGE
(AUTONOMOUS)
THRISSUR - 680 009

**In case of languages like Malayalam, Tamil etc..on which no software is available for plagiarism check, a manual check shall be made by the Doctoral Committee, for which an additional certificate has to be attached.*